

Traceable Radiometric Calibration of Synthetic Aperture Radars

Zur Erlangung des akademischen Grades eines

Doktor-Ingenieurs

von der Fakultät für
Elektrotechnik und Informationstechnik
des Karlsruher Instituts für Technologie (KIT)

genehmigte

Dissertation

von

Dipl.-Ing. Björn J. Döring
geb. in Berlin

Tag der mündlichen Prüfung: 23. Februar 2016

Hauptreferent: Prof. Dr.-Ing. habil. Alberto Moreira

Korreferent: Prof. Dr.-Ing. habil. Jürgen Detlefsen

Preface

Measurements, in one form or another, have always been a part of my life. Already as a boy I built up little circuits and tried to correct my mistakes with the simple measurements I made. During my studies I have especially appreciated combining theory and the touchable, measurable world, and measurements are just at that boundary. Now, as the years have passed, it is somewhat consequential that I ended up working on measurements for my thesis, or more particularly on radiometric measurements, calibration, and traceability in the context of synthetic aperture radar (SAR).

This manuscript was prepared whilst I was employed at the Microwaves and Radar Institute of the German Aerospace Center (DLR). The topic “calibration of SAR systems” has seen an increased demand in recent years due to ever more demanding requirements and the advent of modern SAR systems. It has been exciting to witness and contribute a little bit to this development myself, and I wish for the SAR community to keep on pushing. The principle is synthetic, but the results are real!

I am grateful for all the support that I received throughout this research project. First of all, I am indebted to Prof. Alberto Moreira, the director of our research institute and my doctoral adviser, whose encouragement and commitment to this work were paramount for completing this dissertation. My sincere thanks also go to Prof. Jürgen Detlefsen for assuming the role of co-examiner.

Throughout the years I have received perpetual backing and support from Dr. Marco Schwerdt and Dr. Manfred Zink, from whom I did not only learn many insights on radiometric calibration and calibration at large, but also more generally many insights on work organization and project management.

Special thanks go out to the colleagues from the Calibration Group, who offered me the opportunity for having countless enlightening discussions, and with whom starting a new work day has always been something to look forward to.

Thanks to my colleagues, the working environment at our institute and the immense expertise, which is often just a few doors away, have been outstanding. In particular I would like to thank Dr. Matthias Jiroušek, Dr. Josef Mittermayer, Dr. Andrey Osipov, and Dr. Rolf Scheiber for many informed discussions. Dr. Thomas Jagdhuber has been a good friend in innumerable situations. The commitment to excellency from Peter Heitzer and Bernd Gabler have always been exceptional. My thanks also go to Dr. Markus Bachmann, Dr. Benjamin Bräutigam, Thomas Krauss, Dr. Jens Reimann, Paola Rizzoli, and Dr. Kersten Schmidt for helping to proofread this manuscript. I have especially enjoyed the company of Dr. Andreas Danklmayer, Sebastian Raab, Daniel Rudolf, and Dirk Schrank with whom I had the privilege to share an office for some time throughout the years. Many colleagues remain unmentioned, but may they all be thanked for the plentiful valuable moments spent together at DLR.

Work is not everything, and I would like to especially thank my parents and family, who never stopped to encourage me and therefore made sure that I kept on track.

And most of all I thank my inconceivably patient, understanding, and encouraging wife Perrine who has charmingly endured far too many work-centered weekends and without whose support this work would not have been possible. You are awesome, thank you!

Contents

1	Introduction	1
1.1	State of the Art in Radiometric SAR Calibration	2
1.2	Problem Statement	4
1.3	Contributions and Thesis Structure	5
2	Fundamentals of SAR and Calibration	7
2.1	Synthetic Aperture Radar Principles	7
2.1.1	Image Formation for Point Targets	7
2.1.2	Imaging Geometries	10
2.1.3	The Range-Doppler Algorithm	11
2.1.4	Distributed Targets	13
2.2	Measurement, Calibration, and Traceability Principles	14
2.2.1	Measurements and Measurement Quantities	14
2.2.2	The Guide to the Evaluation of Uncertainty in Measurement . . .	15
2.2.3	Calibration	19
2.2.4	Metrological Traceability	20
2.3	Fundamentals of Radiometric SAR Calibration	21
2.3.1	Influences on Radiometric Measurements and General Calibration Approach	21
2.3.2	Terminology in SAR Calibration	24
2.3.3	The Integral Method for Radiometrically Calibrating Distributed Targets	24
2.4	Typical SAR Calibration Point Targets and Properties	28
2.4.1	Point Target Properties	29
2.4.2	Trihedral Corner Reflectors	30
2.4.3	Transponders	33
2.4.4	Other Passive Calibration Point Targets	37
3	Novel Definition of the Radiometric Measurement Quantity	45
3.1	Introduction	45
3.2	Review of the Current Definition	46

3.3	Problems Arising from the Current Definition	47
3.3.1	Pulse Compression in the Complex Domain	47
3.3.2	Integration Intervals and Weighted Means: Qualitative Examples	48
3.4	Novel Definition of the Radiometric Measurement Quantity	51
3.5	Implications of Proposed Terminology for Calibration	52
3.6	Discussion of Novel Quantity	54
3.7	Conclusions	55
4	Novel Method for Relating Point Target Properties to ERCS	57
4.1	Motivation and Principle	57
4.2	Implementation of the Point Target SAR Simulator	60
4.3	Quantitative Analyses: Link Between Target Properties and ERCS	61
4.3.1	RCS Dependence on Frequency and Angle: Calibration Transponder	61
4.3.2	Frequency-Dependent Phase Response: Ionosphere	67
4.4	Discussion	69
4.5	Conclusions	69
5	The SAR Passband Problem: Analytical Model and Practical Solutions	71
5.1	Introduction and Example	71
5.2	Apodization Functions in SAR Processing	74
5.3	Modeling Passband Effects with Central Moments	75
5.3.1	Derivation of the Governing Equation	77
5.3.2	Modeling with Central Moments: One-Dimensional Case	78
5.3.3	Extension to the Two-Dimensional Case	80
5.4	Quantitative Examples and Verification	82
5.5	Resolving the Passband Problem	89
5.5.1	Accepting Higher Radiometric Uncertainties	89
5.5.2	Introducing Standardized Passbands	89
5.5.3	Conversion Between Different Scales	90
5.6	Conclusions	91
6	The Three-Transponder Method	93
6.1	Introduction	93
6.2	Existing Approaches for Measuring the Transponder RCS	94
6.2.1	Measuring the Loop Gain	94
6.2.2	The Substitution Method	95
6.2.3	The Transponder as a Radar Instrument	96
6.3	The Three-Transponder Method Principle	97
6.3.1	The Three Antenna Method	98

6.3.2	Prerequisites on Transponder Design	99
6.3.3	System of Linear Equations	99
6.3.4	Random Variables, 3TM Equations, and GUM	101
6.3.5	The Maximum-Likelihood versus the James-Stein Estimator	104
6.4	Demonstration Measurement Campaign with DLR's C-Band Transponders	110
6.4.1	Measurement Setup	110
6.4.2	Measurement Data Analysis	113
6.4.3	Uncertainty Analysis and Results	119
6.4.4	Discussion of Measurement Results	123
6.5	Method Extension for an Inherent Plausibility Check	124
6.5.1	Description of the 3TM Method Extension	124
6.5.2	Formulation of Hypothesis Test – Gaussian Distributions	125
6.5.3	Derivation of Hypothesis Rejection Conditions	127
6.5.4	Practical Implications and Conclusions	129
6.6	Discussions of the Three-Transponder Method	129
6.6.1	Advantages	129
6.6.2	Limitations	130
6.6.3	Open Points	130
6.7	Conclusions	131
7	Derivation of Calibration Parameters Through Hierarchical Bayesian Data Analysis	133
7.1	Introduction	133
7.2	Methodology for Radiometric Parameter Estimation from SAR Data Through Bayesian Statistics	135
7.2.1	Hierarchical Models	135
7.2.2	Summary of Method	137
7.3	Case Study: Measurement Campaign Goal and Setup	138
7.3.1	Introduction and Goal	138
7.3.2	Campaign Setup and Reference Targets	138
7.4	Case Study: Data Analysis and Results	139
7.4.1	Overview	140
7.4.2	Energy Estimation for Point Targets from SAR Images	140
7.4.3	Bayesian Statistics and Hierarchical Model Fitting	141
7.4.4	Posterior Predictive Checks: Model Verification	149
7.4.5	Plausibility Check with Classical Statistics	149
7.5	Discussion of Hierarchical Bayesian Data Analysis for Radiometric Calibration	150
7.6	Conclusions	151

8	Conclusions and Outlook	153
A	Pseudo Code for the Method of Point Target SAR Simulation	157
B	Functions of Random Variables	161
B.1	Moments of Functions of Random Variables	161
B.2	Sum and Subtraction of Two Random Variables	164
B.3	Convolution and Correlation of Two Gaussian PDFs	165
B.4	Multiplication of Random Variables	167
C	Introduction to Bayesian Statistics and to the Markov Chain Monte Carlo Method	169
C.1	Bayesian Statistics	169
C.2	Bayesian Computations and Markov Chain Monte Carlo Methods	170
	Glossary	173
	Acronyms	175
	Notation	179
	Symbols and Notational Conventions	179
	Greek Letters	179
	Roman Letters	181
	Bibliography	187

1 Introduction

Synthetic aperture radar (SAR) is a unique and well established approach for remote sensing which provides high-resolution two-dimensional and three-dimensional digital images independent of daylight or cloud coverage [32, 33, 56, 131, 193]. Spaceborne SAR systems such as the current TerraSAR-X [198], TanDEM-X [103], RADARSAT-2 [125], and Sentinel-1 [189] systems continuously yield data from extensive areas of the globe with a revisit time in the order of days. Airborne systems, on the other hand, map on a more local scale but can offer lower revisit times, higher resolutions, or application-adapted hardware such as for multi-spectral acquisitions.

The utilizations for the acquired SAR data range from mapping of land use (forest, water, agriculture, urban) to change detection based on time series, monitoring of sea ice, marine surveillance, traffic monitoring, applications in geoscience such as glacier and land surface motion monitoring, soil moisture and biomass estimation, and quick-response mappings to support humanitarian aid in crisis situations. The constantly growing number of applications is to a large degree due to advancements in instrument hardware and data processing approaches. Modern SAR systems now support phased-array antennas for a flexible antenna beam steering, more than one transmit and receive channel for interferometric and polarimetric applications [149, 212], and advanced commanding and processing techniques such as spotlight, ScanSAR, and TOPS [32, 136].

A SAR system is not simply a tool for remote feature detection, but it is also a measurement instrument to record geolocated terrain reflectivity. As for any other measurement instrument, system calibration is hence necessary to ensure that different SAR acquisitions are comparable to each other. Calibration in SAR is a corner stone for scientific applications as well as for verifiably reliable products for a growing commercial market.

The SAR calibration activities are usually split into geometric and radiometric calibration [61]. In geometric calibration, the SAR image coordinate system is compared with a reference coordinate system, and corrections are determined and applied to ensure that SAR images are geolocated with respect to a known coordinate system. Radiometric calibration, on the other hand, is not concerned with the location but the magnitude of each image pixel. Again the goal is to express the measured pixel magnitudes on a known radiometric scale to achieve comparability across different SAR images. Both types of calibration depend on measurement standards such as corner reflectors, which have an accurately known location and reflectivity.

Despite the tremendous advancements in SAR and its applications during the last decades, radiometric calibration itself has not received the amount of attention it warrants. Techniques such as the pseudo-noise gating method for the drift compensation of

individual antenna modules [163], or the introduction of an antenna pattern model [11] have greatly improved the correction of relative, systematic effects in SAR, but fundamental problems remain to be solved in radiometric calibration itself. In the following, the current status of radiometric calibration is reviewed and problems with the current approach are discussed, which summarize the starting point for this work.

1.1 State of the Art in Radiometric SAR Calibration

Radiometric SAR calibration is the prerequisite for relating the radar reflectivity of a measured point or distributed target to the reflectivity of a (known) measurement standard, and therefore a known measurement unit. After radiometric calibration, the gray-scale values in a typical SAR image indicating the magnitude of the reflectivity can be traced back to a realization of the measurement unit radar cross section (RCS) (for point targets) or normalized radar cross section (for distributed targets) [33, 61].

Radiometrically calibrating a SAR system is a challenging task. The complete signal transmission path needs to be regularly monitored and characterized, and detected deviations need to be compensated. With the introduction of advanced SAR modes like polarimetry, multi-channel acquisitions, interferometry, and complex, phased array antennas more subsystems than ever before need to be characterized and included in any calibration effort. Yet the basic radiometric calibration principle has remained unchanged over the years and is still a two-step process, see Fig. 1.1:

1. The first step is *radiometric normalization* [24]. Normalization is concerned with the estimation and correction of relative effects. This step includes antenna pattern and amplifier thermal drift compensation, characterization of polarization mismatches, atmospheric corrections, hardware frequency response compensations, and the correction of beam-to-beam offsets. Some of these relative contributions have to be estimated and corrected at least once for every overpass.

A system which is not well normalized appears to be less precise than a well corrected system, i. e., measurement results are not as reproducible as for a system that is well normalized.

2. The second step is *radiometric calibration*. Through radiometric calibration, a link between the indication value (a digital number representing the radar reflectivity) and a reference reflectivity is established. A comparison between measurements acquired by different sensors is meaningful only after radiometric calibration. This calibration is the prerequisite for many physical parameter inversion problems, and it also permits data continuity across mission lifetimes, e. g. in the case of the Sentinel-1 satellites.

Radiometric calibration is achieved through measurements of targets with a known radar reflectivity. The two most common radiometric measurement standards today are trihedral corner reflectors and active radar calibrators (transponders) [61, 161, 164], whose design parameters determine their RCS. In rare cases, distributed targets (rain forest) have also been used for the radiometric calibration of SAR systems [112, 168].

Under the assumption of a sufficiently stable SAR instrument, radiometric calibration is only repeated in the order of years, i. e., a repetition is not required for

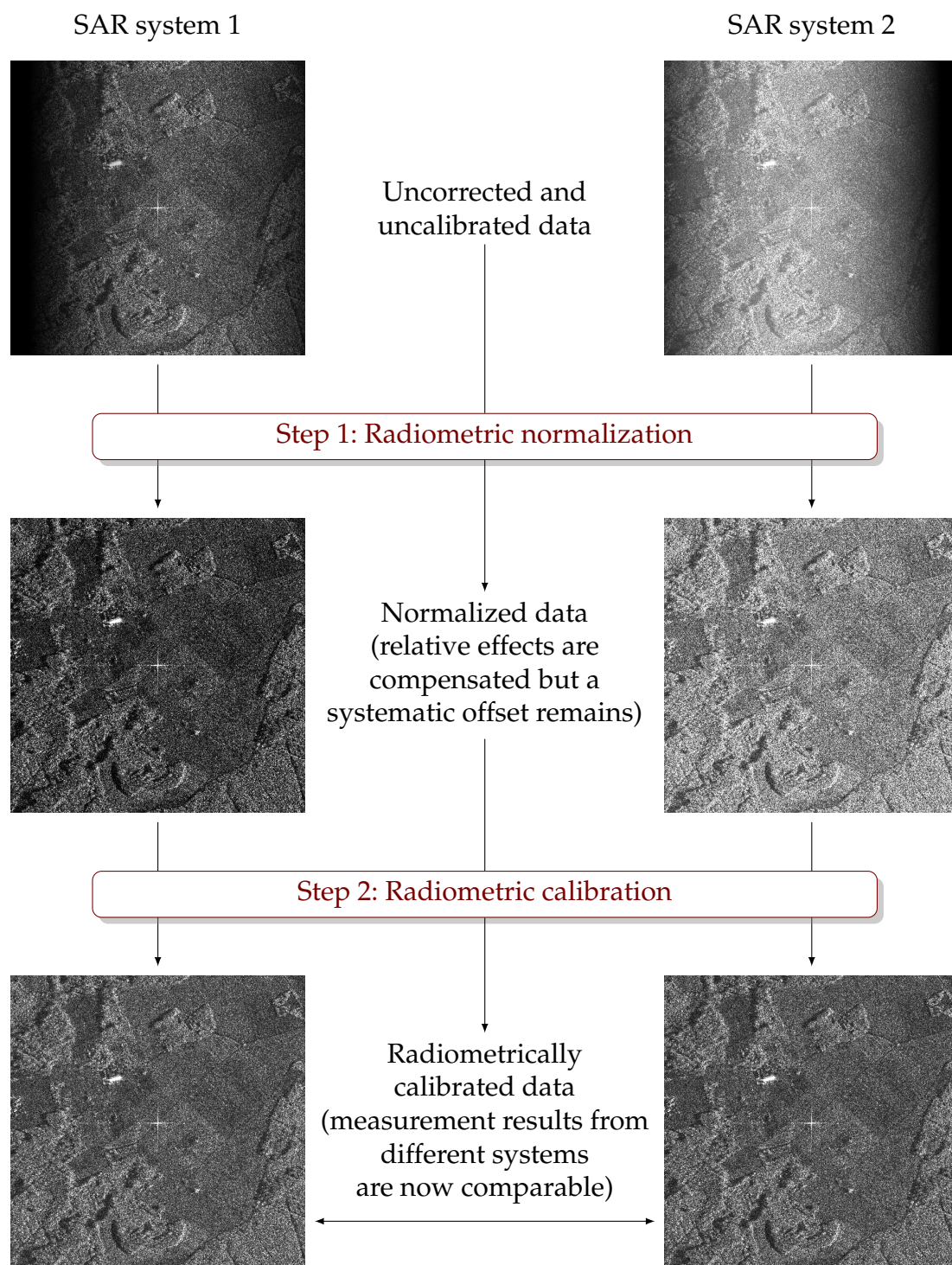


Figure 1.1: Summary of the radiometric calibration principle: To obtain compatible radiometric measurement results (“gray values”) from different SAR systems e. g. for parameter inversion modeling or change detection, two steps are necessary: First, during radiometric normalization relative effects such as the SAR system’s thermal drift and the antenna pattern are compensated. Second, an external, traceably calibrated reference point target (visible here as a cross in the center of each patch) is used to radiometrically calibrate each system. Within known uncertainties, the measurement results of both systems can now directly be compared.

each overpass.

The presented work focuses on this second step, namely the radiometric calibration and the required reference point targets.

How well a system is normalized can be quantified by reproducing measurements of an invariant target under varying conditions (incidence angle, time, instrument temperature, beam and chirp settings, and so on). How well a SAR system is calibrated, on the other hand, cannot be established through measurements alone. At one point, the remaining uncertainty in the knowledge of the reflectivity of measurement standards cannot be reduced any further due to the unavailability of measurement standards with an even smaller radiometric uncertainty. At this point, the remaining uncertainty needs to be quantified in a probabilistic sense through an uncertainty analysis.

1.2 Problem Statement

When the SAR technique was conceived in 1951 [199], radiometric calibration played an inferior role. In the center stood the acquisition of high-resolution radar imagery for military reconnaissance and target detection. Although reconnaissance remains an important SAR application, the field has immensely evolved over the last decades. Technological advancement and the conception of new SAR technologies have resulted in a multitude of applications, many of which stress the measurement aspect, or target estimation, over simpler mapping applications. Multi-channel systems allow polarimetric measurements [212], accurate orbit knowledge and improved instrument phase stability allow single and repeat-pass, monostatic and bistatic interferometric measurements [103, 198], and radiometrically stable systems permit physical parameter inversion modeling for applications as diverse as soil moisture [73, 192, 212] and global biomass estimation [138, 147].

Surprisingly, the evolution of radiometric calibration approaches has not fully kept pace with the remarkable advancements in SAR technology:

- The relative bandwidths of modern SAR systems, once below 1 %, now sometimes exceed 100 % [194]. Over such large bandwidths, the RCS of imaged targets cannot be assumed to be constant over frequency anymore, motivating the question whether RCS is the appropriate measurement quantity for SAR images. Furthermore, a SAR system actually does not measure the RCS of a target. It rather measures the weighted mean (over frequency and aspect angle) of the target's complex reflectivity, making a redefinition of the radiometric measurement quantity in SAR images necessary.
- A second consequence of higher-resolution SAR systems (with higher bandwidths and higher relevant aspect angle ranges) is the increasing influence of the apodization function (such as a Hamming window [32]) for side-lobe suppression on the radiometric measurement result. To date, this effect has not yet been comprehensively analyzed and even less solved in terms of radiometric measurements and calibration.
- Currently, metrological practices well embraced in many other scientific fields have not reached the same importance in the SAR community. Radiometric measurements are currently not traceable to national SI standards, and analyses of

measurement uncertainties are not conducted in accordance with the respective ISO standard [87]. This hinders the adoption of radiometric SAR measurement data in legal metrology and demonstrably dependable products.

- Traceable radiometric calibration is based on the availability of radiometric measurement standards which are themselves traceably calibrated. Yet currently available radiometric standards like corner reflectors and active radar calibrators are not traceably calibrated, partly due to a lacking rigorous uncertainty analysis. First, the reference RCS of trihedral corner reflectors is to-date still derived from a physical optics approximation [61, 212], neglecting field scattering effects which were inconsequential for early, less-accurate SAR systems but which influence the calibration quality of modern systems. Second, the frequency and aspect angle dependence of active radar calibrators cannot be neglected any more for present-day, high-precision and high-resolution SAR systems. Yet the methods have not been adapted.

This set of problems prompts the following key research question which motivates the work:

How can the current radiometric calibration approach be adapted to achieve metrological traceability for radiometric measurements using modern synthetic aperture radar systems?

Answering this question is significant for the ongoing adoption of SAR data in the scientific community and for dependable commercial products. An improvement in radiometric SAR system calibration will permit an evolution of physical parameter inversion modeling, ensure verifiable data continuity, and allow a consistent exchange of SAR data across SAR system boundaries.

1.3 Contributions and Thesis Structure

The challenges posed by the advancement of modern, high-resolution SAR systems and the research question raised above led me to a new take on traceable radiometric SAR system calibration. The topics covered include a novel definition of a measurement quantity, numerical and analytical methods, and a novel transponder calibration strategy. After a review of SAR and calibration fundamentals in Chap. 2, the main and novel contributions of this work are:

- Introduction of the novel radiometric measurement quantity equivalent radar cross section (ERCS) in Chap. 3. The definition of the quantity to be measured is the starting point for any measurement uncertainty discussion and therefore a necessity for traceable radiometric calibrations.
- Development of a numerical method in Chap. 4 for relating a point target's RCS to its ERCS depending on the target and the SAR system properties. This advantageous approach is based on point target SAR simulation and acts as a missing link to achieve metrological traceability.

- Development of a novel analytical approach in Chap. 5 for quantifying the herein identified SAR passband problem, which mostly results from the use of apodization functions in SAR processing. As part of the discussion, standardized SAR passbands are proposed in Sec. 5.5.2. Ideally they should be adopted for future SAR missions to ensure compatible radiometric measurements across SAR modes and missions.
- Introduction of the novel three-transponder method in Chap. 6 for radiometrically calibrating transponders. A measurement uncertainty analysis shows that the method is potentially more accurate than existing approaches, largely because metrological traceability is achieved for the first time solely through a length measurement. More accurate transponder calibrations will eventually allow more accurate radiometric SAR measurements.
- Introduction of Bayesian statistics to SAR calibration in Chap. 7 in order to make optimal use of point target data gathered during SAR calibration campaigns. By exploiting the hierarchical structure of the acquired data, calibration parameters can be derived based on grouped data. Besides offering lower uncertainties, the approach contributes to shorter calibration campaigns.

Finally, the work is summarized in Chap. 8. The chapter also includes an outlook for topics which are expected to contribute to the advancement of radiometric SAR calibration in the future.

This thesis led to several publications in conference proceedings [39, 41–43, 46–50, 93, 155, 156] as well as in peer-reviewed journals [39, 44, 45, 51, 52]. Furthermore, a patent has been issued [53]. The discussions of the novel measurement quantity ERCS at the CEOS workshops¹ in 2013, 2014, and 2015 are of special importance because they initiated a broader debate of the topics presented here. In fact, recently ERCS was adopted as a draft recommendation by the CEOS working group members for the definition of the radiometric measurement quantity in SAR [29]. Hence this definition may, after further review and discussion, eventually lead to ERCS being adopted by the community as the definition of the radiometric measurement quantity in the future.

The methods developed in this work permit to answer the question of how metrological traceability can be achieved for radiometric SAR measurements. The ensuing higher quality for SAR products increases the credibility of SAR data both for scientific and commercial end users. The work is therefore another necessary step on the path of the ongoing broader adoption of the SAR technique for current and emerging applications.

¹The *Synthetic Aperture Radar Subgroup* of the *Committee on Earth Observation Satellites (CEOS) – Working Group on Calibration and Validation* is an international entity where topics on SAR calibration are discussed across institutes and companies, and where recommendations for the larger SAR community may be formulated.

2 Fundamentals of SAR and Calibration

In this chapter, several general principles are described and summarized, which are then referenced to in the coming chapters. In particular, the following topics are covered: the synthetic aperture radar (SAR) technique, calibration principles, SAR calibration, and point targets used in SAR calibration.

2.1 Synthetic Aperture Radar Principles

The angular resolution β_r (in radians) of a radar system at a certain wavelength λ is determined by the physical aperture size L_a of the radar antenna according to [170]

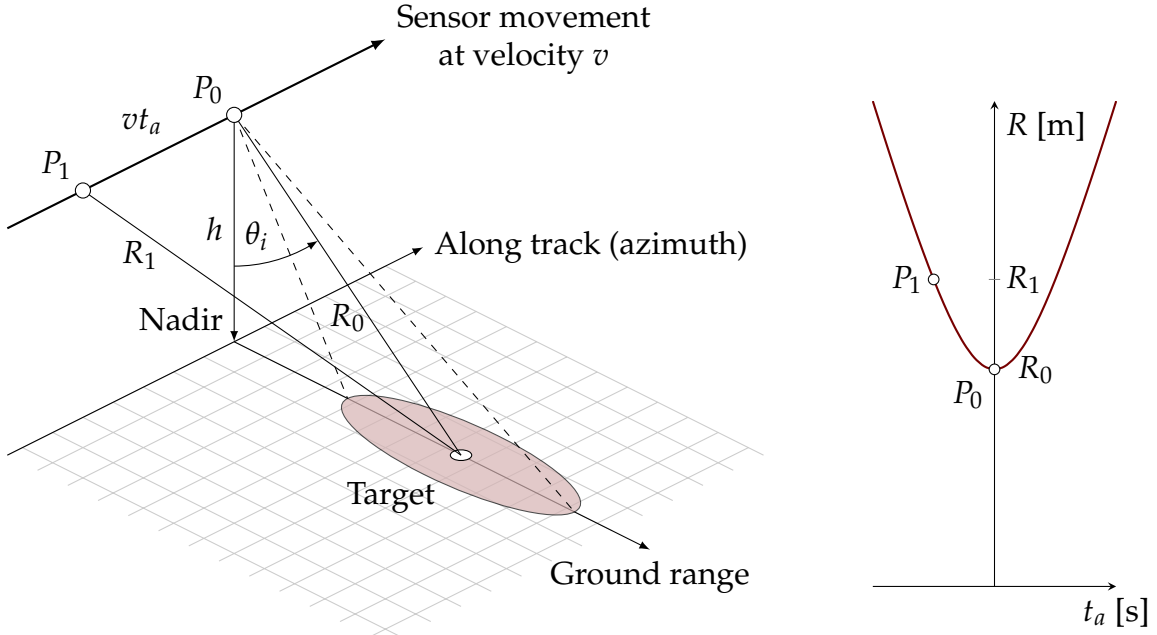
$$\beta_r = \frac{\lambda}{L_a}, \quad (2.1)$$

so a higher resolution requires an antenna with a larger physical aperture. The SAR overcomes this limitation by exploiting the relative movement of the radar platform with respect to the imaged target. A series of coherent pulses is emitted, whose radar echos are stored and then used to synthesize an effective antenna aperture which is much larger than the size of the physical antenna. The result is a high-resolution image despite an antenna with a physically small aperture.

Many excellent publications exist on the SAR principle and specific topics. A good overview is given in [32, 33, 122, 124, 193], from which equations and algorithms in this Sec. 2.1 have been compiled.

2.1.1 Image Formation for Point Targets

A SAR instrument contains the same sub-systems as a real aperture radar instrument: a transmitter, which emits a pulsed signal, a receiver, and typically one antenna which is used both for transmission and reception. In order to form a synthetic aperture, the instrument is mounted on a moving platform such as a plane or a satellite, and the antenna's main beam direction is side-looking with respect to the sensor path, see Fig. 2.1a. The slant range R is the distance from the sensor to a target on the ground, and R_0 is the slant range at closest approach. As the sensor passes by with along-track velocity v , the slant range changes over (azimuth) time t_a (centered on time of closest



(a) Principle imaging geometry of a right-looking SAR sensor, showing its beam footprint.

(b) Change of slant range R over azimuth time t_a .

Figure 2.1: The range R between a stationary ground target and the sensor changes approximately quadratically when a straight flight path is assumed.

approach) according to the hyperbolic range equation

$$R^2(t_a) = R_0^2 + v^2 t_a^2, \quad \text{or} \quad (2.2)$$

$$R(t_a) \approx R_0 + \frac{v^2 t_a^2}{2R_0}, \quad (2.3)$$

where a straight flight path was assumed (see Fig. 2.1b). The approximate expression results from a Maclaurin series expansion of $R(t_a)$ truncated after the second term, leading to the parabolic range equation.

As the sensor moves along, it transmits coherent pulses toward the ground, i.e., all transmitted pulses have a known phase with respect to a master oscillator. Part of the transmitted pulses' energy is then scattered back to the sensor by the imaged terrain. The received SAR signal depends on the transmitted one, which is typically a linearly frequency modulated pulse (also called chirp signal)

$$s_t(t_r) = w_r(t_r) \cos(2\pi f_c t_r + \pi K_r t_r^2), \quad (2.4)$$

where $w_r(t_r)$ denotes the pulse envelope (commonly a rectangular window of length T_r), f_c is the carrier frequency, t_r is the *fast time* or range time, and K_r is the chirp's frequency modulation (FM) rate in the SI unit Hz s^{-1} . Assuming a single ideal point target¹ on ground (see Fig. 2.1a), the transmitted signal is reflected and received again, leading to the received pulse

$$\begin{aligned} s'_r(t_r) &= A_0 s_t(t_r - 2R/c) \\ &= A_0 w_r(t_r - 2R/c) \cos[2\pi f_c(t_r - 2R/c) + \pi K_r(t_r - 2R/c)^2], \end{aligned} \quad (2.5)$$

¹ A possible realization of an ideal point target is a nearly perfectly electrically conducting sphere whose diameter is large with respect to the wavelength of the SAR instrument's lowest frequency. This point will be further developed in Chap. 3.

where A_0 is a complex constant which encodes the reflectivity of the point target, R is assumed to be a fixed slant range distance during pulse transmission and reception, and c is the speed of light. A quadrature demodulation of the received signal removes the high frequency component, resulting in the baseband signal

$$s'_{r,b}(t_r) = A_0 w_r(t_r - 2R/c) \exp[j\pi K_r(t_r - 2R/c)^2]. \quad (2.6)$$

Now as the sensor moves along its flight path, the slant range distance R changes according to Eq. (2.3). This results in a slow-time dependent phase shift of the received signal

$$\phi(t_a) = -4\pi R(t_a)/\lambda_0 = -\frac{4\pi}{\lambda_0} \left(R_0 + \frac{v^2 t_a^2}{2R_0} \right) \quad (2.7)$$

so that the slow and fast time dependent received signal for a point target, also called the system's impulse response, is

$$\begin{aligned} h'(t_a, t_r) &= A_0 w_r(t_r - 2R(t_a)/c) w_a(t_a) \\ &\cdot \exp \left[j\pi K_r(t_r - 2R(t_a)/c)^2 \right] \exp \left[-j\frac{4\pi}{\lambda_0} \left(R_0 + \frac{v^2 t_a^2}{2R_0} \right) \right]. \end{aligned} \quad (2.8)$$

Here $w_a(t_a)$ is the envelope of the azimuth chirp, which is influenced by the antenna's azimuth pattern. The derivative of the phase term (2.7) is the instantaneous angular frequency, from which the instantaneous azimuth-time dependent frequency

$$f_a(t_a) = -\frac{2v^2}{\lambda_0 R_0} t_a = K_a t_a \quad (2.9)$$

follows. Here K_a is the azimuth FM rate similar to the range FM rate K_r . The two phase terms with their quadratic dependence on time in Eq. (2.8) show that the signal has an identical form in range and azimuth direction: It is a two-dimensional frequency modulated signal.

Having determined the impulse response $h'(t_a, t_r)$ of the SAR system, one can determine the measured complex two-dimensional (raw) signal for a given complex ground reflectivity $S(t_a, t_r)$

$$s_r(t_a, t_r) = \iint S(t'_a, t'_r) h'(t_a - t'_a, t_r - t'_r) dt'_a dt'_r, \quad (2.10)$$

where the flying SAR instrument acts as a linear time-invariant filter with impulse response $h'(t_a, t_r)$ on the ground reflectivity signal. Equation (2.10) is also known as the two-dimensional convolution integral.

To optimally reconstruct (with respect to the signal-to-noise ratio (SNR)) the ground reflectivity from the raw data, the raw data are convoluted with a matched filter $h(t_a, t_r)$ to yield

$$s_{\text{out}}(t_a, t_r) = \iint s_r(t'_a, t'_r) h(t_a - t'_a, t_r - t'_r) dt'_a dt'_r, \quad (2.11)$$

where $h(t_a, t_r)$ is the optimal filter kernel, i. e., the time-reversed complex conjugate of the system's impulse response

$$h(t_a, t_r) = h'^*(-t_a, -t_r). \quad (2.12)$$

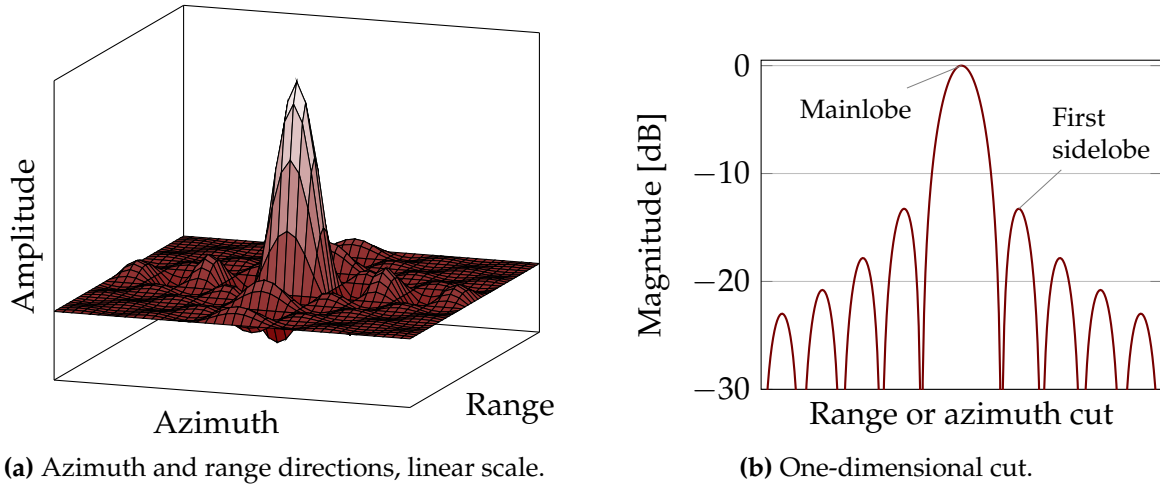


Figure 2.2: SAR impulse response.

Solving the integral (2.11) in time domain is expensive, and one typically uses more efficient albeit approximate methods. One of the more common SAR processing algorithms is the range-Doppler algorithm, which is described in Sec. 2.1.3.

If the range and azimuth pulse envelopes w_r and w_a in Eq. (2.8) are chosen to be rectangular functions of lengths T_r and T_a , respectively, then imaging a point target results in an approximately sinc-like function

$$s_{\text{out}}(t_a, t_r) \sim \text{sinc}(K_a T_a t_a) \text{sinc}(K_r T_r t_r). \quad (2.13)$$

A representation is shown in Fig. 2.2. The peak-to-sidelobe ratio (PSLR), defined as the ratio between the power density of the mainlobe's peak and the peak of the first sidelobe, is only slightly above 13 dB. This value is unacceptable for many applications as large scatterers tend to easily mask weaker nearby scatterers. To increase the PSLR, one usually utilizes weighting windows w_r and w_a whose values are 1 at the center and which taper off to the sides. This approach has an effect on radiometric measurements, a topic that is further discussed in Chap. 5.

2.1.2 Imaging Geometries

Different SAR imaging geometries and modes have been conceived since the realization of the first SAR instrument. The easiest configuration is the stripmap mode shown in Fig. 2.3a. In this configuration, the flight path is linear and the beam direction remains fixed with respect to the platform (e. g. an airplane or satellite). Another common mode is the similar ScanSAR mode, where several parallel strips are imaged by systematically switching the beam from one to the next elevation angle between bursts of pulses, which results in a larger coverage albeit at a lower resolution than for the stripmap mode. The spotlight mode trades off coverage and resolution in the other direction by steering the antenna beam toward the target during an overpass. This increases the illumination period and therefore the synthetic aperture, leading to higher resolutions at the cost of a lower coverage.

A significant variation of the spotlight mode is the circular SAR mode [86, 177], whose imaging geometry is shown in Fig. 2.3b. Here the SAR platform flies on a circular path around the target, resulting in maximal azimuth resolution.

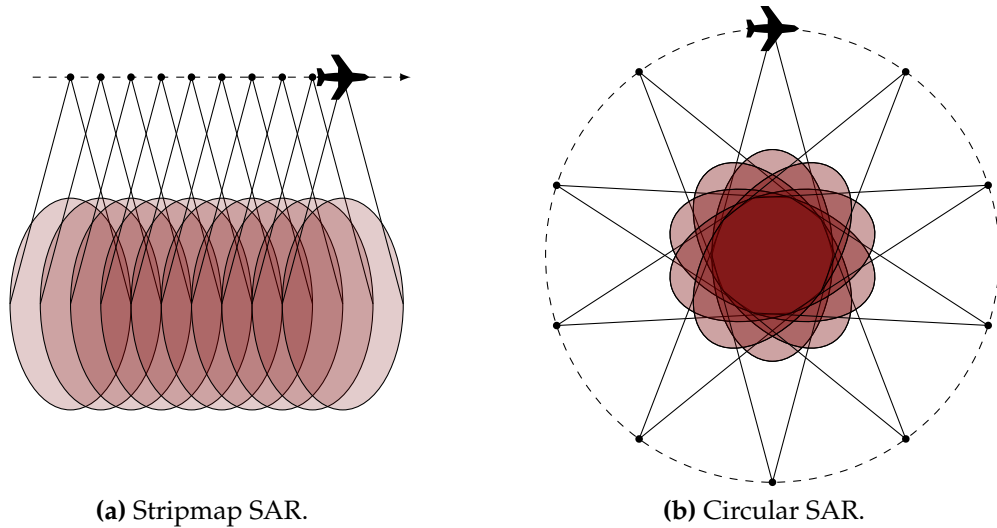


Figure 2.3: Examples of SAR imaging geometries, showing the two extreme cases in terms of a target's angular exposure to the SAR.

From a point of view of radiometric measurements, the stripmap and circular SAR imaging geometries shown in Fig. 2.3 are extremes. In the first case, the target is seen under a minimal angular range; in the second case, the target is seen from all sides. One generally expects targets to show an angular-dependent backscatter so there is a relationship between the imaging geometry (or more generally, the measurement system) and the measurement result. Relationships like this motivate the definition of a new radiometric measurement quantity in Chapter 3, and the subsequent discussions in Chapters 4 and 5.

2.1.3 The Range-Doppler Algorithm

The range-Doppler algorithm (RDA) is possibly the simplest and most commonly used SAR processing algorithm [32, 193]. It is based on performing the matched filtering separately for range and azimuth, each time in frequency domain using the efficient fast Fourier transform (FFT). The RDA is used in Chap. 4 where a novel point target SAR simulator is developed.

A data flow diagram for the RDA is shown in Fig. 2.4. The first step in the algorithm is range compression, where each received and digitized echo is convolved with a weighted replica of the transmit pulse. The expensive convolution in time domain is performed more efficiently in frequency domain, where convolution is equivalent to multiplication. The filtering operation is in most cases not executed with a matched filter, but with what has been called an unmatched filter [33]. The unmatched filter results from deriving an optimal filter and applying a weighting windows such as a Hamming window [74] in order to improve side-lobe suppression. After multiplication in frequency domain, the result is converted back to the time domain with the inverse fast Fourier transform (IFFT).

The azimuth compression is very similar in principle to the range compression because of the exploited approximate separability of the range and azimuth unmatched filtering operations. In order to use an FFT in azimuth, it is assumed that the pulses are evenly

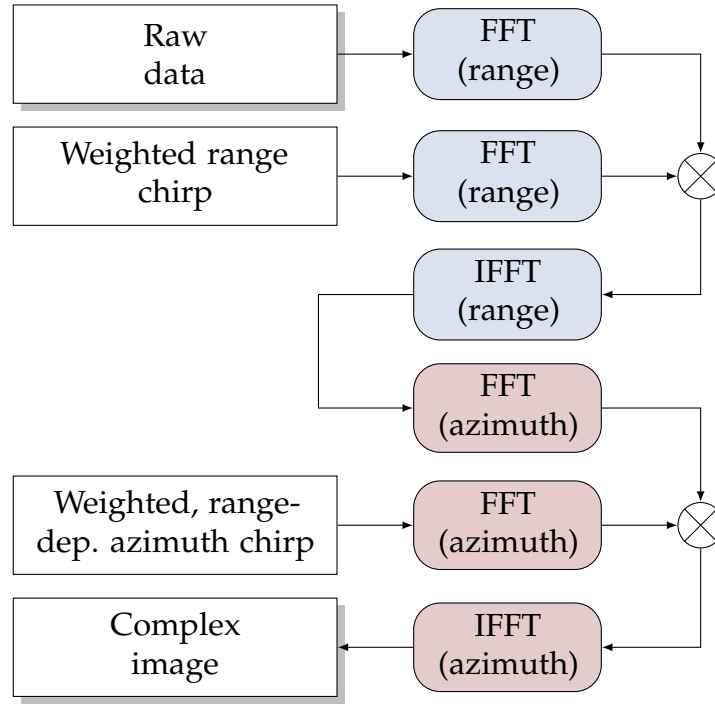


Figure 2.4: Data flow for the range-Doppler algorithm, adapted from [193].

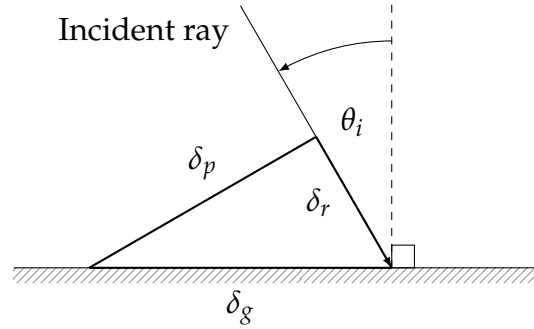


Figure 2.5: Definition of range increments depending on projection. The incidence angle θ_i is measured with respect to a reference ellipsoid.

spaced in time, i. e., the pulse repetition frequency (PRF) must be constant throughout an acquisition. Within the RDA, a weighted and range-dependent azimuth chirp is computed for each range bin. The FFT of the reference chirp is derived and multiplied with the FFT of the range-compressed azimuth line. A final IFFT leads to the range and azimuth compressed SAR image.

Many variations and improvements of this RDA exist, of which the most notable is the inclusion of a range cell migration correction (RCMC) step [32, 202]. This step becomes necessary if the range curvature, which results from the imaging geometry, significantly (more than one range cell) deviates from a straight line after range processing. These and other processing algorithms are described for instance by Cumming and Wong [32].

2.1.4 Distributed Targets

So far only ideal point targets have been considered. In most cases though there is not one dominant scatterer within a SAR resolution cell, but there are many scatterers whose signals appear superimposed at the SAR receiver. For these distributed targets, the radar reflectivity is expressed normalized with respect to a surface area. Different normalization areas can be defined (see Fig. 2.5), leading to different reflectivity coefficients.

The *radar brightness*, or “beta nought” β^0 , is the radar reflectivity coefficient in a slant range image, i. e., before incidence angle correction. Here β , the radar backscatter, shall be defined as being proportional to the pixel intensity or digital number (DN), i. e., proportional to $|s_{\text{out}}|^2$ from Eq. (2.11) after discretization.² With this, the radar brightness is defined as [144]

$$\beta^0 = \frac{\beta}{\delta_a \delta_r} = \frac{\beta}{A_\beta}, \quad (2.14)$$

where δ_r and δ_a are the image pixel spacings in slant range and azimuth. This definition was recommended by Raney et al. [144] as the most useful definition of a radar reflectivity coefficient because of its independence on local incidence angle.

Besides β^0 , other backscatter coefficients exist, of which the most widely used is the *normalized radar cross section* “sigma nought”, where

$$\sigma^0 = \frac{\beta}{\delta_a \delta_g} = \frac{\beta}{A_\sigma} = \beta^0 \frac{A_\beta}{A_\sigma} = \beta^0 \sin \theta_i. \quad (2.15)$$

σ^0 describes the mean reflectivity of a patch of distributed scatterers per unit area on ground, where the ground area is defined as a patch locally tangent to an ellipsoidal model [61, 173].

The last definition results if one defines the reference area to be in the plane perpendicular to the line of sight from the sensor to an ellipsoidal model of the ground surface, which yields “gamma nought”

$$\gamma^0 = \frac{\beta}{\delta_a \delta_p} = \frac{\beta}{A_\gamma} = \beta^0 \frac{A_\beta}{A_\gamma} = \beta^0 \tan \theta_i. \quad (2.16)$$

This definition is useful for relative range antenna pattern corrections when an image of an approximately Lambertian scatterer such as the rain forest is taken because then γ^0 is independent of incidence angle.

The three backscatter coefficient definitions above work well for flat terrain. A more general, terrain-corrected backscatter coefficient, γ_T^0 was proposed by Small [173] in order to remove hill-sloped modulations of radiometry so that weaker thematic-land-cover-induced backscatter differences become apparent. This correction depends on the availability of an accurate digital elevation model.

In the end, no matter which coefficient is used to describe the backscatter of distributed targets, it is critical to be unambiguous about the coefficient used when reporting measured data. One coefficient is transformable into any other as long as supplementary

²Note that the definition $\beta = P_s / P_i$ used in [173] is incorrect, which is apparent when considering the units. The normalized backscatter coefficient β^0 is a dimensionless quantity [61, 144], so that β must have the dimensional unit square meter.

data on geometry are available. Nevertheless, in terms of radiometric SAR calibration, β^0 is the preferred coefficient because it is a natural representation of backscatter in a SAR image which is independent of SAR geometry and terrain slope [144].

2.2 Measurement, Calibration, and Traceability Principles

2.2.1 Measurements and Measurement Quantities

A SAR instrument is a measurement instrument. As for any measurement instrument, its purpose is to determine information about a certain quantity of interest characterizing the measured object, also called the measurand. Many measurement instruments are designed to derive the value of a single measurand, for instance a balance is used to measure the weight (the quantity) of an object, or a folding rule is taken to measure the length of an object. In contrast to this, a SAR system is an imaging system, and several primary quantity values are derived from a single image.

In its most general form, each SAR image is formed by many pixels, where each pixel is described by a complex amplitude (defined by magnitude and phase), see Eq. (2.11). Therefore, the primary measurement quantities of a SAR instrument are:

- amplitude (a measure for the surface or volume radar reflectivity),
- phase (an ambiguous measure for the distance of a pixel's effective phase center from the SAR instrument, influenced by the interaction with the measured medium), and
- location (in a first step determined in slant-range geometry).

The primary measurement quantities form the model inputs for the determination of secondary or derived measurement quantities. Radiometric measurements are derived from the pixel intensities (squared amplitudes), and are used as the most obvious (but not only) choice for land classification and target detection [131]. The pixel intensity is also the input quantity for biomass inversion modeling, one of the two principal mission objectives of the upcoming BIOMASS mission [147]. If the SAR instrument is polarimetric and more than one combination of transmit/receive polarizations is recorded, then numerous additional secondary quantities can be derived from the relation of a pixel's intensity in one polarization channel with respect to the intensity in another channel, for instance soil moisture [192]. The phase and location information, on the other hand, is used for the determination of topography and deformation maps, provided that more than one image is acquired and the principle of interferometry can be exploited [103, 149].

Measurements only ever lead to approximations or estimates of the measured quantity. Repeating the same measurement several times typically leads to different indication values due to random errors caused by the measurement system, the environment, or other influence quantities. Additionally, a set of indication values might be shifted from the true (but unknown) quantity value of the measurand due to systematic errors. It is therefore important to not only report the best estimate for the measured quantity, but also to report information about the reliability, i. e., the uncertainty of the measured quantity value. This allows to determine if the measurement result is appropriate for

a certain application (e. g. to assess the conformance of a product with a requirement), and allows meaningful comparisons of measurement results.

One standardized approach across many metrological fields for describing and deriving the measurement uncertainty is the ISO/IEC Guide 98-3 *Evaluation of measurement data – Guide to the expression of uncertainty in measurement* [87], typically abbreviated as GUM, which is introduced in the following section.

2.2.2 The Guide to the Evaluation of Uncertainty in Measurement

There is undeniable merit in the adoption of a common understanding of what measurement uncertainties are and how they should be reported and interpreted by different laboratories, organizations, and users. The *Evaluation of measurement data – Guide to the Expression of Uncertainty in Measurement* [87] (GUM) is, despite an ongoing controversy toward future modifications, the *de facto* standard to express uncertainties in a unified approach. Its development started in 1980, and it was finally released in its first version in 1993 by seven international organizations including the Bureau International des Poids et Mesures (BIPM), the International Electrotechnical Commission (IEC), the International Organization for Standardization (ISO), and the International Organization of Legal Metrology (OIML).

In this context it is surprising to note that except for publications by the author, the GUM seems to be not specifically mentioned in SAR calibration literature or other publications concerning measurements derived from SAR data. As a point in case, the Sentinel-1 SAR system from ESA does not refer to the GUM when deriving measurement uncertainties, whereas the Sentinel-2 (high-resolution optical images) and Sentinel-3 (several instruments for sea-surface topography, sea and land surface temperature, and ocean and land surface color measurements) missions have adopted the GUM [68, 174]. The GUM approach will be used within this work, and it is hoped that the GUM will find more widespread adoption by the SAR community in the future.

Standard and Combined Measurement Uncertainties

Central to the GUM is the definition of the measurement uncertainty [87]:

Uncertainty (of measurement): Parameter, associated with the result of a measurement, that characterizes the dispersion of the values that could reasonably be attributed to the measurand.

For N repeated measurements of a randomly distributed quantity q , the best estimate \bar{q} is the arithmetic mean

$$\bar{q} = \frac{1}{N} \sum_{i=1}^N q_i, \quad (2.17)$$

and the experimental standard deviation is

$$\sigma_q = \sqrt{\frac{1}{N-1} \sum_{i=1}^N (q_i - \bar{q})^2}, \quad (2.18)$$

which characterizes the variability of the observed values [87]. The best estimate of the standard deviation of the mean $\sigma_{\bar{q}}$ is

$$\sigma_{\bar{q}} = \frac{\sigma_q}{\sqrt{N}}, \quad (2.19)$$

which is also known as the *standard error* in statistics [121], or the *Type A standard uncertainty* in metrology as used in the GUM, where typically the notation

$$u(q) = \sigma_{\bar{q}}$$

is used. Type A uncertainties can never cover calibration uncertainties because repeated measurements cannot identify systematic errors.

In comparison to *Type A* measurement uncertainties, *Type B* uncertainties have not been directly derived from measured data. Instead, they are derived from other sources including previous measurement data, manufacturer specifications, calibration certificates, or expert knowledge. Delineating between Type A and B uncertainties is for documentation only as they are treated equally in subsequent analysis.

In practice, a measurement result always depends on more than one input quantity: The length of a table determined with a measuring rod depends on the calibration of the rod, temperature, human error, etc. The backscatter of a point target measured with a SAR instrument depends on the instrument calibration, its stability, temperature, the atmosphere, the processor, etc. In the GUM, this relationship between n input quantities X_i and the wanted output quantity Y is formalized with a measurement model:

$$Y = f(X_1, X_2, \dots, X_n). \quad (2.20)$$

Here the capital letter Y shall be interpreted as a random variable that represents a possible outcome of an observation of that quantity. The estimate of Y shall be denoted with the small letter y . Similarly, the X_i are random variables with estimates x_i , whose probability distributions describe a degree of knowledge or certainty about this quantity.

In the GUM, no distinction is made between systematic and random errors. It is assumed that known systematic effects have been corrected. The correction of a systematic effect leads again to an uncertainty, and this uncertainty in the applied correction becomes, if significant, another input quantity for the measurement model f . The relationship between *error*, *uncertainty*, and the *value of the measurand* is shown in Fig. 2.6. The true value of the measurand remains unknowable due to measurement errors.

The measurement uncertainty of the output quantity Y is determined by deriving the *combined standard uncertainty* from the individual uncertainties $u(x_i)$. The approach is based on approximating the measurement model f from Eq. (2.20) with a first-order Taylor series expansion about the point (x_1, x_2, \dots, x_n) so that

$$Y \approx f(x_1, x_2, \dots, x_n) + \sum_{i=1}^n c_i (X_i - x_i) \quad (2.21)$$

with

$$c_i = \frac{\partial f}{\partial X_i}(x_1, x_2, \dots, x_n). \quad (2.22)$$

The c_i specify how fast the model f changes around location (x_1, x_2, \dots, x_n) ; they are also called *sensitivity coefficients*. The combined standard uncertainty for Y , $u_c(y)$, is

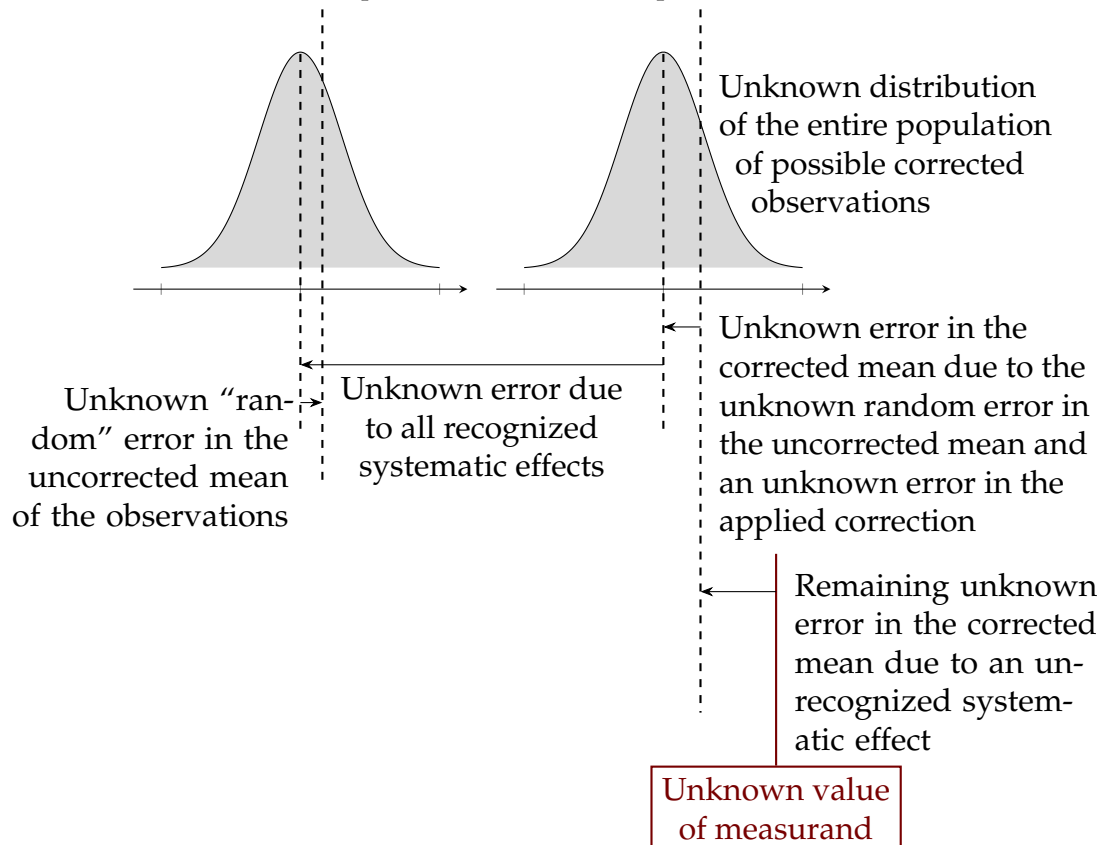
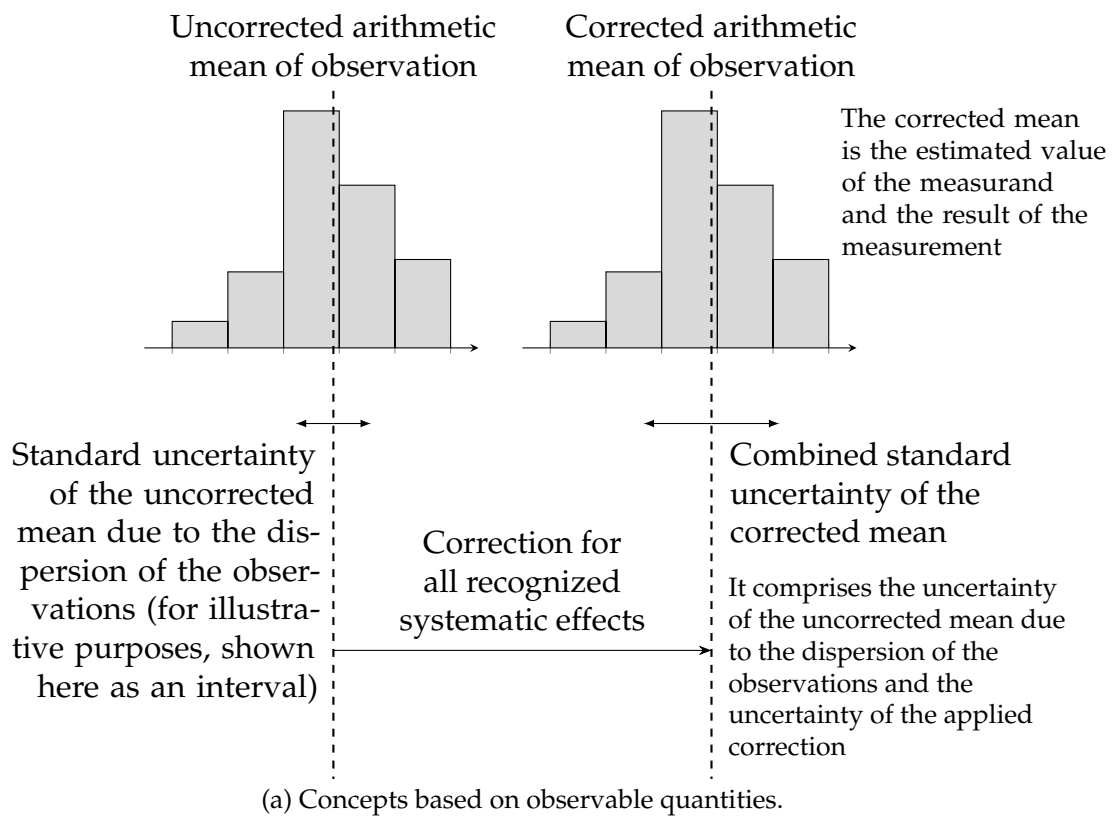


Figure 2.6: Visual representation of key terminology *value*, *error*, and *uncertainty* in the GUM, adapted from [87].

derived from the definition of variance and Eq. (2.21) as

$$\begin{aligned}
u_c^2(y) &= \sigma_Y^2 = E[(Y - y)^2] = E\left[\sum_{i=1}^n c_i(X_i - x_i)^2\right] \\
&= E\left[\sum_{i=1}^n c_i(X_i - x_i) \sum_{j=1}^n c_j(X_j - x_j)\right] \\
&= E\left[\sum_{i=1}^n c_i^2(X_i - x_i)^2 + \sum_{i=1}^{n-1} \sum_{j=i+1}^n c_i c_j (X_i - x_i)(X_j - x_j)\right] \\
&= \sum_{i=1}^n c_i^2 E[(X_i - x_i)^2] + \sum_{i=1}^{n-1} \sum_{j=i+1}^n c_i c_j E[(X_i - x_i)(X_j - x_j)] \\
&= \sum_{i=1}^n c_i^2 \sigma_i^2 + \sum_{i=1}^{n-1} \sum_{j=i+1}^n c_i c_j \sigma_{ij} \\
&= \sum_{i=1}^n \left(\frac{\partial f}{\partial X_i}\right)^2 u(x_i)^2 + \sum_{i=1}^{n-1} \sum_{j=i+1}^n \frac{\partial f}{\partial X_i} \frac{\partial f}{\partial X_j} \sigma_{ij},
\end{aligned} \tag{2.23}$$

where $E[X]$ is the expectation of X and σ_{ij} is the covariance [5]. Equation (2.23) is also known as the *law of propagation of uncertainty* and shows how the uncertainty $u_c(y)$ of the output quantity Y depends on the uncertainties $u(x_i)$ of the input quantities X_i .

In many practical situations the X_i can be assumed to be mutually independent so that the second term in Eq. (2.23) vanishes. The resulting simpler equation

$$u_c(y) = \sqrt{\sum_{i=1}^n \left(\frac{\partial f}{\partial X_i}\right)^2 u(x_i)^2} \tag{2.24}$$

is often called the *root-sum-square* formula.

In many cases it is not the (combined) standard uncertainty which is reported, but the expanded uncertainty

$$U = k_c u_c(y), \tag{2.25}$$

where k_c is a coverage factor so that the range $y - U \leq y \leq y + U$ can be considered to contain a large fraction of the distribution of values that can reasonably be attributed to Y . The coverage factor k_c is often chosen to be in the range 2 to 3.

Summary of Steps for Deriving Standard Uncertainties according to the GUM

In summary, the necessary steps to derive a combined standard or expanded uncertainty are [87]:

1. Define a mathematical model which relates the measurand Y to the n input quantities X_i such that $Y = f(X_1, X_2, \dots, X_n)$. Uncertainties of correction factors are included in the X_i .
2. Derive an estimated input quantity value x_i for every input quantity X_i .

3. Determine the standard measurement uncertainty $u(x_i)$ for all input quantities, either through measurements (Type A uncertainties) or any other means (Type B).
4. Evaluate the covariances for all correlated input quantities.
5. Calculate the result of the measurement y from the estimated input quantities x_i through the measurement model f .
6. Determine the combined standard uncertainty $u_c(y)$ by Eq. (2.23), which reduces to the root-sum-square Eq. (2.24) for the simplest case.
7. Possibly derive the expanded uncertainty $U = k_c u_c(y)$ with k_c typically in the range 2 to 3 so that an interval $[y - U; y + U]$ can be expected to encompass a large fraction of the distribution of values that could reasonably be attributed to the measurand.
8. Report the measurement result together with the standard or expanded uncertainty.

2.2.3 Calibration

Willink [200] gives a concise definition of what is to be understood under calibration:

Calibration is an operation that establishes a relation for obtaining a measurement result from an indication.

Calibration means function estimation. Given a set of known stimuli ϑ_i from one or several measurement standards, one records the indication values I_i which the instrument reports. Now a function \hat{g} is estimated so that

$$\vartheta_i \approx \hat{g}(I_i) \quad \text{for all } i. \quad (2.26)$$

During later measurements, an indication value I can be converted to an estimated quantity value $\hat{\vartheta}$ through the calibration function $\hat{\vartheta} = \hat{g}(I)$.

The definition above does not yet include measurement uncertainties or the specific measurement setup. The wording used in the GUM is more precise in this regard [92]:

Operation that, under specified conditions, in a first step, establishes a relation between the quantity values with measurement uncertainties provided by measurement standards and corresponding indications with associated measurement uncertainties and, in a second step, uses this information to establish a relation for obtaining a measurement result from an indication.

Furthermore, a measurement standard is defined as [92]:

Realization of the definition of a given quantity, with stated quantity value and associated measurement uncertainty, used as a reference.

From the definition of calibration it is clear that three measurement uncertainties must be discriminated:

1. The uncertainty by which the quantity value of the calibration standard is known.
2. The uncertainty which corresponds to the calibration measurements (e. g. a remaining random error).
3. And finally the measurement uncertainty characterizing the uncertainty of a measurement result acquired with a calibrated measurement instrument.

In summary, the distinguished feature of a calibration process is the involvement of a measurement standard.

2.2.4 Metrological Traceability

Calibration alone does not ensure that measurement results are compatible with each other, where compatibility means that the measurement results of different measurements agree with one another within a chosen multiple of the standard uncertainty of the results. Today in SAR, every instrument operator radiometrically calibrates his system with his own set of reference targets, may it be corner reflectors, transponders, or any other type of calibration target. It can happen that the measurement results acquired by two different SAR systems for the same target do not agree with each other despite calibration. Such effects have been reported for the two calibrated X-band systems COSMO-SkyMed and TerraSAR-X in [12, 134], where measured backscatter coefficients sometimes disagree by several decibel between the sensors. In this particular case, one can claim that each system is calibrated in its own right and does produce measurement results which are consistent with earlier measurements by the same sensor. Yet to use the data from both systems jointly in a single inversion model, e. g. for a better temporal coverage, is prohibited because the calibrations are not compatible.

Idealistically assuming for a moment that the two SAR systems were correctly calibrated, then the difference in the measurement results must be due to differences in the measurement standards used for calibration. Errors must have happened when the different measurement standards were calibrated themselves. To avoid such problems, a traceability chain should be established, so that measurement results become traceable to the same or at least compatible measurement standards even after possibly several necessary intermediate calibrations.

This concept of traceability is a common one in metrology. The GUM defines it as [92]:

Metrological traceability: Property of a measurement result whereby the result can be related to a reference through a documented unbroken chain of calibrations, each contributing to the measurement uncertainty.

In SAR, the backscatter of point targets is reported as an equivalent area in square meters with symbol m^2 . For metrological traceability of radiometric measurement results it is hence necessary to trace measurement standards (corner reflectors, transponders, etc.) back to a nationally or internationally recognized realization of the unit meter (with symbol m), which is itself a unit of the international system of units (SI unit).

2.3 Fundamentals of Radiometric SAR Calibration

Having reviewed calibration in general, this section deals with the particularities of radiometric calibration in SAR. Starting with a review of which quantities affect a radiometric measurement, the general approach for radiometric calibration is described, calibration terminology is introduced, and a link between the calibration of point and distributed targets is established.

2.3.1 Influences on Radiometric Measurements and General Calibration Approach

A radiometric SAR measurement is completed in two steps:

1. Correction: Execute a SAR overpass, process the data, and apply corrections where necessary to yield a repeatable and reproducible indication value (often called *digital number*), which characterizes the ground target of interest and is independent of the operating point. This step is also called *radiometric normalization* [24].
2. Radiometric calibration: Apply a previously determined calibration factor to obtain a measurement result from the indication value.

The calibration factor K is determined by placing and aligning a reference target such as a corner reflector or a transponder with a known reference backscatter ς_{ref} in an imaged scene, and, under the assumption of linearity, relating the indication value I of any ground target to the indication value I_{ref} of the calibration standard. Here the indication value of a point target is either set equal to the peak value of the target's impulse response in an intensity (square-law detected) image, or, arguably better, it is determined by an integral over the point target's impulse response, see the later Sec. 2.3.3.

The calibration function $\hat{g}(\cdot)$ from Eq. (2.26) simplifies on the assumption of a linear system to

$$\begin{aligned}\varsigma_{\text{ref}} &= \hat{g}(I_{\text{ref}}) \\ &= K' I_{\text{ref}}.\end{aligned}\tag{2.27}$$

By convention [61], the calibration factor K is defined as

$$K = \frac{1}{K'} = \frac{I_{\text{ref}}}{\varsigma_{\text{ref}}}\tag{2.28}$$

so that a measurement result³ ς can be derived from an indication I with

$$\varsigma = \frac{I}{K}.\tag{2.29}$$

As shown in Tab. 2.1, a multitude of factors influence a SAR's indication value I : The imaging geometry [32] influences the SAR response for instance through the slant range

³The measurement result ς has been erroneously interpreted as the radar cross section (RCS) of a point target in the literature [32, 33, 61, 131, 171, 212]. For reasons to be discussed in Chap. 3 it was avoided to establish this link here.

Table 2.1: Influence factors on radiometric measurements by category.

Geometry
Antenna beam pointing
Slant range distance (free-space path loss)
Topography (for distributed targets)
Layover and shadowing effects
Flight path (orbit) knowledge
Radar target scattering characteristics
Frequency
Polarization
Angle of arrival
Target composition and shape
Stability (static or moving) during overpass
Instrument and RF electronics
Instrument gain and phase stability
Coupling effects (antenna and/or signal routing)
Impedance matching between components
Digitization effects (resolution, step size)
Linearity
Clock stability
Antenna polarization purity
Propagation path
Ionosphere (birefringence)
Troposphere (attenuation)
Processing
Data compression on transfer
Algorithmic approximations for efficiency
Numerical resolution/artifacts
SAR mode
Beam switching
Antenna pattern model
Pulse bandwidth
Integration length in azimuth
Radiometric calibration
Measurement standard
Algorithm
Transfer of single point calibration to other areas and intensities

distance and the antenna pointing. Uncertainties in the pointing knowledge lead to a wrong antenna pattern correction [24, 61, 161]. For many modern SAR modes like spotlight or TOPS [37, 118] the instrument switches between numerous electronically steered antenna beams, and each beam pattern needs to be compensated individually to remove the effect of the antenna pattern from the SAR image. Dedicated calibration of each beam's gain is not possible due to the large effort involved. Instead, an antenna model is used which can predict the relative antenna pattern depending on the feeding parameters (amplitude and phase for individual antenna array elements) [10, 11]. Verification of the antenna model on some selected beams is one of the procedures conducted during a calibration campaign [161].

The indication value I certainly also depends on the terrain [191] or point target reflectivity [100], which itself depends on the target properties but also on angle-of-arrival, the orientation of the polarization plane (see e. g. [13, 142]), frequency, and bandwidth. Furthermore, data to be downlinked from a SAR satellite are typically reduced with lossy compression to increase data throughput. This effectively adds noise to the signal and thus affects radiometric measurements [17, 205]. When the SAR pulses pass through the atmosphere, they are affected by the ionosphere (a birefringent medium which changes the polarization plane, adds dispersion, results in attenuation, and varying group delays) and the troposphere (contributing further signal attenuation and group delays) [34]. If the SAR platform deviates from its nominal straight path, e. g. an airplane due to turbulences, then motion compensation is necessary to achieve well-focused images [59, 123, 131]. This is usually no concern for SAR satellites, yet the compensation of instrument instabilities in gain and phase are applicable to any type of SAR instrument. The instrument stability is affected primarily by temperature drifts, but on a larger timescale component aging is also a relevant factor [21, 33, 61].

If the SAR instrument has more than one channel, either for interferometry, polarimetry, or both, then normalization of these channels allows to use only a single calibration factor throughout [212]. An alternative approach is to consider each channel as an independent SAR instrument which is also independently calibrated. Other factors which play a role in SAR polarimetry like cross talk errors and channel imbalances are important correction steps within polarimetry but not as such in the field of radiometric SAR measurements. A polarimetric measurement has a different set of measurement goals and measurement quantities from a radiometric measurement. A polarimetric measurement requires different corrections and calibrations, just as SAR interferometry [149] defines its own measurement task.

Finally, the SAR processor and the used algorithms play a distinctive role in forming and influencing the indication value I before calibration. Today it is still most common to implement corrections in the processor on ground, and design decisions such as linear or higher order interpolations for derived corrections such as orbit position or gain stability influence the overall radiometric uncertainty. In recent developments some of the correction effort is shifted back to the SAR instrument for a reduction in data transfer. In what has been confusingly called *digital calibration* [97, 207], antenna element amplitude and phase correction terms are derived and applied in real time for use in modern multi-channel SAR systems.

In practice, most factors which influence a radiometric measurement are covered by the correction step, i. e., influencing the indication value I . This is not a necessity. The instrument gain drift or the beam-dependent antenna gain, for instance, could also be

corrected through calibration by incorporating the effect in the calibration factor K . Placing calibration standards into each imaged scene is impractical though, especially for globally operating spaceborne SAR systems. Instead, much of the correction effort is spent so that a point calibration (in space, time, dynamic range, and polarization) can be carried over to a large range of similar measurement situations.

Applying a multitude of corrections to reduce the calibration effort comes at a cost. Any of the many corrections introduces a measurement uncertainty because the correction factors are never perfectly known and necessary interpolations are approximations only. In most cases, the further a correction is applied from the point it was determined at, the higher the uncertainty will become so that a second calibration closer to the point of operation should be performed. Thinking about time scales, this is the reason why basically all precision instrumentation manufacturers mandate regular recalibrations of their instruments, and SAR instruments are no exception. Performing recalibrations of spaceborne SAR systems is common practice across sensors [166, 180].

2.3.2 Terminology in SAR Calibration

In the context of SAR, one misleadingly speaks about external calibration (ECAL) and internal calibration (ICAL) [22, 33, 61, 115, 193]. ECAL refers to the process of acquiring an image of a scene in which targets with a known backscatter (i. e., measurement standards like corner reflectors or transponders) have been placed, and subsequently relating the pixel intensities and locations of the known targets to radiometric and geometric scales. This is compatible with the two definitions of calibration given above. ICAL, on the other hand, is the process of detecting and correcting for possibly mode dependent amplitude and phase drifts and variations of the instrument's frequency transfer function of the instrument's internal radio frequency (RF) loop. No measurement standards are or could be involved in the procedure because a SAR instrument requires all measurement standards to be in its far field, and therefore all measurement standards are by necessity external to the instrument.

Consequently, external calibration should simply be called calibration, and internal calibration should be referred to as internal correction or instrument correction. This terminology would stress that there is only one calibration process, and that the process of instrument drift compensation serves as a relative correction for systematic effects only.

The terms *internal* and *external calibration* are appropriate in other settings though. An example is a precision balance which has a measurement standard (calibration weight) built in and which allows to execute an automated (internal) calibration through a motorized mechanism. In this context, external calibration then refers to placing external measurement standards on the weighing pan.

2.3.3 The Integral Method for Radiometrically Calibrating Distributed Targets

While a point target's response in a SAR image is a finite energy signal, a distributed target's noise-like response (also called clutter) is a finite power signal. In order to estimate the normalized radar cross section σ^0 of a homogeneous region in an image

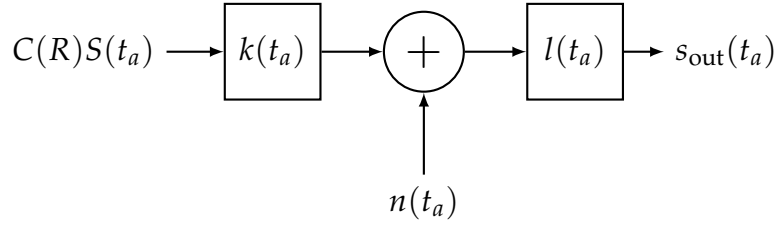


Figure 2.7: Azimuth processing model for range-compressed data $C(R)S(t_a)$ with additive receiver noise $n(t_a)$ resulting in a SAR image $s_{\text{out}}(t_a)$, adapted from [131]. $C(R)$: range-dependent system terms, see Eq. (2.30); $S(t_a)$: range-compressed complex reflectivity at azimuth time t_a ; $l(t_a)$: azimuth processing filter.

with respect to the known backscatter ζ_{ref} of a reference point target, these two must be linked.

Gray et al. [69] compared two methods for determining a point target's backscattered intensity in a cluttered SAR image: the peak and the integral method. Both can be used to establish the relationship between distributed and point targets, but the integral method has become the *de facto* standard in radiometric SAR calibration whenever a reference intensity I_{ref} is to be derived from a target with known backscatter ζ_{ref} in order to derive the calibration factor K according to Eq. (2.28) [46, 61, 151, 168, 190, 210]. This integral method is described in the following.

The derivation of the integral method is based on the linear system model shown in Fig. 2.7, where $S(t_a)$ is the already range-compressed complex reflectivity at azimuth time t_a , and

$$|C(R)|^2 = \frac{P_t G_R^2 \lambda^2 G_P}{(4\pi)^3 R^4 L} \quad (2.30)$$

summarizes the range-dependent system terms including the SAR transmit power P_t , the one-way antenna gain G_R at the specified range, the processing gain G_P due to range compression, and further losses L . The wavelength is denoted as λ . The complex output signal is accordingly

$$\begin{aligned} s_{\text{out}}(t_a) &= [C(R)S(t_a) * k(t_a) + n(t_a)] * l(t_a) \\ &= C(R)S(t_a) * h_a(t_a) + n(t_a) * l(t_a), \end{aligned} \quad (2.31)$$

which is influenced by the receiver noise $n(t_a)$. The filter $k(t_a)$ results from the azimuth beam weighting and the Doppler shift, $l(t_a)$ is the SAR azimuth processing filter, and

$$h_a(t_a) = k(t_a) * l(t_a) \quad (2.32)$$

is the overall azimuth point-spread function (PSF).

Now if an ideal reference point target with a complex reflectivity defined by the magnitude $\sqrt{\zeta_{\text{ref}}}$ and phase ϕ

$$S(t_a) = \sqrt{\zeta_{\text{ref}}} e^{j\phi} \delta(t_a) \quad (2.33)$$

is placed in a zero-clutter environment and is imaged with a zero-receiver-noise SAR system, the following complex SAR image results:

$$s_{\text{out}}(t_a) = C(t_a) \sqrt{\zeta_{\text{ref}}} e^{j\phi} h_a(t_a). \quad (2.34)$$

Integrating over this impulse response intensity (i. e., after square-law detection) yields the point-target energy or reference indication value

$$\begin{aligned}\mathcal{E}_p = I_{\text{ref}} &= |C(R)|^2 \zeta_{\text{ref}} \int_{-\infty}^{\infty} h_a(t_a) h_a^*(t_a) dt_a \\ &= |C(R)|^2 \zeta_{\text{ref}} R_{ha}(0).\end{aligned}\quad (2.35)$$

Here

$$R_{ha}(t_a) = \int_{-\infty}^{\infty} h_a(t'_a) h_a^*(t'_a - t_a) dt'_a \quad (2.36)$$

is the autocorrelation function of $h_a(t_a)$, which evaluated at $t_a = 0$ yields the energy of $h_a(t_a)$.

The complex reflectivity of a homogeneous distributed target is commonly modeled as a zero-mean wide sense stationary (WSS) complex Gaussian random process [114, 143]. This finite-power and stochastic signal cannot be described by an equation like (2.33), but instead one needs to refer to the signal's moments. The signal is completely defined by its autocovariance function [145], or equivalently, by its autocorrelation function as defined in Eq. (2.36) so that

$$R_S(t_a) = \sigma^0 \delta(t_a), \quad (2.37)$$

where σ^0 is the normalized radar cross section from Eq. (2.15) characterizing the mean backscatter of the distributed target. Linear and time-invariant (LTI) system theory for WSS signals dictates that the autocorrelation function of the output of a linear system is given by the double convolution of the input autocorrelation function with the unit impulse response of the system [36, 132]. Hence the autocorrelation function of the intensity image derived from Eq. (2.31) becomes

$$R_{\mathcal{E}_u}(t_a) = |C|^2 \sigma^0 R_{ha}(t_a), \quad (2.38)$$

where the mean power is given by the autocorrelation function evaluated at $t_a = 0$ so that

$$R_{\mathcal{E}_u}(0) = |C|^2 \sigma^0 R_{ha}(0). \quad (2.39)$$

The signal energy in a homogeneous area A_u is therefore

$$\mathcal{E}_u = A_u |C|^2 \sigma^0 R_{ha}(0). \quad (2.40)$$

A similar discussion leads to the signal energy for the noise component $n(t_a)$ from Eq. (2.34) over a similar area A_n . In practice the noise-only measurement can be completed by leaving the transmitter switched off. The noise signal is, like the distributed target, described by its autocorrelation function

$$R_n(t_a) = N \delta(t_a). \quad (2.41)$$

The autocorrelation function of $l(t_a)$ from Eq. (2.34) is

$$R_l(t_a) = \int_{-\infty}^{\infty} l(t'_a) l^*(t'_a - t_a) dt'_a \quad (2.42)$$

so that the autocorrelation of the square-law detected, noise-only SAR image is

$$R_{\mathcal{E}_n}(t_a) = N R_l(t_a) \quad (2.43)$$

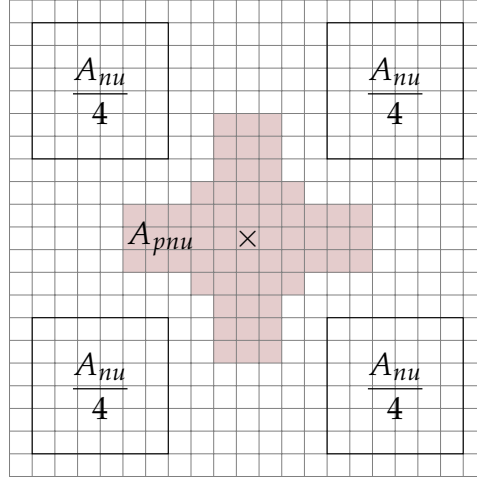


Figure 2.8: Exemplary integration areas for the integral method according to Gray et al. [69]. The peak of the point target is located at the \times . A_{pnu} is the point target integration area (with superimposed noise and clutter components), and the four patches forming area A_{nu} are used to estimate the clutter power.

with mean power

$$R_{\mathcal{E}_n}(0) = NR_I(0), \quad (2.44)$$

which yields

$$\mathcal{E}_n = A_n NR_I(0). \quad (2.45)$$

for the noise energy in area A_n .

The normalized radar cross section of a distributed target can now be derived if a point target with a known reference backscatter ζ_{ref} is located in the vicinity of the distributed target (at the same range distance), and no receiver noise and no background reflectivity are assumed, so that [69]

$$\sigma^0 = \frac{\zeta_{\text{ref}} \mathcal{E}_u}{A_u \mathcal{E}_p}. \quad (2.46)$$

The knowledge of the range-dependent system terms $|C(R)|^2$ is not required.

In the more general case where the receiver noise and background reflectivity cannot be neglected, the three energies \mathcal{E}_p , \mathcal{E}_u , and \mathcal{E}_n cannot be directly determined because the integrals over the respective areas A_p , A_u , and A_n will always contain a superposition of all signal components. With the substitutions

$$\mathcal{E}_u = \mathcal{E}_{nu} - \mathcal{E}_n(A_{nu}/A_n) \quad (2.47)$$

and

$$\mathcal{E}_p = \mathcal{E}_{pnu} - \mathcal{E}_{nu}(A_{pnu}/A_{nu}) \quad (2.48)$$

in Eq. (2.46) one yields [69]

$$\sigma^0 = \frac{(\zeta_{\text{ref}}/A_{nu}) [\mathcal{E}_{nu} - \mathcal{E}_n(A_{nu}/A_n)]}{\mathcal{E}_{pnu} - \mathcal{E}_{nu}(A_{pnu}/A_{nu})} \quad (2.49)$$

which describes a calibration strategy that can be executed in practice. In the case of a digital SAR image, the integrations can be replaced by summations. The ground range

integration areas are proportional to a number N_A of pixels according to

$$A = \frac{N_A \delta_r \delta_a}{\sin \theta_i}, \quad (2.50)$$

where δ_r and δ_a are the pixel spacings in slant range and azimuth direction (see Sec. 2.1.4) and the incidence angle θ_i is assumed to be locally invariant. A practical realization of the integration areas is shown in Fig. 2.8 (with $A_n \equiv A_{nu}$ for convenience) where the energy \mathcal{E}_{pnu} of the point target is derived by summing the square of the complex pixel values a_{ij} over a cross area centered on the peak, and the clutter is estimated from nearby areas outside of the cross area. Then

$$\mathcal{E}_p = \left(\sum_{N_{pnu}}^{(\text{area } A_{pnu})} a_{ij}^2 - \frac{N_{pnu}}{N_{nu}} \sum_{N_{nu}}^{(\text{area } A_{nu})} a_{ij}^2 \right) A_{pnu} \quad (2.51)$$

and

$$\bar{\mathcal{E}}_u = \frac{\mathcal{E}_u}{N_u} = \left(\sum_{N_{nu}}^{(\text{area } A_{nu})} a_{ij}^2 - \frac{N_{nu}}{N_n} \sum_{N_n}^{(\text{area } A_n)} a_{ij}^2 \right) \frac{\delta_r \delta_a}{\sin \theta_i}. \quad (2.52)$$

leads with the definition of the calibration constant

$$K = \frac{\mathcal{E}_p}{\bar{\mathcal{E}}_u} \quad (2.53)$$

to

$$\sigma^0 = \frac{\zeta_{\text{ref}} \sin \theta_i}{\delta_r \delta_a K}, \quad (2.54)$$

which is the final equation relating the known backscatter of a point target ζ_{ref} to the unknown normalized backscatter coefficient σ^0 [69].

The integral method is appealing because all parameters involved are either known or can be derived from a SAR image. Also, Eq. (2.54) does not depend on the processor gain, focusing, or resolution, which sets it apart from the previously used peak method [69].

2.4 Typical SAR Calibration Point Targets and Properties

Measurement standards are required for any calibration activity. In SAR calibration, man-made radar point targets are used for this purpose. For calibration, the point targets are distributed in a scene (e. g. on open fields) from which a SAR acquisition will be taken. In comparison to distributed targets, a calibration point target scatters back an incident SAR pulse with a magnitude which is significantly larger than the backscatter from the surrounding area. Additionally, the echo seems to stem from a single point on the target, its specular point, which makes it ideal as a reference also for phase measurements.

In contrast to distributed (natural) targets, the frequency and angular dependent radar cross section of man-made targets can be precisely calibrated and verified during production. The availability of calibrated measurement standards is the foundation for traceable radiometric calibration of SAR systems. Due to the lacking traceability for distributed targets it is hence questionable to use distributed targets for radiometric calibration.

In the following section, the most important point target properties are discussed before several typical point targets are reviewed in the remainder of the section.

2.4.1 Point Target Properties

Radar Cross Section

The quantity which describes how well a point radar target scatters an incident wave back to the radar is called the (monostatic) radar cross section (RCS). This far field quantity is defined as

$$\zeta = \lim_{R \rightarrow \infty} 4\pi R^2 \frac{|\mathbf{E}^s|^2}{|\mathbf{E}^i|^2}, \quad (2.55)$$

where \mathbf{E}^s and \mathbf{E}^i are the scattered and incident electrical fields, and R denotes the distance to the target [54, 85, 100]. In the words of the *The Authoritative Dictionary of IEEE Standards Terms* [85]:

RCS is defined as 4π times the ratio of the power per unit solid angle scattered in a specified direction of the power unit area in a plane wave incident on the scatterer from a specified direction. More precisely, it is the limit of that ratio as the distance from the scatterer to the point where the scattered power is measured approaches infinity.

Its measurement unit is square meter, but a target's RCS is most often noted in decibels relative to a square meter, or dBm².

A perfectly conducting sphere whose diameter is large with respect to the wavelength is the only target whose RCS is exactly as large as the sphere's geometrical cross section. In the general case, the (monostatic) radar cross section depends on many parameters: frequency, polarization, monostatic angle under which the target is seen by the radar, the target material(s), and its size and shape.

Predicting the RCS of any but the most cardinal objects such as a perfectly conducting sphere [184] or circular disk [80] requires approximations or numerical simulations. The most common methods are:

Geometrical optics (GO) Objects are typically considered perfectly conducting, and wave propagation is modeled with rays which can be reflected on surfaces or refracted at the interface of two media with varying dielectric properties [100]. The approximation leads to comparably fast computations even if several reflections are considered, and it is especially good for objects which are very large with respect to the wavelength. Smaller objects, edges, and other discontinuities cannot be handled well by this approach.

Physical optics (PO) This approach is based on approximating the induced surface fields (caused by an incident field) with geometrical optics, and integrating them to derive the scattered field [100]. With this approach, edges can already be modeled much more accurately, but determining the field after, say, a triple reflection already requires a six-fold integral, which remains difficult to implement efficiently [158].

Method of moments (MoM) The MoM (also called boundary-element method (BEM)) is a low-frequency method which does not make any implicit approximations so that the accuracy of the method is only limited by the accuracy of the model parameters and the geometrical discretization of a model's surface; the volume

touching an object's surface is not discretized [67]. The method is based on iteratively computing the induced surface currents from which the scattered field can then be derived. Due to the need of computing and solving a large, fully populated matrix, this method is the most time consuming (but also most accurate) of the listed methods.

Many other methods and method hybrids exist such as the finite-element method (FEM) and the finite-difference time-domain method (FDTD), but the three methods mentioned above are still the most common building blocks when new algorithms are conceived to determine the RCS of large objects.

Besides through simulations, the RCS of an object can also be determined with measurements. Several existing approaches and a novel, accurate approach for measuring the RCS of a calibration transponder are discussed in Chap. 6.

The quantity RCS is an important concept also for synthetic aperture radars. Currently, RCS is understood to be the radiometric quantity which a SAR system returns when it measures a point target. This understanding is disputed in Chap. 3, where the new measurement quantity *equivalent radar cross section* (ERCS) is introduced.

Polarization Scattering Matrix

The radar cross section depends on the polarization of the transmitter and the receiver. The 2×2 complex scattering matrix \mathbf{S} allows to summarize the scattering behavior of a radar target for two orthogonal polarizations. The most common basis consists of the horizontal (H) and vertical (V) polarizations, so that the scattering matrix is [100, 212]

$$\mathbf{E}^s = \mathbf{S}\mathbf{E}^i, \quad (2.56)$$

$$\begin{pmatrix} E_h^s \\ E_v^s \end{pmatrix} = \begin{pmatrix} S_{hh} & S_{hv} \\ S_{vh} & S_{vv} \end{pmatrix} \begin{pmatrix} E_h^i \\ E_v^i \end{pmatrix}, \quad (2.57)$$

where \mathbf{E}^i and \mathbf{E}^s are the incident and scattered electric fields, respectively. The first index in the scattering parameters denotes the polarization of the transmitter, and the second the one of the receiver.

Here the backscatter alignment convention is used, where the unit vectors which define the horizontal and vertical polarization are defined with respect to the radar antennas [193].

The scattering matrix does only have four elements, but it allows to derive the radar backscatter for any combination of transmit and receive polarizations. A common approach for visualizing the polarimetric response of a target exists in the form of a diagram, which shows the polarization spectrum or polarization response [211, 212].

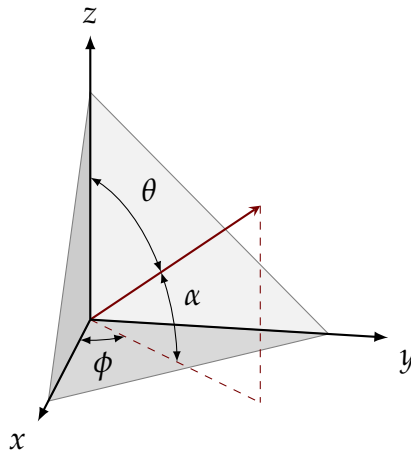
The scattering matrices for common calibration point targets are given in Tab. 2.2.

2.4.2 Trihedral Corner Reflectors

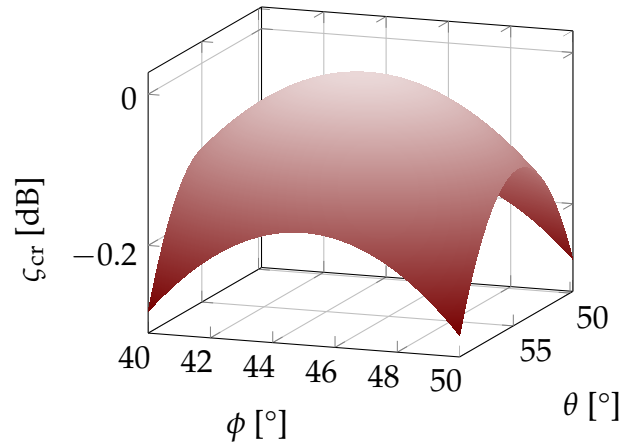
A trihedral reflector is a simple geometrical structure consisting of three metallic plates which are orthogonally aligned with respect to each other, forming a corner. This alignment ensures a large monostatic RCS because incoming waves are mostly scattered

Table 2.2: Scattering matrices of common SAR calibration point targets (first two rows from [61, 212], angle α for the dihedral is defined in Fig. 2.18, last row adapted to fit definition of angles in Fig. 2.14).

Point target	Scattering matrix	Also see page
Sphere, trihedral corner reflector	$\begin{pmatrix} 1 & 0 \\ 0 & 1 \end{pmatrix}$	42, 30
Dihedral corner reflector	$\begin{pmatrix} \cos 2\alpha & \sin 2\alpha \\ \sin 2\alpha & -\cos 2\alpha \end{pmatrix}$	39
Transponder	$\begin{pmatrix} \cos \alpha \cos \beta & \cos \alpha \sin \beta \\ \sin \alpha \cos \beta & \sin \alpha \sin \beta \end{pmatrix}$	33



(a) Definition of coordinate system.



(b) Normalized monostatic RCS around principal backscatter direction, geometrical optics approximation, see Eq. (2.58).

Figure 2.9: Coordinate system and scattering pattern of a triangular-faced trihedral corner reflector. The slow RCS reduction away from the principal backscatter direction is the reason for the popularity of the corner reflector in SAR calibration. The often neglected RCS dependence of the corner reflector on frequency is shown in Fig. 2.11.



Figure 2.10: DLR’s modern, remote-controlled 2.8 m trihedral corner reflector with a form tolerance of 1 mm. The novel approach of installing it upside-down allows for an additional parking position (aperture facing to the ground) for better protection of the reflecting surfaces between overpasses.

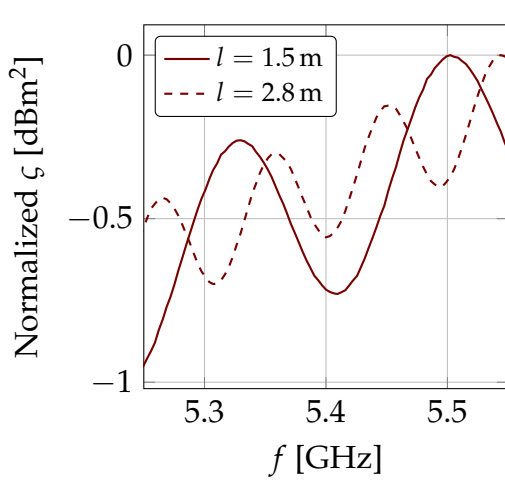
back in the incidence direction due to triple reflections. For a mechanical structure, the monostatic RCS is large with respect to its geometrical size. Also, the orthogonal plate alignment ensures that the monostatic RCS remains high for a wide range of incidence angles, making this target less sensitive with respect to mis-alignments, see Fig. 2.9b.

In principle, the plates can take any shape, but often triangular faced plates as show in Figs. 2.9a and 2.10 are preferred due to the resulting simple and sturdy mechanical design. Other typical designs include square plates and plates which resemble a quarter segment of a circle. For all these designs, only parts of the surface of the plates contribute to the main scattering mechanism: triple reflection. A ray entering the structure near one of the three outer vertices will be reflected at most twice because the reflected ray will not intercept the third plate. Based on this fact, Sarabandi and Chiu [158] proposed a corner design with optimally small plates for a given corner RCS, making the structure lighter and less sensitive to spurious corner-ground reflections (but exposing additional edges which contribute to the cross-polar response and degrade the RCS flatness over frequency).

The direction of maximal monostatic backscatter coincides with the corner’s axis of symmetry. For the geometry shown in Fig. 2.9a, the broadside direction is given by $\phi = 45.00^\circ$ and $\alpha = 35.26^\circ$ (this equals $\theta = 54.74^\circ$). Away from the peak direction, the RCS is reduced. Geometrical optics approximation leads to an expression for the angular-dependent RCS ζ_{CR} of the triangular-faced trihedral corner reflector [129, 212]

$$\zeta_{CR}(\theta, \phi) = \frac{4\pi l^4}{\lambda^2} \left[\cos \theta + \sin \theta (\sin \phi + \cos \phi) - \frac{2}{\cos \theta + \sin \theta (\sin \phi + \cos \phi)} \right]^2, \quad (2.58)$$

where l is the inner-leg length of the reflector, and λ is the wavelength (see Fig. 2.9b for



(a) Frequency dependence of the corner's RCS.

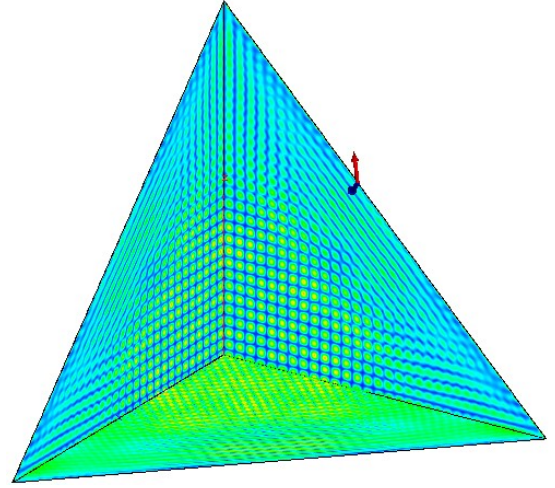
(b) Simulated current distribution for $l = 1.5$ m at 5.405 GHz.

Figure 2.11: Field simulation of the RCS of trihedral corner reflectors with two inner-leg lengths l at nominal alignment and vertical polarization (C-band). The often ignored frequency dependence due to edge effects (visible in (b)) is well noticeable and must be considered for accurate radiometric SAR system calibration.

a visualization). Although the approximate Eq. (2.58), which reduces to

$$\zeta_{\text{CR}} = \frac{4\pi l^4}{3\lambda^2} \quad (2.59)$$

for the peak RCS, is cited frequently in the SAR calibration literature [33, 46, 61, 193, 210], it cannot be regarded applicable anymore for the calibration of high-accuracy SAR systems. Figure 2.11 shows recent analysis results of the author which indicate that the frequency dependence of even a large 2.8 m trihedral corner reflector cannot be disregarded if the RCS of the corner is taken as the radiometric reference. Further discussion on this specific example follows in Sec. 5.1, including an approach about how such variations can be compensated in radiometric SAR calibration.

2.4.3 Transponders

A transponder is an active device which retransmits an amplified and possibly delayed replica of a received signal. Single and dual antenna designs exist, see Fig. 2.12. The transponder RCS ζ_t depends on the receive and transmit antenna gains G_{tr} and G_{tt} , the electronic gain G_e of the transponder's amplifiers, and the wavelength λ according to [27]

$$\zeta_t = \frac{\lambda^2}{4\pi} G_{tr} G_e G_{tt}. \quad (2.60)$$

The derivation of this equation is given in Chap. 6, where also several methods for calibrating the transponder RCS are discussed.

A precision transponder typically requires more effort to be designed and built than a passive target, but it offers three distinctive advantages over passive targets. These are described in the following.

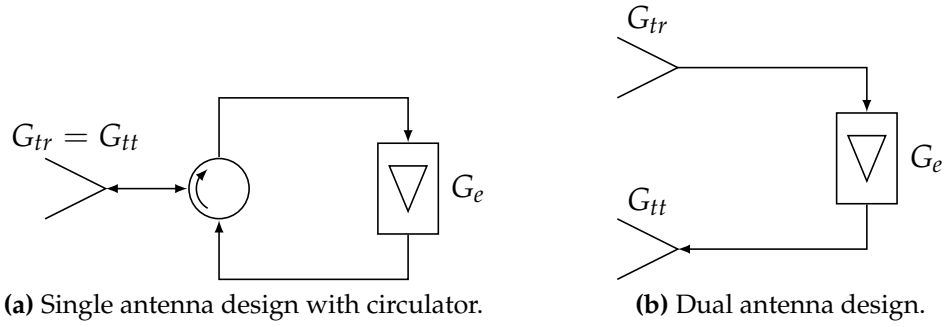


Figure 2.12: Principal block diagrams of radar calibration transponders: A transponder requires an antenna for reception and transmission, and a stable amplifier.

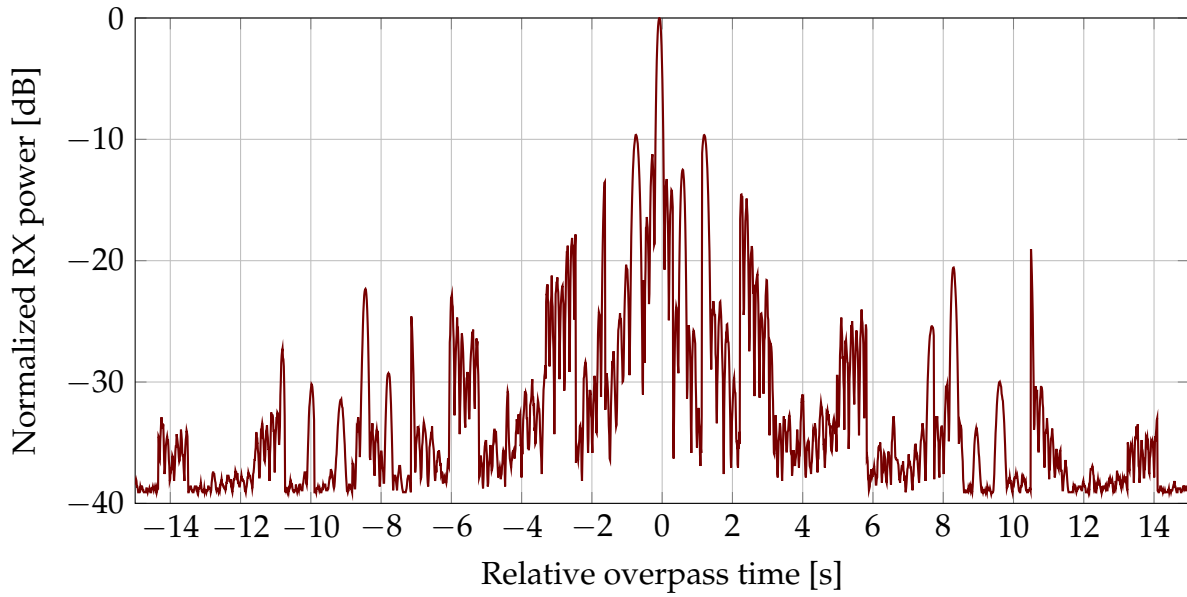


Figure 2.13: Exemplary transponder recording of a Sentinel-1 azimuth antenna pattern. The pattern was recorded on August 31, 2014, for an ascending interferometric wide swath beam in the *terrain observation by progressive scans* (TOPS) mode at Bonlanden, South Germany.

One of the biggest advantages of a transponder is its potentially large RCS with respect to its size. In comparison to passive targets which can never reflect more energy than they receive, a transponder is connected to a power source (possibly a battery) and can actively amplify the received signal. A transponder's small size facilitates its usage during optimized calibration campaigns with few targets because a transponder can be temporarily installed for each overpass and then transported away by car, even by a single person. This approach was used for the TerraSAR-X and TanDEM-X calibration campaign [161]. Besides mobility, a small size is also advantageous for permanent outdoor installation where wind loads resulting from storms would otherwise require much sturdier support structures.

A transponder has a second advantage over passive point targets: The received signal can be recorded. Figure 2.13 shows an exemplary recording by one of DLR's C-band *Kalibri* transponders from a Sentinel-1 overpass. The recording is shown over time. If the transponder and satellite positions are accurately known in the same time and space

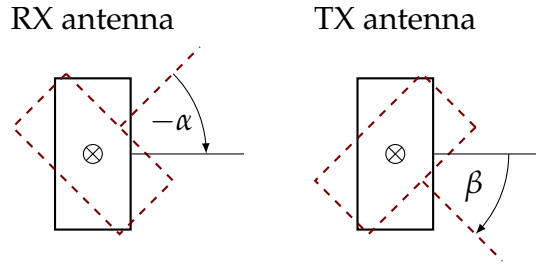


Figure 2.14: Transponder antennas as seen from a SAR satellite: The transponder antenna rotation angles (α for the receiving antenna, and β for the transmitting antenna) are defined in accordance with the backscatter alignment convention. A transponder configured with $\alpha = 0^\circ$, $\beta = 0^\circ$ responds maximally for a HH polarized SAR system; the dashed configuration with $\alpha = -45^\circ$, $\beta = 45^\circ$ shows a common configuration where the transponder's backscatter is equally strong for any of the four SAR system polarizations HH, HV, VH, and VV.

reference frames, then the recording over time can be converted to a cut through the satellite's transmit antenna pattern over angle. Due to the geometry, the transponder approximately records the satellite's azimuth pattern; a slight deviation from a planar cut around the main beam (resulting from the overpass geometry) is typically neglected during later analysis. The resulting antenna pattern diagram is then used for subsequent antenna model verifications, as detailed in [10, 11, 161]. The drop-off of the recorded pattern left and right to the main beam is mostly due to the satellite's high gain antenna, but part of the observed drop-off is also due to the receive antenna pattern of the transponder. The transponder antenna pattern can be characterized by antenna measurements, allowing this effect to be compensated. All in all, the recording capability of the transponder is indispensable for the calibration of modern, multiple mode SAR systems, where approaches without an antenna model are not feasible due to time and cost constraints.

A third advantage of a transponder over passive targets is the ability to adapt the polarization orientation according to the calibration task. Most flexibility is achieved by a dual-antenna design where the receiving antenna can be rotated independently by angle α from the rotation of the transmitting antenna by angle β , see Fig. 2.14. Changing the polarization orientation of the antennas allows to measure a SAR system's cross-polarization suppression and channel imbalances [62].

Instead of relying on two rotatable antennas, a single dual-polarized antenna (i. e., an antenna with two feeds) or in total four antennas (two for reception, two for transmission, respectively orthogonally aligned to each other) might be used. Combined with a dual-channel design, where two amplification loops with a settable phase shift between the two loops is possible, additional operational flexibility is achieved. The transponder's polarization orientation can be changed electronically during an overpass, or several replicas of a received pulse can be retransmitted with different polarizations and slight offsets in time. This flexibility can be exploited to simulate several virtual calibration targets with different polarization settings, although only one target needs to be manufactured and installed. Due to the challenges in achieving the required amplitude and phase balances, this approach has not yet been implemented for SAR calibration transponders.

Transponders have been built for various SAR missions and frequency bands [57, 75, 89,

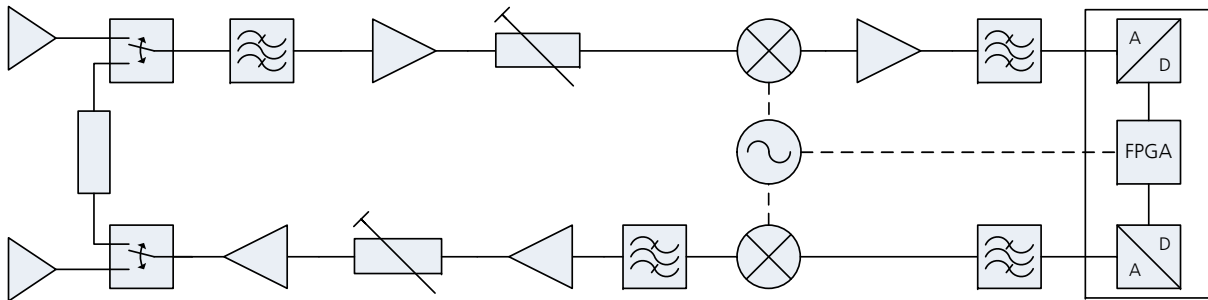


Figure 2.15: Schematic block diagram of DLR's *Kalibri* C-band transponder [41, 93]. The digital sub-system with an ADC, FPGA, and DAC shown on the right allows to implement a digital delay line and fine-tuned gain drift compensations.



Figure 2.16: One of DLR's two-antenna *Kalibri* transponders mounted on a two-axis positioner, initially installed in 2014 for the calibration of the Sentinel-1A SAR system.

90, 93, 105, 108, 159, 175]. An exemplary realization of a transponder hardware design is given in Fig. 2.15, which shows a simplified block diagram of DLR's C-band *Kalibri* transponders [41, 93]. These transponders were designed and built for the radiometric calibration of Sentinel-1. On top is the receiver chain, which contains a receiving antenna, a low-noise amplifier, filters, a down-conversion stage, and terminates at an analog-to-digital converter (ADC). The transmitter chain at the bottom reverses the steps by starting with a digital-to-analog converter (DAC), and then going over an up-converter stage, a filter, and amplifiers to the transmitting antenna. The ADC, DAC, and field-programmable gate array (FPGA) form the digital sub-system. Here the received signal is available digitized with a sampling rate which significantly exceeds the Nyquist sampling rate so that the signal can be reconstructed without loss of information. The digital sub-system implements a digital delay line by storing the incoming pulse in a first-in, first-out (FIFO) stage with variable write and read delays. Furthermore, the digital sub-system allows to store the incoming wave, either detected and down-sampled for increased recording lengths, or at the maximal sampling rate for later analysis of the received pulses. Two electromechanical switches allow to route a reference signal, which is emitted by the DAC, through nearly all transponder loop components (except the antennas and the cables leading to it) so that it can be recorded by the ADC again. This mechanism is used for precise (in the order of 0.01 dB) gain drift compensations.

A variation of the transponder design above is an encoded transponder. Encoded transponders use phase-shift keying with a defined code at the rate of the SAR pulse-repetition frequency to achieve a better transponder-to-clutter separation for point-target analysis [8, 81, 82, 117, 203]. When the transponder transfer function is modified from pulse to pulse, it is not visible anymore as a strong scatterer in a normal SAR image due to decorrelation. Instead, the encoding must be inversed in the SAR processor, requiring code synchronization and leading to improved clutter suppression. Yet the necessary modification of the SAR processor for encoded transponder measurements is conceptually non-ideal for radiometric calibration because the system is not calibrated in its final configuration. Besides for radiometric calibration, encoded transponders can also be used for tagging [8, 117]: If several transponders with different codes are deployed, each target can be identified in a SAR scene if and only if the used code is known.

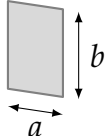
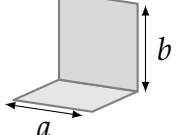
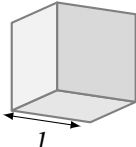
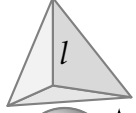
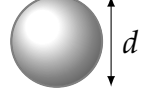
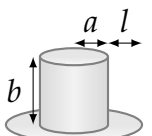
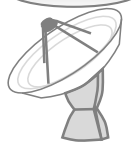
2.4.4 Other Passive Calibration Point Targets

Besides trihedral corner reflectors, many other passive radar targets have been devised, typically trading size, monostatic or bistatic beam width, polarimetric performance, simplicity in design, and manufacturing costs. An overview is given in Tab. 2.3.

Flat, Rectangular, Metallic Plate

The simplest radar target with a large peak RCS per size is the flat, metallic plate. In the context of optics, it is also simply called a mirror. The flat plate is interesting because it forms the building block of more complicated targets like the dihedral corner (two plates), or a trihedral corner (three plates). Furthermore, in many numerical RCS modeling approaches, the surface is discretized into flat facets, and depending on the

Table 2.3: Overview of passive man-made point targets. Used symbols: a, b, d, l : lengths, λ : wavelength, G : antenna gain, A_e : effective antenna area.

Type	Approximate peak RCS	Geometry
Rectangular plate	$4\pi(ab)^2/\lambda^2$ [100]	
Dihedral reflector	$8\pi(ab/\lambda)^2$ [100]	
Square corner reflector	$12\pi l^4/\lambda^2$ [9]	
Triangular corner reflector	$4\pi l^4/(3\lambda^2)$ [9]	
Spherical Luneberg lens	$2\pi d^4/\lambda^2$ [9]	
Tophat reflector	$8\pi ab^2l/[\lambda\sqrt{l^2+b^2}]$ [169]	
(Parabolic) Antenna	$A_e G = 4\pi A_e^2/\lambda^2$ [4]	

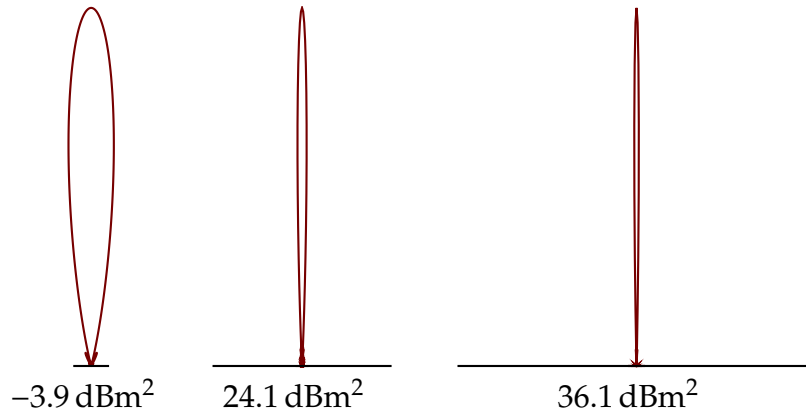


Figure 2.17: Normalized radar cross sections at normal incidence for quadratic, metallic plates with side lengths of 0.1 m, 0.5 m, and 1.0 m (from left to right) at C-band (5.4 GHz), based on Eq. (2.61). Noted below is the peak RCS. A large plate results in a narrow pencil-shaped return so that a flat plate is typically not used for SAR calibration due to the stringent pointing requirements.

wavelength, the results for a single facet can be carried over to more complex objects which are made up from many adjacent facets.

As long as the plate is large with respect to the wavelength and as long as it can be considered perfectly conducting, the monostatic and bistatic RCS ζ can be approximated with the principle of physical optics (PO). Under the PO approximation, the current density on the surface is considered equivalent to the incident field. No currents exist in shadow areas. The scattered field results by integrating over the surface currents. This integral can be solved in closed form for rectangular patches [100]. A simplified solution for normal incidence is given by [78]:

$$\zeta = \frac{(kab)^2}{\pi} \cos^2 \gamma \left[\frac{\sin(ka \sin \theta)}{ka \sin \theta} \right]^2 \left[\frac{\sin(kb \cos \theta \sin \phi)}{kb \cos \theta \sin \phi} \right]^2, \quad (2.61)$$

where $k = 2\pi/\lambda$ is the wave number, a and b are the side lengths of the plate (see Tab. 2.3), and θ and ϕ are the azimuth and elevation angles (centered at broadside). At normal incidence, most of the energy is scattered back in the normal direction. The larger the plate, the more concentrated the broadside pattern appears, see Fig. 2.17 for three examples. This focusing effect is known from antenna arrays, where larger arrays also result in higher gains in the main beam direction as long as all antenna array elements are equally excited in phase.

The pencil shaped return is also the reason why flat plates are not used in SAR calibration: The alignment requirements are too stringent, and slight misalignments (of less than 1°) are sufficient to significantly change the plate's RCS from its peak or reference RCS. However, a flat, often circular plate is a common calibration target for RCS measurement ranges where precision positioners and controlled conditions exist.

Dihedral Corner Reflector

A dihedral corner reflector is the simplest extension of a flat plate target. In its most common form, a dihedral consists of two rectangular flat plates which are mounted

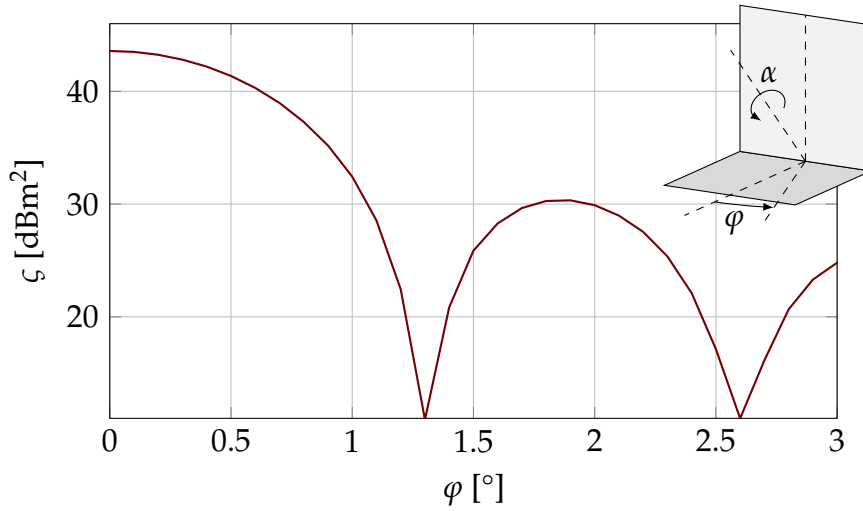


Figure 2.18: RCS of a perfectly conducting dihedral corner reflector, where all side lengths are 1 m, at 9.65 GHz. The azimuth cut was simulated with the method of moments (using FEKO) at an elevation angle of 45° with respect to the vertical plate. At the shown horizontal alignment of one of the plates, α equals 0° .

at a right angle with respect to each other [100]. This configuration makes it an excellent polarimetric target because depending on the rotation angle α (see Fig. 2.18 and Tab. 2.2), the return can be configured to be only co- or cross-polarized, or both. Being a conceptually simple structure, the dihedral (with a right, acute, or obtuse inner angle) is also a popular object for numerical simulations [71, 208].

The main scattering mechanism is the double bounce: An incident ray is reflected by the first plate toward the second plate, from where the ray is reflected back in the direction of the incident ray. This double-bounce mechanism results in a comparably large peak RCS with respect to the dihedral's size, see Tab. 2.3.

The retro-reflection property only exists in the plane perpendicular to the dihedral's inner edge though. For rays entering in this plane, the monostatic pattern is broad. In the plane parallel to the dihedral's inner edge, the return behaves like that of a flat plate and is therefore very narrow, which the simulation results in Fig. 2.18 show. The narrow pattern in one of the scattering planes renders the dihedral unsuitable for radiometric SAR calibration because of practical problems in target alignments, much like the flat plate. Nevertheless, the dihedral has been used extensively for determining polarimetric SAR correction factors [61, 62, 64].

Parabolic Antenna

If a short is inserted at the terminal of an antenna, then most of the power of an incident wave is reflected back. As a first approximation, i. e., assuming total reflection, no losses, and no additional scattering from the mechanical antenna structure, the RCS is simply proportional to the antenna gain G , see Tab. 2.3 [4]. Hence, the RCS is frequency dependent and only significant within the operational bandwidth of the antenna.

High gain antennas like large parabolic antennas [14] necessarily have a narrow beam width so that the antenna needs to be accurately steered toward the SAR sensor if used for calibration – a challenging endeavor. Parabolic antennas at satellite downlink

stations seem to be good candidates as bright radar targets, provided that the antenna feet operates at the SAR frequency: The reflector antennas are often not only very large (10 to 30 m in diameter), but also equipment and well-practiced procedures exist for accurate antenna steering.

Despite these enticing properties, parabolic antennas are in practice not well suited as accurate radiometric measurement standards. In comparison to simpler targets like corner reflectors, more effects need to be considered during the calibration of the antenna's RCS, including uncertainties of gain measurements, alignment, and determination of the scattering of the antenna structure [99]. The sum of the uncertainty contributions leads to a calibration target with an inferior RCS knowledge uncertainty. Nevertheless, downlink reflector antennas might still be exploited as bright targets of opportunity, a good choice for (relative) long-term drift measurements.

Tophat and Bruderhedral Reflectors

A tophat reflector is formed by vertically mounting a metallic cylinder on an extended horizontal metallic plate, see the sketch in Tab. 2.3. The main scattering mechanism is a double-bounce reflection incorporating the ground plate and the cylinder wall. In comparison to a dihedral corner reflector, the backscatter is now independent from the azimuth direction due to the rotational symmetry. In elevation, the RCS is also not so sensitive for varying incidence angles around its peak RCS [169].

The RCS of a tophat reflector is significantly smaller than that of a dihedral corner reflector with similar dimensions because the main monostatic scattering contribution is formed only along a vertical line on the cylinder. Rays which hit the cylinder left or right of the plane of symmetry are mostly reflected away from the incidence direction, reducing the monostatic RCS.

The polarization state of vertical or horizontal incident waves is not changed, i. e., the tophat reflector behaves like a dihedral corner reflector with $\alpha = 0^\circ$, where α is defined in Fig. 2.18.

A Bruderhedral reflector is a compact version of a tophat reflector. It is created by replacing the cylinder with a cylinder segment, which reduces the size and weight, but also limits the operational azimuth range. Within the operational range, the Bruderhedral behaves approximately as a tophat reflector (neglecting secondary scattering mechanisms, formed e. g. by creeping waves or the cylinder's top).

Although tophat and Bruderhedral reflectors offer a double bounce structure with a wide monostatic pattern in azimuth and elevation, they have not been reported to be used as calibration targets for radiometric SAR calibration. This is partly due to the small RCS with respect to the reflector's size, and partly due to difficulties in accurately determining the reflector's absolute RCS. As was reported by Silverstein and Bender [169], predictions and measurements only agree to within 2 dB to 3 dB, which is unacceptable for modern radiometric calibration targets.

Luneburg Lens Reflector

A Luneburg lens, as first introduced by Luneburg and Herzberger [111], is a variable-index, spherically symmetric optical system which has the property of focusing incident parallel rays on a single point of the sphere's surface. More than one radius-dependent

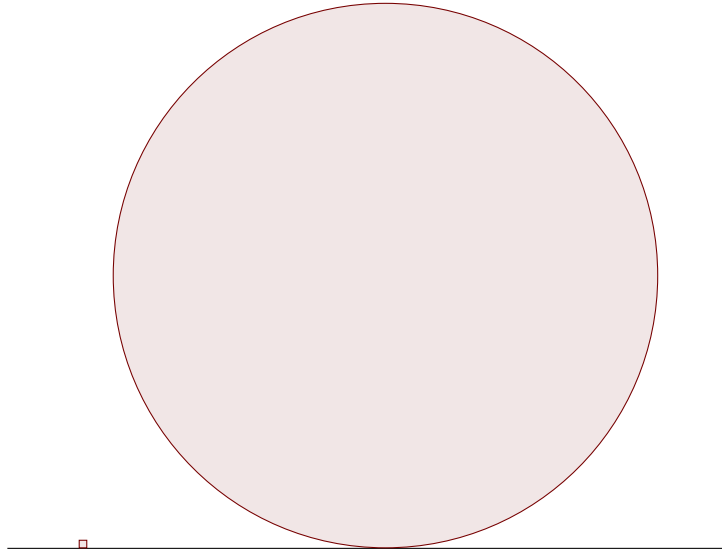


Figure 2.19: Size comparison of a metal square plate (left) at broadside alignment and a metal sphere (right) with the same RCS at C-band (5.4 GHz).

function of the refractive index exists to achieve this feature [126], although the continuous variation of the refractive index is often replaced by a stepped-index approximation for practical reasons [110].

In order to use a Luneburg lens as a radar reflector, part of the sphere's surface (usually up to a hemisphere) is covered with a reflector, i. e., a smooth metal sheet. Incident plane waves are therefore retro-reflected, comparable to the flat metal plate from Sec. 2.4.4 for a broadside alignment.

The advantage of a Luneburg lens reflector over other passive targets is its large and aspect-angle independent RCS. The target is therefore especially suited for the tuning of high-resolution or even circular SAR systems [135]. Due to the weight, size, costs, and uncertainties resulting from the dielectric lens the Luneburg lens reflector though has, as far as is known, not yet been used for the radiometric calibration of SAR systems.

Metal Sphere

A metal sphere is a commonly used RCS calibration target for RCS measurement ranges [54] because its RCS can be accurately determined analytically (under the assumption of perfect conductivity) for monostatic [2, 184] and bistatic [152] configurations at any frequency. Furthermore it has an omni-directional monostatic backscatter pattern so the target neither requires alignment nor can RCS uncertainties result from mis-alignments.

In the high frequency region (where objects are at least two or three wavelengths large), the sphere's RCS can be well described with the geometrical optics (GO) approximation [100]:

$$\zeta_{\text{sphere}} = \pi a^2 \quad (2.62)$$

where a is the radius of the sphere. The RCS of a large sphere is therefore independent of frequency and equals its cross-sectional area.

Although the RCS of a conducting sphere can be accurately computed at any frequency, its RCS is small in comparison to other radar targets. Figure 2.19 shows a size compari-

son between a square plate (broadside alignment) and a metal sphere which have the same RCS. At 5.4 GHz (C-band), the ratio between the sphere's diameter and the plate's edge length is 72, showing that spheres cannot be used as SAR calibration targets for practical reasons.

3 Novel Definition of the Radiometric Measurement Quantity

The first step in any measurement procedure is to precisely define what actually needs to be measured. This is the measurement quantity, which can formally be described as the “property of a phenomenon, body, or substance, where the property has a magnitude that can be expressed as a number and a reference” [92]. Without a clear definition of the measurement quantity, metrological traceability cannot be achieved because any measurement result and uncertainty analysis would be ambiguous.

This chapter introduces a new definition of the actual measurement quantity for radiometric synthetic aperture radar (SAR) measurements. The main findings of this chapter resulted in a peer-reviewed publication [51].

3.1 Introduction

The current quantity for describing the reflectivity of point targets in SAR images is the radar cross section (RCS) [32, 33, 61, 131, 171, 212]. At the moment, no distinction is made between SAR and real aperture radar (RAR) systems when describing the reflectivity of a point target.

In this chapter it is argued that RCS is actually *not* the quantity which is measured by a SAR instrument. This discrepancy is a direct result of pulse compression in the complex domain during SAR processing. Nevertheless, the measured quantity can well be approximated by a target’s RCS if a relatively low-resolution system or “well-behaved” targets are assumed, which explains the current uniform adoption of RCS as the radiometric quantity for SAR systems.

For the general case though, it is argued that a SAR system does not measure a target’s RCS, but rather a different quantity. This quantity is given the new name *equivalent radar cross section (ERCS)*.

The distinction between RCS and ERCS is especially significant for modern high-resolution SAR systems. For them, the RCS of the target can vary significantly over the pulse bandwidth or incidence angle range, a fact that has been ignored thus far.

The new definition does not change in any respect the way in which radiometric measurements are performed. However, the new definition requires an adapted radiometric calibration approach because now the ERCS of a reference target needs to be known. The radiometric link between point and distributed targets, as described in Sec. 2.3.3, remains intact.

3.2 Review of the Current Definition

Currently, RCS is understood to be the radiometric quantity measured by a SAR system. A point target's reflectivity is quantified in square meters. The quantity is the same as the one measured by a real aperture radar system. The radar cross section ς of any target is defined as the scaled ratio of the scattered power (seen at distance R away from the point target) to the incident power, or

$$\varsigma = \lim_{R \rightarrow \infty} 4\pi R^2 \frac{|\mathbf{E}^s|^2}{|\mathbf{E}^i|^2}, \quad (3.1)$$

where \mathbf{E}^s and \mathbf{E}^i are the scattered and incident electrical fields, respectively [54, 100].

For RAR systems, the link between the measurement system (the radar) and the radar target's RCS ς is directly established through the (monostatic) radar equation

$$P_r = \frac{P_t G^2 \lambda^2}{(4\pi)^3 R^4} \varsigma, \quad (3.2)$$

where the received power P_r is expressed in terms of the transmitted power P_t , the receive and transmit antenna gain G , the wavelength λ , the radar-target distance R , and the point target radar cross section ς .

In contrast to a RAR system, a SAR image is formed through focusing. If (and only if) an *ideal* point target can be assumed, a direct link between the square-law detected output pixel intensities and the point target's RCS exists. Ideal targets are currently assumed in the SAR literature [32, 33, 61, 131, 171, 212], albeit only implicitly.

An ideal target, in this respect, shall be defined as a target with a transfer function H_t that is flat over frequency f and angle ψ , i. e.,

$$H_t(f, \psi) = \text{const}. \quad (3.3)$$

The (monostatic) angle $\psi = (\theta, \phi)$ is the angle under which the target is seen by the SAR instrument.

The image is formed as follows [61]: The SAR receiver records the target data as complex amplitudes $s_r(x, y)$; x and y are spatial coordinates. Neglecting noise, the complex SAR image is then formed by

$$s_{\text{out}}(x, y) = \sqrt{K} s_r(x, y) * h(x, y), \quad (3.4)$$

where K is a complex, absolute calibration factor (known through calibration), $*$ denotes convolution, and h is the optimal filter for the SAR system (i. e. the time-inversed complex conjugate of the system replica) [61]. Conventionally [32, 33, 61, 131, 171, 212], it is assumed that the radar backscatter S of a single point target can be described by

$$S(x, y) = \sqrt{\varsigma} \delta(x, y), \quad (3.5)$$

where ς is the point target's radar cross section, and $\delta(x, y)$ is the Dirac delta function. This target description in the spatial domain is equivalent to the target description (3.3) in the spectral-angular domain. The RCS of the point target is derived from the square-law detected complex image [61]

$$|s_{\text{out}}(x, y)|^2 = K \varsigma |\delta(x, y) * h(x, y)|^2 \quad (3.6)$$

by integration over a sufficiently large region A with the approximation [61, 69]

$$\iint_A h(x, y) \, dx \, dy \approx 1,$$

so that the integrated point target pixel intensity is

$$\mathcal{E} = \iint_A |s_{\text{out}}(x, y)|^2 \, dx \, dy = K\zeta. \quad (3.7)$$

The integrated pixel intensity is therefore directly proportional to the point target RCS for uniform targets according to Eq. (3.5).

This concludes the summary of the conventional understanding formulated in [32, 33, 61, 131, 171, 212] of how pixel intensities are linked to RCS.

3.3 Problems Arising from the Current Definition

The previous section reviewed the use of RCS as the radiometric quantity which describes the reflectivity of point targets as observed by a SAR system. The main point of critique is: Point targets need to be ideal (in the sense of Eq. (3.3)). For any other target, the following two problems occur:

- Two targets with identical radar cross sections can appear differently bright in a SAR image, i. e., the pixel magnitudes are different. This results from the RCS being defined as a ratio of powers, whereas the complex reflectivity measured by a SAR system depends both on the amplitude and the phase response of the target.
- The RCS is a frequency and direction-dependent physical property of a radar target; in measurements it is reported per frequency and per angle. A SAR image, on the other hand, can only be formed after integrating over a certain frequency and angular range. At best, a weighted RCS average results, which can differ considerably from most radar cross sections within the integration interval (especially for high-resolution SAR systems).

These two main problems will be elaborated in more detail in the following.

3.3.1 Pulse Compression in the Complex Domain

First, targets with arbitrary amplitude and phase responses (over frequency and angle) shall be permitted now. Equation (3.3) is generalized and becomes

$$H_t(f, \psi) = A(f, \psi) e^{j\varphi(f, \psi)} \quad (3.8)$$

where $A(f, \psi)$ and $\varphi(f, \psi)$ are the frequency and angular-dependent amplitude and phase response functions, respectively. The simplified measurement model in Eq. (3.3) is inherent within the more general definition, Eq. (3.8).

The generalization from Eq. (3.3) to Eq. (3.8) is a necessary step in the light of modern and emerging high-resolution SAR systems. Higher resolutions in range are achieved

through higher bandwidths, whereas higher azimuth resolutions require a wider synthetic aperture so that targets on the ground are illuminated through a larger range of aspect angles. Within these spectral and angular intervals, the RCS of a target can vary by several decibels. Examples for this are given in Secs. 3.3.2 and 5.4.

Now, the discussion of Sec. 3.2 can be repeated, but this time permitting arbitrary targets according to Eq. (3.8). Hence, Eq. (3.5) becomes

$$S_e(x, y) = \sqrt{\zeta_e} h_{tn}(x, y)$$

where h_{tn} is the normalized point target's point-spread function¹ (see the later Sec. 3.5 for a definition), and ζ_e is a scalar scaling factor describing the magnitude of the reflectivity. Hence, the square-law detected image becomes

$$|s_{out,e}(x, y)|^2 = K\zeta_e |h_{tn}(x, y) * h(x, y)|^2, \quad (3.9)$$

and the point target's energy, resulting from an integration of the image intensities, is

$$\begin{aligned} \mathcal{E}_e &= \iint_A |s_{out,e}(x, y)|^2 dx dy \\ &= K\zeta_e \iint_A |h_{tn}(x, y) * h(x, y)|^2 dx dy. \end{aligned} \quad (3.10)$$

The convolution operation effectively performs a weighted average of the point target's point-spread function over frequency and aspect angle. In contrast to Eqs. (3.6) and (3.7), the pixel intensities $|s_{out,e}(x, y)|^2$ and the target energy \mathcal{E}_e therefore do not only depend on the scaling factor ζ_e anymore, but also on the point target's complex transfer function.

The definition of RCS in Eq. (3.1) only considers a ratio of powers, i. e., magnitudes; the phase is irrelevant for its definition. The filtering operation in Eq. (3.10), on the other hand, operates on complex signals, and both the signal magnitude and phase over time influence the filter output. In conclusion, this discrepancy between the definition of RCS (incorporating absolute magnitudes) and filtering (depending on magnitude and phase) is another reason why the target RCS is unsuitable to describe the pixel intensities in SAR images. Two point targets with identical RCSs can result in distinct pixel intensities and target energies.

In conclusion, the SAR signal of a point target after pulse compression is only proportional to its RCS if its frequency and angle-dependent transfer function can be approximated as constant in amplitude and phase over the relevant frequency and angular range. In the general case, the integrated SAR pixel intensity after processing depends on the transfer function of the point target because pulse compression is a filtering process over the system bandwidth and aspect angle range.

3.3.2 Integration Intervals and Weighted Means: Qualitative Examples

Quantitative examples showing the practical significance of differentiating between RCS and ERCS will be given in Chap. 4, where a practical methodology is introduced

¹The dependence of the point spread function h_{tn} on spatial coordinates (x, y) can equivalently be expressed as a dependence on azimuth and range time (t_a, t_r) , or frequency and angle (f, ψ) .

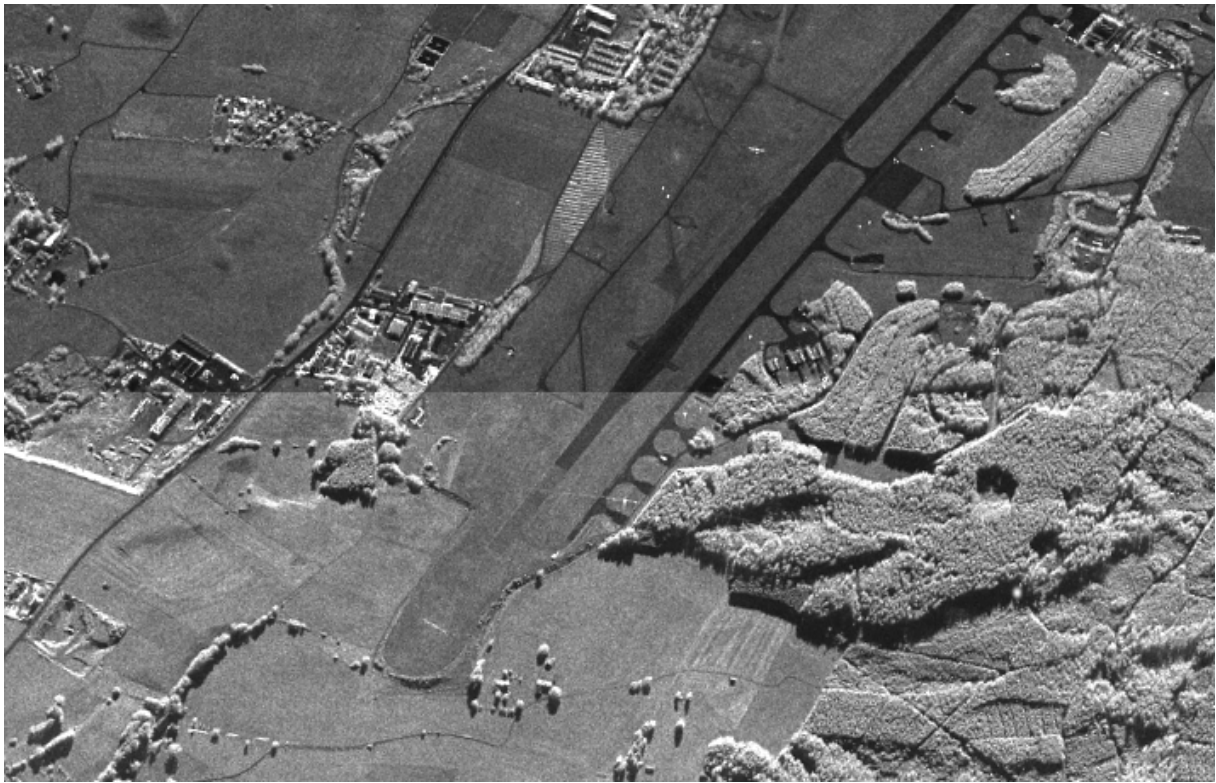


Figure 3.1: One scene imaged synchronously by DLR’s radiometrically calibrated airborne F-SAR sensor in S-band (upper half) and X-band (lower half), taken in VV polarization on June 8, 2010, at Kaufbeuren, Germany. The *desirable* difference in backscatter at the two frequency bands is easily discernible.

for linking the two quantities. Here, on the other hand, three qualitative examples are shown which emphasize why RCS generally cannot be used as the radiometric quantity for describing SAR reflectivity.

Multi-spectral SAR systems. The frequency dependence of natural targets like agricultural terrain is most apparent when comparing images taken at different frequency bands but otherwise at equivalent time and perspective. The SIR-C/X-SAR instrument, which was flown during two missions in 1994, was the first spaceborne SAR system capable of operating simultaneously at L-, C-, and X-bands [94]. The fractional bandwidth for each channel was still small at below one percent. Several multi-spectral airborne SAR systems exist among which is the F-SAR system from the German Aerospace Center (DLR) [146]. One exemplary scene, which was imaged simultaneously at two different frequency bands, is shown in Fig. 3.1, where the fractional bandwidths for the S- and X-band images are 9 % and 8 %, respectively. The resulting calibrated images show significant differences in pixel intensities, exemplifying the frequency dependence of the imaged terrain.² This is, of course, expected and desired. After all, the added information content is the actual impetus for building multi-spectral SAR systems like SIR-C/X-SAR and F-SAR.

So what would happen if the same scene was imaged by an ultra-wideband SAR system?

²The noise-equivalent σ^0 of both channels is well below the measured intensities so as not to significantly contribute to the difference in intensities.

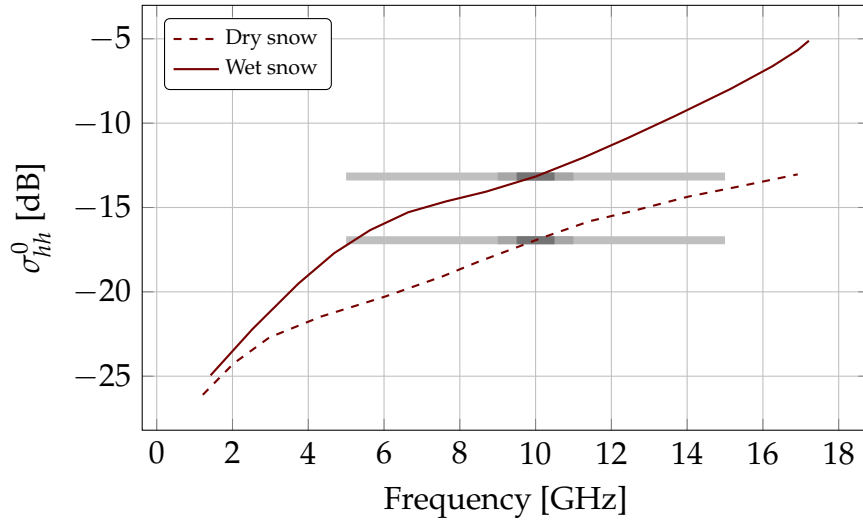


Figure 3.2: Frequency dependent backscattering coefficient σ^0 for two exemplary terrain types: dry and wet snow (measured at HH polarization and an incidence angle of 50° , data from Ulaby [191]). For illustration purposes, fractional bandwidths of (10, 20, 100) % are shown at 10 GHz to emphasize the large frequency dependence within these spectra.

For instance, a fractional bandwidth of 100 % (which is even exceeded by some airborne SAR systems, albeit at the VHF-band [195]) would cover the S- and X-band frequencies in Fig. 3.1 and all frequencies in between. Hence describing all frequency-dependent terrain radar cross sections within the whole spectrum by a single radar cross section is certainly counter-intuitive and misleading. It would mean that the model uncertainty dominates the radiometric uncertainty budget even if the SAR sensor is well designed and calibrated.

Ultra-wide bandwidth (UWB) SAR systems. The frequency dependence of different terrain types was systematically surveyed by Ulaby [191]. As an example, the frequency dependent backscatter coefficients of dry and wet snow are reproduced in Fig. 3.2. For both terrain types the backscatter coefficient varies by about 0.4 dB from its value at 10 GHz within a fractional bandwidth of 10 %, and the difference increases significantly for larger bandwidths. If this variation is compared to the radiometric accuracy of current (narrower bandwidth) spaceborne SAR instruments, which is typically below 1 dB, it becomes apparent how important the definition of the measurand is. This is especially true in the case of wideband SAR sensors which simply do not see an approximately constant frequency response within their larger range bandwidths. The processed SAR images rather show a weighted RCS average over frequency, a quantity which is fundamentally different from RCS.

Circular SAR and multibaseline SAR tomography. When the SAR method was first conceived in 1951 [199], it was based on an imaging geometry which is today commonly known as the stripmap method. Although the stripmap mode has played a key role for all operational SAR missions, further imaging geometries and processing methods were conceived and implemented in order to improve on resolution (horizontal and vertical) or coverage. As discussed in Sec. 2.1.2, the advanced modes include ScanSAR and spotlight, as well as the interferometric, circular (3D), and tomographic (multi-

baseline) SAR modes. These advanced methods can be regarded as a generalization of the stripmap method, or reversely the stripmap method can be regarded as a special case of the more advanced methods.

In the same light, RCS might be regarded as a sufficiently good approximation of the measured quantity for the special case of a (low-resolution) stripmap SAR system. Yet RCS is inappropriate when the SAR principle is generalized to more advanced, higher-resolution modes. Tomographic SAR and circular SAR methods distinctively depend on imaging a target from a wide range of angles. The problem is that within this angular interval, the RCS cannot be regarded as approximately constant anymore. For circular SAR, this was already pointed out by Soumekh [177], although the discussion was not geared toward quantitative radiometric measurements but rather toward high-resolution reconnaissance applications.

A new radiometric quantity is required which is valid both for the common special case (stripmap mode) as well as for the general case (encompassing high-resolution, circular, and tomographic SAR systems). Only an unambiguous definition of the measurement quantity allows traceable radiometric calibration. There is no justification for introducing different radiometric quantities for different SAR imaging modes, and therefore a definition is required which extends from the special to the general case.

3.4 Novel Definition of the Radiometric Measurement Quantity

In the previous section it was argued that, in the general case, the pixel intensities in SAR images are not simply proportional to the target radar cross section ζ , neither are derived quantities like the normalized radar cross section σ^0 (see Sec. 2.1.4). In other words, the measurement quantity in radiometric SAR measurements is not RCS, and therefore it should not be referred to as RCS. It is proposed to instead call the measurement quantity for point targets *equivalent radar cross section* (ERCS), defined as follows:

The equivalent radar cross section ζ_e shall be equal to the radar cross section of a perfectly conducting sphere which would result in an equivalent pixel intensity if the sphere were to replace the measured target.

Here the equivalent pixel intensity is derived according to a documented measurement procedure, which typically specifies either the (often preferred) integral method or the peak method, see Sec. 2.3.3.

The ERCS definition exploits the frequency and angular independence of the RCS of a sphere with radius a

$$\zeta_{\text{sphere}} = \pi a^2, \quad (3.11)$$

which is a valid approximation as long as the sphere circumference is much (say greater than ten times) larger than the wavelength [100].

Replacing RCS by *equivalent RCS* pays tribute to the two principal problems. Now,

- the filtering of *complex* signals according to Eq. (3.4) is correctly distinguished from the definition of RCS, which only takes signal magnitudes into consideration, and

- cases are covered for which the target's RCS dependence on frequency or angle are significant according to Eq. (3.8).

One could say that the terminology of *equivalent RCS* allows distinction between the target RCS (Eq. (3.1)) and the target's pixel intensity as seen through the eyes of the SAR processing filter (Eq. (3.10)). The proposed terminology is applicable to target backscatters with an arbitrary frequency and angular dependence according to Eq. (3.8), including targets with a flat frequency and angular response. Depending on the target, the measurement uncertainty can appear greatly reduced due to the more accurate measurement model, which especially benefits high bandwidth, high-resolution systems requiring a high radiometric accuracy.

The transition from the present to the novel terminology does not pose difficulties. For instance, the measurement unit for RCS and equivalent RCS is the same: square meter. Also, it is straightforward to transform the backscatter coefficient σ^0 and other derived quantities to equivalent quantities, i. e., to an *equivalent* backscatter coefficient σ_e^0 , etc. Furthermore, describing the measurement quantity in terms of an equivalent physical object (a sphere) allows one to form a simple mental model of what this quantity means.

3.5 Implications of Proposed Terminology for Calibration

External radiometric calibration is achieved by placing a point target of known backscatter within the imaged scene so that an adequate calibration factor, called K in Eq. (3.7), can be derived; until now, the reference targets were described by their RCS [33, 61, 161]. With the new understanding that not RCS but equivalent RCS is measured by a SAR instrument, the reference target must now be described by its *equivalent* RCS and not anymore by its RCS. Two strategies are possible:

1. Build reference targets whose amplitude and phase responses are as constant as technically feasible over the relevant range bandwidth (in which case the target RCS at any frequency within the range bandwidth is close to its equivalent RCS). These targets can thus be described by Eq. (3.3).
2. Compute the equivalent RCS, the radiometric quantity seen in a SAR image, based on the arbitrary but known transfer function of a reference target according to Eq. (3.8).

In almost all cases, strategy (1) excludes passive point targets for accurate or wideband SAR systems. Specifically, the RCS of commonly used trihedral corner reflectors is frequency dependent, see Fig. 2.11 on p. 33. Building active targets (transponders) with a constant frequency response over the complete range bandwidth is, while technically possible, still very challenging. For instance, the frequency dependent transmission of antennas, amplifiers, and filters would need to be compensated by the transponder electronics or otherwise a calibration error would result.

Strategy (2) circumvents the mentioned problems for strategy (1), allowing both active and passive reference targets to be used. The following describes how the calibration procedure needs to be adapted in order to take an arbitrary but known reference target transfer function $H_t(f, \psi)$ into account.

Up to now, the calibration coefficient K is simply derived by placing a target of known ERCS ς_e (assuming a sphere-like target according to Eq. (3.3)) within a scene and determining its integrated pixel intensity \mathcal{E}_e so that

$$K = \frac{\mathcal{E}_e}{\varsigma_e} \quad (3.12)$$

according to Eq. (3.7). On the other hand, if an arbitrary target according to Eq. (3.8) is considered, its equivalent RCS ς_e is not immediately known. It can be derived, however, by processing the raw data with a target-dependent correction point-spread function (PSF), explained in the following.

Assumed to be known through laboratory measurements is the target's complex reflectivity over frequency and incidence angle, expressible as the transfer function $H_t(f, \psi)$ or equivalently as the point-spread function (PSF) $h_t(x, y)$. The target PSF can be normalized with respect to a known reference RCS ς_{ref} at a single reference frequency f_{ref} (e.g. the center frequency) and a single reference incidence angle (e.g. the angle at closest approach) ψ_{ref} :

$$|h_t(x, y)| = \sqrt{\varsigma_{\text{ref}}} |h_{tn}(x, y)| \quad (3.13)$$

with the normalized PSF defined in the Fourier domain by

$$H_{tn}(f, \psi) = \frac{H_t(f, \psi)}{H_t(f_{\text{ref}}, \psi_{\text{ref}})}, \quad (3.14)$$

so that

$$\sqrt{\varsigma_{\text{ref}}} = |H_t(f_{\text{ref}}, \psi_{\text{ref}})|. \quad (3.15)$$

A correction filter can now be determined which effectively transforms a point target with an arbitrary transfer function into an equivalent ideal (sphere-like) target with a flat response over frequency and angle:

$$\delta(x, y) = h_{tn}(x, y) * h_{tc}(x, y) \quad (3.16)$$

with the target correction PSF h_{tc} defined in the Fourier domain by

$$H_{tc}(f, \psi) = \frac{1}{H_{tn}(f, \psi)}. \quad (3.17)$$

Now, the recorded complex raw data can be processed with a corrected, target-dependent filter ($h_{tc} * h$):

$$s_{\text{out},c}(x, y) = \sqrt{K\varsigma_{\text{ref}}} [h_{tn} * (h_{tc} * h)](x, y) \quad (3.18)$$

In analogy to Eq. (3.7), an integrated pixel intensity \mathcal{E}_c can be derived from $s_{\text{out},c}$. The equivalent RCS ς_e of the reference target is different from the RCS ς_{ref} at the reference operating point. The two are related through

$$\frac{\mathcal{E}_e}{\mathcal{E}_c} = \frac{\varsigma_e}{\varsigma_{\text{ref}}}. \quad (3.19)$$

by analogy between Eq. (3.4) and (3.18). The ratio $\mathcal{E}_e/\mathcal{E}_c$ is a point target and SAR mode dependent correction factor (which may also be derived numerically with the method

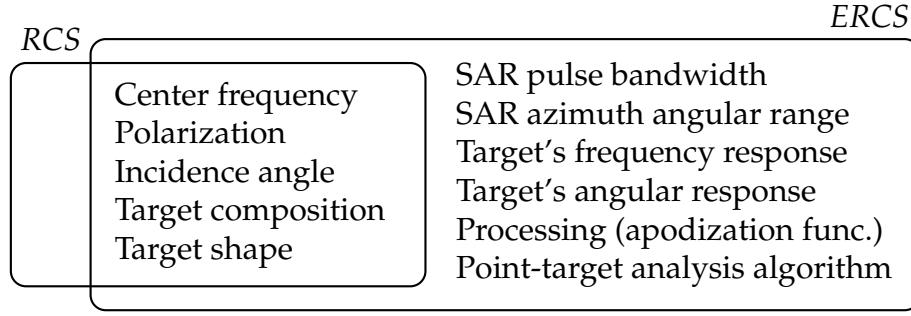


Figure 3.3: RCS and ERCS are two related but different measurement quantities. The ERCS depends on more factors than the RCS because it characterizes a point-target's backscatter as measured by a certain SAR instrument.

laid out in Chap. 4). Substituting the unknown ζ_e in Eq. (3.12) with the expression in Eq. (3.19), the calibration factor is then given as

$$K = \frac{\mathcal{E}_c}{\zeta_{ref}}. \quad (3.20)$$

Measurement traceability is achieved by calibrating the RCS ζ_{ref} of the measurement standard, i. e., the reference point target.

In conclusion, radiometric measurements can and have to be tied down to a known *equivalent* RCS by processing the raw data with a filter reversing the frequency and angular-dependent reflectivity, $h_{tc} * h$. By using targets with a known equivalent RCS (instead of a known RCS) for calibration, it is ensured that radiometric differences in measurements are due to the properties of the imaged target and not due to the reference target properties.

3.6 Discussion of Novel Quantity

The advantages of the novel radiometric quantity *equivalent radar cross section* are:

- **Generalization:** ERCS is applicable for simple to complex targets, for low to high resolution SAR systems, for small to extended angular ranges, and for conventional to advanced imaging modes.
- **Distinction:** The novel terminology underlines the differences between RCS (generally angle and frequency dependent, defined for RAR systems) and the quantity which is measured over an integration interval by a SAR system, see Fig. 3.3.
- **Familiarity:** The measurement unit and the concept (ratio of scattered to incident power) stays the same between RCS and ERCS.
- **Conception:** By relating the abstract quantity ERCS to a concrete physical representation through a conducting sphere, the quantity stays easily approachable even for the SAR novice.

It might be argued that nothing but the name changes when introducing ERCS. This is correct if only measurements themselves (excluding calibration) are considered.

Granted, all SAR systems already measure ERCS, yet they are calibrated to a known RCS. From this, mis-calibrations with varying degrees of calibration errors result, and any comparisons of radiometric measurement results obtained by different SAR systems and acquisition modes are inhibited. This follows from the fact that, after all, a calibration standard must be a realization of a definition of a measurement quantity [92], a matter which is currently violated.

3.7 Conclusions

The shift from SAR systems with good spectral and angular resolutions to systems with good spatial resolutions due to higher bandwidths and longer integration times is ongoing. This has made a revision of the definition of the radiometric measurement quantity necessary and motivated the following contributions in this chapter:

- In Sec. 3.3, I identified that the current definition of the radiometric measurement quantity is flawed, stressed by several qualitative examples.
- In Sec. 3.4, I defined *equivalent radar cross section*, a novel measurement quantity for radiometric SAR measurements. The novel definition properly takes the general frequency and angular dependence of the radar target backscatter into account.
- And in Sec. 3.5, I derived a calibration approach which allows to perform traceable radiometric calibrations with imperfect but known reference point targets.

As mentioned before, I had the chance to present the novel definition and related concepts at several conferences and workshops [39, 47–50]. Ensuing discussions with participants confirmed that the problems raised in Sec. 3.3 are acknowledged. In fact, recently ERCS was adopted as a draft recommendation by the Committee on Earth Observation Satellites (CEOS) Working Group on Calibration and Validation (WGCV) community for the definition of the radiometric measurement quantity in SAR [29]. Change takes time and the future is unpredictable, but the first step was done in revising the radiometric quantity for SAR images.

By adopting *equivalent radar cross section* as the measurement quantity in the future, calibrations and measurement results become truly compatible across current and future narrow and particularly wideband, high-resolution, and high-accuracy SAR systems.

4 Novel Method for Relating Point Target Properties to ERCS

In the previous chapter, the novel radiometric quantity *equivalent radar cross section* (ERCS) was defined. This chapter introduces a method that allows to quantitatively link point target properties, like their frequency or angular dependent radar cross section (RCS) or phase response, to their ERCS. This link is necessary so that targets with a known RCS can be used to calibrate synthetic aperture radar (SAR) systems for which a target with a known ERCS is required. Ultimately, this link is also necessary to establish calibration traceability for radiometric SAR measurements.

The method itself, point target SAR simulation, is described in Sec. 4.1. The following Sec. 4.2 addresses the practical implementation, and several quantitative analyses are discussed in Sec. 4.3. Besides deriving correction terms for non-ideal measurement standards, the quantitative examples also aim to stress the practical significance in distinguishing ERCS from RCS.

Parts of this chapter led to a publication [40].

4.1 Motivation and Principle

Radiometric SAR calibration is most often achieved with reference point targets, i. e., with measurement standards whose radar backscatter is known. This was discussed in Sec. 2.3, and after the introduction of ERCS in Chap. 3 it was argued that the reference backscatter must be expressed as an equivalent radar cross section. The two most common types of radiometric calibration targets are corner reflectors and transponders. Yet considering their properties (for instance shape and size for corners, or frequency response and antenna patterns for transponders) does not immediately allow to reason about their brightness in a SAR image. From the outset it is unclear how much the frequency dependence of the RCS of a corner or how much a local oscillator signal from an imperfect mixer in a transponder affects the target's ERCS. However, the uncertainty with which the ERCS of the measurement standards is known is one of the key contributors to the overall radiometric calibration uncertainty budget. The goal of the method introduced in this chapter is therefore to link measurable point target properties like the frequency dependent RCS or phase response to the measurement quantity ERCS.

Nevertheless, the target properties cannot be discussed in isolation because of the interaction between the measurement system and the measurand. As was discussed in Chap. 3, the pixel brightness in a SAR image, which is proportional to the ERCS of a target, does not only depend on target properties. It is also linked to the properties

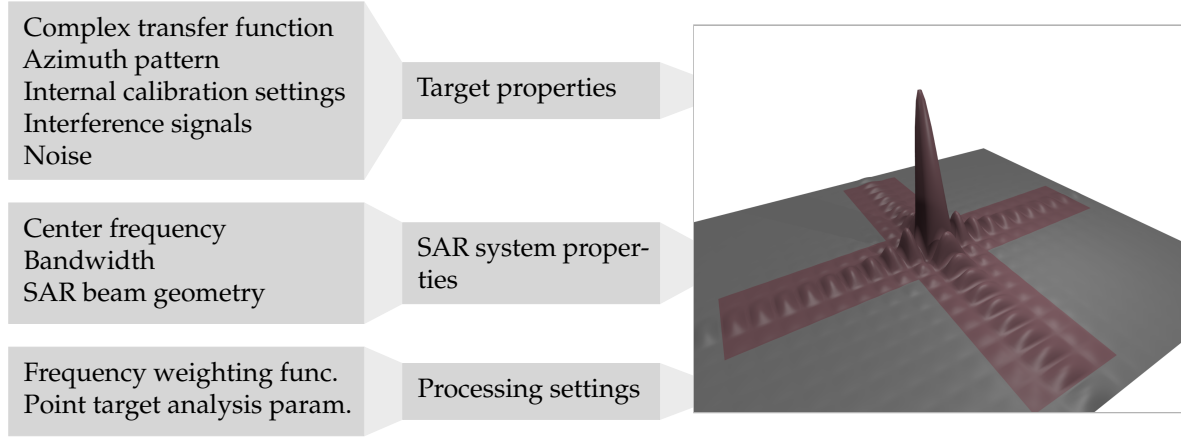


Figure 4.1: Overview of influences which affect the point-target response. On the right, an ideal point-target impulse response is shown, for which a possible integration area (cross) for the derivation of the absolute calibration factor K is highlighted.

of the SAR instrument and the SAR processor, see Fig. 4.1. The frequency response of the SAR instrument hardware influences the frequency weighting during processing. Even more so contributes a windowing operation, which is typically included in the processing for improved side-lobe suppression, to the overall weighting of the target's frequency response during pulse compression.

The method of point target SAR simulation models the complete chain from raw data generation over processing to a derivation of the point target ERCS. The starting point for the analysis is a point target with an arbitrary, complex-valued response function. To recapitulate from Sec. 3.3.1, an arbitrary point target is described by

$$H_t(f, \psi) = A(f, \psi) e^{j\varphi(f, \psi)}, \quad (3.8)$$

where $A(f, \psi)$ and $\varphi(f, \psi)$ are the frequency and angular dependent gain and phase response functions, respectively. The target response function $H_t(f, \psi)$ can equivalently be expressed in the spatial domain as

$$h_t(x, y) = \sqrt{\zeta_e} h_{tn}, \quad (4.1)$$

where h_{tn} is the target's normalized point-spread function and $\sqrt{\zeta_e}$ is a scaling factor.

At the core of the method lies the numerical generation of an uncalibrated, complex-valued SAR image

$$s_{\text{out}}(x, y) = h_t(x, y) * h(x, y) \quad (4.2)$$

which results if a SAR system with respective (weighted) optimal filter h measures a target with the impulse response h_t . The convolution operation resembles a weighted mean. Within the method, the convolution is evaluated numerically so that arbitrary target properties can be modeled.

Once the complex SAR image $s_{\text{out}}(x, y)$ has been generated, a point target analysis is performed on the intensity image (i. e., after square-law detection) according to the peak or the integral method as described in Sec. 2.3.3. In short, both the peak response and the sum of the squared pixel magnitudes over a cross area such as the one shown in Fig. 2.8 are derived. These values, the point target energies, are termed the indication values \mathcal{E}_p of the point target.

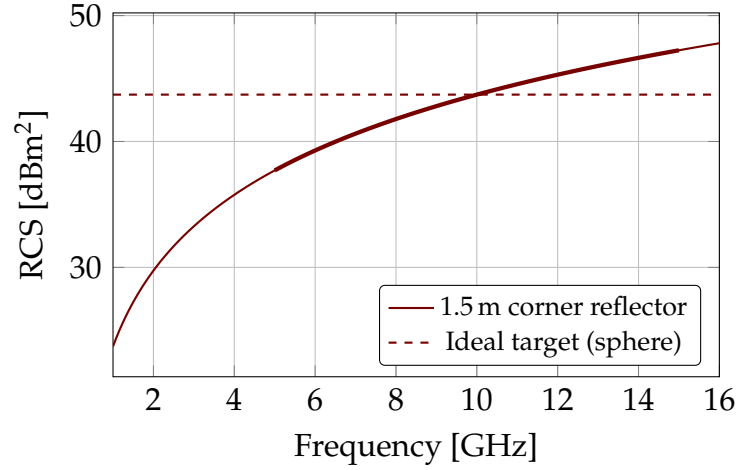


Figure 4.2: Comparison of the approximate frequency dependent RCS of a trihedral corner reflector and a sphere whose RCSs are identical at the center frequency of 10 GHz. With the method of point target SAR simulation, one can quantitatively determine how much less bright the corner reflector appears in a SAR image in comparison to the sphere if the targets are imaged, for instance, with a pulse bandwidth of 10 GHz centered at 10 GHz.

All results up to now are meaningless by themselves because of the missing calibration; the values have been generated with an arbitrary scaling factor. To exploit the method, at least two simulations must be performed, and the information gained lies then in the comparison of the two results. If the two results are named $\mathcal{E}_p^{(1)}$ and $\mathcal{E}_p^{(2)}$ and are expressed in decibels, then

$$\Delta\mathcal{E}_p = \mathcal{E}_p^{(2)} - \mathcal{E}_p^{(1)}, \quad (4.3)$$

also expressed in decibels, describes the change of the second point target's indication value (which is proportional to its ERCS) with respect to the first point target. If the first point target is designated as a reference (an ideal, theoretical, sphere-like target with a flat response over frequency and angle) and the second as an imperfect or real-world target like a corner reflector or transponder, then $\Delta\mathcal{E}_p$ can be considered a target correction coefficient (TCC) which characterizes the imperfect target's change in pixel brightness due to its non-ideal frequency and angular response with respect to an ideal target.

As an example, consider Fig. 4.2 where the frequency dependent RCS of a corner reflector (from Eq. (2.59)) is compared to the RCS of an ideal point target, a theoretical metallic sphere (from Eq. (2.62)). Although the two targets have the same RCS at an exemplary center frequency of 10 GHz, it is not clear without further analysis by how much the point target energy \mathcal{E}_p of the corner reflector is going to be reduced in a SAR image in comparison to that of the sphere, or what the ERCS of the corner reflector actually is. The ERCS $\zeta_e^{(\text{sphere})}$ of the metallic sphere equals its RCS $\zeta^{(\text{sphere})}$ by definition. To determine the ERCS of the corner reflector, both point target impulse responses are simulated with the method of point target SAR simulation. From the two derived indication values $\mathcal{E}_p^{(\text{sphere})}$ and $\mathcal{E}_p^{(\text{corner})}$, the target correction coefficient

$$\Delta\mathcal{E}_p = \mathcal{E}_p^{(\text{corner})} - \mathcal{E}_p^{(\text{sphere})} \quad (4.4)$$

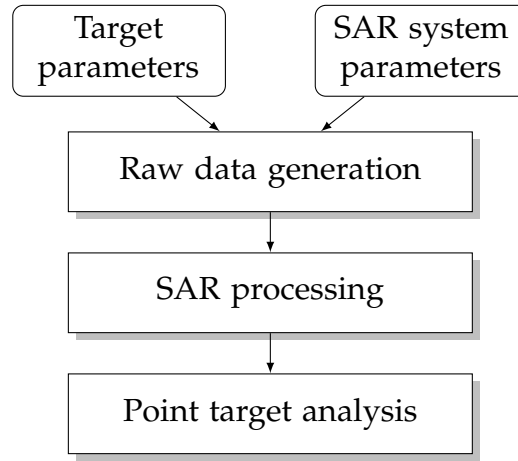


Figure 4.3: Principal structure and data flow of the point target SAR simulator.

can be derived (all quantities expressed in decibels). Because the ERCS of the sphere is known, the ERCS of the corner reflector expressed in dBm^2 is

$$\zeta_e^{(\text{corner})} = \zeta_e^{(\text{sphere})} + \Delta\mathcal{E}_p. \quad (4.5)$$

As mentioned before, the RCS and therefore ERCS of the ideal reference target $\zeta_e^{(\text{sphere})}$ can be arbitrarily chosen. What must be known though is the relationship with the RCS of an imperfect target at one frequency. An obvious choice is to select an ideal target whose RCS is identical to the RCS of the imperfect target at the center frequency, as is shown in Fig. 4.2.

In summary, the method of point target SAR simulation is novel because it puts point targets at its center. All known scientific or commercial SAR simulators assume ideal point targets and imperfect systems to analyze for instance the overall missions performance [179], motion compensation [6], or statistical features of raw SAR data [60]. The point target SAR simulator in this chapter, on the other hand, assumes an ideal system and processor, but imperfect point targets.

4.2 Implementation of the Point Target SAR Simulator

The goal of the point target SAR simulator is to simulate the complete measurement process for performing radiometric SAR measurements: A (possibly non-ideal) point target is placed within an artificial, clutter-free scene, the complex raw data as seen by a specific SAR instrument are simulated, the data are focused, and finally a point target analysis is conducted to derive the integrated pixel intensity \mathcal{E}_p . By performing a set of simulations with varying SAR system or target parameters, the relative effect of these parameters on the derived integrated pixel intensity (which is proportional to the ERCS of the target) can be derived.

A top-level overview of the simulation procedure is shown in Fig. 4.3. The steps are as follows:

1. Raw data generation, incorporating reference target deficiencies (i. e., a frequency and angular dependent transfer function) and SAR system specific settings (e. g. chirp settings such as bandwidth and center frequency).

2. SAR data processing, where the generated raw data are focused with the range-Doppler algorithm.
3. Point-target analysis, where point target parameters like the integrated pixel intensity (integral method) or the peak pixel intensity (peak method) are extracted.

During analysis, it is often advantageous to simulate and compare dozens or hundreds of different sets of SAR system and point target parameters so that computational efficiency and memory usage becomes important. Here the specific goal of the simulation can be exploited: Only a few pixels around the peak of the point target response are required in order to complete the point target analysis with the integral method, i. e., it is not necessary to focus the complete scene. This fact can be exploited during processing to significantly reduce memory consumption and processing time. The details of this approach are described in App. A.

The following section describes several quantitative analyses performed with the method of point target SAR simulation based on the implementation described in App. A.

4.3 Quantitative Analyses: Link Between Target Properties and ERCS

An important application for the method of point target simulation is the characterization and quantification of transponder deficiencies. This is the first example to be discussed in the following Sec. 4.3.1. Understanding the effects of transponder properties like the frequency response flatness or interference signals on the brightness of the point target in a SAR image is particularly relevant because transponders are used as radiometric measurement standards for the calibration of SAR systems.

Most transponder effects are concerned though with how the magnitude of the received signal is modified by the target. As a second example, the effect of the ionosphere on point target measurements shall be analyzed in Sec. 4.3.2. The ionosphere affects the phase response and therefore this example rounds off the demonstration of applicability of the point target SAR simulation for radiometric measurements.

Both examples stress again that there is a fundamental difference between RCS (the state-of-the-art radiometric SAR measurement quantity), and the quantity that a SAR system actually measures: equivalent radar cross section. These quantitative examples therefore supplement the qualitative examples given in Sec. 3.3.2.

4.3.1 RCS Dependence on Frequency and Angle: Calibration Transponder

Calibration transponders are, besides trihedral corner reflectors, the most commonly used SAR calibration point targets. Their basic properties and design was already discussed in Sec. 2.4.3. Here the just introduced method of point target SAR simulation shall be used to exemplarily derive transponder correction coefficients depending on realistic transponder properties. In particular, non-ideal transfer functions, transponder gain stabilization strategies, the effect of interference signals (e. g. from cross-talk), and noise effects are analyzed.

Through an analysis like this, a link is established between the imperfect properties of a calibration transponder and the transponder's measured ERCS. Establishing this link allows to trade off transponder properties such as the flatness of the transfer function against radiometric calibration uncertainties when such an imperfect target is used as a measurement standard. The analysis is therefore indispensable when a new transponder is designed.

According to Fig. 4.3, target and SAR system parameters both need to be known for the simulation. The used SAR system parameters are derived from an X-band TerraSAR-X stripmap beam [63] with the notable difference of a 600 MHz bandwidth range chirp (instead of 150 MHz) in anticipation of higher resolution SAR systems in the future. As for TerraSAR-X, the range sampling rate is 2.2 times the range bandwidth, and the pulse length is 57 μ s. The integration cross area according to Fig. 2.8 is 21 samples long in each direction, and the replica for processing is weighted by a Hamming window [74].

Transfer Functions and Gain Stabilization Strategies

The point target under consideration is a transponder similar to the one shown in Fig. 2.12 on p. 34. Here the complete transponder transfer function is modeled though with a series connection of only four bandpass filters (two per receiver and transmitter chain). Choosing filters allows to modify the filter order to conveniently generate a set of different transponder transfer functions. Filters of two types are used: Bessel and Chebychev [116] (see Figs. 4.4a and 4.4b for exemplary transfer functions). Out of all transponder loop components the filters were chosen as the representative microwave components because they contribute considerably to the overall amplitude and phase response. The specific filter types exhibit, on the one hand, a nearly linear group delay and a smooth gain drop-off away from the center frequency (Bessel) and, on the other hand, a frequency response with comparably large group delays and several amplitude ripples (Chebychev). Different results are therefore to be expected for the point-target analysis after focusing.

The transponder's digital sub-system, the unit between the receiver and transmitter chains in Fig. 2.12, allows the implementation of different gain stabilization strategies. Here, gain stabilization is understood as the modification of the transponder transfer function to ensure a stable point target response even under varying thermal conditions or after component aging. In this example, simulation results for three different strategies are considered:

1. Strategy 1 ("normalization") adjusts the transponder loop gain according to the gain at one (here: the center) frequency. The actuator can be a variable attenuator (no additional frequency dependence assumed) in either or both the receiver or transmitter paths.
2. The second strategy ("weighted average") considers the transponder loop gain over the relevant bandwidth and weights it with the frequency dependence of the processor (e. g. Hamming window). The average yields an amplitude correction term, which can be reversed in hardware, again, by a variable attenuator.
3. In the third approach ("amplitude response compensation"), the amplitude frequency response is measured by the digital sub-system, and the amplitude response is corrected in such a way that it becomes flat again. This frequency (and

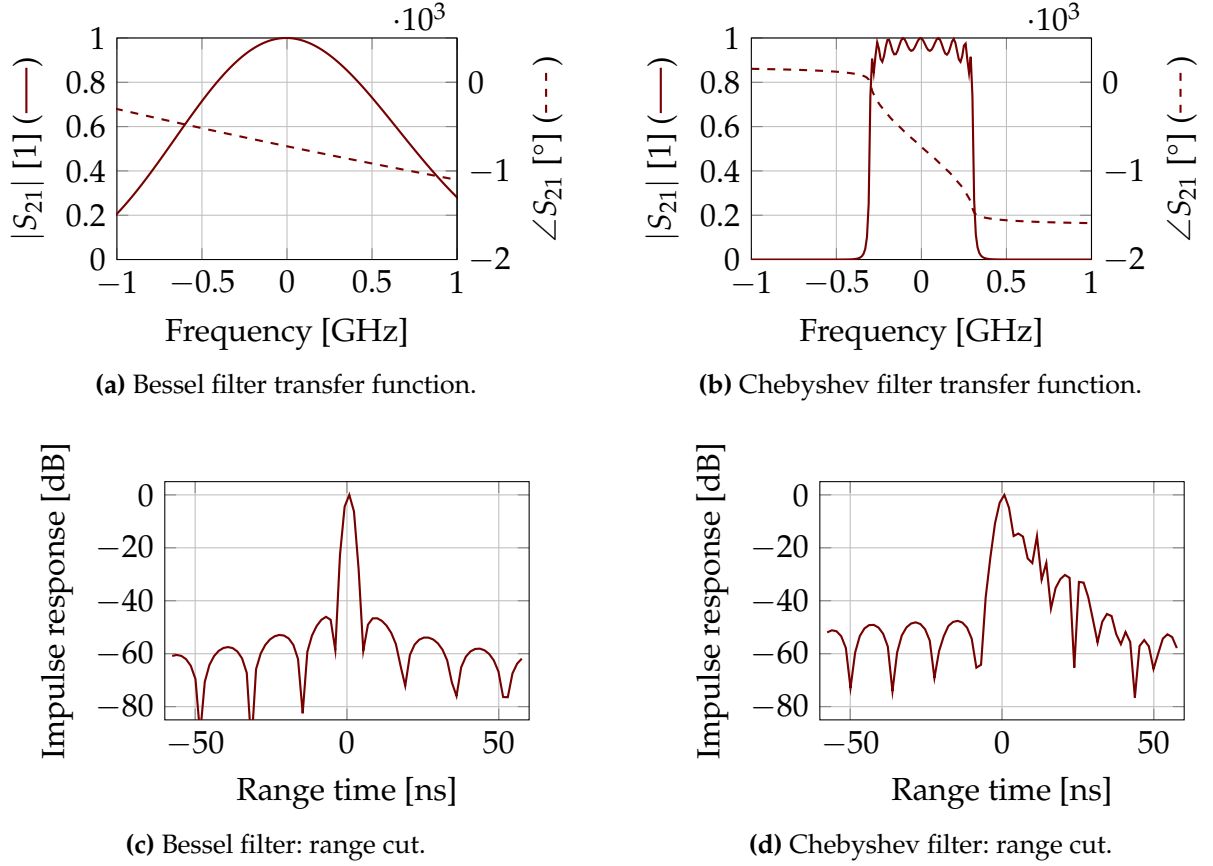


Figure 4.4: Characteristic plots for transponders modeled by four tenth-order Bessel or Chebyshev filters, respectively.

therefore time) dependent approach must be implemented in a programmable real-time processing unit such as a field-programmable gate array (FPGA).

An ideal fourth approach (“perfect compensation”), in which the gain stabilization approach can completely compensate the amplitude and phase response, results in a target correction coefficient of zero according to Eq. (4.3) and is therefore not explicitly pointed out in the resulting plots.

The simulation results for varying filter orders are summarized in Fig. 4.5. The plots show the variation $\Delta \mathcal{E}_p$ of the point target energy \mathcal{E}_p for the integral and peak methods, sorted by filter type and gain stabilization strategy, and plotted over filter order. In the target design phase, the effect of concrete radio frequency (RF) component specifications on the perceived target RCS now becomes apparent. On the other hand, reference target correction coefficients can be stated for observed transfer function variations during operation.

The Bessel filter has a nearly linear phase response, as can be exemplary seen in Fig. 4.4a for a filter order of 10. In the focused SAR image, this results in a slightly in range shifted impulse response, but the impulse shape is not greatly modified (see Fig. 4.4c). The amplitude response acts like a weighting function and shifts energy away from the peak to the side lobes. Therefore, the peak method underestimates the RCS for the normalization strategy, but achieves a perfect compensation for the weighted average strategy (upper and middle plot in Fig. 4.5a). The amplitude response compensation

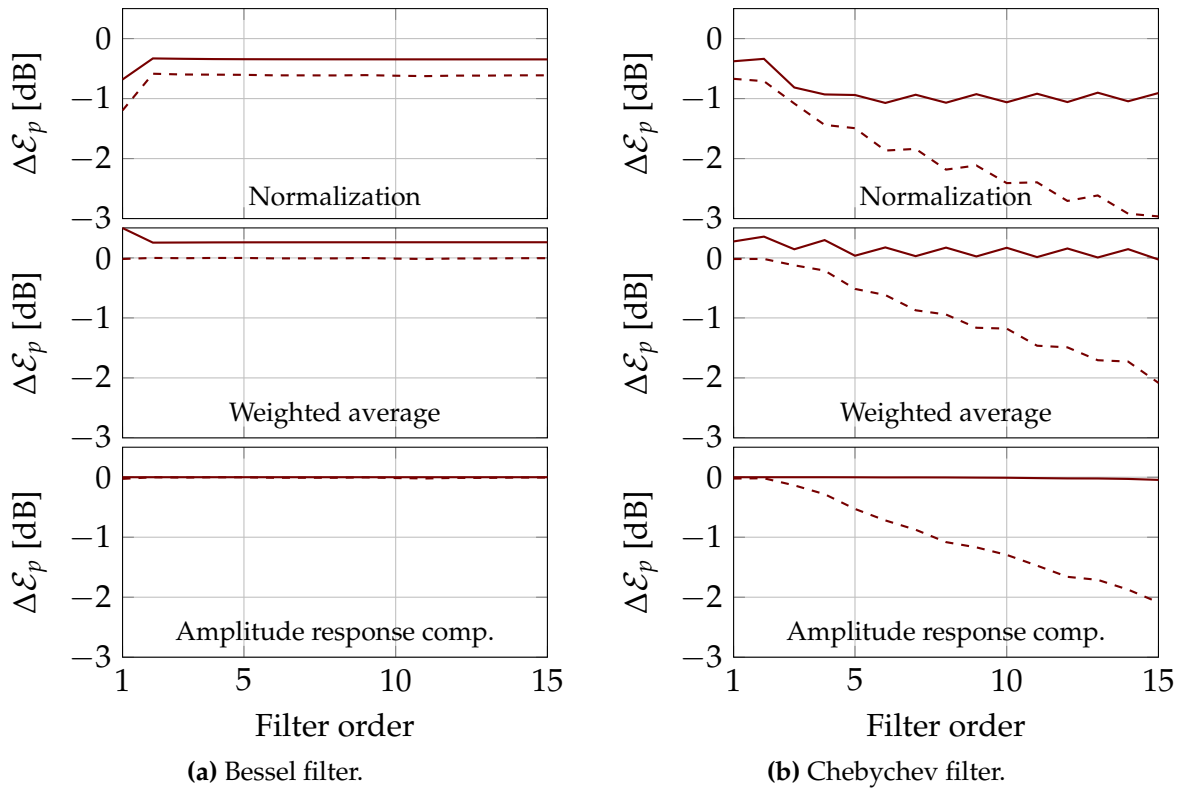


Figure 4.5: Simulation results for two filter types and three transponder gain stabilization strategies. The deviation of the ERCS ς_e from an ideal target (flat amplitude and phase response) versus filter order is given for the integral (—) and peak (---) methods, respectively. These deviations represent the reference target correction coefficients (TCCs), and sometimes exceed even 2 dB.

works very well for a Bessel-style transfer function for both analysis methods (peak and integral) since the phase response can well be neglected (lower plot in Fig. 4.5a).

The amplitude and group delay of the Chebychev filters is much less smooth and linear (Fig. 4.4b). The phase response results in a spreading of the impulse response (Fig. 4.4d), which of course can be better compensated by the integral method for all three gain stabilization strategies. If the amplitude response is perfectly compensated as in the third strategy (lower plot in Fig. 4.5b), then the impulse response spreading due to the imperfect phase response is very well neutralized by the integral method.

In summary, a set of realistic transfer functions have been analyzed. Both the amplitude and phase response result in a spreading of the ideal impulse response. The presented three gain stabilization strategies were focused on compensating the amplitude response function, where arguably the most complex third approach (“amplitude response compensation”) was shown to be most effective in compensating the frequency dependence.

In general, independent of the transfer function or the analysis method, target correction coefficients were computed, some reaching 1 dB even for the preferred integral method. These target correction coefficients can subsequently be applied during radiometric calibration of a SAR system to improve the radiometric accuracy of calibrated products.

Interference Signals

The output signal of an active target might suffer from signal interference, so that the output signal equals the amplified input signal plus a sum of coherent or non-coherent interference signals. Three types of interference signals are distinguished here:

- continuous wave (CW) signals,
- attenuated and delayed versions of the input signal (e. g. caused by coherent multipath effects or by transmit-receive coupling), and
- bandwidth-scaled and attenuated versions of the input signal (from mixer stages).

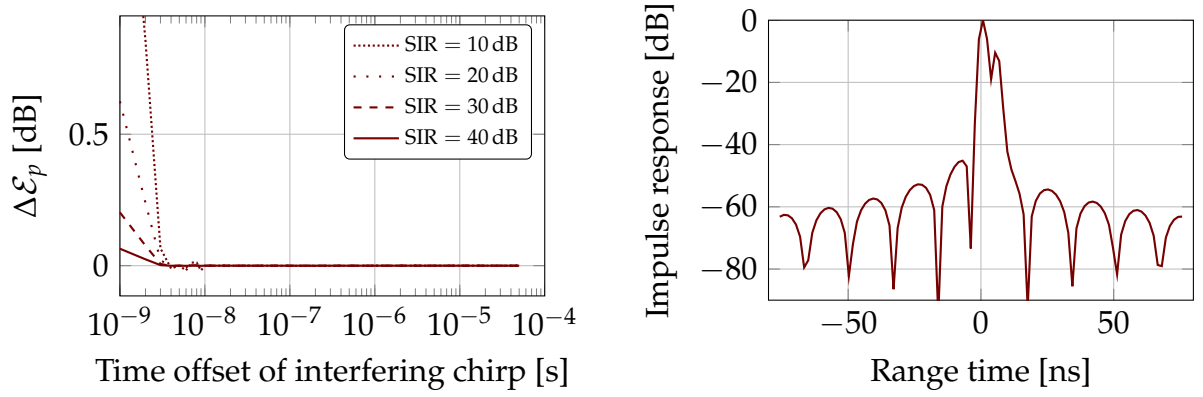
The magnitude of the interference signals shall be characterized by the signal-to-interference ratio

$$\text{SIR} = \frac{P_{\text{original signal}}}{P_{\text{interference signal}}} \quad (4.6)$$

where P is average signal power.

A continuous wave signal might stem from an imperfect isolation of the local oscillator signal at a mixer stage or be the result of an electromagnetic compatibility (EMC) problem so that the computer or power supply clock signal penetrates the RF path. These signal contributions are well filtered out by the matched filter during processing. Simulations showed that even an atypically powerful CW signal with a SIR of 0 dB results in a $\Delta\mathcal{E}_p$ of only 0.1 dB. In terms of radiometric calibration, CW interference signals of more moderate levels hence do not significantly influence the derived absolute calibration factor K .

The second type of interference, an attenuated and delayed but coherent replica of the input signal, can result from a coupling between the transponders’ transmit and receive



(a) Comparison for different signal-to-interference ratios (SIRs), integral method.

(b) Exemplary range cut for SIR = 10 dB, 5 ns time delay.

Figure 4.6: Effect of coherently interfering chirp signals with a time offset (e. g. due to transmit/receive antenna coupling). The effect of interfering chirp signals is only considerable for time offsets below 10 ns in the considered example.

antennas. This is only relevant if the target allows reception and transmission of a pulse at the same time, i. e., the target pulse delay must be less than the pulse length. In the simulation it was assumed that the replica is attenuated with respect to the original signal. This is a practical constraint since otherwise the receiver or transmitter chain would typically be operated in saturation. A repeated feedback was neglected (the pulse delay of the repeated signals would be even larger and the signal further attenuated). The derived simulation results for a set of SIRs and pulse delays are summarized in Fig. 4.6. The right Fig. 4.6b shows exemplarily how the point target analysis is affected: As expected, a secondary peak appears in the final image, whose amplitude is attenuated by the signal-to-interference ratio and whose range offset is given by the time delay. If the time delay is small, then the secondary peak becomes visually indistinguishable from the main peak. Since the spurious peak drifts away and out of the integration area for increasing pulse delays, no effect is observed for pulses which are delayed by more than 10 ns as long as the integration area stays centered around the peak location, see Fig. 4.6a. The cutoff value of about 10 ns depends on the chosen size of the integration area for the integral method. For the peak method, the effect of coherently superimposed but delayed replicas is even less strong since only one sample of the side lobe contributes to the error.

The third type of examined interference signals, a bandwidth scaled and attenuated but not delayed version of the replica, can originate from intermodulation products caused by nonlinear RF components. For those signals, the modulation rate of the linearly frequency-modulated signal is changed with respect to the original signal. Simulations showed that these signals behave like non-coherent signals (comparable to the aforementioned CW signals) and therefore add to the perceived noise floor. Due to the suppression by the matched filter, they do not considerably influence the derived absolute calibration factor.

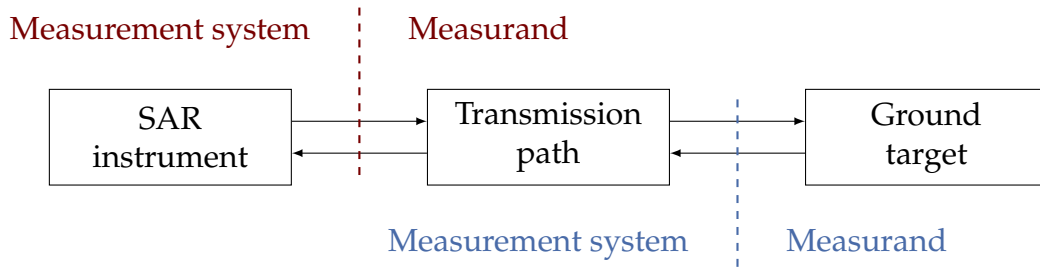


Figure 4.7: The distinction between measurement system and measurand must be made for each measurement task. In case of mapping the total electron content (TEC) of the ionosphere, the upper separation applies.

Transponder Noise

An active point target will always add noise to the received SAR signal before retransmission. Sources of this noise include thermal and shot noise in several RF components, and possibly digitization noise if a digital sub-system is used. In the point target SAR simulator, additive white Gaussian noise is assumed (constant power density and normal amplitude distribution), which can be parameterized by the signal-to-noise ratio. In the simulator, a random number generator is used which generates a separate noise signal for each range line.

Since noise is an uncorrelated signal, it gets considerably suppressed during impulse compression in the processing step. The noise power still exists in the focused image, but it stays spread equally over all image pixels, while the coherent point target response gets focused to a peak. The noise suppression in the power image equals the processing gain, which is approximately given by the product of the pulse bandwidth and the pulse length [32, 98]. For the exemplary SAR system considered in this section, a pulse compression ratio or noise suppression of 45 dB results, so that even a signal-to-noise ratio of e. g. only 10 dB in the active target would still be sufficiently low. This result was confirmed numerically with the method of point target SAR simulation.

It can be concluded that the noise figure of an active SAR calibration target is usually not critical for radiometric SAR calibration due to the noise suppression during processing.

4.3.2 Frequency-Dependent Phase Response: Ionosphere

Typically, the frequency-dependent amplitude response will have a larger effect on the difference between RCS (at the center frequency) and ERCS than the frequency-dependent phase response. This is because the phase response leads to defocussing only, which is typically well compensated by the integral method for the point target analysis (see Sec. 2.3.3). Nevertheless, an example shall be given here which only considers the phase response of a point target and assumes a constant RCS over frequency and angle.

As a first step, the boundary between measurement system and measurand, according to Fig. 4.7, is shifted further toward the SAR instrument so that the atmosphere becomes part of the measurand. In most SAR measurement setups, the atmosphere is rather considered as an artifact that must be estimated and corrected from the measured data, but here the atmosphere shall actually be measured. A general summary of atmospheric effects in SAR images is given by Danklmayer et al. [34].

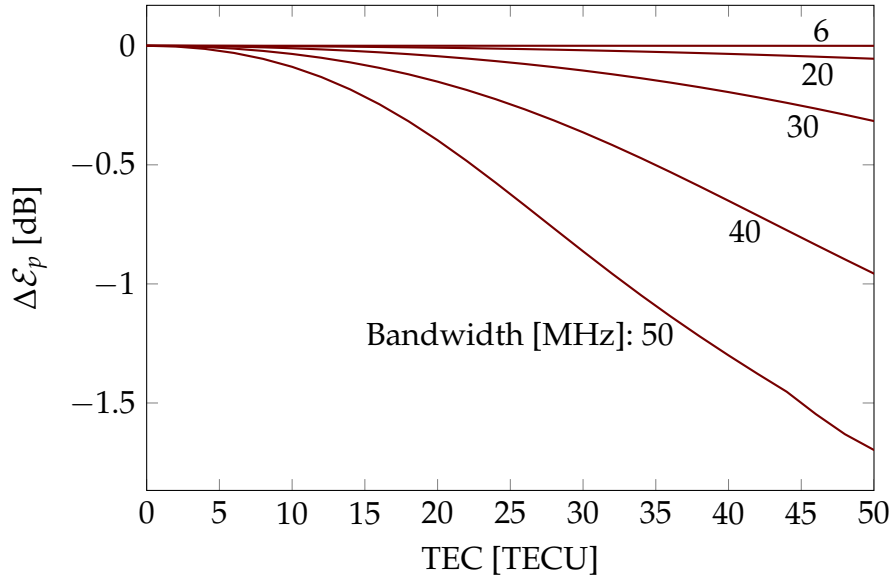


Figure 4.8: Effect of phase distortions on the ERCS for an exemplary P-band system with a center frequency of 350 MHz depending on ionospheric activity. The values are normalized to the ERCS at 0 TECU.

Meyer et al. [120] proposed to use wideband spaceborne L-band SAR systems to map small scale (smaller 10 km) ionospheric effects, i. e., to measure the total electron content (TEC). Such systems exploit the apparent range delay and defocussing of scatterers on ground depending on ionospheric activity.

The ionosphere is dispersive, i. e., the phase delay depends on frequency, and the impulse response of a point target on ground appears distorted. A Taylor series expansion of the phase response around the center frequency f_c leads to the approximate frequency dependence [120]

$$\varphi(f) = -\frac{4\pi}{c} \frac{40.28}{f_c} \mathcal{T} + \frac{4\pi}{c} \frac{40.28}{f_c^2} \mathcal{T}(f - f_c) - \frac{4\pi}{c} \frac{40.28}{f_c^3} \mathcal{T}(f - f_c)^2, \quad (4.7)$$

where c is the speed of light, and \mathcal{T} is the ionospheric TEC in TECU (which seldom exceeds 100 TECU). The first term characterizes a, for this analysis, arbitrary phase shift. The linear second term is equivalent to an additional range delay (shift of the impulse response) and does not have a consequence on a point target's integrated pixel intensity (assuming that the integration cross area is always centered on the peak). Only the third term

$$-\frac{4\pi}{c} \frac{40.28}{f_c^3} \mathcal{T}(f - f_c)^2$$

has an influence on radiometric measurements because it results in a distortion of the transmitted chirp signal.

From this third term, a transfer function

$$H_t(f) = C e^{j\varphi(f)}$$

according to Eq. (3.8) can be derived, where C stands for a constant amplitude response. Now the TEC-dependent variation of the integrated impulse response $\Delta\epsilon_p$ for a P-band system with an exemplary center frequency of 350 MHz can be derived with the method of point target SAR simulation.

The analysis results are shown in Fig. 4.8. Depending on the system bandwidth and ionospheric activity, the integrated pixel intensity (which is proportional to the ERCS) deviates by more than 1 dB from the reference. Note that the point target's RCS, which does not depend on phase (see Eq. (2.55)), stays constant for all simulation runs.

This example stresses again that radiometric measurements in SAR do not only depend on the point target's RCS and amplitude response, but also on the target's phase response. The example concretely demonstrates that ERCS must replace RCS as the radiometric measurement quantity, and the method of point target SAR simulation is a suitable approach to link the two quantities.

4.4 Discussion

Using the method of point target SAR simulation represents an alternative approach to the one described in Sec. 3.5 for calibrating SAR images with imperfect point targets. While the method in Sec. 3.5 depends on modifying the operational SAR processor, the method of point target SAR simulation relies on a dedicated processor, and simulation results are summarized in a simple target correction coefficient (TCC) $\Delta\mathcal{E}_p$. The TCC may then be applied during radiometric calibration, along with other already established corrections like for the SAR antenna pattern or the SAR gain drift.

The implementation of the point target SAR simulator is generic and should be adapted to better reflect the processing approach of a specific mission if highest accuracies are needed. This adaptation should be implemented step by step so that in an early project phase of a new SAR mission the generic implementation is sufficient, and as the project progresses, more and more processing details are implemented. With this approach, the manufacturer of calibration point targets can establish a link between the frequency and angular dependent RCS of a new device already before the operational processor is available.

Implementing a dedicated point target simulator also allows to speed up the analysis runs because of the possible optimizations discussed before. This may become especially relevant for future high-resolution SAR systems where the processing effort is going to increase further.

4.5 Conclusions

After the introduction of the new measurement quantity ERCS in Chap. 3, this chapter was focused on how the link between point target properties like frequency response and ERCS can be established. Whenever point targets are used as measurement standards in SAR calibration, this link is required to establish calibration traceability.

In summary, I made the following contributions in this chapter:

- First, I introduced the method of point target SAR simulation in Sec. 4.1. In contrast to existing SAR simulators, a perfect SAR system but imperfect point targets are assumed. With this approach, the impact of different point target properties on the point target energy in a SAR image can be analyzed.

- In the following Sec. 4.2, I described a practical implementation of the method, where I incorporated several optimizations to reduce memory usage and simulation time. The optimizations are beneficial especially for high-resolution SAR systems, where the effect of imperfect point targets is expected to be largest.
- Finally I could demonstrate the suitability of the method with two quantitative examples, namely simulations on imperfect transponders in X-band, and the effects of the ionosphere on the phase in P-band. The examples stress again that a SAR system does not measure RCS, but ERCS.

Using the method of point target SAR simulation, traceable and more accurate radiometric calibrations become possible because target and SAR system specific correction coefficients can be established, which were shown to exceed 1 dB for several of the simulated examples.

5 The SAR Passband Problem: Analytical Model and Practical Solutions

In Chapter 3, equivalent radar cross section (ERCS) was introduced as a novel radiometric measurement quantity. Chapter 4 then focused on a method for deriving correction factors for imperfect point targets, which are used to calibrate synthetic aperture radar (SAR) systems. In this chapter, further consequences resulting from introducing ERCS are analyzed: The overall process of taking a radiometric SAR measurement, and the interaction between the measurement system and the measurand are studied.

The work presented in this chapter has resulted in a peer-reviewed publication [52].

5.1 Introduction and Example

SAR measurements of the terrain backscatter are the basis for quantitative research through subsequent comparison of the recorded measurement data. When conclusions are drawn from differences in measured data, it is important that the measurement setup has been kept fixed throughout all data acquisitions, or at least that all known modifications of the setup have been corrected during data analysis. Depending on the measurement task, these measurement setup parameters include frequency, looking angle, time of year, precipitation conditions, and so on.

For calibrated radiometric terrain measurements in SAR, one such parameter has so far been neglected though. This is termed here the SAR passband problem, where “passband” refers to the transmission properties of a bandpass filter in frequency domain. A SAR system has two mainly independent passbands: the range and the azimuth passbands. In the range direction, the passband is mostly defined by

- the chirp signal’s center frequency,
- the chirp signal’s bandwidth, and
- the range apodization function used during processing for improved sidelobe suppression.

In the azimuth direction, the passband is similarly given by

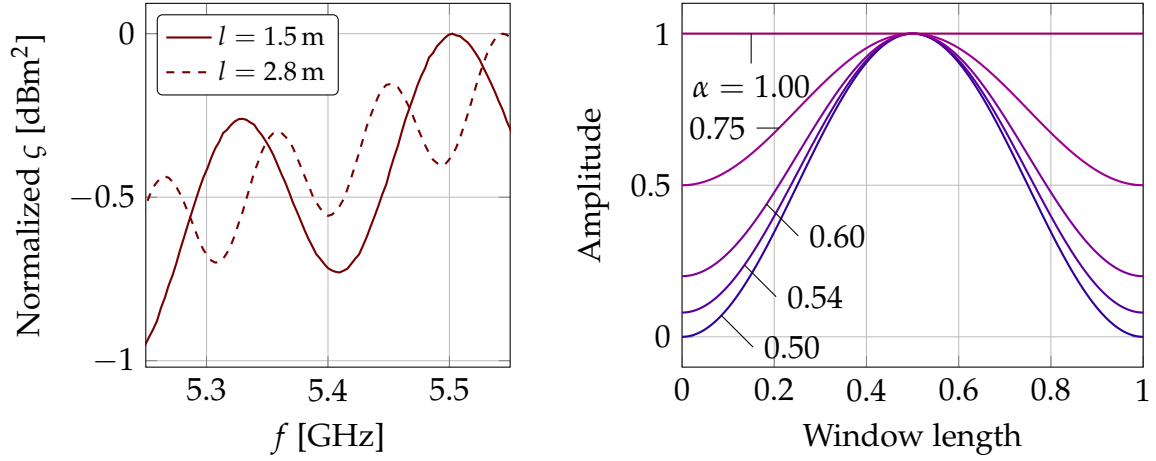
- the central aspect angle during acquisition,
- the aspect angle range exploited during processing, and

- the analogous azimuth apodization function.

These passbands interact with the frequency and angular response functions of the measured target during processing (also see the later Eq. (5.4)). Up to now, the target response functions have been assumed to be approximately constant over frequency and angle [32, 33, 61, 131, 171, 212] so that the “weighted averaging” with the passband function of the SAR system was independent of the target and was characterized through calibration. This approximation is not valid for targets in general, and especially not for modern high-resolution (i. e, high-bandwidth) and high-accuracy SAR systems.

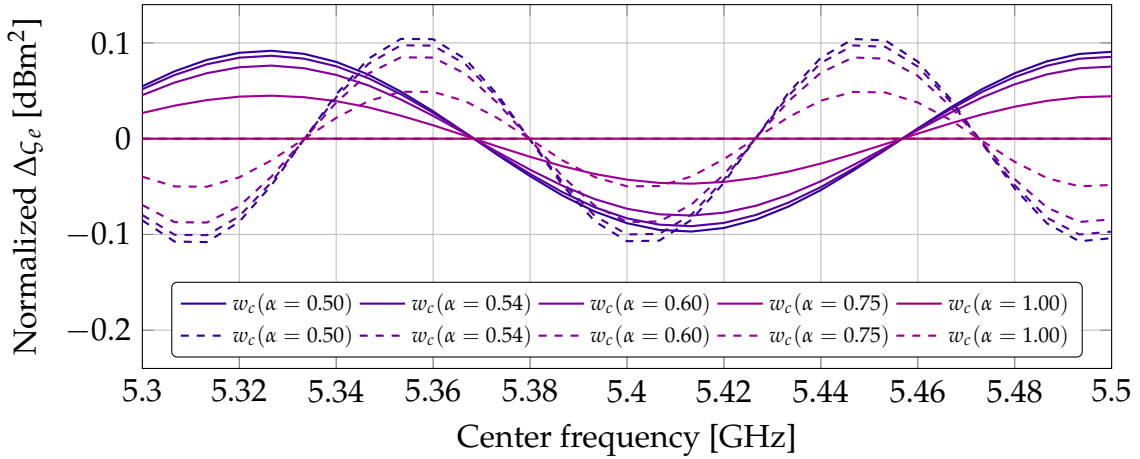
As an example, one can consider an important special case for radiometric measurements: trihedral corner reflectors. If a corner is used for radiometric calibration, then any variation of its measured ERCS directly translates to a variation of the derived system calibration factor, so that all subsequent radiometric measurements are also affected. Figure 5.1a shows RCS simulation results for 1.5 m and 2.8 m trihedral corner reflectors and a Sentinel-1-like C-band system (with a bandwidth of 100 MHz). The corner sizes represent the medium and large sized corner reflectors which are currently used by the German Aerospace Center (DLR) for radiometric calibration of various SAR systems. The frequency response in Fig. 5.1a is not flat, mainly due to edge effects. If raw SAR data acquired from these two corner reflectors are processed with the different range apodization functions shown in Fig. 5.1b, then the resulting derived ERCS (which is proportional to the pixel intensity) in Fig. 5.1c is shown to be considerably affected by the chosen apodization function. These ERCS simulation results were obtained with the point target SAR simulator discussed in Chap. 4. Depending on the passband center frequency, the effect is as large as 0.1 dBm^2 , which represents a good fraction of the Sentinel-1 system’s radiometric measurement uncertainty of only 0.3 dBm^2 [7]. Already this first example demonstrates that the SAR passband problem is relevant and has to be addressed.

In order to generalize the previous example, the principal discussion in this chapter starts with a review of common SAR apodization functions in Sec. 5.2. The passband problem for radiometric measurements can be quantified with numerical simulations as shown above for the corner example, but also with a novel analytical approach which is developed in Sec. 5.3. This analytical model allows to quantify the effect on a measured target ERCS (which is proportional to its pixel intensity) depending on the apodization function of the SAR processor. The model is a mathematical approximation based on a truncated Taylor series, and the accuracy is necessarily limited. Nevertheless, several examples in Sec. 5.4 show that the approximation is useful and accurate enough for practical application in most cases when compared with an exact numerical computation. Based on the results, solutions to the SAR passband problem are proposed in Sec. 5.5. Properly addressing the passband problem will allow more robust merging of SAR data acquired with different sensor systems or sensor settings. Especially for high-resolution and high-accuracy SAR systems, the radiometric measurement uncertainty will be reduced if the interaction between target and system response functions is properly acknowledged in the future.



(a) RCS of two trihedral corner reflectors at nominal alignment and vertical polarization (simulation with commercial field solver).

(b) Family of raised cosine windows $w_c(\alpha)$.



(c) Resulting ERCS variations depending on chosen apodization function $w_c(\alpha)$ for a 1.5 m trihedral (solid) and a 2.8 m trihedral corner reflector (dashed), computed with the point target SAR simulator from Chap. 4.

Figure 5.1: Trihedral (calibration) corner reflectors appear differently bright in a Sentinel-1-like C-band SAR image if different apodization functions shown in (b) are used during processing. This is a result of the frequency dependent RCS of corner reflectors, see (a). The effect varies with the chosen center frequency (c) and can be as high as 0.1 dBm^2 in this example.

5.2 Apodization Functions in SAR Processing

The term *apodization* is borrowed from Greek and means “taking the foot away” [77]. It was first introduced in the field of optics and astronomy. Apodization in Fourier optics is a technique of sidelobe suppression, needed when faint stars are otherwise masked by the sidelobes of a much brighter star. Sidelobe suppression is achieved, for instance, by applying a coating to the lense’s aperture which becomes more opaque the further away one moves from the lense’s principal axis [77]. However, an improved sidelobe performance is traded off with a reduced angular resolution.

In SAR, digital apodization or weighting functions have long been used to the same effect. Target detection in SAR often requires sidelobe control so that strong scatterers like urban structures or ships do not mask weaker, near-by targets. Smaller sidelobes also reduce the risk of false detections, where a sidelobe of a strong target might be misinterpreted for a secondary target. In any case, sidelobe control simplifies visual inspection of SAR images.

Sidelobe control in SAR is typically achieved through the application of a tapering or weighting window in the Fourier domain during range and azimuth compression [32, 33]. Normalized tapering windows have a value of 1 in the center and fall off symmetrically toward the sides. A *rectangular window* (also called a boxcar window),

$$w_{\text{box}}(t, T) = \begin{cases} 1 & \text{if } -T/2 \leq t \leq T/2, \\ 0 & \text{otherwise,} \end{cases} \quad (5.1)$$

does not apply any weighting at all within $[-T/2; T/2]$, where T is the window size and t denotes the free variable. A typical family of weighting windows in SAR is the *general cosine window*

$$w_c(t, T) = \alpha + (1 - \alpha) \cos\left(\frac{2\pi t}{T}\right), \quad -\frac{T}{2} \leq t \leq \frac{T}{2}, \quad (5.2)$$

with its tapering parameter α . When α is 0.5, this window is also called Hann (or Hanning) window, and for $\alpha = 0.54$, the window is called Hamming window [74]. In the limiting case with $\alpha = 1$, the raised cosine window becomes the rectangular window w_{box} . Another typical tapering function is the Kaiser window, which is defined as [32]

$$w_k(t, T) = \frac{I_0\left(\beta\sqrt{1 - (2t/T)^2}\right)}{I_0(\beta)}, \quad -\frac{T}{2} \leq t \leq \frac{T}{2}, \quad (5.3)$$

where I_0 is the zeroth-order Bessel function. The parameter β describes the degree of roll-off. Often β is chosen to be 2.5, which results in a good trade-off between sidelobe suppression and resolution [32]. A comprehensive overview of these and other tapering windows and their characteristics like peak-to-sidelobe ratio is given by Harris [74]. Some commonly used apodization functions and their main properties are summarized in Tab. 5.1.

Besides the classical apodization approaches described above, non-linear and adaptive techniques have been devised in order to achieve good sidelobe control while retaining most of the optimal resolution. Degraaf [38] proposed adaptive sidelobe reduction, which applies space-variant apodization in order to maximize the signal-to-interference ratio. It is a generalization of the multiapodization proposed by Stankwitz, Dallaire,

Table 5.1: Typical apodization functions used in SAR processing, their peak-to-sidelobe ratio, and the widening of their main lobe with respect to a rectangular window.

Function	Symbol	PSLR [dB]	Widening [%]
Rectangular	w_{box}	-13	0
Kaiser	$w_k(\beta = 2.5)$	-21	18
Raised cosine	$w_c(\alpha = 0.75)$	-21	13
Raised cosine	$w_c(\alpha = 0.60)$	-47	32
Hamming	$w_c(\alpha = 0.54)$	-44	47
Hann	$w_c(\alpha = 0.50)$	-31	63

and Fienup [181], where each image is processed with different apodization windows and each final output pixel is determined by choosing the best pixel among the different intermediate images. Whereas non-linear, space-variant techniques can improve target detectability, they void radiometric calibration. The non-linear apodization techniques, while offering strategies in special cases, are currently not widely used in spaceborne SAR processors. Therefore, the discussion in this chapter will be limited to linear apodization strategies, i. e., weighting or tapering windows as described above.

Table 5.2 lists range and azimuth apodization functions of four current spaceborne SAR missions. It can be observed that the choice of apodization function is not uniform across missions, and for some missions the apodization function even varies across modes or across range and azimuth direction. In summary, apodization functions ranging from a rectangular window to a Hanning window (often even at different pulse bandwidths) are used so that relatively large passband effects can be expected. These effects will be explored for exemplary target response functions in Sec. 5.4.

5.3 Modeling Passband Effects with Central Moments

In this section, an analytical model is developed which allows to conveniently quantify the passband problem for different target response and apodization functions. The principal idea is to derive the governing integral equation in Sec. 5.3.1, which establishes the link between the one-dimensional weighting functions and the derived ERCS. This integral equation is then approximated through Taylor series expansion by a truncated sum of scaled moments of the apodization functions in Sec. 5.3.2. Finally, the derivation is extended from the one-dimensional to the two-dimensional case in Sec. 5.3.3.

The trigger for the ideas and the approach developed in this section was a very interesting paper by Young [204]. He described problems in stellar photometry which occur when accurate photometric measurement data are transformed to a photometric reference standard. The governing equation in his work is mathematically speaking identical to Eq. (5.18), which also covers the SAR case and is introduced later in this chapter.

Although the starting point for the modeling of passbands is identical in stellar photometry and SAR, further simplifications are possible in the SAR case. In photometry, the passbands of optical equipment are typically not mirror-symmetric, i. e., even functions, with respect to frequency. The apodization functions used during SAR processing are,

Table 5.2: A multitude of weighting functions is used during processing of spaceborne SAR images. Here the utilized azimuth and range weighting functions are shown for four exemplary SAR missions. Besides the variation in weighting functions, the pulse bandwidth (BW) is also mode-dependent for all missions. Note: The respective mode and beam abbreviations are defined in the referenced documents.

Mission	Mode(s)	Beam(s)	Weighting function	
			Range	Azimuth
ALOS/PALSAR [3, 150]	all modes (BW: [14; 28] MHz)		w_{box}	w_{box}
RADARSAT-2 [172] Bandwidth: 2.9 MHz to 100 MHz	SLC: all but Spotlight		$w_k(\beta = 2.4)$	$w_k(\beta = 2.4)$
	SLC: Spotlight		$w_k(\beta = 2.4)$	$w_k(\beta = 3.5)$
	SGX: Standard, Wide, Extended high/low		$w_k(\beta = 2.8)$	$w_k(\beta = 2.9)$
	SGX: Fine, ML fine, Ultra fine, Std. quad. pol.		$w_k(\beta = 2.4)$	$w_k(\beta = 2.4)$
	SGX: Spotlight		$w_k(\beta = 2.4)$	$w_k(\beta = 3.5)$
	SGF: Standard, Wide, Extended high/low		$w_k(\beta = 2.8)$	$w_k(\beta = 2.9)$
	SGF: Fine, ML fine, Ultra fine		$w_k(\beta = 2.4)$	$w_k(\beta = 2.4)$
	SGF: Spotlight		$w_k(\beta = 2.4)$	$w_k(\beta = 3.5)$
	ScanSAR		$w_k(\beta = 2.8)$	$w_k(\beta = 2.9)$
	{SSG,SPG}: Standard, Wide, Extended h/l, Std. quad. pol.		$w_k(\beta = 2.8)$	$w_k(\beta = 2.9)$
	{SSG,SPG}: Fine, ML fine, Ultra fine, Fine quad. pol.		$w_k(\beta = 2.4)$	$w_k(\beta = 2.4)$
	{SSG,SPG}: Spotlight		$w_k(\beta = 2.4)$	$w_k(\beta = 3.5)$
Sentinel-1 [7, 189] Bandwidth: 4.8 MHz to 100 MHz	SM_SLC	S1–S6	$w_c(\alpha = 0.75)$	$w_c(\alpha = 0.75)$
	SM_{FR,HR,MR}	S1, S4, S6	$w_c(\alpha = 0.75)$	$w_c(\alpha = 0.70)$
		S2	$w_c(\alpha = 0.75)$	$w_c(\alpha = 0.75)$
		S3, S5	$w_c(\alpha = 0.75)$	$w_c(\alpha = 0.52)$
	IW_SLC	IW1	$w_c(\alpha = 0.75)$	$w_c(\alpha = 0.70)$
	IW_GRD_{HR,MR}	IW2, IW3	$w_c(\alpha = 0.75)$	$w_c(\alpha = 0.75)$
		IW1	$w_c(\alpha = 0.70)$	$w_c(\alpha = 0.70)$
		IW2	$w_c(\alpha = 0.73)$	$w_c(\alpha = 0.75)$
		IW3	$w_c(\alpha = 0.75)$	$w_c(\alpha = 0.75)$
	EW_SLC	EW1	$w_c(\alpha = 0.60)$	$w_c(\alpha = 0.50)$
	EW_GRD_{HR,MR}	EW2–EW5	$w_c(\alpha = 0.75)$	$w_c(\alpha = 0.75)$
		EW1	$w_c(\alpha = 0.60)$	$w_c(\alpha = 0.60)$
		EW2	$w_c(\alpha = 0.70)$	$w_c(\alpha = 0.61)$
		EW3	$w_c(\alpha = 0.72)$	$w_c(\alpha = 0.62)$
		EW4	$w_c(\alpha = 0.75)$	$w_c(\alpha = 0.63)$
		EW5	$w_c(\alpha = 0.75)$	$w_c(\alpha = 0.60)$
	WV_SLC	WV1, WV2	$w_c(\alpha = 0.75)$	$w_c(\alpha = 0.75)$
	WV_GRD_MR	WV1, WV2	$w_c(\alpha = 0.75)$	$w_c(\alpha = 0.75)$
TerraSAR-X [23, 63] BW: 0.1 GHz to 0.3 GHz	comm. phase, all modes/beams		$w_c(\alpha = 0.75)$	$w_c(\alpha = 0.75)$
	operational, all modes/beams		$w_c(\alpha = 0.60)$	$w_c(\alpha = 0.60)$

on the other hand, exclusively even functions and centered at the origin.

5.3.1 Derivation of the Governing Equation

The goal of a radiometric measurement is to derive the ERCS of an imaged target after the raw data have been focused. In the one-dimensional case, the focused, complex output data $s_{\text{out}}(t)$ in time domain is generated through convolution of the received chirp signal $s_r(t)$ with the time-reversed and apodization-weighted complex conjugate of the transmitted pulse replica $h(t)$, expressed as

$$s_{\text{out}}(t) = s_r(t) * h(t) = \int_{-\infty}^{\infty} s_r(u)h(t-u) du. \quad (5.4)$$

According to Sec. 2.3.3, the point target ERCS ζ'_e or integrated impulse response is derived from the square-law detected image, i. e., from $|s_{\text{out}}(t)|^2$, by integrating over all sidelobes so that

$$\zeta'_e = \int_{-\infty}^{\infty} |s_{\text{out}}(t)|^2 dt, \quad (5.5)$$

where ζ'_e denotes “one-dimensional” ERCS in contrast to ζ_e (used later in Sec. 5.3.3), which denotes “two-dimensional” ERCS. The ERCS can also be written in frequency domain as

$$\zeta'_e = \int_{-\infty}^{\infty} |S_{\text{out}}(f)|^2 df \quad (5.6)$$

according to Parseval’s theorem, using capital letters for spectra. The time-domain convolution in Eq. (5.4) equals a multiplication in the spectral domain so that

$$S_{\text{out}}(f) = S_r(f)H(f). \quad (5.7)$$

Equation (5.6) suggests that only the signal magnitudes are of importance; the phase terms can be neglected, as in

$$|S_{\text{out}}(f)|^2 = |S_r(f)H(f)|^2 = |S_r(f)|^2|H(f)|^2. \quad (5.8)$$

The phase of the two signals is not important here because it only affects signal focusing; the total energy remains unchanged. Therefore, it is useful to separate the magnitude from the phase in Eq. (5.8), which is done in the next step.

It is assumed that the transmitted signal $g(t)$ is a typical chirp pulse of the form

$$g(t) = w_g(t) \exp(j\pi K_r t^2) \quad (5.9)$$

where $w_g(t)$ is a real-valued weighting (or apodization) function and K_r is the chirp modulation rate. Using symbol W_g for the frequency domain representation of w_g , the magnitude of its spectrum can be approximated as

$$|G(f)| \approx |W_g(f)| = w_g[t(f)] \quad (5.10)$$

according to the principle of stationary phase, and ignoring a constant scaling factor [32, Sec. 3.2.2]. In other words, the shape of the weighting function $w_g(t)$ in the time domain is approximately preserved in the spectral domain due to the linear frequency modulation of the chirp signal. The approximation becomes more accurate for larger

time-bandwidth products, i. e., for larger products between the pulse length and pulse bandwidth. Similarly to Eq. (5.9), the received chirp signal $s_r(t)$ and the matched filter in time domain $h(t)$ can be written as

$$s_r(t) = w_s(t) \exp(+j\pi K_r t^2), \quad (5.11)$$

$$h(t) = w_h(t) \exp(-j\pi K_r t^2), \quad (5.12)$$

separating again magnitude and phase terms. The weighting function $w_s(t)$ describes the frequency or angular dependence of the target backscatter, whereas $w_h(t)$ describes the apodization function used during focusing. After Fourier transformation, the magnitudes of the spectra can again be approximately expressed as

$$|S_r(f)| \approx |W_s(f)| = w_s[t(f)], \quad (5.13)$$

$$|H(f)| \approx |W_h(f)| = w_h[t(f)]. \quad (5.14)$$

Finally, the integrated impulse response, i. e., the target ERCS, is given by

$$\zeta'_e = \int_{-\infty}^{\infty} |S_{\text{out}}(f)|^2 df \quad (5.15)$$

$$= \int_{-\infty}^{\infty} |S_r(f) \cdot H(f)|^2 df \quad (5.16)$$

$$\approx \int_{-\infty}^{\infty} |W_s(f)|^2 \cdot |W_h(f)|^2 df \quad (5.17)$$

$$= \int_{-\infty}^{\infty} \epsilon_s(f) \epsilon_h(f) df, \quad (5.18)$$

where the symbols $\epsilon_s(f)$ and $\epsilon_h(f)$ were introduced for convenience and represent the energy spectral densities (ESDs) of $s_r(t)$ and $h(t)$, respectively.

Equation (5.18) represents the governing equation for the model to be derived in the following section. It is of the same shape as the governing equation in the work of Young [204] mentioned before. This representation is very convenient as it states a point target ERCS in terms of the chirp weighting functions. It highlights the interaction between the magnitude of the measured and squared target response function ϵ_s , and the shape of the squared apodization function ϵ_h . Both functions are slowly varying with f , and are never negative.

5.3.2 Modeling with Central Moments: One-Dimensional Case

The goal of this section is to replace the integral in the governing equation (5.18) by an algebraic approximation. This way, the ERCS does not only become easier to compute, but also general inferences on the interaction between the signal and the apodization functions can be drawn more easily.

As a first step, the squared signal weighting function in frequency domain, $\epsilon_s(f)$, is expanded into a Taylor series around a frequency f_0 so that

$$\begin{aligned} \epsilon_s(f) = & \epsilon_s(f_0) + (f - f_0) \left. \frac{d\epsilon_s}{df} \right|_{f_0} + \frac{(f - f_0)^2}{2!} \left. \frac{d^2\epsilon_s}{df^2} \right|_{f_0} + \frac{(f - f_0)^3}{3!} \left. \frac{d^3\epsilon_s}{df^3} \right|_{f_0} \\ & + \frac{(f - f_0)^4}{4!} \left. \frac{d^4\epsilon_s}{df^4} \right|_{f_0} + \frac{(f - f_0)^5}{5!} \left. \frac{d^5\epsilon_s}{df^5} \right|_{f_0} + O(f^6), \end{aligned} \quad (5.19)$$

where $O(f^6)$ summarizes terms in f of order 6 and higher. Now f_0 is chosen to be the centroid of $\epsilon_h(f)$, i. e.,

$$f_0 = \frac{\int_{-\infty}^{\infty} f \epsilon_h(f) df}{\int_{-\infty}^{\infty} \epsilon_h(f) df}. \quad (5.20)$$

For SAR, all baseband apodization functions are even and therefore centered around $f = 0$, see Sec. 5.2. It follows for the centroid that $f_0 = 0$, so that the Taylor series in Eq. (5.19) is effectively a Maclaurin series [19].

The integral in Eq. (5.18) can now be expanded with Eq. (5.19) to

$$\begin{aligned} \zeta'_e &= \epsilon_s(f_0) \int_{-\infty}^{\infty} \epsilon_h(f) df + \left. \frac{d\epsilon_s}{df} \right|_{f_0} \int_{-\infty}^{\infty} (f - f_0) \epsilon_h(f) df \\ &+ \frac{1}{2!} \left. \frac{d^2\epsilon_s}{df^2} \right|_{f_0} \int_{-\infty}^{\infty} (f - f_0)^2 \epsilon_h(f) df \\ &+ \frac{1}{3!} \left. \frac{d^3\epsilon_s}{df^3} \right|_{f_0} \int_{-\infty}^{\infty} (f - f_0)^3 \epsilon_h(f) df \\ &+ \frac{1}{4!} \left. \frac{d^4\epsilon_s}{df^4} \right|_{f_0} \int_{-\infty}^{\infty} (f - f_0)^4 \epsilon_h(f) df \\ &+ \frac{1}{5!} \left. \frac{d^5\epsilon_s}{df^5} \right|_{f_0} \int_{-\infty}^{\infty} (f - f_0)^5 \epsilon_h(f) df + O(f^6), \end{aligned} \quad (5.21)$$

keeping symbol f_0 for clarity. Equation (5.21) can be reformulated with terms representing the central moments of $\epsilon_h(f)$. In general, the central moment k of a random variable X with mean μ and probability density f_X is given as [176]

$$E[(X - \mu)^k] = \int_{-\infty}^{\infty} (x - \mu)^k f_X(x) dx. \quad (5.22)$$

The second central moment, for instance, is also known as the variance of X . With this definition of central moments, the following scaled central moments for $\epsilon_h(f)$ of order k can be defined:

$$\mu_k^k = \frac{\int_{-\infty}^{\infty} (f - f_0)^k \epsilon_h(f) df}{\int_{-\infty}^{\infty} \epsilon_h(f) df}. \quad (5.23)$$

Hence Eq. (5.21) becomes

$$\begin{aligned} \zeta'_e &= \epsilon_s(f_0) \int_{-\infty}^{\infty} \epsilon_h(f) df \cdot \\ &\left[1 + \frac{\mu_2^2}{2! \epsilon_s(f_0)} \left. \frac{d^2\epsilon_s}{df^2} \right|_{f_0} + \frac{\mu_4^4}{4! \epsilon_s(f_0)} \left. \frac{d^4\epsilon_s}{df^4} \right|_{f_0} \right] + O(f^6), \end{aligned} \quad (5.24)$$

noting that all odd moments μ_k drop out because, as mentioned before, the apodization function $\epsilon_h(f)$ is assumed to be even. Here the notation of moments was adapted from Young [204], denoting μ_k as the k th root of moment μ_k^k , or the k th norm.

Now, ζ'_e is expressed in terms of even moments of the apodization function, and of evaluations of derivatives of $\epsilon_s(f)$ at the center frequency $f = 0$. The scaled moments μ_k^k can be tabulated for common apodization functions in order to easily assess the effect

of the chosen apodization function on the derived ζ'_e for a given angular or frequency dependent target response function.

A further simplification of Eq. (5.24) is possible if $\epsilon_s(f)$ is expressed as a polynomial, which is often done in target measurement data analysis anyway so that

$$\epsilon_s(f) = \sum_{i=0}^n a_i f^i, \quad (5.25)$$

where n is the chosen order of the polynomial, and the a_i are the polynomial coefficients. Equation (5.24) requires the evaluation of derivatives of ϵ_s at $f_0 = 0$. The i th derivative of ϵ_s at $f = 0$ is

$$\epsilon_s^{(i)}(0) = i! \cdot a_i.$$

With this, Eq. (5.24) can now be written more concisely as

$$\zeta'_e = \epsilon_s(f_0) \underbrace{\int_{-\infty}^{\infty} \epsilon_h(f) df}_{\text{const. for all } \epsilon_s(f)} \cdot \left[1 + \frac{\mu_2^2}{\epsilon_s(f_0)} a_2 + \frac{\mu_4^4}{\epsilon_s(f_0)} a_4 + O(f^6) \right]. \quad (5.26)$$

In other words, as soon as $\epsilon_s(f)$ is expressed as a polynomial, one can rather directly deduce the effect of higher order derivatives of $\epsilon_s(f)$ on ζ'_e .

The summation term in Eq. (5.26) represents the new insight into the interaction between a target response function and the SAR system passband function. Up to now, summands of order 2 and higher have been dropped because the signal response functions have been, mostly only implicitly, assumed to be constant over frequency and angle [32, 33, 61, 131, 171, 212]. For low resolution systems or systems with low radiometric requirements, a truncation after the lowest order term is appropriate. In a more general setting, higher order terms have to be considered in order to accurately describe the ERCS of targets with arbitrary response functions.

5.3.3 Extension to the Two-Dimensional Case

Up to now, only the one-dimensional case was considered, i. e., $s_r(t)$ and $h(t)$ represented either the signals along the range or the azimuth axis, and the variable t denoting time was equivalent to a range chirp frequency or an azimuth angle.

For the two-dimensional case, the approach of the previous section can nevertheless be applied. Equations (5.5) and (5.6) become

$$\begin{aligned} \zeta_e &= \int_{-\infty}^{\infty} \int_{-\infty}^{\infty} |s_{\text{out}}(t_r, t_a)|^2 dt_r dt_a \\ &= \int_{-\infty}^{\infty} \int_{-\infty}^{\infty} |S_{\text{out}}(f_r, f_a)|^2 df_r df_a. \end{aligned} \quad (5.27)$$

The integrated impulse response or ERCS ζ_e is hence given as a double integral over slow (azimuth) and fast (range) times t_a and t_r , or after Fourier transformation over range and azimuth frequencies f_r and f_a , respectively. The two-dimensional functions

$s_r(t_r, t_a)$ and $h(t_r, t_a)$ are approximately separable into two one-dimensional functions because of the significant differences in time scales between azimuth and range time [32]. Therefore, the signals in frequency domain can be expressed as

$$S_r(f_r, f_a) = S_{r,r}(f_r)S_{r,a}(f_a), \quad (5.28)$$

$$H(f_r, f_a) = H_r(f_r)H_a(f_a) \quad (5.29)$$

so that the two-dimensional integral in Eq. (5.27) can be written as a multiplication of two one-dimensional integrals:

$$\begin{aligned} \zeta_e &= \int_{-\infty}^{\infty} |S_{r,r}(f_r)H_r(f_r)|^2 df_r \cdot \int_{-\infty}^{\infty} |S_{r,a}(f_a)H_a(f_a)|^2 df_a \\ &= \zeta'_{e,r} \cdot \zeta'_{e,a}. \end{aligned} \quad (5.30)$$

Each of these two integrals resemble the integral in Eq. (5.16) which led to Eq. (5.26).

Now three cases can be distinguished concerning $s_r(t_r, t_a)$:

1. The received signal $s_r(t_r, t_a)$ might be a function which mostly shows a dependence along the range or the azimuth axis. This is a special case often encountered in practice. Several such examples will be shown in the following Sec. 5.4. They include signals scattered back by dihedrals (e. g. double-bounce structures in urban areas) with strong angular dependence, or the pronounced frequency dependence of signals scattered back by distributed targets like snow. For such cases, the signal response function in one dimension, e. g. azimuth, can be described as a polynomial according to Eq. (5.25) with $a_i = 0$ for all $i > 0$. Then the summation term in Eq. (5.26) is reduced to 1 so that

$$\zeta'_{e,a} = \epsilon_s(f_0) \int_{-\infty}^{\infty} \epsilon_h(f) df = C. \quad (5.31)$$

Using this partial result in Eq. (5.30), it follows that

$$\begin{aligned} \zeta_e &= C\epsilon_{s,r}(f_{0,r}) \int_{-\infty}^{\infty} \epsilon_{h,r}(f_r) df_r \\ &\cdot \left[1 + \frac{\mu_2^2}{\epsilon_{s,r}(f_{0,r})} a_2 + \frac{\mu_4^4}{\epsilon_{s,r}(f_{0,r})} a_4 + O(f_r^6) \right]. \end{aligned} \quad (5.32)$$

The result for the two-dimensional case in Eq. (5.32) is identical to the one-dimensional case in Eq. (5.26) except for a constant scaling factor C , which drops out if one relates the ERCs obtained with different apodization functions with respect to each other.

2. Another special case occurs if the azimuth and range response functions $s_{r,a}$ and $s_{r,r}$ are identical in shape, i. e., after normalizing the relevant domains for t_a and t_r to a common “processing” domain. This domain is defined during processing by the length T of the apodization windows, which can be defined to be unequal 0 only within $[-T/2; T/2]$. In this case, $f_a = f_r = f$ and

$$\begin{aligned} \zeta_e &= (\zeta'_e)^2 \\ &= \epsilon_s^2(f_0) \int_{-\infty}^{\infty} \epsilon_h^2(f) df \cdot \left[1 + \frac{\mu_2^2}{\epsilon_s(f_0)} a_2 + \frac{\mu_4^4}{\epsilon_s(f_0)} a_4 + O(f^6) \right]^2. \end{aligned} \quad (5.33)$$

Abbreviating the summation term with

$$\left[1 + \frac{\mu_2^2}{\epsilon_s(f_0)} a_2 + \frac{\mu_4^4}{\epsilon_s(f_0)} a_4 + O(f^6) \right]^2 = \left[1 + c_2 + c_4 + O(f^6) \right]^2, \quad (5.34)$$

the square of the summation term can be expanded so that

$$\varsigma_e = \epsilon_s^2(f_0) \int_{-\infty}^{\infty} \epsilon_h^2(f) df \cdot \left[1 + c_2 + c_4 + \underbrace{c_2^2 + c_2 c_4 + c_4^2 + O(f^6)}_{\text{small in comparison to } 1 + c_2 + c_4} \right]. \quad (5.35)$$

Except for an additional constant scaling factor as in Eq. (5.32), the two-dimensional integral is approximately identical to the one-dimensional one of Eq. (5.26) because the additional summation terms in the square brackets resulting from squaring are small in comparison to the terms that also appear in the one-dimensional case. Therefore, the one-dimensional solution in Eq. (5.26) is approximately valid even if a strong but equal signal response on frequency and angle exists.

3. In the most general case, $s_{r,a}$ and $s_{r,r}$ are different, and neither response function can be approximated as a constant function. In this case, modeling the interaction between response and apodization functions by scaled central moments becomes unwieldy so that the integral in Eq. (5.27) should be solved numerically instead.

In conclusion, modeling the interaction between target response and apodization functions with scaled central moments of the apodization functions extends to the two-dimensional case for the two special cases 1 and 2 shown above. The important first case will be exploited in the following section, where the developed model is applied to several exemplary response functions.

5.4 Quantitative Examples and Verification

This section serves two purposes. Through the introduction of numerical examples for several signal and system passband functions it shall be shown that the passband problem is a relevant one for accurate radiometric SAR measurements. At the same time, radiometric differences resulting from the use of different apodization functions will be computed both with the model introduced in the previous Sec. 5.3 and by numerical integration. The results therefore also serve as an empirical verification of the approach developed in the previous section.

The most commonly used apodization functions in SAR were introduced in Sec. 5.2. In the following Sec. 5.3, a model was introduced which allows to describe the interaction between signal response and apodization functions with respect to radiometric measurements. In order to apply the model, the scaled central moments μ_k^k of the respective apodization functions must be known. Table 5.3 lists these moments up to order 8 for a family of general cosine windows w_c (see Eq. (5.2)) with varying window parameters α . It can be observed that higher order moments quickly get smaller, supporting the idea that a series truncation after moments up to order 2 or 4 might be sufficient in many cases. This, on the other hand, depends on the degree of non-linearity of the signal functions.

Table 5.3: Moments and norms up to order 8 of common squared apodization functions in SAR (see also Sec. 5.2), defined within the normalized domain $-1/2 \leq f \leq 1/2$ and a value of 1 at $f = 0$. The apodization functions are even so that all odd moments vanish.

$\epsilon_h(f)$	μ_2^2 μ_2	μ_4^4 μ_4	μ_6^6 μ_6	μ_8^8 μ_8
w_{box}^2	0.083 33 0.288 68	0.012 50 0.334 37	0.002 23 0.361 51	0.000 43 0.379 92
$w_c^2(\alpha = 0.75)$	0.052 00 0.228 04	0.006 51 0.284 05	0.001 07 0.319 84	0.000 20 0.344 72
$w_c^2(\alpha = 0.60)$	0.030 37 0.174 27	0.002 64 0.226 72	0.000 35 0.265 34	0.000 06 0.294 80
$w_c^2(\alpha = 0.54)$	0.023 37 0.152 88	0.001 51 0.197 27	0.000 15 0.231 16	0.000 02 0.258 66
$w_c^2(\alpha = 0.50)$	0.020 01 0.141 45	0.001 05 0.179 94	0.000 08 0.208 02	0.000 01 0.230 09

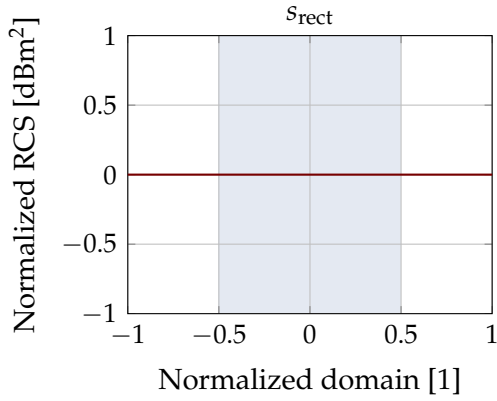
Considering any moment's column in Tab. 5.3 across a set of α values it becomes apparent that the impact of the moments on the ERCS for a target increases with α . This is also intuitively clear. A Hanning window “sees” less of a target response function in comparison to a rectangular window. The weighted averaging, which the focusing operation essentially is, is more affected if the parts away from the center frequency are stronger weighted.

Now, six numerical examples shall be given. Each example is of special case 1 as mentioned on p. 81, i. e., either a frequency or an angular dependence of the target response function is assumed. The six examples are:

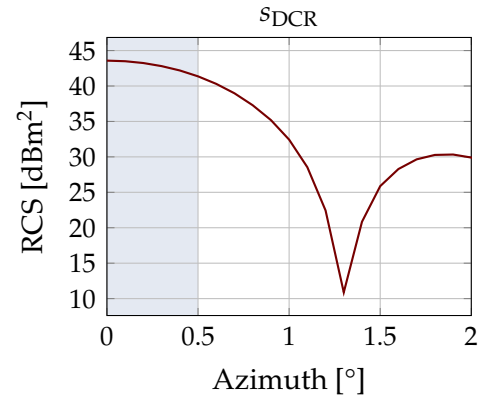
1. Flat response ($w_{\text{rect}} = \text{const.}$)¹: This case is included for comparison. It represents the currently adopted understanding that a target response function is constant within the range bandwidth or the relevant azimuth angular range. It is also a good model for natural and man made targets if the SAR system is sufficiently narrow-band or if the radiometric requirements are not too stringent. For completeness, a plot of this response function is shown in Fig. 5.2a.
2. 1.5 m trihedral corner reflector (w_{CR15}): This target was already introduced in the introductory Sec. 5.1. As it is an often used calibration target, understanding the choice of the apodization function on a derived corner ERCS is of special importance. The frequency response analyzed in this section is taken at the Sentinel-1 center frequency of 5.405 GHz for a bandwidth of 100 MHz, i. e., the maximal operational Sentinel-1 bandwidth.

The frequency-dependent RCS of the corner was determined numerically with FEKO Suite 6.1.1 using the multilevel fast multipole method (MLFMM). The 1.5 m corner geometry was discretized with 540×10^3 triangles. The incident field was vertically polarized.

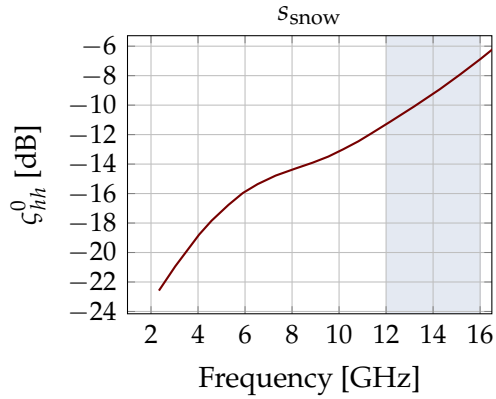
¹The symbols w_{rect} etc. introduced in this list of examples denote signal envelopes which are proportional to amplitude, not power, in accordance with Eq. (5.11).



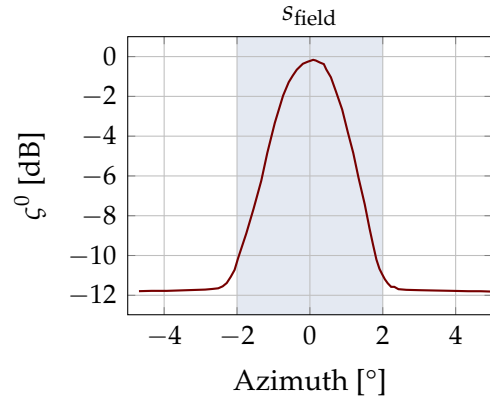
(a) Flat response (over frequency or azimuth angle) target. This represents the target backscatter approximation which is currently assumed in the SAR literature.



(b) Angular-dependent RCS of a dihedral with side lengths of 1.0 m at 9.65 GHz; also see Fig. 2.18 on p. 40. Only the positive half of this even function is shown.



(c) Dry snow; data reproduced from [191]. Note the approximate exponential dependence of the backscatter on frequency within the highlighted region.



(d) Flashing field; simulated European Remote Sensing Satellite 2 (ERS-2) data reproduced from [196].

Figure 5.2: One-dimensional target response functions for four out of six exemplary targets. The response functions of the other two examples, the trihedral corner reflectors, are shown in Fig. 5.1a on p. 73.

It should be mentioned that the RCS undulation over frequency is for a given corner, in general, less pronounced at higher frequencies, e. g. at X-band. At lower frequencies, i. e., for S-, L- and P-band systems, the influence of the apodization function on the derived ERCS can be expected to be significantly higher than the numbers reported below.

3. 2.8 m trihedral corner reflector (w_{CR28}): This corner size was chosen as it represents the type of corner which was used by the DLR to geometrically and radiometrically calibrate the Sentinel-1 system [165]. Except for the geometrical dimensions, the example is identical to the previous one.

The frequency-dependent RCS was again computed numerically using FEKO and is also shown in Fig. 5.1a. The geometry was discretized with 1.08×10^6 triangles.

4. 1.0 m dihedral reflector (w_{DCR}): A dihedral reflector was included as an example because it is a good model for many double-bounce structures found especially but not exclusively in urban areas. As shown on p. 40 in Fig. 2.18, one metallic plate is parallel to the ground, and the other is aligned vertically. The angular-dependent RCS is plotted in Fig. 5.2b, which also denotes the relevant angular range of $[-0.5^\circ; 0.5^\circ]$ used later on. Larger angular ranges (or dihedral dimensions larger than 1 m) would further increase the RCS variance within the processed range.

The stated 1° angular range represents much less than the 4.4° angular range which was already exploited for an experimental high-resolution TerraSAR-X staring spotlight acquisition [137]. Hence it might be reasonably assumed that the influence of the chosen apodization function on the derived ERCS will further increase for future high resolution SAR systems.

5. Snow (w_{snow}): The next example represents a distributed target, dry snow. The frequency dependent data were acquired by Ulaby [191]. For the analysis, an arbitrary frequency range extending from 12 GHz to 16 GHz was chosen, see Fig. 5.2c. This represents a relative bandwidth of nearly 30 % and a domain where the backscatter increases exponentially with frequency.

Although a relative bandwidth of 30 % is above the ones currently used by civil spaceborne SAR systems, several airborne systems exist which exploit even larger relative bandwidths. One of these systems is the PAMIR sensor, operating at 9 GHz with a relative bandwidth of 40 % [25]. It is to be expected that civil spaceborne SAR systems with similar bandwidths will be available in the future.

6. Flashing fields (w_{field}): As the last example, a distributed target with strong directional scattering shall be considered. Agricultural fields which appear especially bright for certain orientations are known as flashing fields. The data used for this example, shown in Fig. 5.2d together with the considered domain, were measured and modeled by Wegmüller et al. [196].

This example is somewhat exotic, but it serves well as a counterpart to the first example. The flat response of the first example and the extremely distorted response of the last example form a lower and upper bound for most other cases found in practice.

Table 5.4: Polynomial coefficients of the exemplary target response functions described in the text. For comparability, the coefficients were derived by first normalizing the frequency domain of all functions to $[-0.5; 0.5]$, and by scaling the amplitude so that $\epsilon_s(f = 0) = 1$. The highest polynomial degree was determined empirically to ensure a good fit of the polynomial with the original data. Coefficients of order 15 to 22 for w_{DCR} are too small to be displayed here, but they are still included in the analysis.

$\epsilon_s(f)$	Orders	Polynomial coefficients				
w_{rect}^2	0–0	1.0000				
w_{CR15}^2	0–4	1.0001	–0.0285	0.4385	0.1356	–0.4359
	5–8	–0.0710	0.1488	0.0112	–0.0175	
w_{CR28}^2	0–4	1.0014	0.0998	1.5569	–0.6353	–10.5866
	5–9	2.4132	26.6221	–3.8088	–30.9808	2.7054
	10–12	17.1397	–0.7196	–3.6743		
w_{DCR}^2	0–4	0.9959	0.0000	–1.8851	0.0000	1.3893
	5–9	0.0000	–0.5279	0.0000	0.1185	0.0000
	10–14	–0.0169	0.0000	0.0016	0.0000	–0.0001
w_{snow}^2	0–4	0.9968	1.0106	0.5754	0.2705	0.2141
	5–7	0.1330	0.0379	0.0039		
w_{field}^2	0–4	1.0207	0.2075	–12.2790	–3.4258	67.9242
	5–9	19.2595	–206.1609	–51.9135	371.9196	75.2807
	10–14	–407.3653	–60.1218	264.9804	24.8833	–93.9141
	15–16	–4.1659	13.9420			

Measurement data on the wide-bandwidth frequency dependence of distributed target backscatter do unfortunately only scarcely exist. This is the reason why, besides snow, no further terrain types are included in the set of examples. Especially the frequency dependent backscatter of rain forest would be interesting for further investigations. Rain forest is regularly used for relative radiometric corrections [161, 164], sometimes even for radiometric calibrations [112, 168]. At significant relative bandwidths of above 10 % or 20 %, a comparatively large RCS variance should be expected because the features of trees are, depending on tree type and frequency, in the order of a wavelength.

As the next step in the example, polynomial approximations of the six exemplary response functions were derived. For this, the response functions were first normalized for better comparability: The relevant domains highlighted in Fig. 5.1 were scaled to fit the normalized domain $[-0.5; 0.5]$, and the amplitude was scaled so that the response function is 1 at $f = 0$. The derived polynomial coefficients are shown in Tab. 5.4. Already at first sight one can single out functions which are more affected than others by the choice of apodization function, namely those with larger coefficients.

It was mentioned before that apodization functions are even functions so that all odd moments drop out. Therefore, all odd coefficients of a polynomial describing a signal's response function (see Eq. (5.25)) have no influence on the derived target ERCS. This is because contributions for $f < 0$ are exactly outweighed by contributions for $f > 0$. Existing odd polynomial coefficients result, graphically speaking, in a horizontal shift of a polynomial function. Given that the odd coefficients are of no consequence to the

resulting ERCS, one can conclude that horizontal shifts of a signal's response function are also of no importance as long as the value at the center frequency remains the same. By now, all the necessary precursory steps have been completed to finally derive the apodization-dependent, normalized target ERCSs. For each combination of apodization function from Tab. 5.3 and for each target response function from Tab. 5.4, the resulting ERCS has been computed with two approaches. The normalized results are shown in Tab. 5.5. The two computation approaches are:

1. Approximate ERCS derived with central moments according to Eq. (5.26) with data from Tables 5.3 and 5.4. Several approximations were computed by truncating the summation terms in Eq. (5.26) after the first, second, \dots , up to the fifth term (moments up to order 8), respectively.
2. ERCS derived by evaluating the original integral Eq. (5.5) numerically in time domain. The results are shown in column *INT*.

The resulting ERCSs shown in Tab. 5.5 have been calibrated/normalized in two steps to allow easy comparability:

- a) Each system (defined by the respective apodization function W_h) is calibrated with the ideal target w_{rect} . This equals calibration with a (theoretical) sphere as proposed in Chap. 3, or in other words, with a target that has a known ERCS. The different integrals over the apodization functions are such compensated, and consequently the values in row w_{rect} are all 0.0 dB.
- b) The effects of the chosen apodization function on the derived ERCS are normalized with respect to the effect of the rectangular apodization function w_{box} (so that the values in these rows are always 0.0 dB). Therefore, all numbers in Tab. 5.5 represent a target's change in ERCS with respect to processing with no apodization window.

Several conclusions can be drawn from the numerical results in Tab. 5.5. First, the approximate results derived from moments agree well with the exact one-dimensional solutions (column *INT*, from Eq. (5.5)), especially for targets with comparatively low RCS variation within the relevant processing range. The 1.5 m corner response is sufficiently well approximated by a square function so that moments up to order 2 already result in a good approximation. This reemphasizes that the model based on moments of the apodization function is useful in getting a quick estimate of the effects to be expected if different apodization functions are used during processing.

Another observation concerns the two trihedral corner reflectors. The difference in ERCS for both analyzed corner reflectors between using no apodization function and using a Hanning window (the two extreme cases for currently used apodization functions, see Tab. 5.2) is nearly 0.1 dBm². For a system like Sentinel-1, where a radiometric uncertainty of not more than 0.3 dBm² is targeted, this effect simply cannot be ignored anymore, and a solution to the passband problem needs to be found.

On the other hand, smaller adjustments of the cosine window parameter α can result in ERCS changes which might be ignored for many applications. For instance, switching from $\alpha = 0.60$ to $\alpha = 0.54$ for w_{snow} results in a change of the equivalent backscatter coefficient of only about 0.02 dB. The observed effect, however small for snow, always depends on the shape of the respective target response function, which can be expected to be less uniform the larger the range bandwidth or the aspect angle range becomes.

Table 5.5: Differences in ERCS depending on which apodization function was used during processing – six different targets. Two computation approaches are compared to demonstrate the applicability of the new method: (1) approximate method using moments up to order 8 as developed in Sec. 5.3, (2) one-dimensional signal convolution in time domain (column *INT*, from Eq. (5.5)). Reading example: A dihedral corner reflector (w_{DCR}) processed with a Hanning weighting window appears 0.500 dB (a) brighter than when processed with a boxcar window (b). Computing the ERCS with moments up to order 4 (c) is already a good approximation of (a), whereas the state of the art only considers moments up to order 0 (d).

Input envelopes		Normalized ERCSs (different methods) [dB]					
W_s	W_h	Moments up to order ¹					INT ²
		0	2	4	6	8	
w_{rect}	w_{box}	0.000	0.000	0.000	0.000	0.000	0.000
	$w_c(\alpha = 0.75)$	0.000	0.000	0.000	0.000	0.000	0.000
	$w_c(\alpha = 0.60)$	0.000	0.000	0.000	0.000	0.000	0.000
	$w_c(\alpha = 0.54)$	0.000	0.000	0.000	0.000	0.000	0.000
	$w_c(\alpha = 0.50)$	0.000	0.000	0.000	0.000	0.000	0.000
w_{CR15}	w_{box}	0.000	0.000	0.000	0.000	0.000	0.000
	$w_c(\alpha = 0.75)$	0.000	-0.058	-0.047	-0.048	-0.048	-0.048
	$w_c(\alpha = 0.60)$	0.000	-0.098	-0.080	-0.082	-0.082	-0.081
	$w_c(\alpha = 0.54)$	0.000	-0.112	-0.092	-0.093	-0.093	-0.093
	$w_c(\alpha = 0.50)$	0.000	-0.118	-0.097	-0.098	-0.098	-0.098
w_{CR28}	w_{box}	0.000	0.000	0.000	0.000	0.000	0.000
	$w_c(\alpha = 0.75)$	0.000	-0.191	0.063	-0.067	-0.038	-0.041
	$w_c(\alpha = 0.60)$	0.000	-0.329	0.094	-0.117	-0.069	-0.075
	$w_c(\alpha = 0.54)$	0.000	-0.374	0.099	-0.135	-0.082	-0.088
	$w_c(\alpha = 0.50)$	0.000	-0.396	0.097	-0.144	-0.090	-0.096
w_{DCR}	w_{box}	0.000	0.000	0.000	0.000	0.000	0.000 ^b
	$w_c(\alpha = 0.75)$	0.000	0.296	0.250	0.253	0.253	0.252
	$w_c(\alpha = 0.60)$	0.000	0.488	0.416	0.422	0.421	0.420
	$w_c(\alpha = 0.54)$	0.000	0.549	0.470	0.475	0.475	0.474
	$w_c(\alpha = 0.50)$	0.000 ^d	0.578	0.495 ^c	0.501	0.501	0.500 ^a
w_{snow}	w_{box}	0.000	0.000	0.000	0.000	0.000	0.000
	$w_c(\alpha = 0.75)$	0.000	-0.076	-0.081	-0.081	-0.081	-0.081
	$w_c(\alpha = 0.60)$	0.000	-0.129	-0.137	-0.138	-0.138	-0.137
	$w_c(\alpha = 0.54)$	0.000	-0.146	-0.156	-0.156	-0.156	-0.155
	$w_c(\alpha = 0.50)$	0.000	-0.154	-0.164	-0.165	-0.165	-0.164
w_{field}	w_{box}	0.000	nan	0.000	0.000	0.000	0.000
	$w_c(\alpha = 0.75)$	0.000	nan	-0.115	1.938	0.925	1.089
	$w_c(\alpha = 0.60)$	0.000	nan	-0.100	2.912	1.516	1.750
	$w_c(\alpha = 0.54)$	0.000	nan	-0.051	3.189	1.713	1.962
	$w_c(\alpha = 0.50)$	0.000	nan	-0.001	3.319	1.818	2.072

In conclusion, contrasting the two extreme cases w_{rect} and w_{field} , the choice of the apodization function can make a difference of up to 2 dB in radiometric measurements. In many practical cases, the differences will be close to zero. But as soon as the differences are systematic and measurable by modern SAR systems, the passband problem should and has to be addressed for accurate radiometric measurements. Otherwise seemingly calibrated radiometric data would exhibit backscatter effects which physically do not exist, possibly leading to false conclusions in subsequent research.

5.5 Resolving the Passband Problem

The previous section showed through numerical examples that the passband problem is real. Radiometric measurements are already affected by it today, and with emerging high resolution and high accuracy SAR systems, the passband problem will become more pronounced in the future.

In the following three sections, possible ways of handling the passband problem are sketched.

5.5.1 Accepting Higher Radiometric Uncertainties

The easiest way of dealing with the passband problem is to continue with nowadays' approach: no special treatment. From a viewpoint of radiometric measurements, this option is the least favorable.

The advantage of non-treatment is, of course, simplicity and that apodization functions can continue to be chosen solely on other than radiometric criteria. Each mission, and even each mode per mission could continue to use apodization functions which trim other aspects of the SAR system, like resolution or side. This reflects the current use of apodization functions as shown in Tab. 5.2 on p.76.

As a consequence, higher radiometric uncertainties need to be accepted. When a radiometric error budget is created, an up-to-now missing uncertainty contribution needs to be added due to variable interactions between target response and apodization functions. Further more, part of the additional uncertainty would already result from using calibration targets like corner reflectors which have a nonuniform spectral or angular response.

5.5.2 Introducing Standardized Passbands

The passband problem only occurs if non-uniform target response functions encounter different apodization functions during processing. Target response functions lie outside of the scope of the measurement system. Therefore the problem would be avoided altogether if all SAR systems used a fixed set of standard passbands. Each passband, for instance in range described by center frequency, bandwidth, and apodization function, would define a radiometric scale. Calibrated radiometric measurements reported for any of the standard scales were consequently directly comparable to each other.

From a radiometric calibration point of view, this approach is most favorable. First, no additional uncertainties are introduced, which were necessary for the simplest approach

in the previous Sec. 5.5.1. Data fusion from different systems or system modes could be achieved without ambiguity, loss of accuracy, or additional compensation measures.

On the downside, standardization takes away some freedom from the engineer during system design. Accurate radiometric measurements are an important component of any SAR mission, but by far they are not the only motivation behind building a SAR system. Other system aspects might just be traded off against highly accurate radiometric measurements. Furthermore, freely choosing a (possibly standardized) bandwidth is not always an option for the system designer due to frequency allocation restrictions. And finally, already today a multitude of systems with a multitude of beam-dependent settings exist, which for good reasons of data continuity will certainly be operated without modifications for the foreseeable future, and even carrying on these settings to follow-up missions.

As a compromise between using exclusively non-standardized or exclusively standardized passbands, only a few standardized passbands could be introduced and operated alongside other system or mode specific passbands. The standardized passbands would especially be used for applications in which highest radiometric accuracies are required. Examples include physical parameter inversion modeling for soil-moisture and biomass estimation, or radiometric cross calibrations of different SAR systems.

Proposing standardized passbands is a new concept in SAR, but it has been good practice and the only answer to measurement artifacts observed in another field of metrology: astronomical photometry. Astronomical photometry is concerned with quantifying the apparent brightness of stellar objects with respect to each other. Much like in SAR, spots of varying brightness are analyzed on a two-dimensional surface (photographic film or sensor plates). As in SAR, the interaction between the instruments' passbands (for instance defined by optical filters) and the stars' colors influences the measurement results despite most accurate calibration attempts: In the one scale (defined by a passband response), one star might appear brighter than another; in a second scale (resulting from different equipment of another researcher), the result might be reversed. The solution to reproducible results was the introduction of standardized photometric systems (i. e., passbands), of which one of the most known ones is the UBV system. A good overview of the history of this and other photometric systems is given by Bessell [18]. Adopting some of the experience and practice gained in the field of astronomical photometry might also smooth the path toward highly accurate radiometric measurements in SAR through passband standardization.

5.5.3 Conversion Between Different Scales

As was already mentioned, many practical reasons can restrain the adoption of standardized passbands as proposed in the previous section. Even in the illusory case of immediate adoption of standardized passbands, there would still exist a vast amount of archived SAR data for which a third approach is necessary. It is therefore desirable to have methods available which allow to transform calibrated radiometric measurements acquired with one passband to be comparable to measurements which were acquired in another passband. Two approaches are possible:

1. Reprocessing of an existing SAR image with a standard passband. This requires focused data to be processed in reverse first, undoing the effects of the original passband. In a second step, the yielded raw data are then reprocessed with a

standard apodization function (and possibly after trimming bandwidth or aspect angle range).

For most scientific end users, this approach is certainly far too complex and complicated. Additionally, reprocessing the data in reverse is only possible if all necessary auxiliary data are available to the end user. For instance, this is not the case for standard TSX products.

2. Introducing radiometric correction factors. If (and only if) the measured target response function is known, correction coefficients can be derived either numerically or approximately through the approach introduced in Sec. 5.3.

This approach is not generally applicable but it might reduce the radiometric uncertainty of specialized measurements, e. g. when doing SAR system cross calibrations over rain forest.

Another important special case where this approach is suited is the calibration of different modes of a single SAR system. As long as the properties of the reference point target and of the SAR system are known, a SAR calibration campaign can be conducted with a single mode and the calibration result can be applied to all other modes by deriving correction coefficients (also see [40]). Similar in spirit to the antenna model approach [161], the calibration effort can be greatly reduced while maintaining most of the calibration accuracy.

5.6 Conclusions

The starting point for this chapter was acknowledging the frequency and angular dependence of point target or terrain backscatter, which had already led to the introduction of ERCS in Chap. 3. In the present chapter the idea was advanced to the interaction between the target backscatter and the SAR system's passband. This led me to the following original contributions in this chapter:

- First, I identified the SAR passband problem in Sec. 5.1 which had so far been overlooked for radiometric SAR measurements. The passband problem denotes changes in the measured target ERCS due to the choice of the used range and azimuth apodization functions, range center frequency and bandwidth, and aspect angle range. It occurs despite current radiometric calibration efforts.
- Next, I reviewed commonly used apodization functions across missions in Sec. 5.2, showing that nowadays indeed many apodization functions and pulse bandwidths are used concurrently.
- In Sec. 5.3, I derived a novel analytical model based on the central moments of apodization functions. The model allows to easily estimate the effects of any apodization function on a measured target ERCS. I empirically verified the model in Sec. 5.4 by analyzing several exemplary target response functions, which also served as quantitative evidence supporting that the passband problem exists today. Depending on the target, I could show that different SAR passbands result in an ERCS difference of up to 2 dB.

- Finally, I proposed three possible solutions for the passband problem in Sec. 5.5, where from a point of accurate radiometric measurements I favored the introduction of standardized passbands across missions.

Overall, the SAR passband problem will have to be handled in one way or another. Only by acknowledging it will more accurate and consistent radiometric SAR measurements become possible in the future, especially for high-resolution SAR systems. Systematic measurement errors must be avoided so that subsequent research does not result in misleading conclusions.

6 The Three-Transponder Method

Several methods for measuring the radar cross section (RCS) of a transponder exist. In this chapter, a novel and potentially more accurate method for transponder calibration is introduced, which can contribute to obtain more accurately calibrated synthetic aperture radar (SAR) systems in the future.

Parts of this chapter have been published in [44], and a patent for this method was issued [53].

6.1 Introduction

The calibration of SAR instruments, as any other calibration effort, depends on measurement standards. A transponder, i. e., an active electronic device which consists of a receiving unit, a stable amplifier, and a transmitting unit, is one of the two most commonly used devices for the radiometric calibration of SAR instruments (also see Sec. 2.4.3). Its potentially high RCS, compact size, polarization agility, and the ability to record the received signal set it apart from passive trihedral corner reflectors, the other commonly used target for SAR calibration.

The use of a transponder device as a radiometric measurement standard requires to radiometrically calibrate the transponder itself. As a dominant contribution to the radiometric uncertainty budget for a SAR instrument, the quality of the transponder calibration has a direct impact on the overall radiometric measurement uncertainty of the SAR instrument.

The following Sec. 6.2 details three already existing transponder calibration approaches: The first one requires to separately measure the components and component assemblies forming the transponder amplification loop. In practice, the approach naturally leads to comparatively large measurement uncertainties due to possible systematic biases and additional uncertainties which result from reassembling the transponder. The following two methods, paradoxically enough, require yet another radiometric reference, typically a conducting, circular, flat plate or a trihedral corner reflector. If the SAR instrument is calibrated with a transponder, and a transponder is calibrated with a corner reflector, one might ask why the satellite is not calibrated with a corner reflector directly, thereby omitting the additional measurement uncertainty introduced by the transponder calibration step.¹

¹This argument, of course, neglects the additional features offered by a transponder over a trihedral corner reflector, including (a) a potentially large RCS despite small device dimensions even for lower frequencies, (b) the possibility to calibrate cross-polarization channels of the SAR instrument, (c) the ability to record the antenna pattern of the SAR instrument, (d) the potential introduction of a range delay, and (e) the opportunity to include real-time signal modification or encoding in the signal path

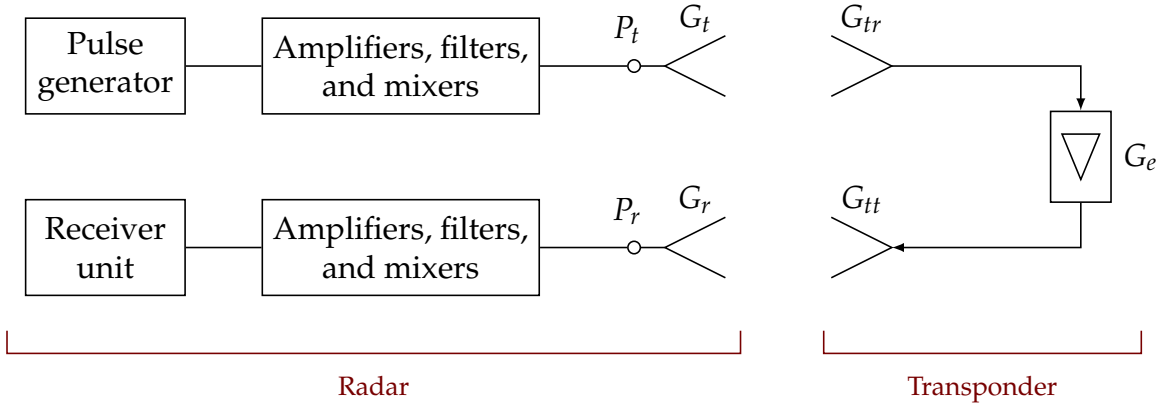


Figure 6.1: Schematic diagrams of a radar and a transponder.

As a fourth calibration approach, this chapter introduces the *three-transponder method* in Sec. 6.3. The method allows to calibrate the frequency and angular dependent RCS of three transponders with unknown RCS without requiring an additional radiometric standard, quite like the three antenna method (see Sec. 6.3.1) allows to determine the antenna gain of three antennas with unknown gain, as long as the distance between them is measured. A realization of such a measurement setup and measurement results are described in Sec. 6.4.

The main advantages of the novel approach are that the transponders are measured in their final configuration (no parts are disassembled for the measurement), and that metrological traceability is established through length measurements, which in practice can be executed with low relative uncertainty. These two elements describe a transponder calibration approach which compares very favorably against the existing three approaches, and in the end can lead to lower overall radiometric uncertainties in calibrated SAR instruments.

6.2 Existing Approaches for Measuring the Transponder RCS

Currently, at least three approaches for calibrating the RCS of transponders (sometimes also called active radar calibrators (ARCs) or polarimetric active radar calibrators (PARCs)) exist. Each approach has a distinct set of advantages and trade-offs, and all of them have been used in the past to characterize transponders for the calibration of SAR systems.

6.2.1 Measuring the Loop Gain

The radar cross section of a transponder can be determined by separately characterizing the gains of the components or component assemblies of a transponder. The necessary relationship between component gains and the transponder RCS ζ_t was derived by

(also see Sec. 2.4.3 for further details on transponders). Nevertheless the argument is applicable if only a very accurate radiometric calibration of the co-polar channel is required.

Brunfeldt and Ulaby [27]. Let the radar and the transponder components be denoted by symbols as shown in Fig. 6.1, then the first step in the derivation is

$$P_{tr} = P_t G_t G_{tr} \left(\frac{\lambda}{4\pi R} \right)^2, \quad (6.1)$$

where P_{tr} is the power received by the transponder, P_t is the transmit power of the radar, G_t is the antenna gain of the radar's transmit antenna, G_{tr} is the antenna gain of the transponder's receive antenna, λ is the wavelength, and R is the distance separating radar and transponder. This equation is also known as Friis transmission formula. The transponder amplifies the received power by G_e so that the transponders's transmit power is

$$P_{tt} = G_e P_{tr}. \quad (6.2)$$

A second application of Friis transmission equation leads to the receive power P_r of the radar:

$$P_r = P_{tt} G_{tt} G_r \left(\frac{\lambda}{4\pi R} \right)^2, \quad (6.3)$$

where G_{tt} is the antenna gain of the transponder's transmit antenna, and G_r is the receive antenna gain of the radar. Combining Eqs. (6.1) and (6.3) leads to the radar equation

$$P_r = \left(\frac{P_t G_t G_r \lambda^2}{(4\pi)^3 R^4} \right) \left(\frac{\lambda^2}{4\pi} G_{tr} G_e G_{tt} \right) = \frac{P_t G_t G_r \lambda^2}{(4\pi R)^2} \zeta_t, \quad (6.4)$$

where

$$\zeta_t = \frac{\lambda^2}{4\pi} G_{tr} G_e G_{tt} \quad (6.5)$$

is the transponder's radar cross section [27].

In practical terms Eq. (6.5) means that the two antenna gains G_{tr} and G_{tt} can be conveniently measured in an antenna measurement test range and the electronic loop gain G_e can be determined by network analyzer measurements in a laboratory. This approach has successfully been used by the author for the calibration of the 18 TerraSAR-X transponders [46] developed and built by the University of Karlsruhe under Lenz [108] and Lenz et al. [109]. The comparatively large radiometric uncertainty of the specified 0.5 dB partly results from the measurement approach itself: Determining the RCS according to Eq. (6.5) requires two antenna gain measurements. Systematic offsets for absolute antenna gain measurements are often in the order of 0.1 dB, but can exceed 0.4 dB between any two measurement chambers as range cross calibration campaigns have shown [58]. This uncertainty has to be accounted for twice (once per antenna) because the two required measurements are correlated.

Therefore, the uncertainty in measuring the antenna gains alone results in total uncertainties which are large in comparison to the uncertainties expected for the two methods described in the following.

6.2.2 The Substitution Method

The second measurement approach is the most common measurement method for determining the RCS of any object: the substitution method. It is made up of the following steps:

1. Using a linear radar, which operates at the desired frequency and emits a stable transmit power P_t .
2. Recording the receive power P_r^{ref} of a target with a known reference radar cross section ζ_{ref} (a measurement standard).
3. Repeating the measurement by substituting the measurement standard with the device under test (DUT) having an unknown RCS ζ_{DUT} and recording the second receive power as P_r^{DUT} .
4. Deriving the RCS of the device under test through proportionality:

$$\zeta_{\text{DUT}} = \frac{P_r^{(\text{DUT})}}{P_r^{(\text{ref})}} \zeta_{\text{ref}}. \quad (6.6)$$

Different realizations of this scheme are possible. The most typical ones depend on (possibly compact) indoor or outdoor measurement ranges [100]. Alternatively, one can also use a SAR instrument to directly measure the transponder's equivalent radar cross section (ERCS), an approach which is described in detail in Chap. 7.

The advantage of the approach is the end-to-end nature of the measurement setup. Ideally, the transponder does not need to be disassembled. A disadvantage is the need for an additional radiometric reference, whose radiometric uncertainty defines a practical lower bound on the transponder calibration uncertainty. Also, outdoor ranges typically suffer from not perfectly controllable conditions leading for instance to multipath effects. Shielded indoor ranges, on the other hand, pose another challenge: A transponder connects a receiving antenna through a high-gain amplifier chain with a transmit antenna. Due to the high sensitivity of the receiver, even small stray (noise) signals are picked up by the transponder and are emitted again amplified. The absorbers of an anechoic chamber can suppress most but not necessarily all of this amplified signal, so that it eventually is received again by the transponder, leading to resonance and saturation of the transponder electronics. During the calibration campaign of DLR's C-band transponders, this problem was solved by introducing a temporary additional attenuator in the transmitter chain, effectively reducing the loop gain by 20 dB to suppress resonance. Consequently, the highly sensitive DLR transponders could not be measured in their final configuration using an indoor compact measurement range.

6.2.3 The Transponder as a Radar Instrument

The third known method for deriving the RCS of a transponder combines ideas from the first two approaches and was introduced for the characterization of the European Remote Sensing Satellite 1 (ERS-1) transponder by Jackson and Woode [89]. If the transponder can be operated as a radar, i. e., if the transponder loop can be opened (see Fig. 6.2), then the measurement of the ratio of the received power over the transmitted power, the knowledge of the RCS of an external reference, and the knowledge of the distance between the reference and the transponder are sufficient to derive the transponder RCS. Assuming a conducting, circular, flat plate with a surface A_p as the radiometric reference, then its RCS ζ_p is approximately given by [100]

$$\zeta_p = \frac{4\pi}{\lambda} A_p^2. \quad (6.7)$$

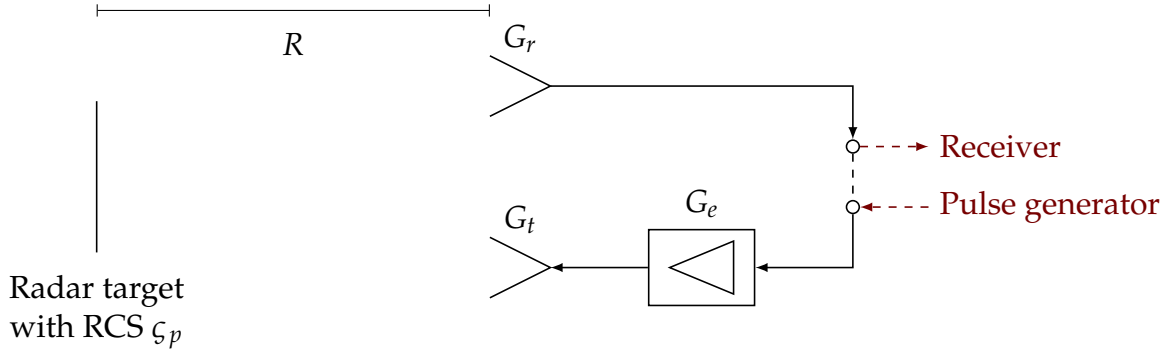


Figure 6.2: Measurement setup for the approach *transponder as a radar instrument*. The shown transponder can also be operated as a radar, i. e., the amplifier loop can be opened.

Now, the radar equation for a transponder being operated as a radar and measuring a target with a radar cross section ς is

$$P_{tr} = \frac{P_{tt} G_{tt} G_{tr} \lambda^2}{(4\pi)^3 R^4} \varsigma. \quad (6.8)$$

The equation can be reformulated by substituting ς with Eq. (6.7) and the factor $G_{tt} G_{tr}$ with $4\pi \varsigma_t / \lambda^2$ from Eq. (6.5) (incorporating G_e into G_{tt} , for instance), leading to

$$\varsigma_t = 4\pi \frac{P_{tr} \lambda^2 R^4}{P_{tt} A_p^2}. \quad (6.9)$$

The advantage of the approach is that the transponder can be measured in its final configuration (provided it was designed for opening the amplification loop), and no additional measurement device like an expensive network analyzer is needed. Some disadvantages arise in practical implementations: The limited transmit/receive decoupling of the transponder antennas typically requires very short pulses or long distances, so that transmission and reception are separated in the time domain. If the reference plate is installed on a remote site (e.g., the roof of a house), then sufficient time-gating in post-processing for background removal is not an option because of the limited bandwidth of most transponders (leading to large time gates). Further problems typically found in other outdoor measurement setups like multipath are similar with respect to the substitution method described above.

6.3 The Three-Transponder Method Principle

In the following, the measurement principle behind the novel three-transponder method (3TM) is introduced. No additional radiometric reference target (e. g. a trihedral reflector with an accurately known RCS) is required for the measurement, eliminating the related RCS knowledge uncertainty, which is often the lower bound for the combined standard uncertainty. The method is an advancement of the well known three antenna method [84], which is used to determine the gains of three unknown antennas. The three antenna method is to-date the most accurate method for determining antenna gains,

down to a reported uncertainty of ± 0.05 dB [106].² The proposed three-transponder method might result in similarly accurate transponder RCS measurements in the future. In the following section, the three antenna method is quickly reviewed, before the equations for the proposed three-transponder method are developed in Sec. 6.3.3. A discussion of the probability distribution function of measurement uncertainties and a recommended point estimator for the transponder RCSs follows in Sections 6.3.4 and 6.3.5.

6.3.1 The Three Antenna Method

The three antenna method is used whenever absolute antenna gains of three unknown antennas A , B , and C need to be measured [84, 188]. The method is based on Friis transmission formula, which describes the power P_r received by a receiving antenna with a gain G_r , depending on the transmitted power P_t emitted by a source connected to an antenna with gain G_t a distance R away

$$\frac{P_r}{P_t} = G_t G_r \left(\frac{\lambda}{4\pi R} \right)^2, \quad (6.10)$$

where λ is the wavelength. If the distance R is known, the ratio P_r/P_t can be measured for all three antenna combinations AB , BC , and AC . Due to assumed reciprocity it does not matter which antenna is the transmitting and which the receiving antenna, respectively.

The three measurements result in a non-linear system of equations. Knowing that each antenna gain is by definition above zero, the non-linear system can be converted to a more convenient linear system of equations by logarithmic transformation. The following set of equations results:

$$(G_A)|_{\text{dB}} + (G_B)|_{\text{dB}} = 10 \log \left(\frac{P_r}{P_t} \right)_{AB} - 20 \log \left(\frac{\lambda}{4\pi R} \right), \quad (6.11a)$$

$$(G_A)|_{\text{dB}} + (G_C)|_{\text{dB}} = 10 \log \left(\frac{P_r}{P_t} \right)_{AC} - 20 \log \left(\frac{\lambda}{4\pi R} \right), \quad (6.11b)$$

$$(G_B)|_{\text{dB}} + (G_C)|_{\text{dB}} = 10 \log \left(\frac{P_r}{P_t} \right)_{BC} - 20 \log \left(\frac{\lambda}{4\pi R} \right). \quad (6.11c)$$

From these three equations and the knowledge of λ and R , the three unknown antenna gains G_A , G_B , and G_C can be determined.

In practice, measurement uncertainties result from a number of sources including proximity (R is too low so that the near field is not sufficiently attenuated) and multipath effects. These effects also have an impact on measurements done in an anechoic chamber. The effects can be mitigated considerably by an extrapolation technique [127], which is also recommended in [84].

For standard gain X-band horns, a remaining gain knowledge uncertainty of 0.11 dB at a confidence level of 99.7% was reported [127]. These results are a good basis for accurate transponder RCS measurements.

²Kummer and Gillespie [106] do not state precisely what they understand by the term *uncertainty*. Considering the publication year 1978, their definition does most likely not coincide with the term *standard uncertainty* [87] used throughout most parts of this work.

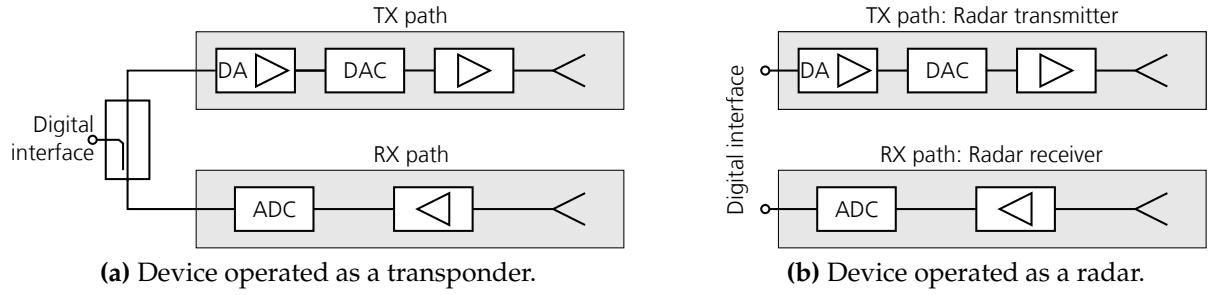


Figure 6.3: Required principal transponder design: An operation as a radar target *and* as a radar instrument are both possible. The digital signal is coupled out and in at the same point; a possible digital amplification (DA) is part of the TX path.

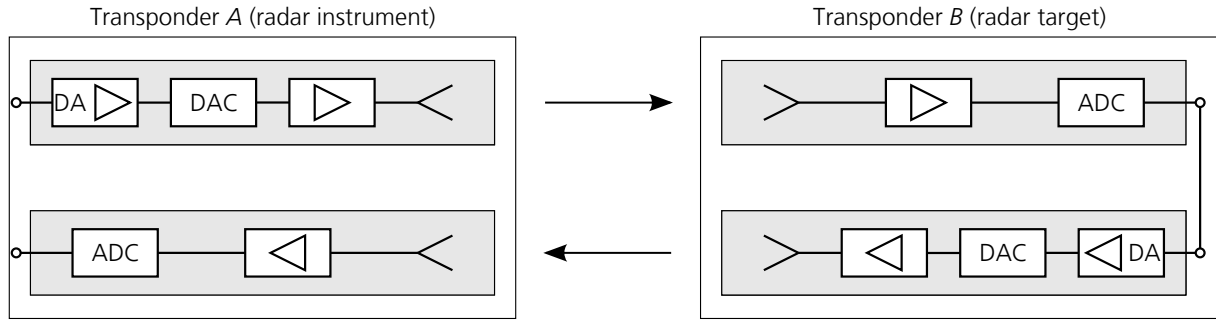


Figure 6.4: The three-transponder method measurement setup: one transponder is operated as a radar, and the other as a transponder.

6.3.2 Prerequisites on Transponder Design

The three-transponder method as described below is only applicable for a certain transponder type. Specifically, two out of three transponders must not only be operable as radar targets *but also* as a radar, i. e., the transponder must be able to emit and record test signals within the transponder bandwidth. One possible implementation is shown in Fig. 6.3 where the transponder's receiving (RX) and transmitting (TX) paths are connected digitally. The three C-band transponders recently developed and built by DLR fulfill this requirement [41].

The (by design exactly known) digital amplification (DA) is permitted to be different from 1.0. For the example shown in Fig. 6.3a, the digital amplification is counted toward the TX path. Here, coupling the digital signals out or in (for transmission or recording) is implemented at the same point in the amplification loop, so that the digital amplification does not need to be treated separately from the radio frequency (RF) amplification.

6.3.3 System of Linear Equations

The three antenna method is based on the threefold application of Friis transmission formula to make three independent gain measurements with three antennas. In contrast, the three-transponder method is based on the threefold application of the radar equation to make three independent RCS measurements of three transponders. Each RCS measurement is performed by one of the three transponders operated as a radar, where the radar target under test is one of the other two transponders operated as a

transponder, see Fig. 6.4.

The first essential equation for the method is once again the radar equation

$$P_r = P_t \frac{G_r G_t \lambda^2 \varsigma}{(4\pi)^3 R^4}. \quad (6.12)$$

The equation describes a radar instrument's received power P_r by an antenna with gain G_r as a function of a target's scattering cross section ς a distance R away, and the radar's power P_t transmitted by an antenna with gain G_t at a wavelength λ .

The second essential equation describes a transponder's radar cross section ς by its loop gain G_l (cf. Eq. (6.5) on p. 95). It is given as [27]

$$\varsigma = \frac{\lambda^2}{4\pi} G_l, \quad (6.13)$$

where the total loop gain is usually given as $G_l = G_t G_e G_r$, i. e., the multiplication of the transponder's transmitting and receiving antenna gains and the electronic amplification G_e . In the nomenclature of Fig. 6.3a, this can be expressed as

$$\varsigma = \frac{\lambda^2}{4\pi} G_{tx} G_{rx}, \quad (6.14)$$

where G_{rx} and G_{tx} are the gains of the RX and TX paths (including the digital amplification, analog-to-digital converter (ADC), and digital-to-analog converter (DAC)). The gains of the TX and RX paths are a combination of electronic amplifications and antenna gains.

The two equations (6.12) and (6.13) can be combined into one. Assuming that transponder A is operated as a radar and transponder B as a radar target (abbreviated as combination AB), it follows that

$$\left. \frac{P_r}{P_t} \right|_A = \frac{\lambda^2}{(4\pi)^3 R^4} \cdot \frac{4\pi}{\lambda^2} \cdot \varsigma_A \cdot \varsigma_B. \quad (6.15)$$

By exchanging the transponders, two more equations for the combinations AC and BC can be derived.

The resulting three equations can be converted to a linear set of equations by logarithmic transformation. This is possible because all terms are larger than zero. For convenience the same symbols are used for the transponder RCS, but it is understood that they refer to values expressed in decibel, i. e., after the transformation $10 \log(\cdot)$. Hence, Eq. (6.15) can be expressed as³

$$\varsigma_X + \varsigma_Y = P_{XY} + C, \quad (6.16)$$

with P_{XY} being the ratio $10 \log(P_r/P_t)$ measured by device X and using device Y as the radar target. All known terms are summarized in

$$C = 20 \log(4\pi R^2). \quad (6.17)$$

³For brevity, a normalization cross section $\varsigma_0 = 1 \text{ m}^2$, which is required to convert values with dimension $[\text{m}^2]$ to dimensionless values before taking the logarithm, was omitted. In logarithmic form, the RCS ς is then given as dBm^2 .

The linear set of equations can now be expressed in matrix form

$$\begin{pmatrix} 1 & 1 & 0 \\ 1 & 0 & 1 \\ 0 & 1 & 1 \end{pmatrix} \begin{pmatrix} \zeta_A \\ \zeta_B \\ \zeta_C \end{pmatrix} = \begin{pmatrix} P_{AB} \\ P_{AC} \\ P_{BC} \end{pmatrix} + C. \quad (6.18)$$

Inverting the matrix yields the three unknown transponder cross sections

$$\begin{pmatrix} \zeta_A \\ \zeta_B \\ \zeta_C \end{pmatrix} = \frac{1}{2} \begin{pmatrix} 1 & 1 & -1 \\ 1 & -1 & 1 \\ -1 & 1 & 1 \end{pmatrix} \begin{pmatrix} P_{AB} + C \\ P_{AC} + C \\ P_{BC} + C \end{pmatrix}. \quad (6.19)$$

In summary, the three unknown transponder radar cross sections are determined by completing three measurements with different pairs of transponders, where one transponder is operated as a radar during each measurement. Each measurement is performed at a single frequency (using a sine tone). The measurements can be repeated in a stepped frequency fashion in order to determine the frequency dependent transponder RCS within the transponder bandwidth.

It is interesting to note that only a length measurement (R in Eq. (6.17)) needs to be traced back to a national standard in order to establish calibration traceability.

It is not important which transponder is operated as a target and which one as a radar within each of the three measurement combinations. In a set of measurements AB , AC , BC only the two transponders A and B need to be operated as radars, and only transponders B and C need to be operated as transponders. Therefore, only transponder B needs to be operated as a radar *and* a transponder during the measurement campaign, relaxing the hardware requirements for devices A and C .

If the RCS of more than three transponders shall be determined, more transponder measurement combinations are possible according to

$$\binom{n}{2} = \frac{n!}{2(n-2)!} \quad (6.20)$$

where n is the number of transponders. For a set of four transponders, a total of six transponder combinations become possible, resulting in six distinct measurements. The resulting matrix similar to Eq. (6.18) then has a shape of 6×4 ; the linear system of equations is overdetermined. This property might be exploited in a probabilistic sense in order to derive the most probable set of radar cross sections when measurement uncertainty is considered. It can be noted though that for each additional transponder, one additional measurement is sufficient. This is because the RCS' of the first three transponders were determined with Eq. (6.19), and the RCS of each additional transponder can then directly be determined through Eq. (6.15). Every additional device also only needs to be operable as a transponder, i. e., not as a radar.

6.3.4 Random Variables, 3TM Equations, and GUM

The 3TM system of equations (6.19) yields transponder RCSs after only three power-ratio measurements in the form of

$$\left. \frac{P_r}{P_t} \right|_X = \tilde{P}_X. \quad (6.21)$$

The tilde symbol \sim signifies that \tilde{P}_X is a linear power ratio, i. e., before applying the transformation $10 \log(\cdot)$. If no measurement errors occur, e. g. due to noise, three measurements are sufficient. In practice, one has to expect measurement noise, and an actual observation x is composed as

$$\tilde{x} = \tilde{P}_X + e, \quad (6.22)$$

where e is a measurement error.

Not least because of the central limit theorem, the error e shall be assumed to come from a normal distribution with zero mean and standard deviation σ , i. e.,

$$e \sim N(0, \sigma^2).$$

As it is described in Sec. 2.2.2, modeling measurement uncertainties as normal distributions is the default choice in the norm *Evaluation of measurement data – Guide to the Expression of Uncertainty in Measurement* [87] (GUM), which shall be applied later on to derive the uncertainty of the derived transponder RCSs. Furthermore, it is assumed that e can be modeled to stem from the same distribution for all measurements, an assumption which well fits the case where transponders of the same type are characterized with a single measurement setup.

Now e is only the error in measuring the three linear power ratios \tilde{P}_A , \tilde{P}_B , and \tilde{P}_C . In the remainder of this section it shall be analyzed how the 3TM equations (6.19) affect the distribution, and if the uncertainties in the transponder RCSs ζ_A , ζ_B , and ζ_C can still be modeled as samples from a normal distribution. This is a prerequisite for applying the GUM.

To go from the measured power ratios \tilde{P}_A , \tilde{P}_B , and \tilde{P}_C to the transponder RCSs ζ_A , ζ_B , and ζ_C according to Eq. (6.19), three algorithmic transformations are necessary:

1. Function application: $10 \log(\tilde{P}_X)$.
2. Summation and subtraction of random variables.
3. Multiplication of random variables.

These three steps are examined in App. B, and the results are used in the following.

Approximate Distribution and Moments for ζ due to 3TM Equations

The intermediate results from App. B for function application, summation, and multiplication concerning random variables can now be combined to derive approximate first and second moments for the transponder RCS ζ_X . The second moment is of special importance with respect to an uncertainty analysis according to GUM, where standard uncertainties are expressed as standard deviations.

The three-transponder method equations (6.19) all have the same form according to

$$\zeta_X = \frac{1}{2}(P_{XY} + P_{XZ} - P_{YZ} + C) \quad (6.23)$$

where ζ_X , P_{XY} , P_{XZ} , and P_{YZ} are considered to be random variables after the logarithmic transformation $10 \log(\cdot)$. C from Eq. (6.17) is assumed to be constant. Approximations for the first and second moments of the random variable ζ_X result from three algebraic steps:

1. Applying function $g(X)$ from Eq. (B.2), leading to Eqs. (B.12) and (B.19).
2. Summation and subtraction of random variables, see Eqs. (B.43) and (B.45).
3. Multiplication of a random variable, see Eqs. (B.50) and (B.52).

In the second step, a further approximation can be introduced for convenience. The intermediate mean μ_2 of the second step is

$$\begin{aligned}\mu_2 &\approx 10 \log \left(\frac{\tilde{\mu}_{XY} \tilde{\mu}_{XZ}}{\tilde{\mu}_{YZ}} \right) - \frac{5\tilde{\sigma}_{XY}^2}{\ln(10)\tilde{\mu}_{XY}^2} - \frac{5\tilde{\sigma}_{XZ}^2}{\ln(10)\tilde{\mu}_{XZ}^2} + \frac{5\tilde{\sigma}_{YZ}^2}{\ln(10)\tilde{\mu}_{YZ}^2} + C \\ &\approx 10 \log \left(\frac{\tilde{\mu}_{XY} \tilde{\mu}_{XZ}}{\tilde{\mu}_{YZ}} \right) - \frac{5\tilde{\sigma}^2}{\ln(10)\tilde{\mu}^2} + C.\end{aligned}\quad (6.24)$$

A tilde symbol \sim over a variable marks variables in the linear domain (not expressed in decibels). The term after the second approximation symbol results from the approximation

$$\tilde{\mu}_{XY} \approx \tilde{\mu}_{XZ} \approx \tilde{\mu}_{YZ} \approx \tilde{\mu}$$

for small second order terms, which is valid if all three transponders are identically built and are expected to have a nearly identical RCS. Similarly, the approximation

$$\tilde{\sigma}_{XY} \approx \tilde{\sigma}_{XZ} \approx \tilde{\sigma}_{YZ} \approx \tilde{\sigma}$$

is valid if uncertainties in the measurements of the power ratios P_r/P_t (e. g. due to noise) are nearly identical for all three transponder measurement pairs.

With the same reasoning, an approximate expression can be derived for the intermediate variance σ_2^2 of the second step so that

$$\begin{aligned}\sigma_2^2 &= \left(\frac{10\tilde{\sigma}_{XY}}{\ln(10)\tilde{\mu}_{XY}} \right)^2 + \left(\frac{10\tilde{\sigma}_{XZ}}{\ln(10)\tilde{\mu}_{XZ}} \right)^2 + \left(\frac{10\tilde{\sigma}_{YZ}}{\ln(10)\tilde{\mu}_{YZ}} \right)^2 \\ &\approx \frac{300\tilde{\sigma}^2}{\ln(20)\tilde{\mu}^2}.\end{aligned}\quad (6.25)$$

Finally, after applying multiplication according to the third step, one yields the following expressions for the mean μ_ζ and variance σ_ζ of ζ_X :

$$\mu_\zeta \approx 5 \log \left(\frac{\tilde{\mu}_{XY} \tilde{\mu}_{XZ}}{\tilde{\mu}_{YZ}} \right) - \frac{5\sigma^2}{2\ln(10)\mu^2} + C, \quad (6.26)$$

$$\sigma_\zeta^2 \approx \frac{75\tilde{\sigma}^2}{\ln(20)\tilde{\mu}^2}. \quad (6.27)$$

This approximate analytical result can be validated through a Monte Carlo simulation. As above, the following values shall be chosen for the first and second moments of the measured power ratios P_r/P_t :

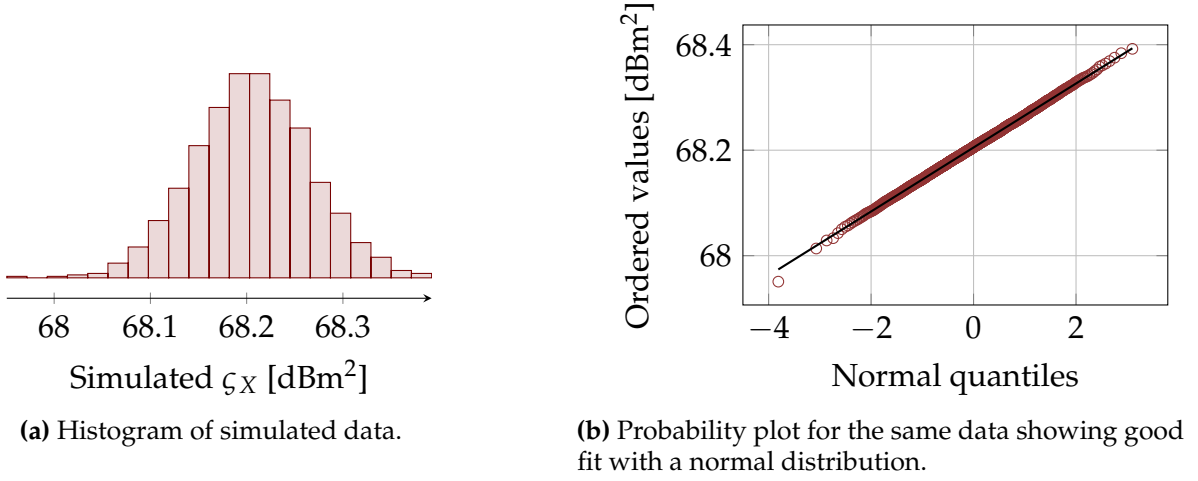
$$\tilde{\mu} = 260^2 = 67\,600, \quad (6.28)$$

$$\tilde{\sigma} = 1081 \quad (\text{equivalent to } 0.07 \text{ dB at } \tilde{\mu}). \quad (6.29)$$

A comparison of values derived analytically and through simulation is given in Tab. 6.1. The histogram and the probability plot of the simulated data in Fig. 6.5 confirm that

Table 6.1: Comparison of approximate analytical results (Eqs. (6.26) and (6.27)) and results from Monte Carlo simulation (also see Fig. 6.5).

Method	μ_ζ in dB	σ_ζ in dB
Analytical approximation	68.21	0.08
Monte Carlo simulation	68.21	0.06

**Figure 6.5:** 1000 simulated samples for ζ_X after application of the three-transponder method equation (6.19) including $10 \log(\cdot)$ transformation.

the original normal distribution for P_r/P_t remains approximately normal even after application of the three-transponder method equations (6.19). The result is important because it allows to directly apply GUM principles for uncertainty analysis of ζ_X . In the GUM, measurement samples are most often assumed to be independently drawn from a Gaussian distribution, and hence this result will be exploited in the following.

6.3.5 The Maximum-Likelihood versus the James-Stein Estimator

The result of the 3TM equation (6.19) leads to a vector of three observations

$$\mathbf{X} = (x_A, x_B, x_C)^T.$$

If no measurement errors existed, one could write

$$\mathbf{X} = \boldsymbol{\zeta} = (\zeta_A, \zeta_B, \zeta_C)^T.$$

The observation would directly lead to the transponder RCSs. Measurement uncertainties though cannot be avoided in practice, so the observation vector \mathbf{X} can actually be written as

$$\mathbf{X} \sim N_p(\boldsymbol{\zeta}, \sigma^2 \mathbf{I}) \quad \text{with } p = 3 \quad (6.30)$$

or

$$X_i \sim \zeta_i + \sigma z_i \quad \text{with } z_i \sim N(0, 1), i = 1 \dots p. \quad (6.31)$$

Here the result from the previous section is exploited, i. e., the uncertainties are modeled as being independently drawn from an identical normal distribution with standard

deviation σ . Considering the noisy observations leads to the central question for this section: What is a good estimator for ζ given observation \mathbf{X} ?

The most intuitive estimator is

$$\hat{\zeta}^{\text{ML}}(\mathbf{X}) = \mathbf{X}, \quad (6.32)$$

i. e., the actual noisy observation is taken as the estimate. An estimate for ζ_A , for instance, does not depend on observations x_B or x_C ; the estimates are independent. This unbiased estimator is also known as the maximum likelihood (ML) estimator [76]. Note that several observations \mathbf{X} can be summarized through averaging per component of \mathbf{X} to once again yield a single observation vector \mathbf{X} , so having several observations results in the same estimation problem.

In an influential publication, Stein [182] showed in 1956 that contrary to common believe at that time the sample mean is not the best estimator if three or more parameters ($p \geq 3$) are estimated simultaneously. Stein's finding is now often called *Stein's paradox* or *Stein's phenomenon* [30, 157]. In 1961, James and Stein [91] showed that the biased estimator

$$\hat{\zeta}^{\text{JS}}(\mathbf{X}) = \left(1 - \frac{p-2}{\|\mathbf{X}\|^2}\right) \mathbf{X} \quad (6.33)$$

for $\sigma = 1$ actually has a lower average mean-squared error than the ML estimator. The estimator (6.33) is now often called James-Stein (JS) estimator.

The JS estimator is a shrinkage estimator which shrinks the observation vector \mathbf{X} toward zero. As will be shown below, the biggest estimator improvement in comparison to the ML estimator can be observed when $\|\mathbf{X}\|$ is close to zero. The estimator can be generalized to shrink toward any value ζ_0 so that [133, 157]

$$\hat{\zeta}_{\zeta_0}^{\text{JS}}(\mathbf{X}) = \zeta_0 \left(1 - \frac{p-2}{\|\mathbf{X} - \zeta_0\|^2}\right) (\mathbf{X} - \zeta_0). \quad (6.34)$$

This estimator $\hat{\zeta}_{\zeta_0}^{\text{JS}}$ should be used over $\hat{\zeta}^{\text{JS}}$ whenever an approximate sample mean is already known.

The estimator can be further generalized to cases where $\sigma \neq 1$ by exploiting the fact that normal random variables $X \sim N(\mu, \sigma^2)$ can be expressed as a standard normal variable $\tilde{X} \sim N(0, 1)$ through the scaling [154]

$$\tilde{X} = \frac{X - \mu}{\sigma}. \quad (6.35)$$

By applying this scaling, one yields the general JS estimator [55]

$$\hat{\zeta}_{\zeta_0}^{\text{JS}}(\mathbf{X}) = \zeta_0 \left(1 - \frac{\sigma^2(p-2)}{\|\mathbf{X} - \zeta_0\|^2}\right) (\mathbf{X} - \zeta_0). \quad (6.36)$$

In the 3TM, three or more normally distributed parameters, i. e., three or more transponder RCSs are estimated, so Stein's phenomenon applies. In a typical scenario, three transponders are built and calibrated with the 3TM. Afterward, all three transponders are used for the calibration of a SAR instrument. In this context, it can be argued that it is advantageous to reduce transponder calibration errors on average by permitting biased transponder RCS estimators, thereby reducing the overall SAR instrument calibration error which itself incorporates all calibrated transponders.

Furthermore it can be assumed that approximate transponder RCSs are known from Eq. (6.5) prior to conducting the 3TM measurements because network analyzer and antenna gain measurements are certainly being conducted in any transponder development effort. Hence estimator $\hat{\zeta}_{\zeta_0}^{\text{JS}}$ in Eq. (6.36) is particularly relevant for the 3TM.

In the remainder of this section, the risks of the maximum-likelihood and the James-Stein estimators shall be compared, first in general, and then specifically with respect to the three-transponder method. The goal is to devise a suitable estimator for the 3TM.

Risk of the Maximum Likelihood Estimator

As a metric for comparing different estimators, one typically defines a loss function L , and considers its expectation. This expectation of the loss function is called the risk function R , which is given as

$$R(\hat{\zeta}, \zeta) = E_{\zeta}[L(\hat{\zeta}, \zeta)], \quad (6.37)$$

where $\hat{\zeta}$ is a point estimator of ζ . An estimator with a lower risk, i. e., an estimator with a lower expected or average loss is considered better than an estimator with a higher risk.

The “most popular” [88] loss function is the squared error loss function

$$L(\hat{\zeta}, \zeta) = \|\hat{\zeta} - \zeta\|^2, \quad (6.38)$$

where $\|\cdot\|$ is the Euclidean norm. The expectation of this loss function is often also called the mean squared error (MSE).

The expected loss or risk function for the maximum-likelihood estimator is [91]

$$\begin{aligned} R(\hat{\zeta}, \zeta) &= E[\|\mathbf{X} - \zeta\|^2] = E\left[\sum_{i=1}^p (X_i - \zeta_i)^2\right] \\ &= E\left[\sum_{i=1}^p (\zeta_i + \sigma z_i - \zeta_i)^2\right] = \sigma^2 E\left[\sum_{i=1}^p z_i^2\right] \\ &= p\sigma^2, \end{aligned} \quad (6.39)$$

where Eq. (6.31) was exploited.

Risk of the James-Stein Estimator

The risk of the James-Stein estimator $\hat{\zeta}^{\text{JS}}$ for a normalized standard deviation $\sigma = 1$ is derived in [79, 183]. Here the risk for estimator $\hat{\zeta}_{\zeta_0}^{\text{JS}}$ which shrinks toward ζ_0 shall be derived, again with $\sigma = 1$. The goal is to show that the risk of the JS estimator is smaller than risk for the ML estimator, see Eq. (6.39).

The estimator $\hat{\zeta}_{\zeta_0}^{\text{JS}}$ from Eq. (6.34) can be written as

$$\hat{\zeta}_{\zeta_0}^{\text{JS}} = \mathbf{X} - \frac{p-2}{\|\mathbf{X} - \zeta_0\|^2}(\mathbf{X} - \zeta_0) = \mathbf{X} - g(\mathbf{X}) \quad (6.40)$$

with

$$g(\mathbf{X}) = \frac{p-2}{\|\mathbf{X} - \zeta_0\|^2}(\mathbf{X} - \zeta_0). \quad (6.41)$$

From Eq. (6.37), the risk of this estimator is

$$\begin{aligned} R(\hat{\boldsymbol{\varsigma}}_{\boldsymbol{\varsigma}_0}^{\text{JS}}, \boldsymbol{\varsigma}) &= \mathbb{E}[\|\mathbf{X} - g(\mathbf{X}) - \boldsymbol{\varsigma}\|^2] \\ &= \mathbb{E}[(\mathbf{X} - g(\mathbf{X}) - \boldsymbol{\varsigma})^2] \\ &= \mathbb{E}[\|\mathbf{X} - \boldsymbol{\varsigma}\|^2] + \mathbb{E}[\|g(\mathbf{X})\|^2] - 2\mathbb{E}[g(\mathbf{X})(\mathbf{X} - \boldsymbol{\varsigma})]. \end{aligned} \quad (6.42)$$

The first summand is p , see Eq. (6.39). The second summand is

$$\mathbb{E}[\|g(\mathbf{X})\|^2] = (p-2)^2 \mathbb{E}[1/(\mathbf{X} - \boldsymbol{\varsigma})^2]. \quad (6.43)$$

In order to evaluate the third term in Eq. (6.42), one can exploit the multivariate *Stein's identity* [79, 183]

$$\mathbb{E}[g(\mathbf{X}) \cdot (\mathbf{X} - \boldsymbol{\varsigma})] = \sigma^2 \mathbb{E}[\nabla \cdot g(\mathbf{X})] \quad (6.44)$$

for a multivariate, normally distributed random variable $\mathbf{X} \sim \mathcal{N}_p(\boldsymbol{\varsigma}, \sigma^2 \mathbf{I})$, with

$$\nabla \cdot g(\mathbf{X}) = \sum_{i=1}^p \frac{\partial g(\mathbf{X})}{\partial X_i} \quad (6.45)$$

and given that $\mathbb{E}[\nabla \cdot g(\mathbf{X})]$ exists. The divergence of $g(\mathbf{X})$ is (with the quotient rule)

$$\begin{aligned} \nabla \cdot g(\mathbf{X}) &= (p-2) \sum_{i=1}^p \frac{(\mathbf{X} - \boldsymbol{\varsigma}_0)(\mathbf{X} - \boldsymbol{\varsigma}_0) - 2(X_i - \varsigma_{0,i})^2}{[(\mathbf{X} - \boldsymbol{\varsigma}_0)(\mathbf{X} - \boldsymbol{\varsigma}_0)]^2} \\ &= (p-2) \frac{p(\mathbf{X} - \boldsymbol{\varsigma}_0)^2 - 2(\mathbf{X} - \boldsymbol{\varsigma}_0)^2}{[(\mathbf{X} - \boldsymbol{\varsigma}_0)(\mathbf{X} - \boldsymbol{\varsigma}_0)]^2} \\ &= \frac{(p-2)^2}{\|\mathbf{X} - \boldsymbol{\varsigma}_0\|^2}. \end{aligned} \quad (6.46)$$

Combining Eq. (6.46) with (6.44), one yields an expression for the third term in Eq. (6.42)

$$-2\mathbb{E}[g(\mathbf{X})(\mathbf{X} - \boldsymbol{\varsigma})] = -2(p-2) \mathbb{E}[1/\|\mathbf{X} - \boldsymbol{\varsigma}_0\|^2], \quad (6.47)$$

with $\sigma = 1$. Comparing expression (6.47) with (6.43) one recognizes that one is a multiple of the other. The risk of the JS estimator can now be written as

$$R(\hat{\boldsymbol{\varsigma}}_{\boldsymbol{\varsigma}_0}^{\text{JS}}, \boldsymbol{\varsigma}) = p - (p-2)^2 \frac{1}{\mathbb{E}[\|\mathbf{X} - \boldsymbol{\varsigma}\|^2]}. \quad (6.48)$$

In order to simplify the expression, an upper bound for the risk can be found [28]. First, the expectation in Eq. (6.48) can be written with Eq. (6.31) so that

$$\mathbb{E}[\|\mathbf{X} - \boldsymbol{\varsigma}_0\|^2] = \mathbb{E}\left[\sum_{i=1}^p (X_i - \varsigma_{0,i})^2\right] = \mathbb{E}\left[\sum_{i=1}^p ((\varsigma_i - \varsigma_{0,i}) + \sigma z_i)^2\right]. \quad (6.49)$$

Exploiting the definition of variance [76]

$$\mathbb{V}[X] = \mathbb{E}[X^2] - (\mathbb{E}[X])^2 \quad (6.50)$$

and noting again that the mean of z_i is zero, one can write Eq. (6.49) as

$$\begin{aligned} \mathbb{E}[\|\mathbf{X} - \boldsymbol{\varsigma}_0\|^2] &= \sum_{i=1}^p [(\varsigma_i - \varsigma_{0,i})^2 + \sigma^2] = \|\boldsymbol{\varsigma} - \boldsymbol{\varsigma}_0\|^2 + p\sigma^2 \\ &\geq \|\boldsymbol{\varsigma} - \boldsymbol{\varsigma}_0\|^2 + (p-2)\sigma^2. \end{aligned} \quad (6.51)$$

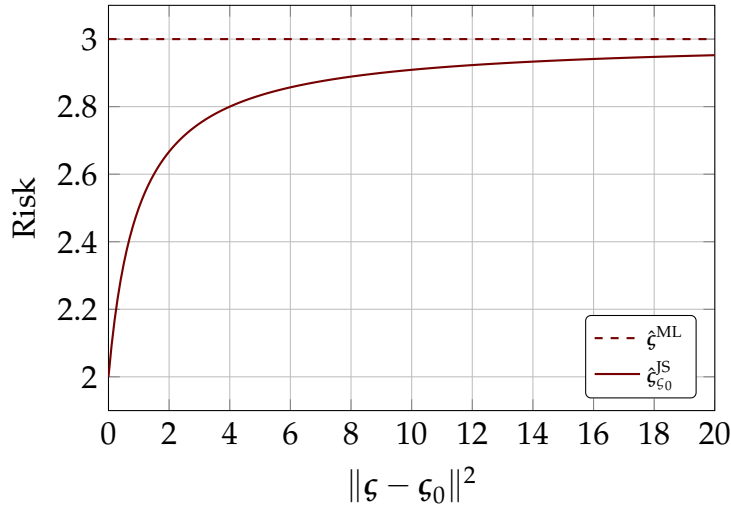


Figure 6.6: Comparison of the risks of the maximum likelihood estimator $\hat{\varsigma}^{\text{ML}}$ and the James-Stein estimator $\hat{\varsigma}_{\varsigma_0}^{\text{JS}}$ for $p = 3$.

For $\sigma = 1$, the upper bound of the risk of the JS estimator in Eq. (6.48) is then

$$R(\hat{\varsigma}_{\varsigma_0}^{\text{JS}}, \varsigma) \leq p - \frac{p-2}{1 + \frac{\|\varsigma - \varsigma_0\|^2}{p-2}}. \quad (6.52)$$

This shows that the risk of the James-Stein estimator is indeed always smaller than the risk of the maximum likelihood estimator, see Eq. (6.39). Two special cases can be pointed out: First, as $\|\varsigma - \varsigma_0\|^2$ approaches infinity, the risk of the JS estimator approaches the risk of the ML estimator. Second, the risk of the JS estimator is minimal if ς_0 coincides with ς , the expectation of \mathbf{X} . In this case, the risk does not exceed 2. Especially for cases where p is large, the risk of the JS estimator is therefore significantly lower than the risk of the ML estimator.

A graphical representation of the ML and JS estimator risks is shown in Fig. 6.6, here for the case which is especially relevant to the three-transponder method, i. e., with $p = 3$.

Comparison of the ML and JS Estimators for the Three-Transponder Method Case

In the previous sections it was shown that the biased James-Stein shrinkage estimator leads to lower risks than the unbiased maximum likelihood estimator. In this section, an empirical example based on Monte Carlo simulations shall demonstrate the average difference between transponder RCSs estimated with the ML estimator, and transponder RCSs estimated with the JS estimator. The goal is to show how large the differences are in practice. With this in mind, the simulation parameters shall be based on realistic values which were encountered during the demonstration measurement campaign (to be described in Sec. 6.4).

The Monte Carlo simulation consists of the following steps:

1. Draw three random power ratios P_r/P_t (linear domain) from the normal distribution $N(260^2, \sigma^2)$. The three power ratios represent the measurement results for the three 3TM measurement triplets. σ represents the standard deviation, i. e., the standard measurement uncertainty according to the GUM. Three values for σ

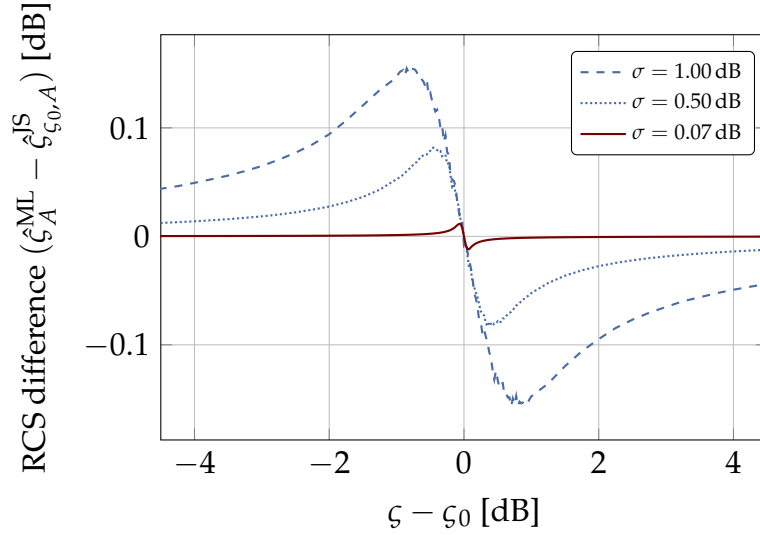


Figure 6.7: Monte Carlo simulation results: Comparison of RCS of transponder *A* derived with maximum likelihood (ML) and James-Stein (JS) estimators, depending on the accuracy of the *a priori* knowledge ξ_0 of the true transponder RCS ξ .

shall be distinguished in separate simulation runs: 0.07 dB (realistic value from demonstration campaign), 0.5 dB, and 1.0 dB (for comparison).

2. Compute transponder RCSs according to the 3TM system of equations (6.19). This step includes logarithmic transformation, summation, and multiplication of the random variables.
3. Estimate transponder RCSs with ML estimator $\hat{\xi}^{\text{ML}}$ from Eq. (6.32) and JS estimator $\hat{\xi}_{\xi_0}^{\text{JS}}$ from Eq. (6.36). Consider different offsets ξ_0 for the JS estimator.
4. Compute the difference $\hat{\xi}^{\text{ML}} - \hat{\xi}_{\xi_0}^{\text{JS}}$.

The Monte Carlo simulation results (first vector component of mean of $(\hat{\xi}^{\text{ML}} - \hat{\xi}_{\xi_0}^{\text{JS}})$ after 10 000 simulation runs) are shown in Fig. 6.7. It can be seen that the difference between the two estimators never exceeds 0.01 dB for the realistic case where the standard uncertainty is $\sigma = 0.07$ dB. In most cases, where the prior transponder RCS knowledge ξ_0 is only accurate to about 1 dB, the difference is considerably less. In other words, the shrinkage factor in the JS estimator in Eq. (6.36) is nearly 1 if the standard deviation σ is small. Consequently, there is only a negligible difference between the JS and the ML estimators in practice.

The situation changes when the standard deviation σ increases, e. g. to 1 dB as shown in Fig. 6.7. Now the differences between the estimators can increase to about 0.15 dB, a relevant figure with respect to targeted transponder calibration uncertainties in the order of 0.1 dB. Nevertheless, a large standard deviation in the measured power ratios P_r/P_t can be reduced further by repeating the measurements and taking an average. Depending on the number of repetitions, the so reduced standard deviation can again be 0.07 dB or below.

In summary, it is important to distinguish between the estimation of a single and three or more parameters. It could be shown that the James-Stein estimator leads to lower

Table 6.2: Mapping between transponder device names and symbols as used in Eq. (6.19) for the 3TM, and additional attenuators used during the campaign.

Device name	3TM letter	Attenuator [dB]
Kalibri 1	C	21.87
Kalibri 2	A	21.99
Kalibri 3	B	22.11

risks, but that the differences between the maximum likelihood and the James-Stein estimator are negligible in practice for the three-transponder method. Consequently, the far more commonly used and understood unbiased maximum likelihood estimator is recommended for estimating transponder RCSs from noisy observations. This conclusion is applied in the demonstration measurement campaign, which is described in the following.

6.4 Demonstration Measurement Campaign with DLR's C-Band Transponders

The first demonstration of the novel method described before was set up to calibrate the frequency-dependent RCS of DLR's new three C-band Kalibri transponders⁴. The Kalibri transponders down-convert and digitize the incoming signal for an adaptable delay and real-time signal filtering before the regenerated signal is up-converted, amplified, and retransmitted again. The transponder design with a digitizing unit in the signal path makes them an ideal fit for the demonstration of the three-transponder method.

The transponder RCS measurement campaign was completed within two weeks in December 2013. An appropriate outdoor measurement range for the demonstration campaign did not exist at DLR so that an *ad hoc* measurement range needed to be set up. During measurements, two transponders were placed in the far-field of each other on the roofs of adjacent buildings, which reduced multipath contributions considerably. Although the *ad hoc* range worked very well for the first demonstration of the three-transponder method, future and more accurate measurements would require a dedicated antenna measurement range with improved multipath suppression.

Although the overall concept and the organization of the campaign stemmed from the author, the actual campaign activities were supported by several DLR colleagues (all coauthors of [44]) without whose input the work could not have been completed. The final data analysis was again performed by the author alone.

6.4.1 Measurement Setup

The three-transponder method procedure requires three transponders to be measured against each other with at least three measurements. As above, the three pairs of mea-

⁴These transponders were developed at DLR for the calibration of the Sentinel-1A satellite from the European Space Agency (ESA) [41, 160, 165]. Further details on the transponders are given in Sec. 2.4.3.

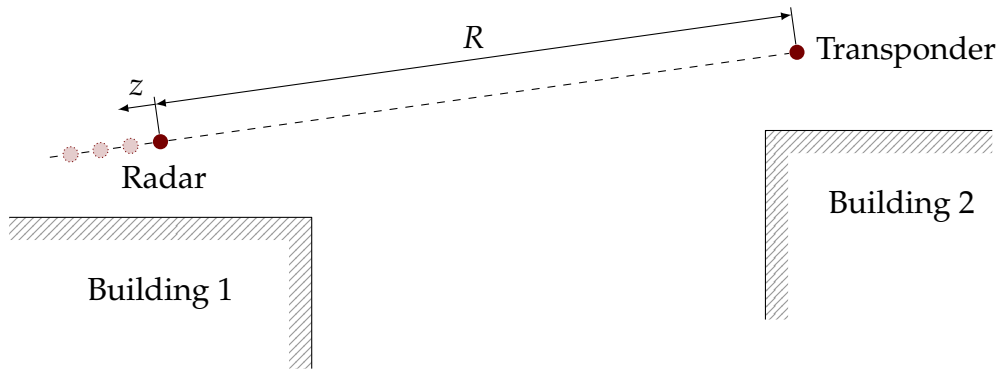


Figure 6.8: Side view of the measurement setup with two transponders installed on the roofs of two adjacent buildings. The red circles denote the transponder antenna phase centers. Dotted and shaded circles indicate additional slide positions for the transponder on the first building.

measurements are denoted with AB , AC , and BC , where the mapping between the actual transponder and the letter is shown in Tab. 6.2.

The goal of the three-transponder method is to derive the frequency dependent RCS of all three transponders. The RCS is only meaningfully defined for the far field. With a maximum antenna dimension D , the far-field region is commonly defined for distances R fulfilling

$$R > \frac{2D^2}{\lambda}, \quad (6.53)$$

where λ is the wavelength [186, 188]. Here, transponders with two antennas are used, where each antenna aperture has a diameter of about 20 cm, and the antenna feeds are separated by about 40 cm. Therefore, with a D of 60 cm and a wavelength at C-band of 5.6 cm, the far field approximately begins 13 m away from the transponders.

An *ad hoc* far-field range was installed at the DLR site in Oberpfaffenhofen which fulfills the far-field requirement. The transponders were installed about 45 m apart on the roofs of two adjacent buildings, see Fig. 6.8. The elevated position attenuates possible multipath contributions from the ground due to the longer path lengths. The transponder on the second building was installed on a Kalibri elevation-over-azimuth, remote-controlled positioner unit, facilitating easy alignment of the transponder along the line-of-sight. The second transponder on building 1 was mounted on a custom-built motorized slide, which itself was accurately aligned with the line-of-sight between the two transponders. The slide axis allows to repeat measurements at varying transponder-to-transponder distances to detect a possible standing wave due to multipath effects. The maximum traversing range of the slide is 95 cm.

All RCS measurements reported here were performed in main beam direction of the transponders. All antennas were rotated by $\pm 45^\circ$ with respect to the vertical. The transmitting antenna of one transponder was always co-polar aligned with the receiving antenna of the other transponder.

The transponders' main beam directions were accurately aligned by night using a laser and mirrors mounted on the transponder structures between the transponder antennas. The approach is described in detail in [140]. The distance $R = 46.0$ m at a slide position of $z = 0$ cm was measured with a tachymeter [140], whose recent calibration can be

traced back to national standards.

All three-transponder method measurements were performed in an automated fashion, which required modification of the transponder software *kaliserve*⁵. Generally, the transponder on building 1 was operated as the radar device (transmitting a programmed signal, and subsequently recording it again), and the transponder on the second building as the transponder device (delayed retransmission of the received signal). In order to reduce multipath effects, the timing of the transmit signal and the delay of the second transponder was finely tuned to exclude most multipath effects. The transmit signal consisted of 1001 short ($0.25\ \mu\text{s}$ long) continuous wave (CW) pulses interrupted by $1.35\ \mu\text{s}$ pulse pauses, covering the complete 100 MHz wide transponder bandwidth. A pulse length of below $0.3\ \mu\text{s}$ at a two-way distance between the buildings of about 90 m ensured that strong reflections from the facade of the second building are filtered out in time domain. In order to decouple transmission and reception for the first transponder, the programmable delay for the second transponder was set to $1.2\ \mu\text{s}$.

The amplitude of the transmit signal, generated by an ADC, was programmed to a digital code of 368 (out of 511). This ensured that the transponders were measured at the same operating point which is expected during later satellite overpasses.

The loop gain of the transponders needed to be reduced for the measurement campaign because the short distance between the transponders and the large transponder output power would drive the receiving chain into saturation. Each measured transponder was therefore fitted with an additional fixed attenuator, which was inserted into the transponder loop just before the transmit antenna so that the gain stabilization loop was not affected. The required attenuation was about 22 dB; accurately measured attenuations for each of the three attenuators, as measured with three network analyzers, are listed in Tab. 6.2.

Although the main multipath contribution resulting from the reflection of the signal by the second building facade is removed in time domain, a second multipath contribution could not be avoided. The second major reflection occurs due to the metallic building protrusion in front of the first transponder. As will be shown later, reflections from this protrusion result in an undulation of the receive signal for varying z positions. As a remedy, some later measurements were performed with flat outdoor wideband foam absorbers covering the protrusion. The two sets of measurements (without and with absorbers) will be compared with each other in the following Sec. 6.4.2 because a comparison of the final measurement results also serves as a check of plausibility.

For each of the three measurement pairs AB , AC , BC ⁶, measurement data were recorded for 96 z (slide) positions at 1 cm increments. At each position, a single signal with 1001 pulses as described above was transmitted and recorded. After recording, a threshold analysis of the received signal in time domain allowed to extract the pulse root mean square (RMS) amplitudes of all 1001 pulses, which were then stored along with the z position in a database for later analysis.

All measurements were completed at fair weather, so that radiometric effects due to the atmosphere, humidity, or ice covering the antenna apertures can be excluded. Furthermore, a gain stabilization procedure was performed for each transponder prior to every sweep, ensuring a constant transponder RCS (within the short-term transponder gain

⁵The *kaliserve* software allows the transponder hardware to be remotely parameterized and controlled, including the steps of pulse generation and recording.

⁶The first letter denotes the radar device, and the second letter the transponder device.

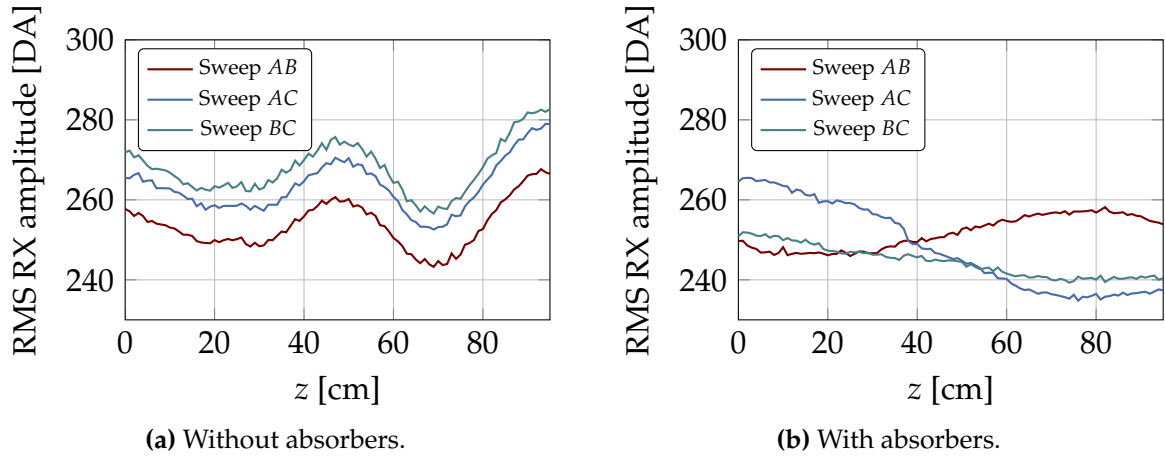


Figure 6.9: Original received RMS amplitude (in digital amplitude (DA) or ADC codes) in dependence of slide position z for two different sweep triplets (a) and (b) at the (baseband) center frequency of 200 MHz.

stability) throughout all measurements.

6.4.2 Measurement Data Analysis

The three-transponder method requires nothing more than measuring the receive-to-transmit power ratios P_{XY} for the three transponder combinations AB , AC , and BC at broadside alignment and at a known distance R , and substituting the measured values into the system of linear equations (6.19). The measurements and computations might be repeated for all frequencies of interest.

In practice, it is highly desirable to derive a standard measurement uncertainty along with the derived transponder RCSs. To estimate the uncertainty and to possibly lower it through exploitation of additional information (repetitions), it is advantageous to perform more than the strictly required number of measurements. Here, one of the main uncertainty contributions was assumed to be multipath due to a non-optimal outdoor measurement range. Therefore, measurements were repeated at varying slide positions.

In the following, two measurement triplets shall be analyzed. For the first triplet, no foam absorbers were used to cover the protrusion at the first site. In contrast, flat foam absorbers were used to cover the protrusion for the second triplet.

Original Data

The original RMS receive amplitudes for sweeps AB , AC , and BC are shown in Fig. 6.9 for both measurement triplets. A standing-wave pattern is clearly apparent, which cannot be explained by the z dependent free-space path loss. The receive power varies by more than 0.5 dB for sweep AB in Fig. 6.9a in z range from 45 cm to 70 cm, for instance.⁷

⁷Using the acronym DA for digital amplitude, the value in decibel is equivalent to an amplitude difference of 15 DA at a reference amplitude of 253 DA.

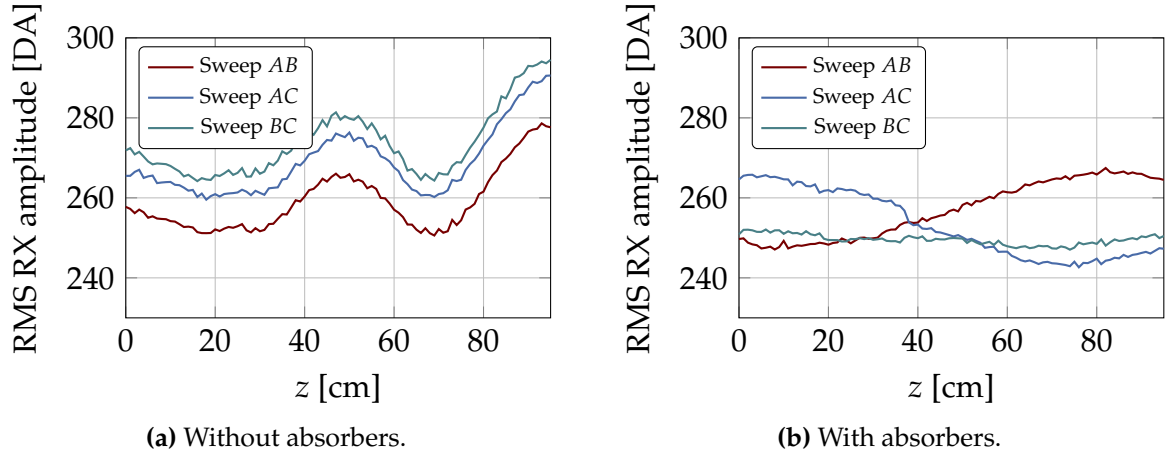


Figure 6.10: Received RMS amplitudes from Fig. 6.9 normalized for a far-field distance R at $z = 0$ cm for the two different sweep triplets (a) and (b). The slight downward drift of the curves in Fig. 6.9 for increasing z appears removed thanks to this free-space path loss compensation.

It can be observed that only for sweep BC in Fig. 6.9b (measurement with absorbers) the amplitude of the undulation appears greatly reduced. For the other two sweeps in Fig. 6.9b, the absorbers mostly affect the period (and therefore the multipath geometry) and not so much the amplitude. The explanation most likely lies in the angular dependent reflectivity coefficient of the absorbers. The foam absorbers were laid out flat on the building protrusion, resulting in flat angles of the multipath ray. At these angles, the effectiveness of the foam absorbers is much reduced in comparison to normal incidence, a fact which was unfortunately only considered after completion of the measurement campaign. Nevertheless, the absorbers have helped in producing a more regular undulation pattern, simplifying analysis as will be detailed later.

Compensation of Free-Space Path Loss

Before the data at different slide positions can be exploited in subsequent steps, the varying free-space path loss for different slide positions z (proportional to $(R + z)^4$ according to the radar equation (6.12)) needs to be compensated. The transponder-to-transponder distance R was measured at $z = 0$ cm, so that all data are normalized here to R at $z = 0$ cm. The distance-compensated data shown in Fig. 6.10 results.

Modeling of the Multipath Effect

Knowing the transmit amplitudes (from the configured transmit signal amplitude), a set of 96 power ratios P_{AB} , P_{AC} and P_{BC} can be derived, covering all z positions. A highly over-determined linear system of equations (6.19) results, which most likely does not have a solution (due to noise of the measured samples). One might be tempted to solve this overdetermined system of equations with a multivariate regression analysis and the method of least squares. This approach readily results in one RCS per transponder, but it violates several assumptions which are required for this kind of regression analysis [65, 154], suggesting wrong conclusions. First, the error terms (difference between estimated

and measured values) are not normally distributed, and second, the error terms do not result from independent observations with common variance. The violations are a direct consequence of the strong dependence of measured data on z (because of multipath effects), where ideally samples scattered normally around a horizontal line would be expected.

The recommended approach for removing multipath effects (undulations) from measured data for varying slide positions is averaging [84]. Several periods of the standing wave pattern should hence be recorded to get accurate results. Unfortunately, the geometry (flat angle of arrival for the multipath ray) produced a pattern with not even two periods within the slide range, see Fig. 6.10a. Therefore, another approach was sought. In order to estimate the transponder RCSs (and their standard uncertainties) under the standing wave assumption, the standing wave is modeled and approximately removed from the data. To this end, a single dominant, coherent multipath reflection is assumed. The reflection signal interferes with the much stronger direct path signal at the receiver, resulting in a standing wave in z direction. If the reflected signal and the direct path signal are assumed to have a constant amplitude independent of slide position z , then the measured RMS receive amplitude A_{XY} (where again X denotes the device operated as a radar, and Y denotes the device operated as a transponder) can be modeled as a constant RMS amplitude \hat{A}_{XY} resulting from the direct path signal, and a sinusoidal undulation with amplitude a , period $1/f$, and phase offset θ according to

$$A_{XY} = \hat{A}_{XY} + a \sin(2\pi fz + \theta). \quad (6.54)$$

This model can be applied for any slide sweep within one triplet, defining \hat{A}_{AB} , \hat{A}_{AC} , and \hat{A}_{BC} .

Once the three multipath-corrected signal RMS amplitudes \hat{A}_{AB} , \hat{A}_{AC} , and \hat{A}_{BC} have been estimated, the receive to transmit power ratios P_{AB} , P_{AC} , and P_{BC} can be derived. Together with Eq. (6.19), the three transponder RCSs result.

The model of Eq. (6.54) is fitted to the measured data through Bayesian data analysis and the Markov chain Monte Carlo (MCMC) approach. The immediate advantage of this approach is that all estimated model parameters like \hat{A}_{XY} are treated as probability densities, which characterize the uncertainty with which the parameters are estimated. Highest probability density intervals for all estimated and subsequently derived parameters (transponder RCSs) can easily be stated.

One Bayesian hierarchical model is created per sweep triplet per frequency. For each sweep, the model parameters \hat{A} , a , and θ are assumed to be different per sweep. f is assumed to be identical for all sweeps, i. e., it is a hyperparameter for the model. This assumption is not only physically sound because the measurement geometry between the sweeps is mostly identical, it also seems to be a good assumption given the observed data.

The Bayesian model requires priors (probability density functions) for all parameters before parameter estimation. These are summarized in Tab. 6.3. The parameters of the uniform priors were chosen to have little effect on the derived posterior distributions so that the priors can be considered non-informative. The unknown parameters are then estimated numerically with the MCMC approach [65, 70]. For each model evaluation, 100 000 samples are drawn. The first 3000 samples are discarded, and only every 300th is recorded for an improved sample-to-sample independence.

In order to verify that the model can reasonably well represent the data, the last 100

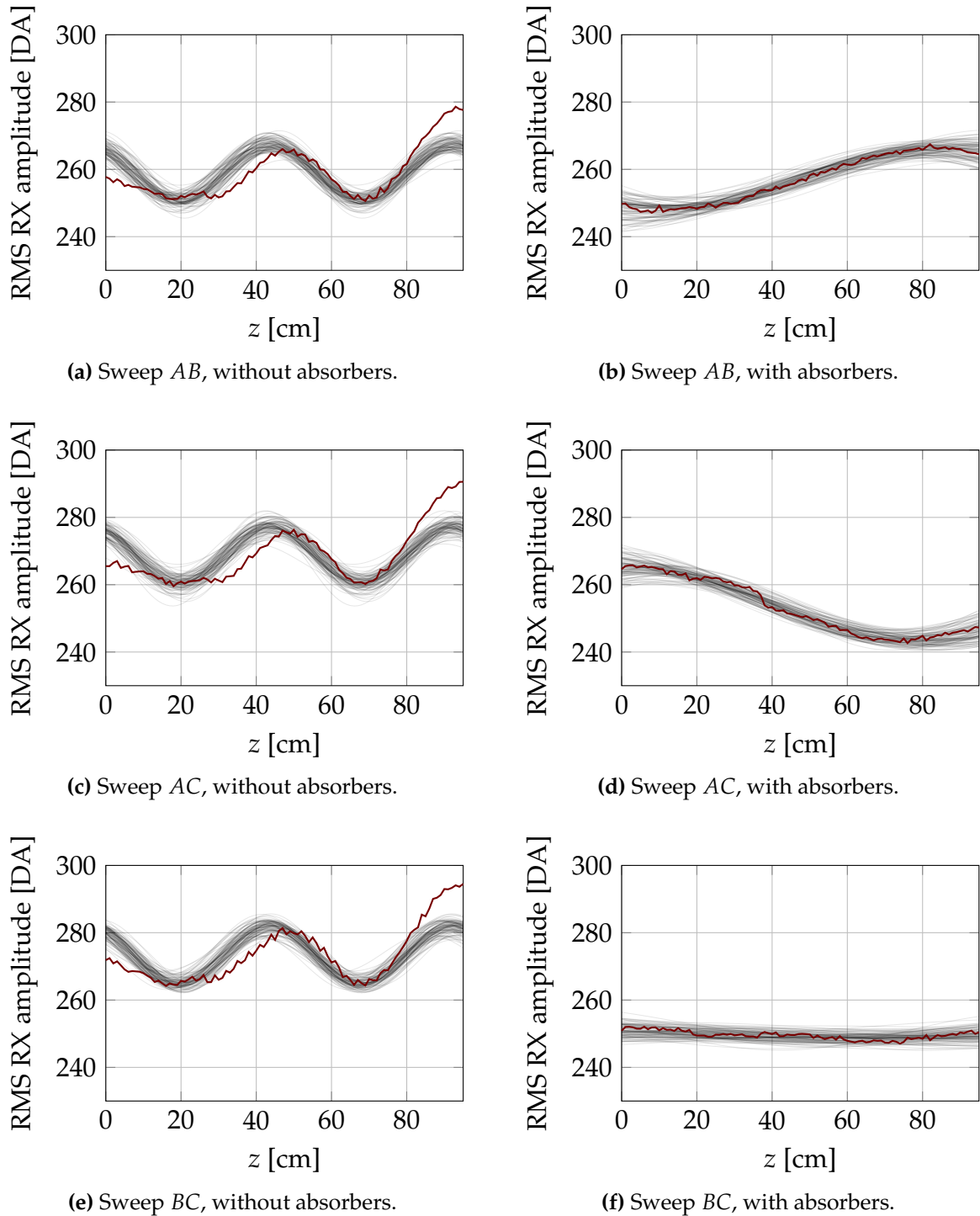


Figure 6.11: Received RMS amplitudes from Fig. 6.10 (in red, at center frequency) and 100 random sine fits per curve. It becomes apparent that the model from Eq. (6.54) fits the recorded data better when absorbers are used.

Table 6.3: Priors for the hierarchical Bayesian model used to fit a sine curve to each of the measured RMS amplitudes from Fig. 6.10. All priors are identically chosen for the two sweep triplets except for f , which is constrained in order to achieve a faster model convergence.⁸

Variable	Prior	Count
\hat{A}	$N(\mu, \sigma)$	3
μ	$U(100, 400)$	3
σ	$U(0, 40)$	3
a	$U(0, 25)$	3
θ	$U(0, 2\pi)$	3
f_1	$U(0.2, 1)$	1
f_2	$U(1, 5)$	1

sampled fitted sine curves are superposed on the measured sweep data in Fig. 6.11. For sweeps with absorbers, the sinusoidal fits seem to closely follow the measured data. Sweeps without absorbers, on the other hand, are less well represented by the model. Instead of fitting a single sine curve, a more complex model with two or more sinusoidal functions would be required to better separate the direct and multipath components. Yet, the limited data available does not justify the derivation of model parameters of a more complex model because for that a larger traversing range (or a different measurement geometry) would be required. In the end, differences between the model and measured data have to be accounted for in an additional uncertainty analysis because the uncertainty components cannot be estimated from the data directly.

Now having estimated the probability density functions for \hat{A}_{XY} for all frequencies, the frequency dependent transponder RCSs can be computed with Eq. (6.19). The computation step can be done directly within the numerical Bayesian model so that the output quantities are also given as probability density functions. A summary of the computations is shown in Fig. 6.12, where the best estimate along with the 95 % highest probability interval is shown. Superimposed are some earlier (normalized) network vector analyzer (NVA) transmission measurements, which show the principal frequency response of each transponder. The network analyzer measurements cannot include the frequency response of the antennas, and this explains some of the differences between the NVA and the three-transponder method measurements. In principle, a remarkable resemblance between the NVA and three-transponder method curves can be observed, stressing that the novel three-transponder method principle works.

Table 6.4 summarizes the RCSs of all three transponders at the center frequency. Again, the non-overlapping 95 % highest probability intervals for the two sweep triplets indicate that the model (6.54) is insufficient in explaining the data. A more detailed uncertainty analysis follows in the next section, addressing this issue.

⁸Note on notation: $U(a, b)$ denotes a uniform distribution with lower and upper bounds a and b ; $N(\mu, \sigma)$ denotes a normal distribution with mean μ and standard deviation σ .

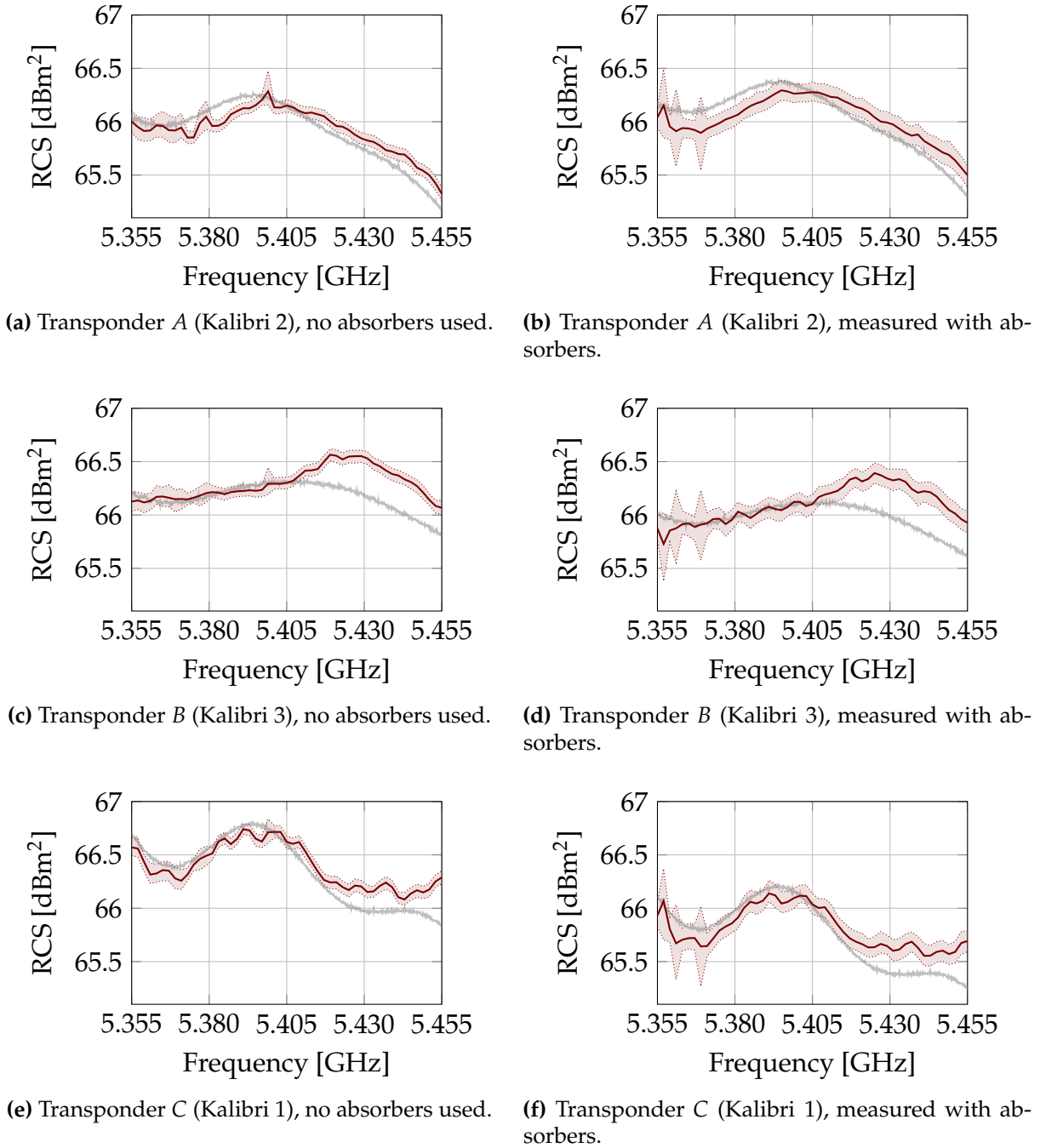


Figure 6.12: Estimated transponder RCSs in dependence of frequency resulting from Bayesian analysis and Eq. (6.19). The filled area between the dotted lines indicate the bounds for the 95 % highest-probability density intervals (considering uncertainties in estimation of P_{XY} only). The gray lines show network analyzer transmission measurements (necessarily excluding antennas) for comparison, normalized to estimated RCS at the center frequency. The network analyzer measurements follow the three-transponder method measurements to a large extent.

Table 6.4: Best transponder RCS estimates at the center frequency 5.405 GHz, the results of the Bayesian analysis applied to the two sweep triplets. Values in brackets denote the 95 % highest probability density interval resulting *solely* from Bayesian model fitting. Non-overlapping intervals especially for device C indicate model errors.

Transponder	Without absorbers [dBm ²]		With absorbers [dBm ²]	
Device A (Kalibri 2)	66.15	[66.09; 66.21]	66.28	[66.20; 66.37]
Device B (Kalibri 3)	66.30	[66.24; 66.35]	66.10	[66.01; 66.19]
Device C (Kalibri 1)	66.62	[66.56; 66.68]	66.04	[65.94; 66.14]

6.4.3 Uncertainty Analysis and Results

The uncertainty analysis for the measured transponder RCSs is performed in accordance with the Evaluation of measurement data – Guide to the Expression of Uncertainty in Measurement [87] (GUM), see Sec. 2.2.2. In short, the GUM approach depends on a measurement model relating the measurement quantity (transponder RCS ζ in dBm²) to the input quantities, assigning uncertainties (probability distributions) to the input quantities, and deriving the combined uncertainty for the output quantity through computations and the measurement model.

From Eqs. (6.17) and (6.19), the measurement model is given as (for instance for device A):

$$\zeta_A = \frac{1}{2}(P_{AB} + P_{AC} - P_{BC} + C) + D_A, \quad (6.55)$$

$$C = 20 \log(4\pi R^2). \quad (6.56)$$

D_A refers to the attenuation of the additional attenuator in decibel (see Tab. 6.2), which was part of the measurement setup but is removed again afterward.

In the following sections, the individual uncertainties for the input quantities P_{XY} , C , and D_X are derived and finally combined to yield the overall uncertainty budget.

Uncertainties in Estimations of P_{XY}

P_{XY} is the ratio of the received power to the transmitted power in decibel, when device X is used as a radar and device Y is operated as a transponder. This ratio varies if the transponders are not perfectly aligned with each other, the transponder loop gain drifts during a measurement, the antenna polarizations do not lie within the same plane, or the propagation path attenuation varies. The uncertainties resulting from these contributions are given in the next four paragraphs. The uncertainty in estimating P_{XY} from the data has been analyzed before, as summarized in Tab. 6.4.

(1) Alignment errors. Ideally, the two transponders should be aligned in main-beam direction with respect to each other. Deviations from this main beam direction are a result of mechanical alignment errors during the alignment process (using a laser and mirrors), and of the fact that the main beam direction is, strictly speaking, frequency dependent.

The alignment uncertainty of each transponder is assessed to be 1° (estimated from alignment repetitions and main-beam direction knowledge), which translates to a radiometric uncertainty of 0.03 dB due to the shape of the antenna pattern (known through previous antenna pattern measurements [139]).

(2) Gain drift errors. Each measurement sweep across all slide values took about 1 h to complete. During this time, the transponder gain varies slightly despite the thermal control. Previous repeated measurements have shown that the transponder gain is stable within a standard uncertainty of 0.02 dB during 1 h intervals.

The uncertainty due to drift is remarkably low, but it could be reduced further in future measurements by interleaving internal calibrations with the three-transponder method sweep measurements (and therefore reducing the time interval between subsequent internal calibrations). The total measurement time would increase though.

(3) Antenna misrotation. All antennas were operated at a nominal rotation of $\pm 45^\circ$ with respect to the vertical direction (adjusted with a level). The transmitting antenna of one transponder and the respective receiving antenna of the other were always co-polar aligned with respect to each other.

A rotation which deviates from the nominal rotation results in a reduced received signal amplitude due to polarization mismatch. The sensitivity of P_{XY} on the angular deviation φ of an antenna, e. g. from device X , from perfect co-polar alignment can be derived from Eq. (6.15), which becomes

$$P_{XY}(\varphi) = 10 \log \left(\frac{\xi_Y}{16\pi^2 R^4} \right) + 10 \log(\hat{\xi}_X \cos^2 \varphi) \quad (6.57)$$

after logarithmic transformation. Here, $\hat{\xi}_X$ denotes the RCS of device X without polarization loss.

Usually, one would determine the sensitivity coefficient of P_{XY} on φ by taking the partial derivative of P_{XY} with respect to φ , under the assumption that P_{XY} is approximately linear around the point of evaluation ($\varphi = 0$) [87]. The linearity assumption is not fulfilled here; the sensitivity coefficient would become zero.

Instead of computing the partial derivative, the resulting uncertainty can be approximated by evaluating Eq. (6.57) at the two close values $\varphi = 0$ (ideal alignment) and $\varphi = 1^\circ$ (estimated rotation uncertainty). The difference, which reduces to $20 \log(\cos 1^\circ) = 0.001$ dB, yields the uncertainty in P_{XY} due to antenna misrotation.

(4) Additional propagation path attenuation. Water drops or thin layers of ice on the transponder aperture covers can result in a modified value for P_{XY} . For the completed measurements, it was ensured that no humidity or ice was covering the apertures. Furthermore, no measurements were taken in heavy precipitation conditions so that no additional propagation path losses need to be considered in the following.

Combined standard uncertainty for P_{XY} . Table 6.5 summarizes all uncertainties described above which contribute to uncertainties in P_{XY} . Note that many contributions appear twice, i. e., once per transponder.

Table 6.5: Mutually uncorrelated standard uncertainties u contributing to a combined standard uncertainty for estimates of P_{XY} .

Contribution	Value	u [dB]
\hat{P}_{XY} estimation (Bayesian analysis)		0.05
Alignment error X	1°	0.03
Alignment error Y	1°	0.03
Gain drift X		0.02
Gain drift Y		0.02
Antenna misrotation X (polarization)	1°	0.001
Antenna misrotation Y (polarization)	1°	0.001
Additional propagation path attenuation		0
Resulting combined standard uncertainty for P_{XY}		0.07

The contributions are assumed to be mutually uncorrelated, so that the combined relative standard uncertainty of 0.07 dB results from the root-sum-square formula (2.24).

Top-level Uncertainties

The combined standard uncertainty u_c for the transponder RCSs follows from deriving sensitivity coefficients c_i for all N input quantities X_i , estimating the standard uncertainties $u(x_i)$ of the input quantities X_i , and then taking the positive square root of the combined variance, given as (also see Eq. (2.24))

$$u_c^2(\zeta) = \sum_{i=1}^N \left(\frac{\partial \zeta}{\partial X_i} \right)^2 u^2(x_i) = \sum_{i=1}^N [c_i u(x_i)]^2. \quad (6.58)$$

This is under the assumption that all uncertainties $u(x_i)$ are mutually uncorrelated.

The following sections address the separate input quantities X_i from Eq. (6.55), and the derivation of the respective sensitivity coefficients c_i . Finally, the combined uncertainty is computed.

Estimates of P_{XY} . The absolute value of the sensitivity coefficients c_p for the input quantities P_{AB} , P_{AC} , and P_{BC} are identical and given by

$$|c_P| = \left| \frac{\partial \zeta}{\partial P_{AB}} \right| = \left| \frac{\partial \zeta}{\partial P_{AC}} \right| = \left| \frac{\partial \zeta}{\partial P_{BC}} \right| = \frac{1}{2}. \quad (6.59)$$

The value of $u(P_{XY})$ was given in the last row of Tab. 6.5.

Multipath model error. The previous uncertainty for P_{XY} does not contain a term which addresses inconsistencies observed before. Measurements with and without absorbers resulted in significantly different values for P_{XY} (see Fig. 6.11), which consequently resulted in different derived RCSs (see Fig. 6.12). The inconsistency was attributed to the multipath model in Eq. (6.54), which apparently is too simple to explain the observed undulations in P_{XY} .

In order to quantify the model error, the worst-case difference between estimated \hat{P}_{XY} with and without absorbers at the center frequency is taken. This certainly discussible approach results in an estimated model uncertainty of 0.75 dB (see Figs. 6.11e and 6.11f). The value dominates the overall uncertainty budget, and it is therefore especially unfortunate that a more objective approach does not exist for estimating this model uncertainty. A repetition of the three transponder measurement campaign should address the multipath issues in more detail.

The multipath model error affects all three measurements simultaneously, which is why the uncertainty was not included in Sec. 6.4.3. Nevertheless, it is also scaled by the sensitivity coefficient c_P derived in the previous section.

Uncertainties due to external attenuators. Additional fixed attenuators were inserted into the signal path of each transponder just before the transmitting antenna. Opening and closing of coaxial connectors, and the limited knowledge of the attenuators' attenuation D_X result in uncertainties for the final RCS.

The overall standard uncertainty arising from using additional fixed attenuators is assessed to be 0.02 dB. This value was derived by measuring the fixed attenuation in C-band with three different network analyzers and three different network analyzer calibration kits. Opening and closing of coaxial connectors was automatically included as part of the measurement procedure.

Distance measurements. The sensitivity coefficient c_R of the transponder RCS on measurements of the transponder-to-transponder distance R follows from

$$c_R = \frac{\partial \zeta}{\partial R} = \frac{20}{\ln(10)R} = 8.87R^{-1}. \quad (6.60)$$

At $R = 46$ m, this results in $c_R = 0.193 \text{ m}^{-1}$. For larger values of R , i. e., for $z > 0$ m, c_R decreases so that the value at $R = 46$ m can be taken as the worst-case figure.

The main uncertainty in determining R is not seen in the tachymeter measurement, which can be completed with a standard uncertainty of much below 1 cm. The main contribution rather stems from the insufficient knowledge of the location of the horn antenna phase centers. For this analysis, a standard uncertainty of 20 cm, a conservative estimate, is assumed. The radiometric uncertainty then results from a multiplication of the sensitivity coefficient with this value, giving a standard uncertainty of 0.04 dB.

Vector antenna measurements could help in more accurately determining the antenna phase centers through measurements in the future.

Resulting Best RCS Estimates and Combined Standard Uncertainty

The uncertainties from the previous section are now joined using Eq. (6.58) to yield the final combined standard RCS uncertainty of 0.38 dB. An overview of the top-level uncertainty contributions is given in Tab. 6.6.

The combined standard uncertainties and the best RCS estimates from Sec. 6.4.2 form the final measurement results, summarized in Tab. 6.7. Here the best estimate is taken from the sweep triplet where absorbers were used, as the model (6.54) seems to more reasonably fit the data (see Fig. 6.11) so that the results seem more credible.

Table 6.6: Overview of top-level contributions to the combined standard uncertainty $u_c(\zeta)$ of transponder RCSs' derived during the first demonstration of the three-transponder method.

Uncertainty contribution	$u(x_i)$	c_i	$c_i u(x_i)$ [dB]
Multipath model error	0.75 dB	0.5	0.375
Measurement of distance R	0.2 m	0.19 m^{-1}	0.039
Estimate of P_{AB}	0.07 dB	0.5	0.036
Estimate of P_{AC}	0.07 dB	0.5	0.036
Estimate of P_{BC}	0.07 dB	0.5	0.036
External attenuator D	0.02 dB	1	0.02
Resulting combined standard uncertainty in dB			0.38

Table 6.7: Final measurement results of the 3TM demonstration campaign. The RCS estimates at the center frequency of 5.405 GHz are taken from Tab. 6.4 for the sweep triplet using absorbers. The 95 % confidence intervals (CIs) are derived from the combined standard uncertainty from Tab. 6.6.

Transponder	ζ [dBm ²]	95 % CI [dBm ²]
Device A (Kalibri 2)	66.28	[65.5; 67.0]
Device B (Kalibri 3)	66.10	[65.3; 66.9]
Device C (Kalibri 1)	66.04	[65.3; 66.8]

In summary it can be concluded that all three measured DLR C-band transponders have a co-polar RCS of slightly above 66 dBm², or equivalently, an RCS of slightly above 60 dBm² when the transponders are operated in the nominal 45° configuration, fulfilling the transponder requirements.

Furthermore, the measurement results were shown to be compatible (within a confidence level of 95 %) with the results of two other independent transponder calibration campaigns. These results are documented in [155].

The frequency response fits approximately in a band with an extent of ± 0.25 dBm². For accurate SAR system calibrations using these transponders, their ERCS should be derived in accordance with Chapters 3 and 4 to properly account for the frequency dependence.

6.4.4 Discussion of Measurement Results

Overall, the three-transponder method demonstration measurement campaign can be considered a full success. The method allowed for the first time to derive the transponder RCSs of three transponders in an end-to-end configuration without the need for additional RCS calibration targets.

Further principal confidence in the results can be drawn from a comparison of the derived frequency dependent RCS with the transponder frequency response measured (without antennas) in the laboratory with a network analyzer, see Fig. 6.12. The drop of the measured transmission with respect to the RCS for higher frequencies is partly

explained by the frequency dependence of the antenna gains. Between the lower and upper frequencies of the transponder band, ranging from 5.355 GHz to 5.455 GHz, an RCS difference of

$$20 \log \left(\frac{5.455 \text{ GHz}}{5.355 \text{ GHz}} \right) = 0.16 \text{ dB}$$

is expected alone because of the principal antenna gain dependence on frequency. Although this value does not exclusively explain the difference between the three-transponder method and NVA curves, the sign and the general trend is certainly correct. Despite the encouraging findings for this first demonstration campaign, the derived combined RCS standard uncertainty of 0.38 dB is rather large in comparison to other measurement methods (e. g. 0.2 dB for measurements with corner reflectors (main uncertainty contributors) exploiting satellite overpasses, see Chap. 7). Yet there is no reason in ascribing the uncertainty to the three-transponder method itself. The comparatively large measurement uncertainty is rather attributed to the *ad hoc* demonstration measurement setup and the multipath contributions. Consequently, the following steps can be taken to improve the accuracy of future three-transponder method measurements:

- Ensure a better suppression of multipath signals, e. g. by installing absorbers with a higher reflection loss on all relevant reflection areas.
- Increase the vertical separation between transponders and ground (or building protrusions). This results in steeper angles for the incoming reflection signal at the transponder antenna, which results in a higher frequency of the observed standing wave. Consequently, the multipath amplitude can more easily be estimated or simply averaged out even if the maximum traversing range of the slide is only about 1 m.
- Use a slide with a larger maximum traversing range. Again, this helps to capture more periods of the standing-wave pattern so that a more accurate estimation of multipath parameters becomes possible.

Should these measures lead to a suppression of the modeling error of 0.75 dB in Tab. 6.6, a total RCS uncertainty of only 0.08 dB would result.

In summary, the three-transponder method promises to deliver transponder RCS measurements with unprecedented low measurement uncertainties in the future, as the main source of measurement uncertainties, the calibration RCS target, could be excluded from the uncertainty budget.

6.5 Method Extension for an Inherent Plausibility Check

6.5.1 Description of the 3TM Method Extension

Selvan [167] devised an adaption of the three-antenna method by which uncertainty calculations can be simplified but still stay compatible with the GUM [87]. He replaced one of the three unknown antennas with a standard gain horn, and then exploited the *a priori* knowledge to determine a bias in the measurement results due to antenna mismatches.

An uncertainty analysis for the three transponder method was shown in Sec. 6.4.3. It is straightforward and does not need to be simplified. Antenna mismatches are part of a transponder's characteristics and as such do not need to be especially treated as for the three-antenna method. Yet the idea of Selvan [167] can be exploited differently. By replacing one of the three transponders with a traceable reference target, whose RCS is known before the measurement, one can derive a plausibility statement about the measurement results. This is useful as an approach to detect systematic measurement errors.

The approach is as follows: When the three measurements are executed, the reference target RCS is assumed to be unknown and its RCS is derived in the usual way according to Eq. (6.19). After the measurement, an RCS bias and its uncertainty can be estimated for the reference target by subtracting the *a priori* known RCS from the measurement result, assuming the results are expressed in decibels. Should the bias be statistically significant different from zero, then a measurement error was detected and the results must be treated as not plausible. This result could be an indication that the length measurement was faulty, a systematic multipath effect has not been detected, or one of the transponder RCS's drifted between measurements. On the other hand, should the bias not be statistically significantly different from zero (i. e., should the null hypothesis not be rejectable), the RCS measurement results can be regarded plausible.

Checking for plausibility is especially important for the calibration of SAR calibration transponders. After RCS calibration, the transponders are often used as the only reference point target for the calibration of a SAR instrument [113], and so there is no chance of detecting transponder calibration errors by other cross comparisons. The three-transponder method extension using a corner reflector or circular metallic plate with known RCS can therefore contribute to an increased confidence in the calibration results, without any additional measurement effort required.

6.5.2 Formulation of Hypothesis Test – Gaussian Distributions

A check for plausibility has only two outcomes. Such a check can be formulated, in statistics terminology, as a hypothesis test. The starting point of the discussion is the null hypothesis:

The *a priori* known RCS of the reference target is identical to the three-transponder measurement result.

The question is: Under which conditions can the null hypothesis be rejected in a statistically significant way, i. e., at a given confidence level? Should the hypothesis test indicate acceptance of the null hypothesis, then it is not yet proven that the measurement (or the RCS knowledge of the reference) is without error. Should the test, on the other hand, result in a rejection of the null hypothesis, then there is a significant indication that the measurement results should not be trusted; the results are not plausible.

It shall be assumed that the measurement uncertainty and the *a priori* RCS knowledge uncertainty are both given as standard uncertainties in accordance with the GUM [87]. The Gaussian random variables X and Y shall describe the possible values for realiza-

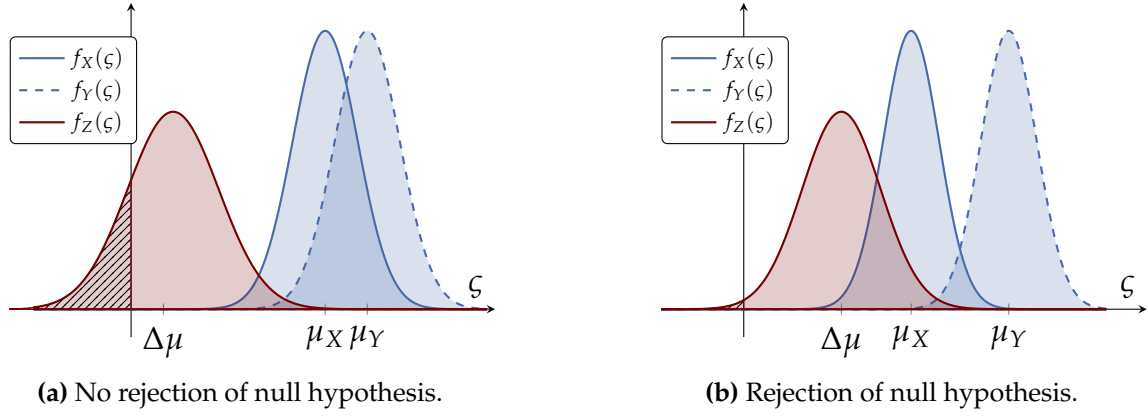


Figure 6.13: The red curve, $f_Z(\zeta)$, shows the result of subtracting the two Gaussian distributions $f_X(\zeta)$ and $f_Y(\zeta)$ from each other. The hatched areas show the probability $P[\zeta < 0]$ and is taken as the measure for a possible rejection of the null hypothesis.

tions of the reference RCS and the measurement results:

$$X \sim N(\mu_X, \sigma_X^2), \quad (6.61a)$$

$$Y \sim N(\mu_Y, \sigma_Y^2). \quad (6.61b)$$

The variables μ_X and μ_Y describe the means of the distributions, and σ_X and σ_Y denote the distributions' standard deviations.⁹ Without loss of generality, X and Y shall be attributed to the *a priori* RCS knowledge and the measurement result so that $\mu_Y > \mu_X$.

To complete the introduction of notation, $f_X(\zeta)$ and $f_Y(\zeta)$ shall denote the probability density functions (PDFs) from which X and Y are drawn, and $F_X(\zeta)$ and $F_Y(\zeta)$ shall denote the respective cumulative distribution functions (CDFs).

Expressed this way, the plausibility check reduces to the question: How large must the estimated RCS difference

$$\Delta\zeta = \mu_Y - \mu_X \quad (6.62)$$

of the random variable

$$Z = Y - X \quad (6.63)$$

be so that the null hypothesis can be rejected at a certain confidence level, given the standard uncertainties σ_X and σ_Y ? A visualization of this question is shown in Fig. 6.13. The red curve shows the PDF $f_Z(\zeta)$ of Z . If the null hypothesis shall be rejected at a confidence level α (e. g. 95 %), then the condition

$$P[Z \leq 0] = F_Z(0) \leq 1 - \alpha \quad (6.64)$$

must be fulfilled. At the exemplary confidence level of $\alpha = 0.95$ the difference between the measurement result and the *a priori* RCS knowledge is not large enough to be significant in Fig. 6.13a, but it is large enough in Fig. 6.13b, fulfilling condition (6.64).

The condition under which the null hypothesis may be rejected is derived in the following Section 6.5.3. In particular, formulas for the following two special cases are derived:

⁹In reference to the GUM, standard uncertainties are customarily denoted with the symbol u . In contrast to this, the symbol σ is chosen here to be in line with the notation used in most texts on statistics.

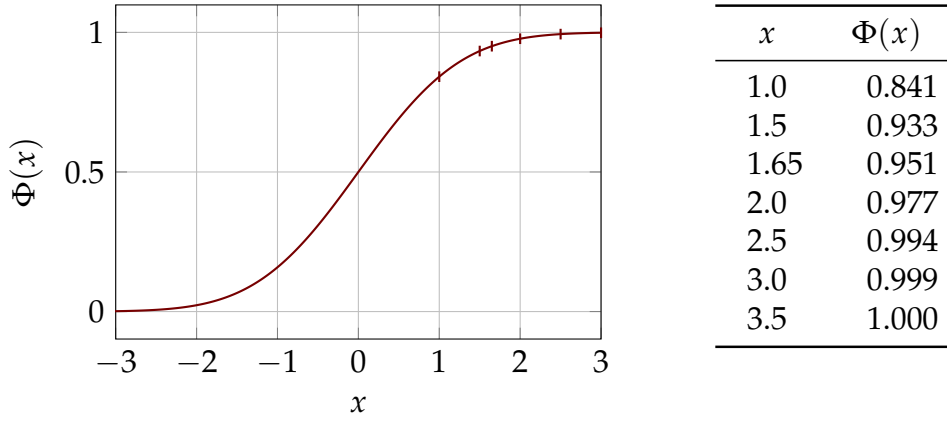


Figure 6.14: Cumulative distribution function of a standard Gaussian random variable.

1. Theoretical, lower bound case: The reference target's RCS is accurately known; its stated uncertainty is negligible in comparison to the measurement uncertainty of the three-transponder method. At what RCS difference can the null hypothesis be rejected at a confidence level α ?
2. Special practical case: The reference target's relative RCS knowledge uncertainty is as large as the three-transponder measurement uncertainty. This might be the case if the reference target has been characterized in an earlier three-transponder method measurement campaign. At which RCS difference can the null hypothesis be rejected at a confidence level α in this case?

6.5.3 Derivation of Hypothesis Rejection Conditions

In this section, the conditions are derived under which the null hypothesis formulated above can be rejected, i. e., when inequality (6.64) holds.

As a first step, one needs to derive the PDF of Z in Eq. (6.63), i. e., the PDF of a random variable which is the result of subtracting the random normal variable X from the random normal variable Y . Here a previous result from p. 167 can be reused:

$$Z \sim N(\mu_Y - \mu_x, \sigma_X^2 + \sigma_Y^2). \quad (\text{B.45})$$

This result can now be used in the plausibility check condition Eq. (6.64), so that

$$P[Z \leq 0] = \int_{-\infty}^{\infty} \frac{1}{\sqrt{2\pi(\sigma_X^2 + \sigma_Y^2)}} \exp\left(-\frac{x - (\mu_Y - \mu_x)^2}{2(\sigma_X^2 + \sigma_Y^2)}\right) < 1 - \alpha. \quad (6.65)$$

The integral cannot be solved analytically [154], but approximate results can be derived numerically. Integration results are commonly tabulated for a normal cumulative distribution function $\Phi(x)$, i. e., the CDF of a Gaussian random variable with zero mean and a standard deviation of 1, see Fig. 6.14. The function $\Phi(x)$ is strictly monotonic. It is 2-fold rotationally symmetric around the point $(0, 1/2)$.

An arbitrary Gaussian variable Z can be transformed to a standard Gaussian variable Q with [154]

$$Q = \frac{Z - \mu_Z}{\sigma_Z}. \quad (6.66)$$

The probability in Inequality (6.65) can then be expressed as

$$P[Z \leq 0] = P[(X - \mu_Z)/\sigma_Z \leq 0] = \Phi[-\mu_Z/\sigma_Z] \leq 1 - \alpha, \quad (6.67)$$

which is equivalent to

$$-\frac{\mu_Z}{\sigma_Z} \leq \Phi^{-1}(1 - \alpha) = x \quad (6.68)$$

where

$$\Phi^{-1}(p) = x$$

is the probit function, i. e., the inverse of the standard normal CDF shown in Fig. 6.14 so that

$$\Phi(\Phi^{-1}(p)) = p.$$

If σ_X and σ_Y are given and $\Delta\zeta$ is sought, the following first final condition results from Inequality (6.68):

$$\Delta\zeta \geq x\sqrt{\sigma_X^2 + \sigma_Y^2}. \quad (6.69)$$

A second conclusion follows if $\Delta\zeta$ and one of the standard uncertainties, e. g. σ_X , are known so that

$$\sigma_Y \leq \sqrt{\frac{\Delta\zeta^2}{x^2} - \sigma_X^2}. \quad (6.70)$$

As a numerical example, the conditions for the two special cases described in Sec. 6.5.2 on p. 127 shall be given. For this, it is assumed that a condition is sought at which the null hypothesis (measured RCS equals an *a priori* known RCS of a measurement standard) can be rejected at a confidence level α of 95 %, i. e., the measurement results are identified as not plausible. For an α of 0.95, an x of 1.65 results, see Fig. 6.14. Hence:

1. If the standard measurement uncertainty of the reference can be neglected, then the observed difference between measured and *a priori* known RCS $\Delta\zeta$ must fulfill

$$\Delta\zeta \geq 1.65\sigma \quad (6.71)$$

according to Eq. (6.69) so that the null hypothesis can be rejected. Here, σ is the standard measurement uncertainty of the three-transponder method. At an exemplary relative standard measurement uncertainty of 0.2 dB, the null hypothesis can be rejected at a confidence level of 95 % if the observed $\Delta\zeta$ exceeds 0.34 dB.¹⁰

2. If the standard measurement uncertainty of the reference is equal to the standard uncertainty of the three-transponder method measurement σ , then $\Delta\zeta$ must fulfill condition

$$\Delta\zeta \geq 2.33\sigma \quad (6.72)$$

according to Eq. (6.69) so that the null hypothesis can be rejected. At an exemplary relative standard measurement uncertainty of 0.2 dB, the null hypothesis can be rejected at a confidence level of 95 % if the observed $\Delta\zeta$ exceeds 0.48 dB.

It must be noted that even in the first case the observed $\Delta\zeta$ must be comparatively large to identify measurement results as not plausible.

¹⁰The multiplication in (6.71) is executed in the linear domain.

6.5.4 Practical Implications and Conclusions

The plausibility check requires a measurement standard with a known RCS. It is likely that a passive reference target, e. g. a circular plate or a corner reflector, will be used for this purpose because of the ready availability of such targets. A passive target though has a practical impact on the measurement procedure. In comparison to a transponder, a passive target cannot delay the inbound signal before reflection. Parasitic reflections from the measurement setup, e. g. the house facade of the second building in Fig. 6.8 on p. 111, cannot be suppressed any more in the time domain. This either requires an improved measurement setup with additional absorbers, or larger measurement uncertainties must be tolerated.

Nevertheless, the presented extension of the three-transponder method to include an inherent plausibility check for derived measurement results is very advantageous: First, no additional measurements or measurement setups are required on top of the three measurements needed for the three-transponder method. Time, effort, and costs can be saved. Second, the check allows to place more confidence into the transponder calibration results through verification. This is important because often the transponders are used as the single radiometric standard for the calibration of a SAR system, and systematic calibration errors could otherwise not be detected.

6.6 Discussions of the Three-Transponder Method

In the following, the main advantages, limitations, and open points of the novel three-transponder method are discussed.

6.6.1 Advantages

These are the reasons which render the three-transponder method advantageous in comparison to existing methods:

1. The transponder RCSs can be determined without the need of an additional (passive) radar target with known RCS. By avoiding a comparative RCS measurement, uncertainties resulting from the RCS measurement standard are eliminated.
2. The transponders' RX and TX paths are measured in their final configuration. No additional uncertainties result from reassembling cabling after the end of the measurement campaign.

Furthermore, antenna mismatches are inherently characterized due to the same reason and do not pose a problem with the three transponder method. In contrast, mismatches between generator and antenna or antenna and receiver need to be handled separately for the three-antenna method.

3. The method allows to determine the full polarization scattering matrix of the transponder. This is achieved by rotating the transponder antennas and repeating the measurements for each new configuration; the procedure requires that the transponder antennas can actually be rotated. Alternatively, if the antenna rotation is precisely known, it can be derived analytically from a set of measurements at one polarization setting.

4. No additional RF measurement instrumentation is needed to complete the measurements. This might help in reducing the costs of a measurement campaign.
5. The three-antenna measurement technique is well established. A lot of experience exist in the metrology community (e. g. with respect to multipath suppression), which can directly be carried over to the three-transponder measurement method.
6. The transponders which are operated as radar targets can easily implement a (digital) delay between receive and transmit. This results in a decoupling of reception and transmission. Effectively, the transponder is not operated in a “closed-loop” anymore, so that unwanted oscillations, which were observed during previous measurement campaigns in an anechoic chamber, are impossible. Also, the background RCS (e. g. from a tower on which the transponder is mounted, or the back wall in an anechoic chamber) has no effect on the derived transponder RCS when the radar transmit and receive windows are separated in time.
7. A verification of measurement results can be achieved through an inherent plausibility check according to Sec. 6.5. For the plausibility check, at least one of the measured (three or more) targets must have a known RCS with a known standard uncertainty.

6.6.2 Limitations

The main limitations of the novel method are:

1. More than one transponder is needed for a single measurement campaign. Transponders cannot be measured separately according to the proposed method.
2. At least one transponder needs to be designed according to Fig. 6.3, i. e., the transponder must allow operation as a radar and as a transponder instrument. It is sufficient if one of the transponders is replaced by a passive target with an unknown but constant RCS though (see Eq. (6.19), where device C is only operated as a radar target, not as a transponder).
3. The transmit and receive power cannot be freely chosen as for the three antenna method. Rather, the transponder transmit power is determined by the transponder RCS and a maximal transponder input power (depending on the SAR system the transponder was designed for). To complete the three transponder measurements, the free-space path loss (and therefore the distance R between the devices) needs to be adjusted so that the measurements can be performed within the operational range of the transponder.

Ideally, the different transponders should have comparable characteristics so that all three measurement setups with the three transponder combinations can be completed at the same distance R , simplifying the measurement campaign.

6.6.3 Open Points

The three-transponder method can only determine the transponder RCS. In SAR system calibration, a system should not be calibrated to a target with a known RCS but a known

ERCS, see Chap. 3. The RCS can be converted to an ERCS if the SAR system parameters and the complex transponder transfer function are known, e. g. through the use of a point-target simulator, see Chap. 4.

With the three-transponder method, only the amplitude response can be derived. The phase response cannot directly be measured through the three-transponder method because a common time and frequency source is missing between the different transponders A , B , and C .

Nevertheless, the phase response is typically less of a concern for determining an accurate transponder ERCS, as long as the transponder's frequency-dependent amplitude response is known.

The phase response can be measured in the laboratory using a network analyzer which is connected to the RX and TX ports of the transponder. With this approach, the antennas' phase response is not measured, but depending on the antenna type, it should have little influence on the total phase response, which is dominated by active components and filters in the TX and RX paths.

6.7 Conclusions

This chapter covered the radiometric calibration of transponders, which is a prerequisite step before using these point targets as measurement standards for SAR system calibration. The discussion started with a review of existing transponder RCS calibration methods in Sec. 6.2, which led to the following novel contributions:

- First, I introduced the novel *three-transponder method (3TM)* for RCS calibration in Sec. 6.3. The method puts some (nowadays commonly fulfilled) requirements on the design of the transponders under test, but it offers in principle greatly reduced measurement uncertainties. This is achieved by realizing metrological traceability solely through a length measurement, which can be completed with high accuracy.
- In the following Sec. 6.4, I presented the setup and measurement results for a demonstration measurement campaign. Despite the nature of the *ad hoc* measurement setup, I could not only demonstrate that the method works in practice but also show that the measurement results are compatible within uncertainties with the ones of two independent measurement campaigns [156] (also see Chap. 7).
- Finally, I introduced a 3TM extension in Sec. 6.5, with which the plausibility of measurement results can be inherently checked. The method extension is especially relevant as an additional validation of the measurement results before the calibrated transponders are used as measurement standards for SAR system calibration.

The three-transponder method promises to become one of the, if not the most accurate method for calibrating the RCS of transponders in the future, and it is therefore contributing to radiometrically more accurate SAR systems.

7 Derivation of Calibration Parameters Through Hierarchical Bayesian Data Analysis

In order to perform a calibration, knowledge of the quantity to be calibrated, a system needing calibration, specified measurement conditions, and a calibration standard are required. These topics were discussed in the previous parts. This chapter discusses the actual calibration process itself, or more specifically, a novel method for how to estimate calibration parameters including their uncertainties from samples acquired during the calibration campaign for a synthetic aperture radar (SAR) system.

Parts of the work presented in this chapter resulted in a publication [45].

7.1 Introduction

SAR calibration campaigns are very much alike across SAR missions. Mostly during the commissioning phase, many point targets are repeatedly deployed in the field and realigned from overpass to overpass. After focussing of the raw data, point target analysis yields a set of measurement samples. In subsequent data analysis, parameters like the calibration factor (see Sec. 2.3) are derived from these measurement samples.

The acquired data points are typically grouped during the analysis, e. g. by beam, local incidence angle (near/mid/far range beams), polarization, orbit direction (ascending versus descending), calibration site, point target, or polarization. An exemplary plot of such data for the German X-band TerraSAR-X mission has been reproduced in Fig. 7.1, showing the derived calibration factor versus measurement (i. e., time) grouped by beam. Similar plots of grouped data summarizing point target measurements have been reported for X-SAR [209, Fig. 7], RADARSAT-1 [113, Fig. 1], ALOS/PALSAR [168, Figs. 5 and 7], and TanDEM-X [164, Figs. 4 and 5].

Up to now, this grouping of data has, to the best of the author's knowledge, only been applied for plotting, not during quantitative data analysis itself. When the calibration factor is derived from grouped data, grouping is undone and all samples are treated as if they belonged to one group. This strategy is exemplarily described in [46]. Ungrouping data is convenient, but valuable information is lost. Questions as to if there is a dependence of the calibration factor on beam, incidence angle, orbit direction, point target type, and so on, have been answered only qualitatively by visual inspection of data point distributions in diagrams. A quantitative method which would allow the estimation of the overall calibration factor and calibration factors for several sub-groups

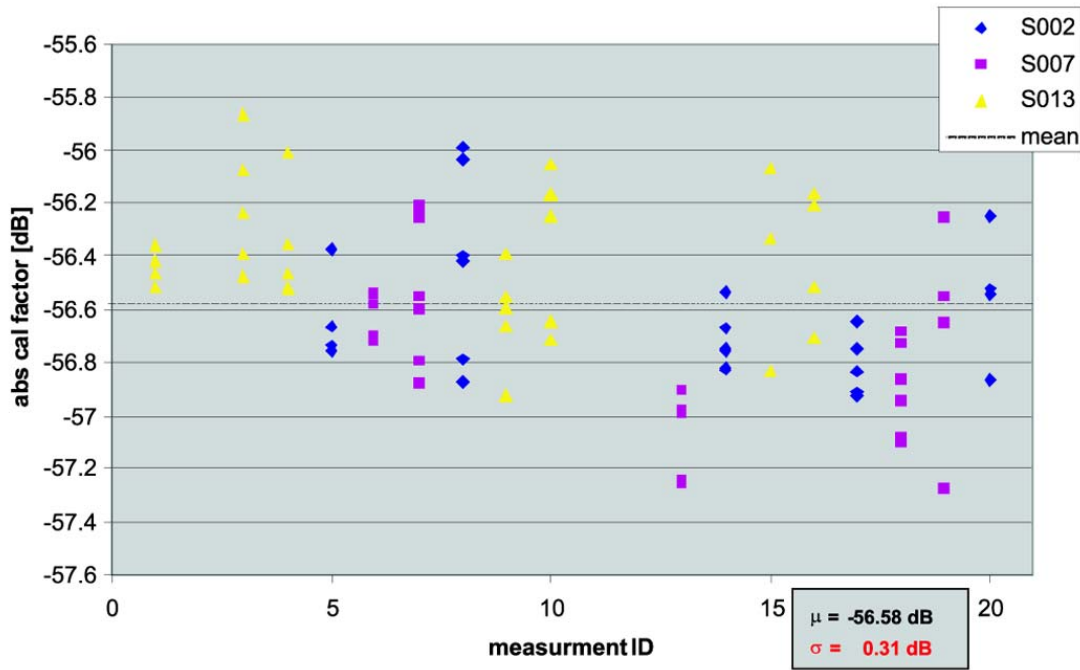


Figure 7.1: Exemplary SAR calibration data from a calibration campaign using point targets. The data shows typical data grouping. It was acquired during the TerraSAR-X commissioning phase and is shown grouped by three SAR beams, from [161, Fig. 17].

of the same body of data including statements on estimation uncertainties has so far been lacking.

In this chapter, Bayesian data analysis is introduced as this missing quantitative method for grouped data. Bayesian data analysis has been proven advantageous in many parameter estimation problems [66, 70], but so far it has not yet been applied for radiometric SAR calibration. Bayesian analysis lends itself well to grouped data and hierarchical data modeling [15, 31, 66, 107], and is therefore a very good fit for the estimation problems that one faces during an external SAR calibration campaign. A general but short review of the methodology and examples of its application in the domain of radiometric calibration are given in Sec. 7.2.

The suitability of the proposed method is shown through a case study in Secs. 7.3 (campaign setup) and 7.4 (data analysis). The objective of the case study is conceptually equal to the derivation of the calibration factor, although here the reflectivity of a point target is accurately determined. The presented case study is based on an external calibration campaign which was executed in April 2013. 15 corner reflectors were deployed as reference targets, and the reflectivity of DLR's C-band *Kalibri* transponder prototype [41, 93] was derived from a series of eight data acquisitions by the Canadian RADARSAT-2 SAR system.

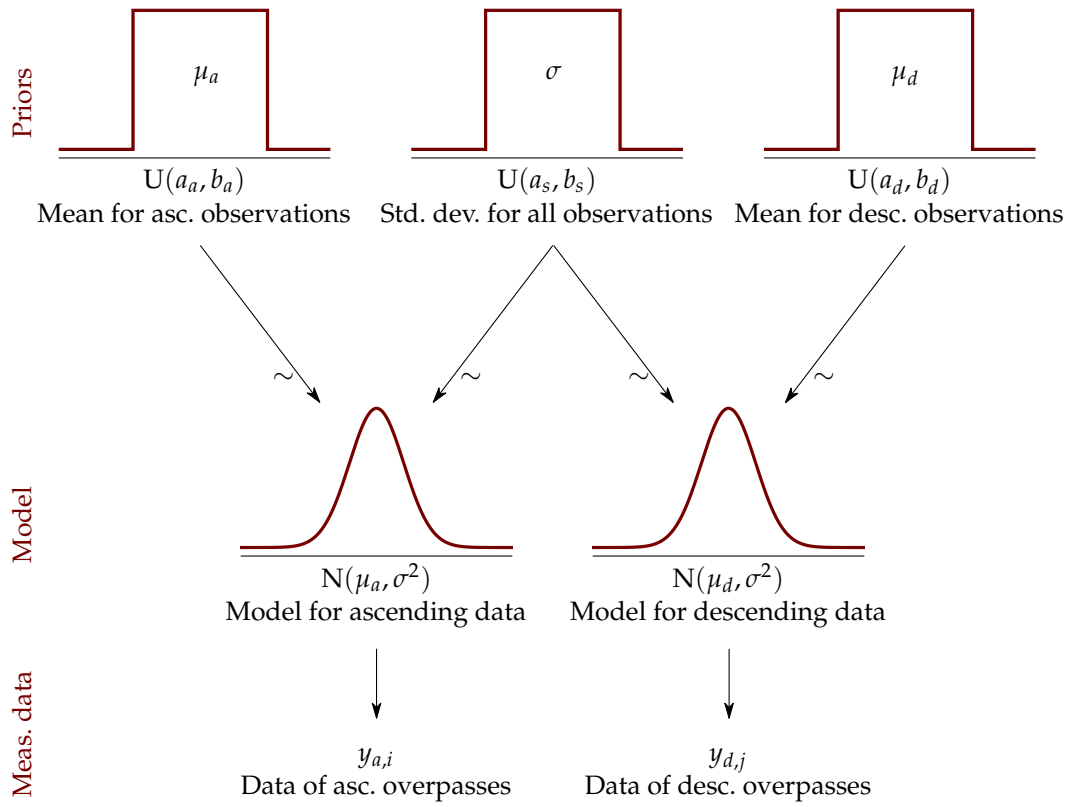


Figure 7.2: Simple hierarchical model where the standard deviation σ is modeled on all data samples, but the means μ_a and μ_d for ascending and descending overpasses are modeled on each data group separately. The symbol \sim means “is sampled from”. The diagram style is inspired by [104].

7.2 Methodology for Radiometric Parameter Estimation from SAR Data Through Bayesian Statistics

Bayesian statistics is, like classical (also called frequentist) statistics, a well established field with applications in many scientific areas. It is extensively covered in the literature (see for example [20, 66, 70]). A short overview on the Bayesian approach and the numerical Markov chain Monte Carlo (MCMC) method is given in App. C.

The proposed method for radiometric parameter estimation from SAR data is based on exploiting the often found hierarchical structure of the acquired data. This hierarchical modeling and the derived methodology are detailed in the following.

7.2.1 Hierarchical Models

One of the main advantages of the Bayesian approach is how well hierarchical problems can be modeled [66, 104]. A hierarchical model involves several parameters of which at least some are meaningfully related by the structure of the problem, and it allows to represent and reason about knowledge at multiple levels of abstraction. Available data are grouped, where partial pooling is possible and favored, in contrast to not pooling or completely pooling the data which is often done in classical statistics.

As a simple example of a hierarchical model for SAR calibration, one can consider the

data acquired by repeatedly overpassing reference point targets with a known, stable equivalent radar cross section (ERCS), both with descending and ascending passes. One question that arises is if and by how much ascending measurements deviate from descending overpasses (where differences may stem for instance from the atmosphere or the satellite attitude control). Moreover it shall be assumed that the variance, e. g. due to instrument or point target drifts, is equal for all overpasses. Such a model is visualized in Fig. 7.2, where the parameters to be estimated are the two per-group means μ_a and μ_d for ascending and descending overpasses, and the standard deviation σ for all overpasses, which is a shared parameter. Instead of partial pooling, one would otherwise follow one of these two alternative approaches:

1. Combine all data into one group.
2. Treat each group individually.

The first approach ignores group effects, and the second ignores the similarities between groups. The hierarchical model, on the other hand, can be seen as a compromise which better fits the structure of the data.

Generalizing from the first example, the main characteristics of hierarchical Bayesian models are:

- There are two or more model parameters which have meaningful dependencies.
- Inference about one unobserved quantity affects the inference about another unobserved quantity.
- A hierarchical data structure can be conveniently mapped to a hierarchical model.
- Groups of data can have different numbers of sample without affecting the benefits of the approach.
- Multiple groups of observations can exist, where each group has its own parameters.
- A joint probability model allows to determine all model parameters at once, where densities are typically derived numerically using the MCMC approach.

Capturing the structure of data in the simple example above and more complicated cases is difficult with classical approaches, yet data in SAR calibration is often naturally grouped. Other questions in SAR calibration involving grouped data include:

- What is the best estimate of the calibration factor and its respective confidence interval if several types of reference point targets (i. e., transponders and corner reflectors of different sizes) with different ERCSs and stabilities are deployed?

Solving this problem with frequentist statistics would require to estimate the population mean of each group, and deriving the calibration factor after ERCS compensation between groups. The information on the variance within each group is lost, and a reliable statement of the final uncertainty or confidence interval on the estimated calibration factor is difficult to achieve. With hierarchical Bayesian modeling though, the variance within each group (target type) and the variance across all target types can be derived simultaneously because group and total dispersion are handled within a joint probability model.

- Is there a significant systematic dependence on the chosen antenna beam (or near/far range, or left/right looking geometries, or ascending/descending geometries) for radiometric measurements?

Once again the same set of data samples as before should be grouped, but this time by antenna beam (or near/far range, left/right looking acquisitions, or ascending/descending orbits). For each group, a posterior distribution for the respective calibration factor can now be derived. Comparing the different posterior distributions allows to conclude if a significant radiometric inter-beam offset exists.

- For a plausibility check: Is the ERCS of one of the reference point targets systematically different from the others? Here repeated overpasses over the same set of targets are assumed.

In order to answer this question, the overpass-dependent effect of the SAR system and the atmosphere should be modeled out of the analysis. This can be done by grouping the samples according to overpass and utilized target. All target samples of one overpass can be used to compensate for SAR system and atmospheric effects, and in a second step the group ERCS of each target can be determined.

In fact, all of these questions can be conveniently answered by setting up a single joint probability model. Partial results contribute to the particular derivation of posterior distributions without loss of information. On the other hand, a frequentist approach would require independent analyses, and carrying over results from one model to the next would result in loss of information due to the summarizing nature of the frequentist approach.

7.2.2 Summary of Method

In SAR calibration, much of the recorded data can and should be grouped for analysis, but this fact has so far not been exploited. The proposed method based on hierarchical Bayesian data analysis aims to close this gap, and to make better use of the available information. The method consists of the following steps:

1. Acquire data samples and organize them in groups.
2. Derive a probabilistic, hierarchical model of the parameters which describe the data.
3. Assign prior probabilities to the parameters.
4. Compute the posterior densities of the model parameters with the numerical MCMC approach, incorporating the observed data.
5. Using the derived probability densities, extract information on the measurement uncertainty based on probability intervals.

One of the main advantages of the approach is that, in contrast to frequentist statistics, all parameters are described by probability densities. Furthermore, the considered parameter distributions are not limited to Gaussian distributions. In general, meaningful dependencies in the structure of the data can be exploited, and uncertainties are managed and quantified.

The possible downsides of the approach, namely that it may be considered more complicated and computationally more demanding, are counteracted by today's availability of efficient MCMC implementations and improved computing power.

How the approach can be applied in practice to a more complex case is discussed in the following two sections on a case study analysis.

7.3 Case Study: Measurement Campaign Goal and Setup

The following case study applies hierarchical Bayesian data analysis to a practical problem. This Sec. 7.3 describes the campaign goal and setup, whereas the following Sec. 7.4 applies the proposed method of hierarchical Bayesian data analysis for the estimation of a parameter in radiometric calibration.

7.3.1 Introduction and Goal

As mentioned before, the German Aerospace Center (DLR) has recently developed and manufactured a set of modern active radar calibrators (*Kalibri* transponders) [41, 93] for the Sentinel-1 SAR mission, see Fig. 2.16 on p. 36. A first transponder radar cross section (RCS) measurement approach was introduced in Chap. 6.

The goal of the campaign described in this section was to verify the *Kalibri* prototype's measured backscatter with an independent measurement method. Instead of using an RCS measurement range, the spaceborne RADARSAT-2 SAR system was used as a measurement device. For reasons to be described later, the SAR system was considered radiometrically uncalibrated for this campaign; several deployed corner reflectors fulfilled the role of calibration standards.

For the data analysis in Sec. 7.4, hierarchical Bayesian modeling is used as described above. The research question answered in the case study (What is the transponder ERCS $\zeta_{e,t}$?) is conceptually equal to the derivation of the calibration factor K . The calibration factor links the SAR system indication values I to the measurement quantity ERCS, see Eq. (2.28), so the roles of knowns and unknowns are simply reversed:

$$\zeta_{e,t} = \frac{I}{K} \quad \Longleftrightarrow \quad K = \frac{I}{\zeta_{e,t}}. \quad (7.1)$$

The approach used in the case study is hence also applicable to the radiometric calibration of SAR systems.

7.3.2 Campaign Setup and Reference Targets

The campaign consisted of eight repeated RADARSAT-2 acquisitions of an area around the DLR site at Oberpfaffenhofen, Germany. 15 trihedral reference corner reflectors of two different sizes (inner leg lengths of 1.5 m and 3.0 m) and the *Kalibri* transponder prototype were deployed and aligned for each respective acquisition. The data were acquired between April 7 and April 25, 2013.

The RADARSAT-2 SAR system operates at a center frequency of 5.405 GHz. The maximal mode-dependent bandwidth is 100 MHz. Center frequency and maximal band-

Table 7.1: Corner reflectors with two different inner-leg lengths were used during the campaign. The peak RCS was computed with Eq. (7.2).

Size	Peak RCS	Number of targets
1.5 m	38.38 dBm ²	9
3.0 m	50.43 dBm ²	6

width are therefore identical to those of the Sentinel-1 mission for which the *Kalibri* transponder was designed.

All eight RADARSAT-2 products were acquired in the *Wide Ultra-Fine* mode in VV polarization and delivered as single-look complex (SLC) images. The products offer a nominal single-look geometric resolution of 1.6 m × 2.8 m (slant range × azimuth resolution) [148]. A high-resolution mode was chosen to increase the target-to-clutter ratio for the used point targets. Special care had to be taken in choosing the dynamic range of the processed products so that the peak of the transponder pulse response is still within the dynamic range of the processed image.

Within this study, the RADARSAT-2 system was considered radiometrically uncalibrated because of the mismatch between the specified relative radiometric uncertainty of the system (< 1 dB) [148] and the much lower uncertainty of 0.2 dB which was required in the *Kalibri* project. Therefore, reference point targets have been placed in the imaged scenes for manual, day-to-day calibration.

As mentioned before, in total 15 trihedral corner reflectors were used as reference point targets to derive the transponder ERCS. The comparatively large number was deemed necessary in order to profit from averaging during data analysis. Corner reflectors with two different inner leg lengths were deployed, resulting in two distinct values for their ERCS.

The RADARSAT-2 system operates at C-band with a small relative bandwidth of 2%. Under this precondition, the ERCS of the corner reflectors are, with in this case sufficient accuracy, equal to their RCS at the center frequency. As was explained in Sec. 2.4.2, the peak RCS of an ideal corner reflector can be estimated with the physical optics approximation

$$\zeta_{\text{CR}} = \frac{4\pi l^4}{3\lambda^2}, \quad (7.2)$$

where l is the inner leg length of the corner reflector and λ is the wavelength [129]. The resulting values are listed in Tab. 7.1.

7.4 Case Study: Data Analysis and Results

In this section, the proposed method is applied and the transponder ERCS is derived based on hierarchical Bayesian data analysis.

7.4.1 Overview

The RADARSAT-2 datatakes were processed by MDA and the resulting SLC images were the starting point for the data analysis.

The primary analysis goal is to derive the ERCS of the transponder and, equally important, an associated uncertainty statement. In principal, the ERCS $\zeta_{e,t}$ of the transponder can be derived if the ERCS of a reference target (placed in the same scene) ζ_{ref} is known according to the proportionality

$$\zeta_{e,t} = \frac{\mathcal{E}_t}{\mathcal{E}_{\text{ref}}} \zeta_{\text{ref}}. \quad (7.3)$$

Here, \mathcal{E}_t and \mathcal{E}_{ref} are the integrated point target intensities of the transponder and the reference target, derived from the processed SAR images and expressed as digital numbers.

The analysis is split into two parts:

1. Point target analysis: Extract the relative point target impulse response powers for all point targets in all scenes (see Sec. 7.4.2).
2. Parameter estimation: Set up a joint hierarchical Bayesian model to derive the estimated ERCS of the transponder and corresponding uncertainty from all datatakes (see Sec. 7.4.3).

7.4.2 Energy Estimation for Point Targets from SAR Images

The imaged point targets appear as bright crosses in the processed SAR image, see Fig. 7.3. As was discussed in Sec. 2.3.3, two methods are distinguished when deriving the point target energy: the peak and the integral method. Here, the integral method [69] is implemented.

The goal of this analysis step is to derive a table of relative point target intensities for all point targets in all images. Although an absolute scale is not necessary (and the RADARSAT-2 calibration factor is ignored here), it is crucial that the point target intensities derived from different images are all corrected with respect to each other. This is achieved by applying the (range-dependent) *beta naught* (β^0) look-up table delivered together with the images [141]. It was confirmed during this study that no obvious incidence-angle dependence remained in the data.

In accordance with Sec. 2.3.3, the following steps were performed to derive the integrated impulse response intensity of a target:

1. Define a search window around the point target in the georeferenced, processed image.
2. Find and record the brightest pixel location.
3. Define an analysis window, centered on the brightest pixel of the previous step.
4. Estimate the clutter power from four non-overlapping areas surrounding the peak.

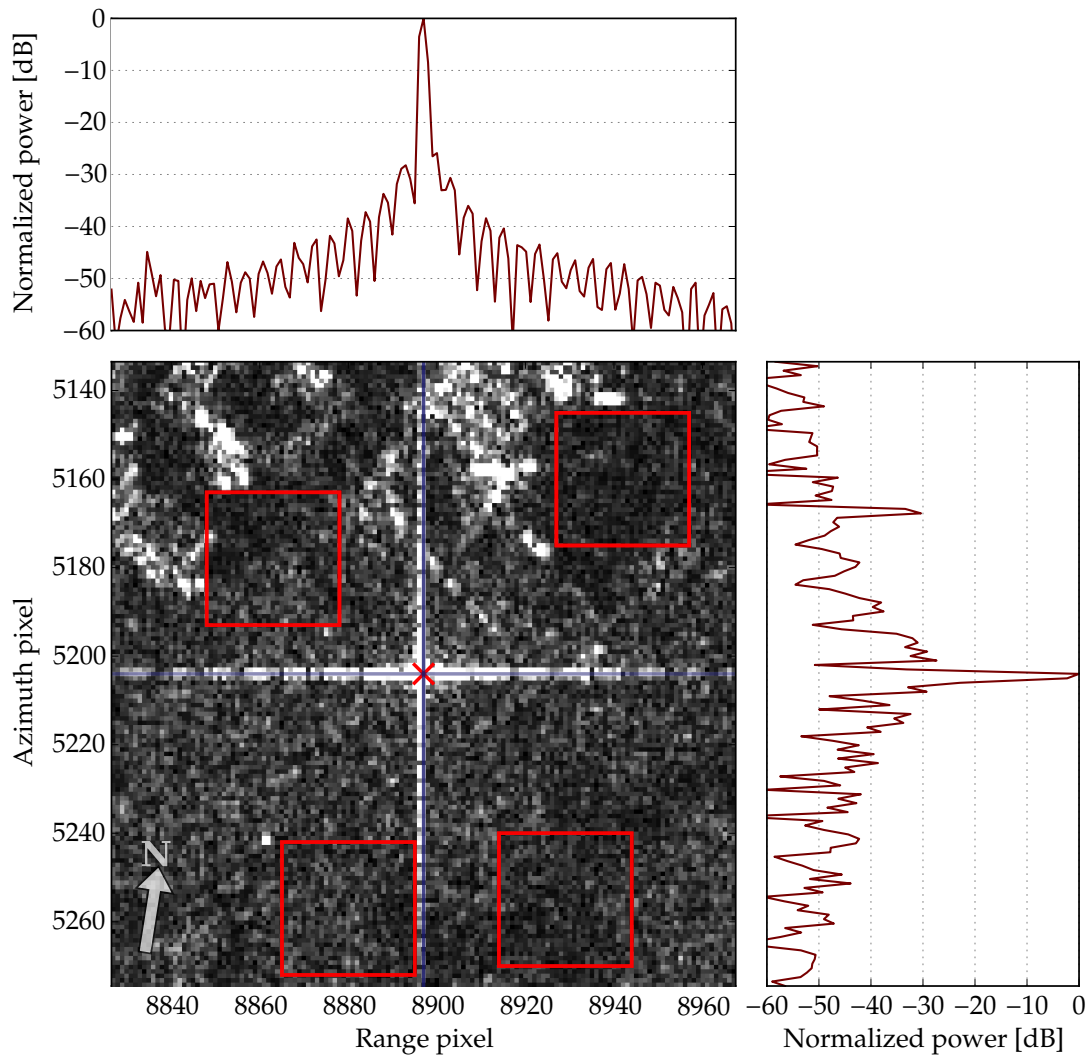


Figure 7.3: Transponder impulse response for the first overpass on April 7, 2013. A large target-to-clutter ratio of more than 50 dB is apparent. The four red squares indicate the areas from which the clutter power was estimated.

5. Integrate the target power over a cross area 21 pixels wide (a commonly used value [151], capturing all pixels with significant point target power).
6. Subtract the estimated clutter power from the integrated target power to get a clutter-compensated target power.

An exemplary transponder impulse response is shown in Fig. 7.3. The peak power lies more than 60 dB above the clutter level. This large separation is already an indication that clutter power compensation, in practice, is not necessary. Nevertheless, it was performed for all 126 analyzed point targets.

7.4.3 Bayesian Statistics and Hierarchical Model Fitting

The output of the previous processing step is a table which reports a relative point target power per target and scene. A graphical representation is shown in Fig. 7.4. This is the input data to derive the ERCS of the transponder and its uncertainty.

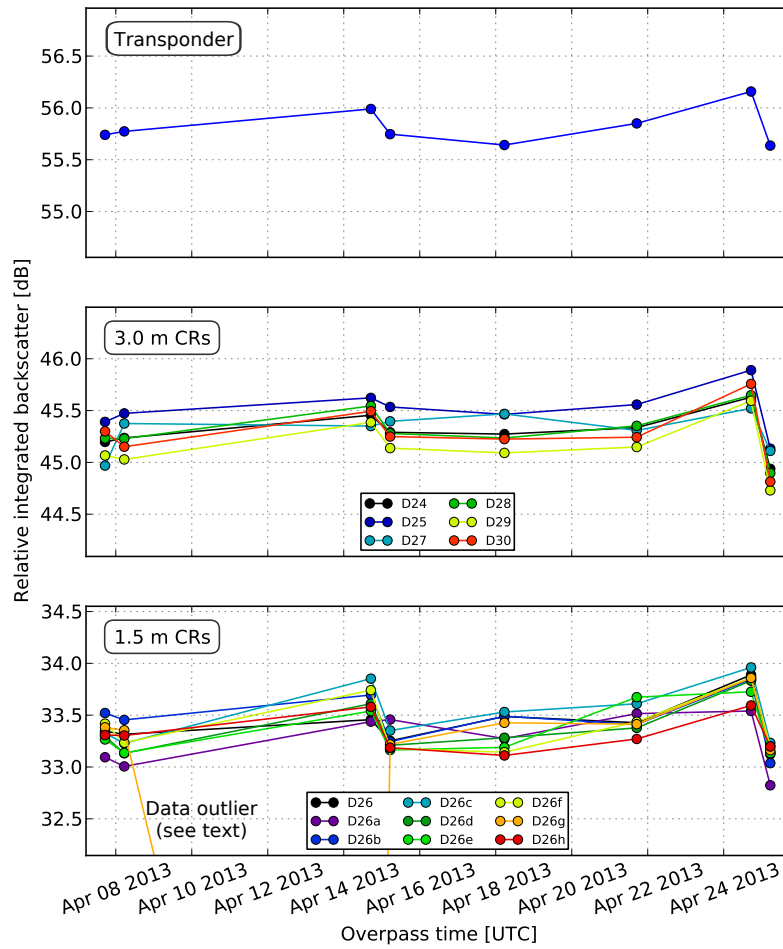


Figure 7.4: Uncompensated and unmasked data (i. e., including outlier), the immediate result of the processing described in Sec. 7.4.2. The data points lie on a common ordinate; for better visibility, one region per target group is plotted.

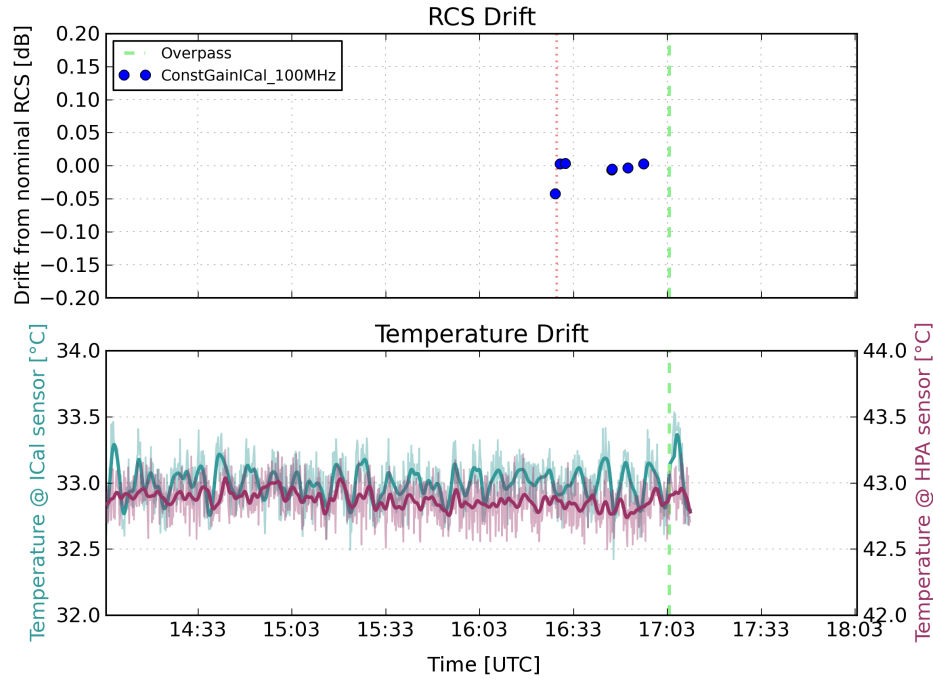


Figure 7.5: Estimated transponder drift and temperature stability measured with the two sensors labeled *ICal* and *HPA* (main influence for gain drift) for the overpass on April 21, 2013. The transponder operates with its nominal loop gain if a relative drift of 0 dB is detected. The loop gain was adjusted at 16:30 UTC (red dotted line), after which the drift was monitored (blue circles) until the overpass (dashed green line). After drift correction, the drift is estimated to be with high probability within the range $[-0.02; 0.02]$ dB at 17:03 UTC.

In order to estimate the target powers from all available data, daily RADARSAT-2 and transponder drifts need to be estimated and compensated. In a second step, the transponder ERCS can be computed with the measurement model Eq. (7.3). The final, combined uncertainty shall include the uncertainties which are incorporated in each step. As described before, this problem is solved with Bayesian statistics, which directly allows to estimate the uncertainty for all derived parameters through a joint probability model.

Daily RADARSAT-2 and Transponder Drifts

A plot of the original data from the first processing step was shown in Fig. 7.4. On first impression, the non-uniformity in the data is dominated by a daily systematic drift. For instance, independent of the radar target group (transponder, 3.0 m, or 1.5 m corner reflectors), a radiometric drift of more than 0.5 dB can be observed between the last and the previous overpass. The estimation and compensation of a daily RADARSAT-2 radiometric drift was hence included in the analysis.

Also, there is one immediately apparent data outlier: The corner at site D26g on the third day was clearly not aligned and was masked out prior to further analysis.

Besides the RADARSAT-2 drift, the (mostly temperature-dependent) transponder drift can be estimated and compensated. The compensation is based on gain drift compen-

Table 7.2: Daily transponder ERCS drift, estimated maximal error bounds on the estimated drift, and resulting standard uncertainties according to Eq. (7.4).

Overpass date	Estimated drift μ_s [dB]	Maximal error [dB]	Resulting σ_s [dB]
2013-04-07*	0.00	0.05	0.03
2013-04-08	0.00	0.02	0.01
2013-04-14	0.02	0.03	0.02
2013-04-15	-0.01	0.03	0.02
2013-04-18*	0.00	0.07	0.04
2013-04-21	0.00	0.02	0.01
2013-04-24*	0.05	0.05	0.03
2013-04-25	0.02	0.03	0.02

sation data recorded by the transponder itself. Exemplary transponder loop gain and temperature drift data are shown in Fig. 7.5. The dashed red line in the upper plot defines the point in time when the transponder ERCS was corrected to its nominal ERCS. The blue markers, on the other hand, indicate times at which the transponder RCS was merely estimated. In the case of Fig. 7.5, the drift at the overpass time is estimated to be nonexistent (0.0 dB). An upper bound on the uncertainty of this estimated drift can be stated from the plot as 0.02 dB, i. e., the true drift should lie, with high probability, in the range $[-0.02; 0.02]$ dB.

A similar assessment has been performed for all other days. The estimated transponder drifts and their estimated error bounds are listed in Tab. 7.2. A higher drift and/or error is stated for overpasses when a transponder software problem prohibited a nominal, temperature controlled operation of the prototype. These days are marked with a (*) in the table.

The estimated SAR system and transponder drifts are then included in the Bayesian model described in the next section.

Hierarchical Bayesian Model

The Bayesian model requires the definition of priors, i. e., probability distributions for all model parameters. These are defined in the following.

For the eight overpass days d , eight different daily RADARSAT-2 drifts r_d need to be determined. It is estimated from Fig. 7.4 that the daily drift, expressed as a scaling factor, will certainly be in the range 0.4 to 1.6 (i. e., -4 dB to 2 dB). The prior can thus be written as $r_d \sim U(0.4, 1.6)$, where $U(a, b)$ describes a uniform distribution with lower and upper bounds a and b , respectively.

Besides the RADARSAT-2 drift, the transponder drift needs to be modeled. The values in the third column of Tab. 7.2 define maximum error bounds, i. e., a lower bound a and an upper bound b . According to [87], this information can be converted to a standard uncertainty (i. e., standard deviation σ) with

$$\sigma = \frac{1}{\sqrt{12}}(b - a). \quad (7.4)$$

Hence, the daily transponder drift s_d is modeled as a normal distribution $N(\mu, \sigma)$, where

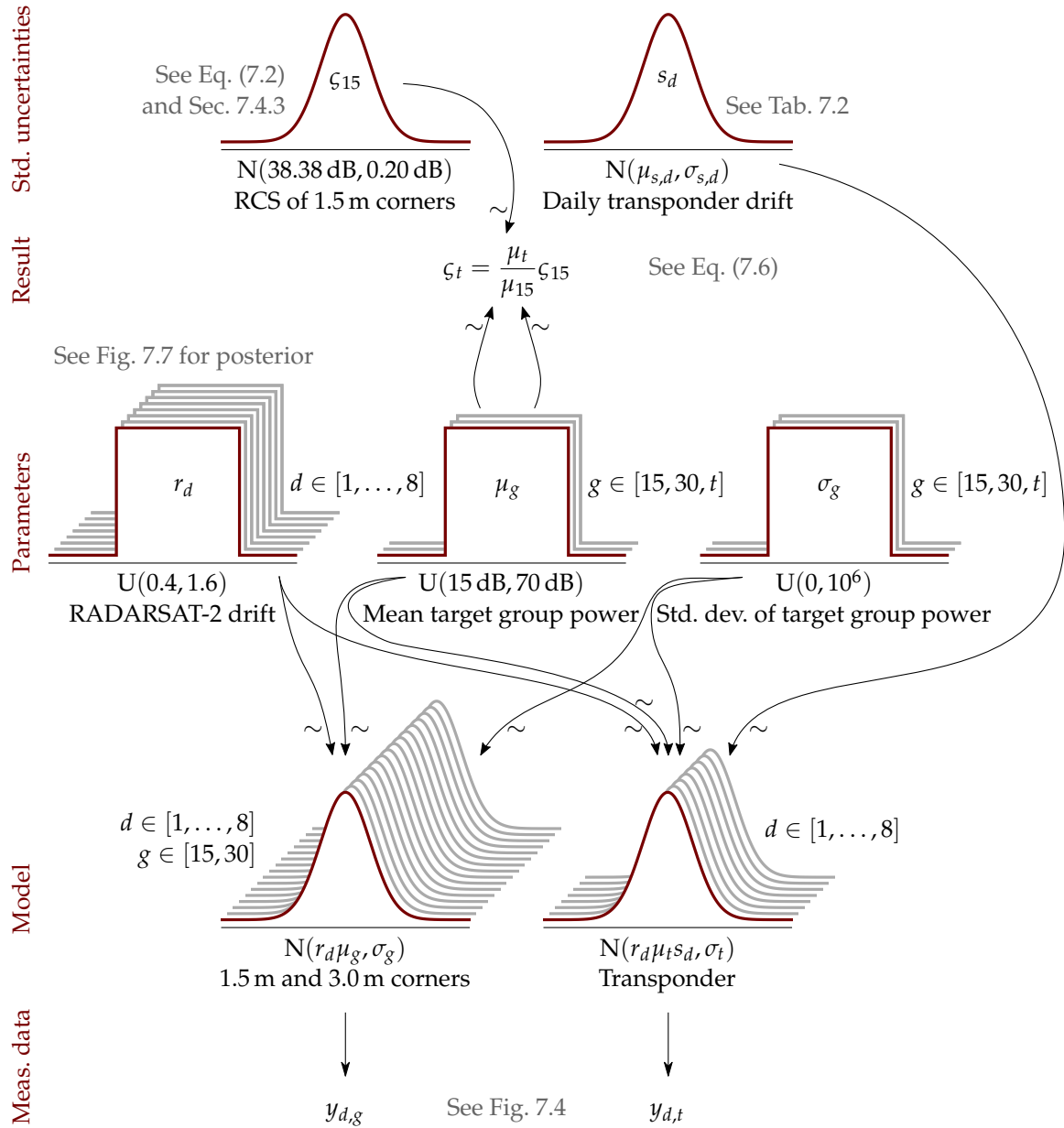


Figure 7.6: Diagram of the hierarchical Bayesian model, which shows how the distributions of different random variables contribute to the distribution of the wanted random variable ζ_t , which describes the estimate of the transponder RCS. The symbol \sim means that a parameter is drawn from the respective distribution; $U(a, b)$ is a uniform distribution with a probability density unequal zero within the range $[a; b]$; $N(\mu, \sigma)$ is a normal distribution with mean μ and standard deviation σ ; d stands for one of the eight over-pass dates; g describes the target group; ζ_{15} is the uncertainty in the RCS knowledge of the 1.5 m reference corner reflectors; s_d is the uncertainty attributed to the knowledge of the daily transponder drift; μ_t and μ_{15} describe the uncertainty in the estimate of the mean point target power for the transponder and 1.5 m corners, respectively; $y_{d,g}$ and $y_{d,t}$ are the observed data samples, both for the 1.5 m and 3.0 m corner reflectors, and for the transponder. The diagram style is inspired by [104].

μ describes its mean and σ its standard deviation: $s_d \sim N(\mu_{s,d}, \sigma_{s,d})$. The best estimate $\mu_{s,d}$ is taken from Tab. 7.2, where also the $\sigma_{s,d}$ (resulting from Eq. (7.4)) are listed.

It is assumed that all measured point target powers of all targets within one target group g (transponder t , 3.0 m “30”, and 1.5 m corner reflectors “15”) belong to the same population, which can be described by a normal distribution $N(\mu_g, \sigma_g)$, having the group location (mean) μ_g and group scale (standard deviation) $\sigma_g > 0$. A normal distribution was chosen for two reasons: First, because it is symmetric, and no plausible reason can be found for an asymmetric distribution. Second, the distribution of the measured values results from several physical effects like thermal drift of the satellite instrument, satellite and target alignment errors, target stability, clutter, etc., so that the central limit theorem suggests a normal distribution as well. Each μ_g and σ_g are modeled to originate from uniform distributions: $\mu_g \sim U(10^{1.5}, 10^7)$ (i. e., $U(15 \text{ dB}, 70 \text{ dB})$) and $\sigma_g \sim U(0, 10^6)$. The σ_g are nuisance parameters, i. e., they are not required to derive the ERCS of the transponder, but they are nevertheless necessary in order to describe the normal distributions N_g .

Now, for every overpass d , the data $y_{d,g}$ are fitted depending on their group $g \in [t, 15, 30]$:

$$\begin{aligned} y_{d,30} &\sim N(r_d \mu_{30}, \sigma_{30}), \\ y_{d,15} &\sim N(r_d \mu_{15}, \sigma_{15}), \\ y_{d,t} &\sim N(r_d s_d \mu_t, \sigma_t). \end{aligned} \quad (7.5)$$

This way, the daily drift parameter r_d is a shared parameter which is estimated from all available data, exploiting the fact that the daily drift should be equal for data across all three groups.

Estimating parameters with the model equations (7.5) results in estimates for the relative point target energies per group (μ_t , μ_{30} , and μ_{15}) after drift compensation.

The next step is to relate the point target powers to ERCS. For this, a reference ERCS is necessary. It was chosen to be the group ERCS of the 1.5 m corner reflectors.¹

The value of the reference ERCS is modeled as $\zeta_{15} \sim N(10^{3.838} \text{ m}^2, 10^{0.02} \text{ m}^2)$, i. e., $N(38.38 \text{ dBm}^2, 0.2 \text{ dBm}^2)$. Its location is defined by Eq. (7.2). The standard deviation, or standard uncertainty according to [87], characterizes the state of knowledge about the reference ERCS. The statement that the ERCS of 1.5 m corner reflectors can be determined with Eq. (7.2) up to a standard uncertainty of 0.2 dBm^2 is certainly the weakest point in the argument. It is based on previous experience gained from numerical field simulations on corner reflectors of the same size at X-band, and on plausibility.² Nevertheless, it cannot be proofed and further work should be conducted in determining the

¹The not more than 7 years old 1.5 m corner reflectors were, mechanically speaking, in a better shape than the more than 20 years old 3.0 m corner reflectors, which show apparent deformations due to damages and their continuous exposition on a field. Mechanical deformations result in a reduction of the monostatic ERCS of a corner reflector because some of the incident power is reflected away from the incident beam direction. The visual observation was confirmed by looking at the ERCS dispersion within each group: $\sigma_{15} = 0.15 \text{ dBm}^2$ and $\sigma_{30} = 0.41 \text{ dBm}^2$. These observations lead to the conclusion that the ERCS of the utilized 3.0 m corner reflectors should not be used as an absolute reference, and that the 1.5 m corner reflectors provide a better link to an absolute ERCS. Nevertheless, the 3.0 m corner reflectors and their large ERCS helped in determining more accurately the daily RADARSAT-2 drift.

²A standard uncertainty of 0.2 dBm^2 is plausible because with it the theoretical RCS difference of 3.0 m and 1.5 m corner reflectors can be (well) explained. The theoretical difference, according to Tab. 7.1, is 12.05 dBm^2 . The difference between the estimated mean target powers (in MCMC parameters: $\mu_{30} - \mu_{15}$)

knowledge of a trihedral corner reflector's ERCS.

According to the measurement model equation (7.3), the final transponder ERCS is now deterministically related to the already derived model parameters through

$$\zeta_{e,t} = \frac{\mu_t}{\mu_{15}} \zeta_{e,15}. \quad (7.6)$$

The complete Bayesian model described above is visualized in Fig. 7.6.

Posterior Simulation

The hierarchical model developed in the previous section is now solved iteratively with the numerical MCMC method (see Sec. C.2). The goal is to find the most probable set of parameters (e. g. r_d , μ_{30} , etc.) which is most likely in describing the given data.

If the model is well posed, then the iterative MCMC will converge to the true distribution of the parameters. This also means that the first simulation runs, also called draws, need to be discarded, and only values after this *burn in* period should be considered. To improve the required independence between successive draws, only every n th simulation draw is considered, i. e., *thinning* is applied.

In order to compute the parameters of the hierarchical model, 2×10^5 simulation runs were conducted, allowing for a burn in of 1×10^4 and a thinning of 20. These parameters were determined empirically by observing the traces and autocorrelations of the model parameter draws.

MCMC Results

The solution of the hierarchical model describes all parameters at the same time. Nevertheless, the results can be visualized step by step.

The first result is the estimated RADARSAT-2 drift. The estimated drift is shown in Fig. 7.7. The error bars indicate the range of values which define the 95 % probability intervals. From this it can be seen that the drift between the first and the second overpass is statistically not significant, but the drift between the last two overpasses, for instance, is. The drift was estimated with a standard uncertainty (according to [87]) of always less than 0.1 dB.

This estimated RADARSAT-2 drift can now be applied to the measured data. The original data in Fig 7.4 appear now much more uniform, see Fig. 7.8. No apparent systematic drift remains.

After RADARSAT-2 drift compensation, the estimated transponder drift can be compensated in the upper plot in Fig. 7.8; Fig. 7.9 results. Already visually it becomes clear that the transponder drift is small in comparison to the remaining dispersion of the measurement data. This can also explain why at times the transponder drift compensation results in updated values which lie further away from the population mean.

is 11.92 dB, i. e. 0.13 dB away from the predicted value despite the already discussed deformation of the 3.0 m corner reflectors. It is still possible though that the RCS of all corner reflectors is, due to deformation and the approximate nature of Eq. (7.2), lower than assumed. Nevertheless, Eq. (7.2) seems to characterize the absolute RCS of trihedral corner reflectors despite some mechanical deformations with a standard uncertainty of not more than 0.2 dBm².

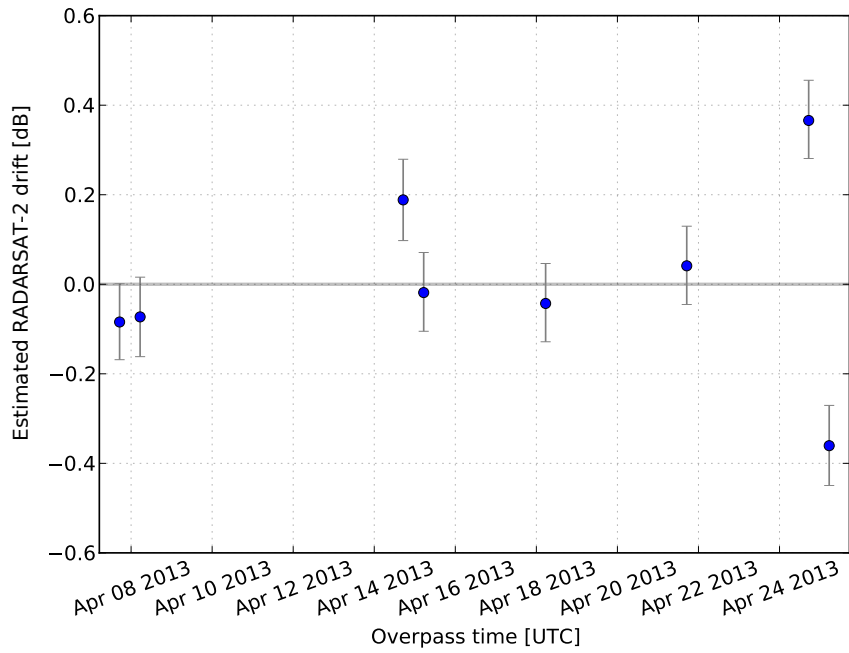


Figure 7.7: Estimated daily drifts r_d of the RADARSAT-2 system. The error bars indicate 95 % highest-probability density intervals.

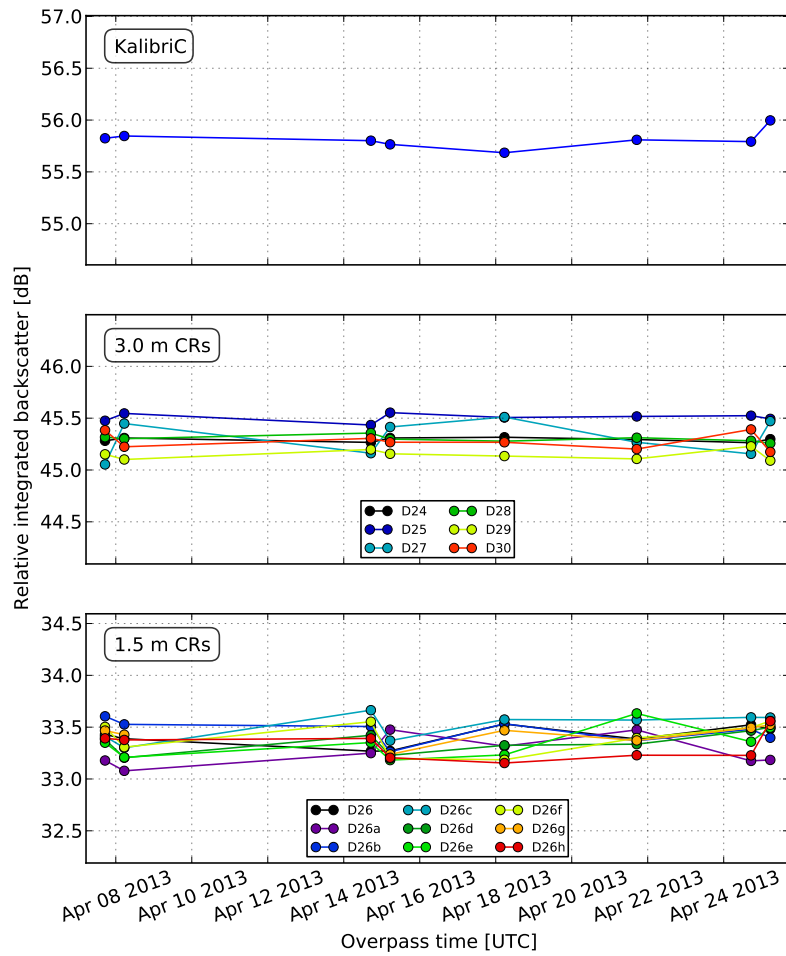


Figure 7.8: Measured impulse response powers with RADARSAT-2 drift compensation (see Fig. 7.7) applied. The dispersion within one target group is now greatly reduced with respect to Fig. 7.4.

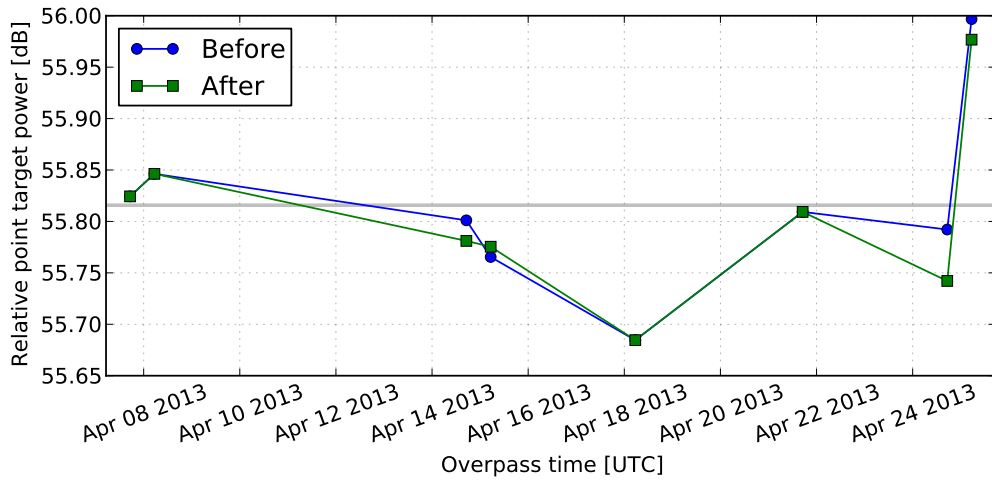


Figure 7.9: Visualization of the *Kalibri* transponder drift compensation with data from Tab. 7.2. For visual guidance, the gray line marks the sample mean of the data before transponder drift compensation.

Now the most important result of the MCMC simulation is the derivation of the transponder ERCS $\zeta_{e,t}$ and its standard uncertainty. The resulting ERCS of the transponder is estimated to be 60.80 dBm^2 with a standard uncertainty according to [87] of 0.206 dBm^2 . The 95 % highest probability density interval is given as $[60.38, 61.17] \text{ dBm}^2$. Note that the standard uncertainty is clearly dominated by the assumed ERCS knowledge uncertainty of the 1.5 m corner reflectors of 0.2 dBm^2 .

7.4.4 Posterior Predictive Checks: Model Verification

In Sec. 7.4.3, a normal distribution was chosen in order to model the observed integrated pixel intensities. Here it shall be demonstrated that this model is indeed plausible and adequate.

Focusing on the transponder data $y_{d,t}$, test statistics $T(y_{d,t})$ of the observed data can be compared to the test statistics of replicated data samples $T(y_{d,t}^{\text{rep}})$, i. e., samples which were generated numerically through the model [66, p. 188]. If this analysis is conducted for the four test statistics mean, standard deviation, minimum value, and maximum value across all eight overpasses, Fig. 7.10 results. A good model fit is found if the test statistic of the observed data (vertical line) lies close to the center of mass of the histogram. As a criterion, the p -value can be used, which states the relative number of samples above the observed test statistic. At a confidence level of 95 %, the p -value should therefore be within the range of 2.5 % to 97.5 %. This is observed for all four test statistics, and especially the most important aspect of the model, its mean, is well reproduced by the model with a p -value close to 0.5.

7.4.5 Plausibility Check with Classical Statistics

As a means of verification, the result of the previous section can be reproduced approximately with frequentist statistics. One way of handling the hierarchical data structure is to derive one transponder ERCS per overpass, and then to combine the resulting eight ERCS values through averaging into an overall transponder ERCS. The disadvantage of

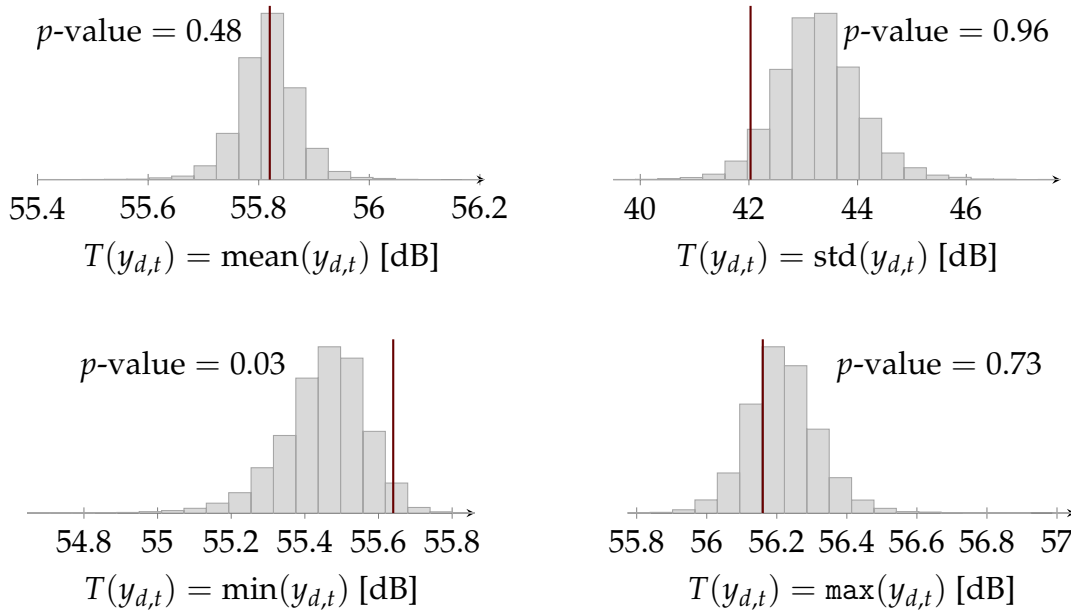


Figure 7.10: Posterior predictive checking for predicted (modeled) transponder data $y_{d,t}^{\text{rep}}$ and four different test statistics. The simulated data are shown as a histogram, and the test statistics derived from the observed data are shown as solid vertical lines. It can be seen that especially the most important aspect of the predicted data, its mean, is well modeled.

this simplified approach in comparison to the approach using hierarchical Bayesian data analysis as shown before is the loss of information about the uncertainty of each of the eight transponder ERCS values, which does not contribute to the combined uncertainty. After averaging, an estimated standard deviation of the mean can be derived from the eight estimated ERCS values, resulting in a standard uncertainty for the estimated transponder ERCS [87]. The third step is then to derive a combined standard uncertainty by incorporating the ERCS knowledge uncertainty of the 1.5 m corner reflectors of 0.2 dB through the analysis method of “root-sum-square”. Lastly, the expanded uncertainty [87] with a coverage factor of $k_c = 2$ is derived.

This approach results in an estimated transponder ERCS of 60.80 dBm² with a standard uncertainty of 0.20 dB or an expanded standard uncertainty of 0.41 dB at a confidence level of 95 % ($k_c = 2$). The result confirms the findings of the previous section.

Note that once again the combined uncertainty is dominated by the assumed ERCS knowledge uncertainty of the 1.5 m corner reflectors. The transponder’s combined backscatter uncertainty is sufficiently low to permit the calibration of SAR instruments like Sentinel-1 to an absolute radiometric uncertainty of 1.00 dB at a confidence level of 99 %, provided that the SAR instrument is otherwise sufficiently precise [162].

7.5 Discussion of Hierarchical Bayesian Data Analysis for Radiometric Calibration

The advantages of using hierarchical Bayesian data analysis for radiometric calibration were laid out before: The approach can jointly answer typical analysis questions in

radiometric calibration while fully exploiting the hierarchical nature of external calibration data and fulfilling the requirement on reporting measurement uncertainties and confidence intervals. This section shall add a critical discussion of the proposed method.

First, the most recognized approach in metrology for deriving measurement uncertainties is the ISO *Guide to the expression of uncertainty in measurements* (GUM) [87], see Sec. 2.2.2. The GUM, which was introduced in 1993, fundamentally applies frequentist statistics, and is not directly compatible with a Bayesian approach as used in this chapter. Nevertheless, the current GUM approach has been repeatedly criticized, and Bayesian methods have been proposed as a consistent and universally applicable replacement [95, 197, 201]. In practice, uncertainties derived by Bayesian statistics are often equal or approximately equal to uncertainties derived by frequentist statistics [95] so that both approaches lead to the desired results. Yet thanks to the availability of numerical tools, Bayesian computations are now often simpler than frequentist approaches if hierarchical data are analyzed [15]. Therefore, taking a Bayesian approach for deriving the measurement uncertainty of the calibration factor seems justified.

From the outset, using MCMC simulations to infer model parameters appears to be more complicated than employing frequentist statistics. The added initial work is offset though by a joint probability model, which allows to derive model parameters on arbitrary hierarchical levels without loss of information. Hence the improved analysis justifies the initial extra work.

If numerical methods like MCMC are used, problems of non-convergence can occur and must be addressed during analysis. Care must be taken in the assessment of simulation results, and plausibility checks such as shown in Sec. 7.4.4 should be conducted.

7.6 Conclusions

The length of the commissioning phase for a new spaceborne SAR instrument is largely determined by the time required to collect necessary calibration data. Maximally exploiting the available information after recording does not only improve the reliability of the data analysis itself, but it also helps in reducing the commissioning phase duration. In this chapter, I introduced for the first time hierarchical Bayesian data analysis to the field of SAR calibration to improve on current techniques. In particular, my contributions are:

- First I identified that most data analyses in SAR calibration are based on grouped data (data grouped by beam, SAR mode, orbit direction, target type, etc.), but that current analysis methods based on frequentist statistics do not exploit this structure.
- Then I established that hierarchical Bayesian data analysis is a better fit to such problems. Per-group and shared parameters coexist in a joint probability model, and a hierarchical structure reflects the nature of the data. Additionally, all estimated parameters are not point estimates, but are described by densities in the Bayesian approach so that meaningful statements about the uncertainties of the parameters can be made, which is a major benefit for any calibration activity.

- In a case study analysis on transponder calibration, I could show that the approach can well handle hierarchical data in practice as, in this case, per day SAR instrument drifts and per target group ERCSSs. I could confirm the outcomes with posterior predictive checks and a comparison with the results yielded by frequentist statistics.

The transponder calibration approach as described in this chapter was selected as the most accurate approach for calibrating DLR's transponders in preparation of the Sentinel-1 calibration campaign [156]. The other two investigated approaches were indoor measurements in a compact test range, and measurements according to the three-transponder method from Chap. 6.

In order to convert the case study approach to an operational uncertainty analysis procedure for SAR missions in the future, a database of point target measurements could be set up. Filling the database incrementally with measurements of permanently installed reference point targets over the mission lifetime would allow to continually derive radiometric uncertainty estimates based on Bayesian statistics.

The rising popularity of the Bayesian approach in many other fields than SAR calibration has greatly benefited from the practical progress in Bayesian computations, diminishing much of the earlier operative hurdles. With the work presented in this chapter, the adoption of the Bayesian approach in radiometric SAR calibration has now taken an important first step.

8 Conclusions and Outlook

The trouble with measurement is its seeming simplicity.

— Author unknown

A synthetic aperture radar (SAR) system is not simply an imaging system for target detection, it is a veritable measurement instrument which measures and maps the terrain reflectivity. The results of these measurements are used for many demanding applications such as soil moisture or biomass estimation. Although any such measurement will readily yield a quantity value, reporting measurement results along with a reliable estimate of the measurement uncertainty is a challenging task. Furthermore, ensuring that different measurements, possibly acquired with different sensors, are comparable on a common scale requires metrological traceability. Traceability is the property of a measurement result whereby it can be related to a known reference through an unbroken chain of calibrations, considering all measurement uncertainties.

It was argued that today's core problem in radiometric SAR measurements is the missing metrological traceability, and the question was raised how this traceability could be achieved. The problem was first of all attributed to the definition of the radiometric measurement quantity. The currently used quantity radar cross section (RCS) by its definition does not incorporate phase, and is furthermore generally a frequency and angular dependent property. The pixel intensity in a SAR image however results from a complex filtering operation, whose output depends on the target properties within a spectral and angular range, and on the transfer function of the SAR system in range and in azimuth.

In order to answer how metrological traceability can be achieved for radiometric SAR measurements, I made the following novel contributions in this work:

- Introduction of the novel radiometric measurement quantity *equivalent radar cross section* (ERCS) in Chap. 3.
- Development of a numerical approach for relating the frequency and angular dependent backscatter of imperfect calibration point targets to their ERCS in Chap. 4.
- Identification of the SAR passband problem, development of an analytical approach for quantifying it, and proposition of several strategies to take the SAR passband problem into account for the calibration of future SAR systems, see Chap. 5.
- Development of a novel transponder calibration approach, the *three-transponder method* (3TM), thanks to which traceable radiometric calibrations are possible based on a comparably simple and accurate length measurement, see Chap. 6.

- Introduction and demonstration of Bayesian hierarchical statistics to the field of SAR calibration in Chap. 7 in order to derive estimates and measurement uncertainties especially for hierarchically structured data.

These contributions discuss the central topics required for traceability: definition, measurements, calibrations, standards, and uncertainty analysis.

Traceability is especially relevant when different parties are involved in sharing calibrated data. The most important first step in achieving radiometric traceability in SAR is the introduction of a standardized definition of the actual measurement quantity. As discussed, RCS has to be superseded. The introduced quantity ERCS is at the moment the only contender, but further discourse in the community may lead to additional developments.

The past has shown that probably the best suited forum for discussing and formulating a recommendation on a standard definition is the SAR subgroup of the Committee on Earth Observation Satellites (CEOS) Working Group on Calibration and Validation (WGCV). In fact, the author had repeatedly brought up the topic at this workshop [48–50], and recently ERCS was adopted as a *draft proposal* by the community [29]. To reach a common definition is only a prerequisite though, and its application in practice is yet to follow. Changing a definition which is so central to the trade-offs in SAR system design realistically cannot be achieved in the middle of a running mission. Therefore the goal must be to introduce the new definition upfront when the first version of the system requirements for a new SAR mission are formulated.

As a next step to achieve better data comparability across SAR missions and modes, the SAR passband problem and its possible resolution from Sec. 5.5.2 should be addressed. Radiometric measurements both depend on the terrain and on the SAR system properties. The terrain is to be measured and is outside the control of the metrologist, so what needs to be controlled are the properties of the SAR system. By introducing a set of standardized passbands (mostly defined by center frequency, range bandwidth, azimuth angular range, and apodization functions), true radiometric measurement comparability is achieved. The proposed approach follows the same idea that was implemented about 50 years ago when standard passbands were adopted in the field of stellar photometry [18].

The discussion on the passband problem in Chap. 5 was limited to the typical case of linearly frequency-modulated transmit pulses. Other signals such as those based on orthogonal frequency division multiplexing (OFDM) have recently gained traction, either to realize multiple transmitter and multiple receiver SAR systems (often dubbed MIMO SARs) or to make additional use of the radar signal spectrum for data communication [96, 102, 185]. The influence of such advanced radar signals on radiometric measurements is currently unknown, and the problem will have to be addressed in the future. Particularly challenging seem to be radar instruments for which the pulse spectrum changes per pulse as is the case for communication systems because the interaction of the passbands of the radar target and the SAR system would change on a pulse-by-pulse basis.

Beyond revised definitions, radiometric SAR measurements would also benefit from more accurate measurement standards. Their radiometric uncertainty currently limits the achievable radiometric uncertainty of the complete SAR system after calibration. The three-transponder method from Sec. 6.3 is an approach that is expected to yield highly accurate transponder calibrations in the future. Nevertheless more work is missing

for the commonly used trihedral corner reflectors, whose radiometric uncertainties are currently not well understood. A numerical model should be developed which allows to determine a corner's RCS and ERCS while incorporating corner imperfections. At the moment, it cannot be reliably quantified by how much its backscatter is affected due to possible metallic plate deformations, a finite edge thickness, the mounting structure, and the interactions with the environment, and so an uncertainty analysis according to the standard "Evaluation of measurement data – Guide to the Expression of Uncertainty in Measurement [87] (GUM)" cannot be satisfactorily derived.

The mathematical concept behind the three-transponder method (3TM) from Chap. 6, i. e., the exploitation of three pairs of relative measurements, has already spurred a new research idea: The concept was adapted by the author to accurately determine the polarization plane of linearly polarized antennas such as those used in calibration transponders. Up to now the electromagnetic polarization planes of transponder antennas have been approximated simply by the mechanical alignment of the antenna, e. g. with respect to the rotation of one of the antenna walls. The novel approach allows to replace this approximation with an actual measurement, so previously undetected errors caused for instance by a slightly bend feeding pin can be compensated. Measurements following this new approach have already been completed, and the results are in preparation for publication. The improvement in the knowledge of the polarization plane will allow more accurate polarimetric SAR system calibrations, which depends on accurately known calibration standards. This is especially important with respect to the advent of further compact polarization SAR [128, 178] and fully polarimetric SAR systems.

The accuracy of radiometric SAR measurements is currently limited by two factors: imperfect corrections, and imperfect calibration. Whereas the presented 3TM already offers a significant improvement for the second challenge, the correction and data normalization step has become more complex and more important than ever before. Calibration by itself is rather pointless if one cannot assume a sufficiently stable and well-behaved system which allows to carry over calibration results to later measurements, possibly executed with a different antenna beam, processor setting, or under different atmospheric conditions. As a current example, modern SAR systems which exploit digital beam-forming, such as for the proposed Tandem-L mission, add further correction terms and therefore uncertainties to radiometric measurements [101, 206]. The trend of replacing a complete system characterization based on measurements with system models and a few selected validation measurements is therefore unbroken because otherwise the calibration effort would be too costly. Here the risk of introducing errors or failing to notice additional measurement uncertainties is large. It is foreseeable that the effort invested for system characterization, correction, and monitoring will hence have to increase in the future. Although potentially cheaper monitoring techniques have been developed for this purpose which do not depend on man-made calibration targets (such as the one exploiting permanent scatterers [35]), further assumptions need to be made during analysis so that in the end point targets with accurately known properties remain indispensable. As systems become more complex, an inherent trade-off between coverage, resolution, and radiometric measurement uncertainty materializes which must be constantly balanced in order to achieve maximal utility of the SAR system.

The effort invested in reducing measurement uncertainties and achieving metrological traceability for radiometric SAR measurements will in any case lead to a strengthening of the field. Genuine data comparability allows a more seamless and dependable data

exchange across missions. Combining data from missions such as RADARSAT-2 and Sentinel-1 leads to a higher temporal and spatial coverage, possibly inspiring new products or even applications. Achieving traceability also permits to use SAR data for legal metrology, where a proof of the data quality e. g. for conformity assessments is required. Furthermore, reports on apparent mis-calibrations between different sensors should become a problem of the past when traceability is achieved [12, 134].

The SAR approach and its implementations for Earth observation including radiometric measurements have seen tremendous improvements during the past decades. Uncountable achievements have been reached and no doubt many still lie ahead!

A Pseudo Code for the Method of Point Target SAR Simulation

The following describes the algorithm of the point target synthetic aperture radar (SAR) simulator as discussed in Chap. 4.

With the layout of the simulated data arrays shown in Fig. A.1, the three main processing steps

- raw data generation,
- SAR processing, and
- point target analysis

(also see Fig. 4.3 on p. 60) can be broken down in pseudo-code as detailed below. In a first step, one-dimensional baseband azimuth and range chirps are generated:

Data: SAR system parameters (geometry, frequency, bandwidth, etc.); point target parameters

Result: One-dimensional azimuth and range chirps

```
/* Generate 1D range chirps */
idealRgChirp ← bbRgChirp(SAR system parameters);
 $H_t^{(rg)}$  ← loadTransferFunc(point target parameters);
 $\hat{H}_t^{(rg)}$  ← applyGainCompensation( $H_t^{(rg)}$ , gain compensation settings);
interferenceSignal ← loadIFSignal(interference signal data);
staticRgChirp ←  $\hat{H}_t^{(rg)}$  * idealRgChirp;
staticRgChirp ← staticRgChirp + interferenceSignal;

/* Generate 1D azimuth chirps */
idealAzChirp ← bbAzChirp(SAR system parameters);
 $H_t^{(az)}$  ← loadAngularDependency(point target parameters);
staticAzChirp ←  $H_t^{(az)}$  * idealAzChirp;
```

The idealRgChirp and idealAzChirp baseband chirp signals are derived from the SAR system parameters. The idealRgChirp signal represent the transmitted chirp and depends on the chirp settings like center frequency, bandwidth, and sampling rate. The signal which is reflected by the point target is deformed by the following target dependent properties:

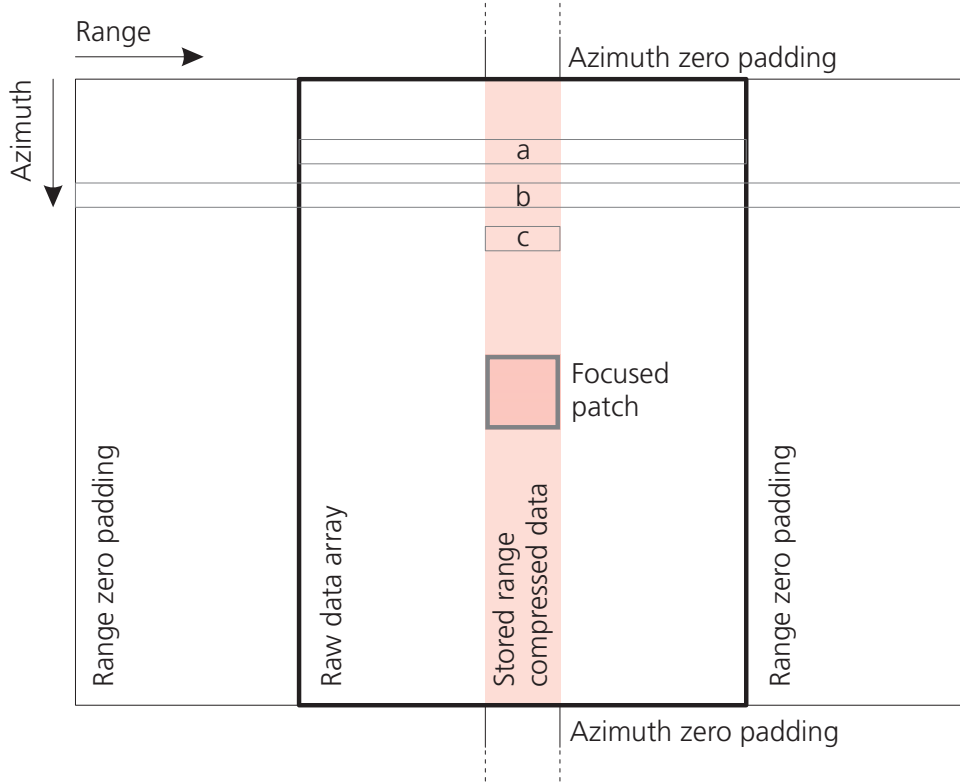


Figure A.1: Data arrays during range and azimuth processing. The labels a , b , and c are explained in the text.

- one or several chained complex target transfer functions $H_t^{(rg)}$,
- a two-way angular pattern $H_t^{(az)}$ which represents the point target's angular backscatter dependence,
- interference signals (e. g. due to imperfect isolation between local oscillator (LO) and radio frequency (RF) ports of a mixer, or multipath effects),
- and different transponder gain compensation strategies.

These effects either modify the range or the azimuth chirp due to the separability of the effects in range and azimuth direction. The resulting staticRgChirp and staticAzChirp contain all point target dependent effects which do not change per range or azimuth line.

The definition of the one-dimensional chirps allows to derive complex valued range lines of the raw data array by incorporating the azimuth history into the range chirps:

Data: one-dimensional, target-weighted chirps; target noise parameters

Function generateRgLine(*azimuth time t_a*) **is**

```

    noise ← generateNoise(noise parameters);
    rgChirp ← staticRgChirp + noise;
    rawRgLine ← rgChirp · staticAzChirp[ $t_a$ ];
    return rawRgLine;

```

end

In this function transponder noise is added because the noise is modeled to be independent between different range lines.

In the next step, the raw data are focused in the frequency domain, first in range, and then in azimuth, with the range-Doppler algorithm (RDA) described in Sec. 2.1.3. The processing filters in range and azimuth, $rgFilter$ and $azFilter$, are derived from the ideal chirps and are weighted to improve side-lobe suppression. The RDA depends on the fast Fourier transform (FFT) and therefore requires zero-padding of the data array so that a straight-forward implementation would require twice as much memory than the original raw data array (see extended area in Fig. A.1). In the present implementation each range line a in Fig. A.1 is processed separately so that zero-padding is limited to a single range line b . After range compression and back-conversion to the time domain, only the central part c is kept in the intermediate array which appears highlighted in Fig. A.1. The algorithm for azimuth compression is identical in principal. Since only the central patch is required for subsequent point target analysis, only a fraction of the total number of azimuth lines actually needs to be processed, further reducing processing time. The SAR processing step is therefore:

Data: Ideal one-dimensional azimuth and range chirps

Result: Focused patch of range-compressed data (see central square in Fig. A.1)

$rgFilter \leftarrow getWeightedFilter(idealRgChirp);$

$azFilter \leftarrow getWeightedFilter(idealAzChirp);$

forall the range lines at azimuth times t_a do

$rawRgLine \leftarrow generateRgLine(t_a);$

 compress $rawRgLine$ with $rgFilter$ in frequency domain;

 keep central part c of result array in memory;

end

/* Intermediate resulting array (highlighted in Fig. A.1) has the shape of a strip */

forall the azimuth lines around point target peak do

 compress azimuth line with $azFilter$ in frequency domain;

 keep central part of result array in memory;

end

/* Final result has the shape of a square */

Since the raw range lines are generated one by one inside of the processing loop, the main memory requirement is driven by the array dimension in azimuth direction, see the highlighted vertical strip in Fig. A.1. This strip holds the range-compressed data. The full complex-valued raw image is never completely held in memory which allows to simulate high-resolution SAR data with moderate computing hardware.

Many processing steps which are found in an operational SAR processor have been deliberately left out. Therefore, range cell migration, instrument antenna pattern compensation, pointing correction, motion compensation, etc. have been excluded. Instead, the raw data are generated in such a way that the mentioned effects do not need to be reversed during processing. This results in a processor which does not introduce any additional perceived radar cross section (RCS) deviations not caused by the target during the raw data generation step. Nevertheless, the frequency dependent focusing (e. g. a Hamming window) is included in the processing step.

The conclusive step of the analysis is the point target analysis according to the peak and

integral method described in Sec. 2.3.3:

```

Result: integratedPixelIntensity (integral method), peakPixelIntensity (peak method)
interpolatedSARData  $\leftarrow$  interpolate(complexSARData);
forall the pixels in integration cross area of interpolatedSARData do
|   integratedPixelIntensity  $\leftarrow$  integratedPixelIntensity + |SARDataSample|2;
end
peakPixelIntensity  $\leftarrow$  max(|interpolatedSARData|2);

```

The integratedPixelIntensity equals the indication value \mathcal{E}_p derived with the integral method, and peakPixelIntensity equals \mathcal{E}_p derived with the peak method. With this, the final numerical results of a single point target SAR simulation have been derived.

B Functions of Random Variables

This appendix examines the properties of random variables after function application. The results are relevant in the context of the three-transponder method (3TM), which is discussed in Chap. 6.

B.1 Moments of Functions of Random Variables

The goal of this section is to derive the first and second moment of a normally distributed variable X after function application, so that

$$Y = g(X). \quad (\text{B.1})$$

The location and squared scale of X shall be denoted as μ_X and σ_X^2 , and for Y as μ_Y and σ_Y^2 . The special case

$$g(X) = 10 \log(X) \quad (\text{B.2})$$

is of particular concern with respect to the three-transponder method. The logarithmic transformation is necessary in order to set up the linear system of equations (6.18), and it is not self-evident that the Evaluation of measurement data – Guide to the Expression of Uncertainty in Measurement [87] (GUM) approach to uncertainty analysis (assumption of normal distribution) is still applicable.

Actually, the logarithm of X in Eq. (B.2) is undefined because X can take on negative values. In practice, it is still useful to assume an approximately normal distribution which is truncated at zero. In the case of the three-transponder method, the approximation can be considered valid because generally

$$\mu \gg 3\sigma, \quad (\text{B.3})$$

i. e., the mean is well separated from zero, and the probability for any samples to be below zero is small. Assuming now that the logarithm of this (approximate) normal distribution exists, one can derive approximate formulas for the first and second moment through Taylor series expansion around μ_X (see e. g. [16]). The expectation of $g(X)$ is then given as

$$\begin{aligned} E[g(X)] &= E[g(\mu_X + (X - \mu_X))] \\ &\approx E[g(\mu_X) + g'(\mu_X)(X - \mu_X) + \frac{1}{2}g''(\mu_X)(X - \mu_X)^2]. \end{aligned} \quad (\text{B.4})$$

Exploiting the general properties of expected values [153]

$$E[X + Y] = E[X] + E[Y], \quad (\text{B.5})$$

$$E[c] = c, \quad c = \text{const.}, \quad (\text{B.6})$$

$$E[cX] = c E[X], \quad (\text{B.7})$$

and the definitions for the first and second moments

$$E[X] = \mu_X, \quad (\text{B.8})$$

$$E[(X - \mu_X)^2] = \sigma_X^2 \quad (\text{B.9})$$

it becomes apparent that the second term in the Taylor expansion in Eq. (B.4) vanishes, and the remaining terms can be written as

$$E[g(X)] \approx g(\mu_X) + \frac{g''(\mu_X)}{2} \sigma_X^2. \quad (\text{B.10})$$

The second derivative of $g(X)$ is

$$g''(X) = -\frac{10}{X^2 \ln(10)} \quad (\text{B.11})$$

so that

$$E[Y] = E[10 \log(X)] \approx 10 \log(\mu_X) - \frac{5\sigma_X^2}{\mu_X^2 \ln 10}. \quad (\text{B.12})$$

The second term is very small if $\mu_X \gg \sigma_X$, which should generally be the case for transponder measurements. In conclusion, the first moment of Y is approximately the logarithmic transformation of the first moment of X .

In a similar fashion, an approximate expression for the second moment can be found [16]. The variance is

$$\begin{aligned} E[(Y - \mu_Y)^2] &= E[Y^2] - 2\mu_Y E[Y] + \mu_Y^2 \\ &= E[Y^2] - \mu_Y^2. \end{aligned} \quad (\text{B.13})$$

Concentrating on the first term

$$E[Y^2] = E[h(X)]$$

with

$$h(X) = g^2(X),$$

one can reuse the result of Eq. (B.10) so that

$$E[Y^2] = E[h(X)] \approx h(\mu_X) + \frac{\sigma_X^2}{2} h''(\mu_X). \quad (\text{B.14})$$

The first and second derivatives of $h(X)$ follow from the chain and product rules:

$$\begin{aligned} h'(X) &= 2g(X)g'(X), \\ h''(X) &= 2[g'(X)]^2 + 2g(X)g''(X). \end{aligned}$$

Therefore it follows that

$$E[Y^2] \approx g^2(X) + \frac{\sigma_X^2}{2} \{2[g'(\mu_X)]^2 + 2g(\mu_X)g''(\mu_X)\}. \quad (\text{B.15})$$

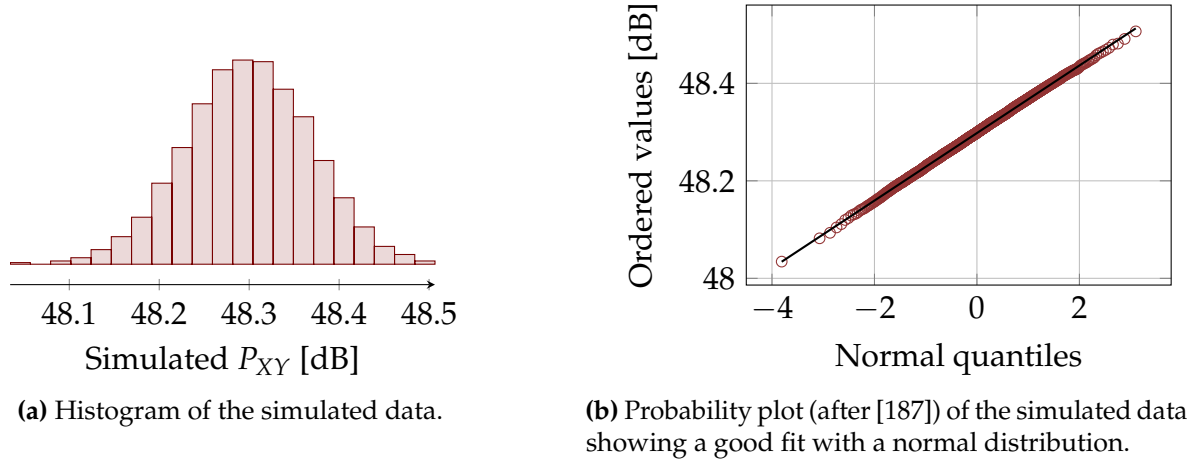


Figure B.1: 1000 simulated samples for P_{XY} after $10 \log(\cdot)$ transformation.

This result can be applied to Eq. (B.13) so that

$$E[(Y - \mu_Y)^2] \approx \left[g^2(X) + \frac{\sigma_X^2}{2} \{2[g'(\mu_X)]^2 + 2g(\mu_X)g''(\mu_X)\} \right] - \left[g(\mu_X) + \frac{\sigma_X^2}{2} g''(\mu_X) \right]^2, \quad (\text{B.16})$$

where μ_Y was again approximated with the expression in Eq. (B.10). Summarizing terms yields

$$E[(Y - \mu_Y)^2] \approx \sigma_X^2 [g'(\mu_X)]^2 - \frac{\sigma_X^4}{4} [g''(\mu_X)]^2. \quad (\text{B.17})$$

The last term is comparatively small so that the first order approximation for the variance of a function of a random variable is [16]

$$\sigma_Y^2 = E[(Y - \mu_Y)^2] \approx \sigma_X^2 [g'(X)]^2. \quad (\text{B.18})$$

For the special case where $g(X)$ is given by Eq. (B.2), the standard deviation of $g(x)$ becomes

$$\sigma_Y \approx \frac{10}{\mu_X \ln(10)} \sigma_X. \quad (\text{B.19})$$

It was stated before that the probability density function (PDF) for $Y = 10 \log(X)$ cannot be derived analytically because the logarithm is not defined for negative values. The approximations for the first and second moments in Eq. (B.12) and Eq. (B.19) can nevertheless be confirmed empirically through a Monte Carlo simulation. For this, 1000 samples were drawn from the normal distribution

$$X = P_r/P_t \sim N(260^2, 1081^2)$$

and then converted to the logarithmic domain with Eq. (B.2). The specific values taken for this example are based on values acquired during the demonstration measurement campaign, which are described in Sec. 6.4.

The results of the Monte Carlo simulation are shown in Fig. B.1. It is apparent that a normal distribution remains approximately normal even after logarithmic transformation, as long as the standard deviation is small in comparison to the mean.

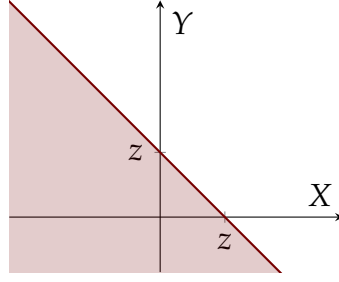


Figure B.2: Integral over the joint probability density function $f_{\tilde{Z}}(X, Y) = X + Y$, showing the integration bounds.

B.2 Sum and Subtraction of Two Random Variables

In a first step, the joint probability distribution function $f_{\tilde{Z}}(z)$ for

$$\tilde{Z} = X + Y \quad (\text{B.20})$$

is derived, where X and Y are two random variables. The cumulative distribution function (CDF) $F_{\tilde{Z}}(z)$ of \tilde{Z} is given by definition as [154]

$$F_{\tilde{Z}}(z) = p(\tilde{Z} \leq z) = p[X + Y \leq z] = p[X + Y \in (-\infty, z)] = F_{X,Y}(x, y). \quad (\text{B.21})$$

This is an integral over the two random variables X and Y . The area of this integral is shown in Fig. B.2, where the line denotes the equality condition $X + Y = z$, which defines the bounds of the integral. The CDF is then given as

$$F_{X,Y}(x, y) = \int_{x=-\infty}^{\infty} \int_{y=-\infty}^{z-X} f_{X,Y}(X, Y) dy dx. \quad (\text{B.22})$$

This integral is difficult to solve in general, so instead of deriving the CDF, the PDF $f_{\tilde{Z}}(z)$ can be derived, which by definition is [154]

$$\begin{aligned} f_{\tilde{Z}}(z) &= \frac{d}{dz} F_{\tilde{Z}}(z) = \frac{d}{dz} \int_{x=-\infty}^{\infty} \int_{y=-\infty}^{z-X} f_{X,Y}(X, Y) dy dx \\ &= \int_{x=-\infty}^{\infty} \frac{d}{dz} \int_{y=-\infty}^{z-X} f_{X,Y}(X, Y) dy dx. \end{aligned} \quad (\text{B.23})$$

Now the principal property of integrals can be exploited whereby a differentiation of a definite integral with respect to a variable in the upper bound is equal to the integrand at the upper boundary so that

$$f_{\tilde{Z}}(z) = \int_{x=-\infty}^{\infty} f_{X,Y}(X, z - X) dx. \quad (\text{B.24})$$

Here $f_{X,Y}$ is the joint probability density function, which by definition is the product

$$f_{X,Y}(x, y) = f_X(x)f_Y(y) \quad (\text{B.25})$$

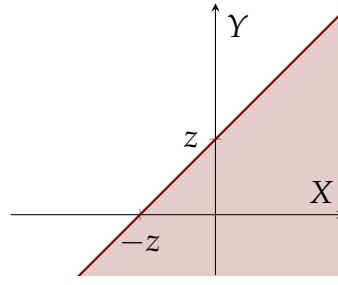


Figure B.3: Integral over the joint probability density function $f_Z(X, Y) = X - Y$, showing the integration bounds.

of the probability densities of X and Y if X and Y are independent [154]. Equation (B.24) is then equal to

$$f_Z(z) = \int_{x=-\infty}^{\infty} f_X(X) f_Y(z - X) dx. \quad (\text{B.26})$$

This equation is also known as the convolution of f_X and f_Y at z , also written as

$$f_Z(z) = (f_X * f_Y)(z). \quad (\text{B.27})$$

The PDF of the sum of two independent random variables is therefore the convolution of the PDFs of the two random variables [72].

A similar relationship can be derived for the subtraction of two random variables

$$Z = Y - X. \quad (\text{B.28})$$

The integration bounds change, as shown in Fig. B.3, so that Eq. (B.23) becomes

$$f_Z(z) = \frac{d}{dz} F_Z(z) = \int_{x=-\infty}^{\infty} \frac{d}{dz} \int_{y=-\infty}^{z+X} f_{X,Y}(X, Y) dy dx. \quad (\text{B.29})$$

After equivalent transformation as above and under the assumption that X and Y are independent, one yields

$$f_Z(z) = \int_{x=-\infty}^{\infty} f_X(X) f_Y(z + X) dx. \quad (\text{B.30})$$

This equation is also known as the cross correlation integral, often also written

$$f_Z(z) = (f_X \star f_Y)(z). \quad (\text{B.31})$$

The intermediate result is accordingly that the PDF of the difference of two independent random variables is the cross correlation of the PDFs of the two random variables [72].

B.3 Convolution and Correlation of Two Gaussian PDFs

It was shown before that logarithmic transformation of a normal random variable approximately results in another normal random variable. In this section the joint PDFs

of the sum and the difference of two normal random variables X and Y is derived, where

$$X \sim \mathcal{N}(\mu_X, \sigma_X^2), \quad (\text{B.32a})$$

$$Y \sim \mathcal{N}(\mu_Y, \sigma_Y^2). \quad (\text{B.32b})$$

In a first step, a relationship for the sum of the two Gaussian random variables X and Y from Eq. (6.61) is inferred (see for example [26]). Their PDFs are given as

$$f_X(\varsigma) = \frac{1}{\sqrt{2\pi}\sigma_X} \exp\left(-\frac{(\varsigma - \mu_X)^2}{2\sigma_X^2}\right), \quad (\text{B.33a})$$

$$f_Y(\varsigma) = \frac{1}{\sqrt{2\pi}\sigma_Y} \exp\left(-\frac{(\varsigma - \mu_Y)^2}{2\sigma_Y^2}\right). \quad (\text{B.33b})$$

According to Eq. (B.27), the joint distribution of the sum of two random variables can be determined by the convolution of the two PDFs. Exploiting the convolution theorem, the convolution can be expressed as a multiplication in the frequency domain, so that

$$(f_X * f_Y)(\varsigma) = \mathcal{F}^{-1}\{\mathcal{F}(f_X(\varsigma))\mathcal{F}[f_Y(\varsigma)]\} \quad (\text{B.34})$$

with

$$\mathcal{F}[f(\varsigma)] = \int_{-\infty}^{\infty} f(\varsigma) e^{-2\pi j k \varsigma} d\varsigma = F(k), \quad (\text{B.35})$$

$$\mathcal{F}^{-1}[F(k)] = \int_{-\infty}^{\infty} F(k) e^{2\pi j k \varsigma} dk = f(\varsigma) \quad (\text{B.36})$$

being the forward and inverse Fourier transform, respectively. Using the variable substitution $\varsigma = \varsigma' + \mu_X$, the Fourier transform of $f_X(\varsigma)$ is

$$\begin{aligned} \mathcal{F}[f_X(\varsigma)] &= \frac{1}{\sqrt{2\pi}\sigma_X} \int_{-\infty}^{\infty} e^{-\varsigma'^2/(2\sigma_X^2)} e^{-2\pi j k(\varsigma' + \mu_X)} d\varsigma' \\ &= \frac{e^{-2\pi j k \mu_X}}{\sqrt{2\pi}\sigma_X} \int_{-\infty}^{\infty} e^{-\varsigma'^2/(2\sigma_X^2)} e^{-2\pi j k \varsigma'} d\varsigma'. \end{aligned} \quad (\text{B.37})$$

With Euler's formula

$$e^{-j\varphi} = \cos\varphi - j \sin\varphi, \quad (\text{B.38})$$

this becomes

$$\mathcal{F}[f_X(\varsigma)] = \frac{e^{-2\pi j k \mu_X}}{\sqrt{2\pi}\sigma_X} \int_{-\infty}^{\infty} e^{-\varsigma'^2/(2\sigma_X^2)} \cos(2\pi k \varsigma') - j \sin(2\pi k \varsigma') d\varsigma'. \quad (\text{B.39})$$

The sine term vanishes because the sine function is odd. The remaining integral can be solved in closed form [1, Eq. (7.4.6)]:

$$\int_0^{\infty} e^{-at^2} \cos(2xt) dt = \frac{1}{2} \sqrt{\frac{\pi}{a}} e^{-x^2/a} \quad \text{with } \Re(a) > 0. \quad (\text{B.40})$$

Finally the Fourier transformation of the Gaussian function $f_X(\zeta)$ is given as

$$\mathcal{F}[f_X(\zeta)] = e^{-2\pi j k \mu_X} e^{-2\pi^2 k^2 \sigma_X^2}. \quad (\text{B.41})$$

Analogously, one can derive an expression for $f_Y(\zeta)$. The convolution of f_X and f_Y is then

$$\mathcal{F}[f_X(\zeta)]\mathcal{F}[f_Y(\zeta)] = e^{-2\pi j k (\mu_X + \mu_Y)} e^{-2\pi^2 k^2 (\sigma_X^2 + \sigma_Y^2)}, \quad (\text{B.42})$$

which is again a Gaussian function. By comparison with Eq. (B.41) it becomes apparent that the sum \tilde{Z} of two normally distributed variables is again a normally distributed variable:

$$\tilde{Z} = X + Y \sim N(\mu_X + \mu_Y, \sigma_X^2 + \sigma_Y^2). \quad (\text{B.43})$$

To compute the difference $Z = Y - X$ of the two normally distributed variables X and Y , one can exploit the relationship between correlation and convolution:

$$(f_X \star f_Y)(\zeta) = f_X^*(-\zeta) * f_Y(\zeta). \quad (\text{B.44})$$

Due to the square in the Gaussian function (B.33a), this is equivalent to changing the sign of μ_X . It results that the difference of two normally distributed random variables is again a normally distributed variable with mean $\mu_Y - \mu_X$ and standard deviation $\sqrt{\sigma_X^2 + \sigma_Y^2}$, i. e.,

$$Z \sim N(\mu_Y - \mu_X, \sigma_X^2 + \sigma_Y^2). \quad (\text{B.45})$$

B.4 Multiplication of Random Variables

As a last mathematical operation necessary to convert power ratios P_r/P_t to transponder radar cross sections (RCSs) according to the 3TM system of equations (6.19), the multiplication

$$Y = aX$$

of a random variable X with a constant a shall be examined. The PDFs of X and Y are given as $f(x)$ and $g(y)$. By definition of the PDF

$$\int_{-\infty}^{\infty} f(x) dx = 1, \quad (\text{B.46})$$

$$\int_{-\infty}^{\infty} g(y) dy = 1. \quad (\text{B.47})$$

Variable substitution for the second integral in the form of

$$dy = a dx$$

leads to

$$1 = \int_{-\infty}^{\infty} g(y) a dx. \quad (\text{B.48})$$

Comparing this equation with (B.47) it is apparent that $g(x)$ must fulfill

$$g(y) = \frac{f(x)}{a}. \quad (\text{B.49})$$

Accordingly it follows for the first moment of Y that [154]

$$\begin{aligned}
 \mu_Y = E[Y] &= \int_{-\infty}^{\infty} yg(y) dy \\
 &= \int_{-\infty}^{\infty} ax \frac{f(x)}{a} dx \\
 &= a \int_{-\infty}^{\infty} xf(x) dx = a\mu_X.
 \end{aligned} \tag{B.50}$$

In conclusion, the expectation of a constant multiplied by a random variable is equal to the multiplication of the expectation of the random variable with this constant.

A similar derivation can be completed for the second moment. With the definition of variance of a random variable X it follows that [154]

$$\begin{aligned}
 \sigma_X^2 = E[(X - \mu_X)^2] &= \int_{-\infty}^{\infty} (x - \mu_X)^2 f(x) dx \\
 &= \int_{-\infty}^{\infty} x^2 f(x) dx - 2\mu_X \int_{-\infty}^{\infty} xf(x) dx + \mu_X^2 \\
 &= \int_{-\infty}^{\infty} x^2 f(x) dx - \mu_X^2.
 \end{aligned} \tag{B.51}$$

Accordingly, the following relationship for the variance of Y follows:

$$\begin{aligned}
 \sigma_Y^2 = E[(Y - \mu_Y)^2] &= \int_{-\infty}^{\infty} y^2 g(y) dy - \mu_Y^2 \\
 &= \int_{-\infty}^{\infty} a^2 x^2 \frac{f(x)}{a} a dx - a^2 \mu_X^2 = a^2 \sigma_X^2.
 \end{aligned} \tag{B.52}$$

In conclusion, the variance of a random variable after multiplication by a constant equals the variance of the random variable times the square of the constant.

C Introduction to Bayesian Statistics and to the Markov Chain Monte Carlo Method

This appendix supplements the discussion in Chap. 7. It gives a short overview of what Bayesian statistics is, where it differs from frequentist statistics, and how the numerical Markov chain Monte Carlo (MCMC) method helps to efficiently solve Bayesian problems.

C.1 Bayesian Statistics

Gelman et al. [65] define: “Bayesian inference is the process of fitting a probability model to a set of data and summarizing the result by a probability distribution on the parameters of the model and on unobserved quantities such as predictions for new observations.” Hence there is a fundamental difference between Bayesian and frequentist statistics. In frequentist statistics, fictitiously large populations are assumed. The underlying parameters of a sample (like its mean or standard deviation) are considered to be fixed, i. e., they remain constant during the sampling. In Bayesian statistics, on the other hand, parameters are treated probabilistically. Each model parameter is a random variable, and the knowledge about these parameters is expressed in terms of probability densities.

Describing a parameter by a probability density function is a good choice when not only the point estimate of a parameter is needed, but also a statement about the parameter uncertainty. In synthetic aperture radar (SAR) calibration, it is not sufficient to only estimate for instance the calibration factor (from Sec. 2.3) but also to state the uncertainty of that estimate. With the Bayesian approach, this measurement uncertainty, as it is called in the *Guide to the Expression of Uncertainty in Measurement* (GUM) [87] (see Sec. 2.2.2), can be derived from the probability density of the parameter as a probability interval.

The general principle of Bayesian statistics is deducted from simple probability theory, leading to Bayes’ rule. The rule follows from conditional probability. The conditional probability $p(A|B)$ denotes the probability of an event A , supposing that the event B is

true.¹ This conditional probability can be written as

$$p(A|B) = \frac{p(A \cap B)}{p(B)}, \quad (\text{C.1})$$

$$p(A \cap B) = p(A|B)p(B), \quad (\text{C.2})$$

where the joint probability $p(A \cap B)$ is written $p(A, B)$ in the following. It denotes the probability that A and B are true. Equation (C.1) can be rewritten as the Bayes' rule

$$p(A|B) = \frac{p(B|A)p(A)}{p(B)} \quad (\text{C.3})$$

by using variable substitution in Eq. (C.1). Now A can be replaced by observations y , B by a parameter θ , and probabilities by densities so that one yields the familiar form of the Bayes' theorem [31]:

$$p(\theta|y) = \frac{p(y|\theta)p(\theta)}{p(y)}. \quad (\text{C.4})$$

$p(y|\theta)$ is the *likelihood* of the observations y under a model, and $p(\theta)$ is a *prior density*, i. e., the density of θ before y is observed. $p(\theta|y)$ is the *posterior density* or the updated knowledge of the parameter θ after the data y was observed.

In summary, Bayes' theorem describes a learning process. The starting point is the more or less informative prior information about a parameter θ . If θ is chosen to describe the equivalent radar cross section (ERCS) of a transponder, one might claim even without any observation that the parameter needs to be positive and that it certainly will not exceed a certain large threshold. If now some new data y becomes available, e. g. during the case study RADARSAT-2 campaign described below, one can update ones believe on θ with Eq. (C.4) to yield the posterior distribution $p(\theta|y)$.

C.2 Bayesian Computations and Markov Chain Monte Carlo Methods

Deriving the posterior distribution $p(\theta|y)$ is in practice mostly achieved through numerical methods, which allow to consider more complex problems and arbitrary distributions in comparison to an analytical approach. The simulation method used in the case study described in Chap. 7 is the Markov chain Monte Carlo (MCMC) approach [66]. The posterior distribution is approximated by sequentially drawing samples from approximate iterative intermediate distributions until the simulation converges to the target distribution.

The maybe easiest implementation of such an iterative MCMC algorithm was proposed by Metropolis et al. [119] in 1953, and the algorithm is now commonly called the *Metropolis algorithm*. It proceeds as follows [65]:

1. Choose an initial state θ^0 , often simply based on a rough estimate.

¹Note on notation: To stay in line with texts such as [70], $p(\cdot)$ denotes probabilities and probability density functions (PDFs). The distinction between the two becomes apparent from the argument. $p(\cdot|\cdot)$ denotes a conditional probability. If the random variable θ has a normal distribution with mean μ and variance σ^2 , this is written as $\theta \sim N(\mu, \sigma^2)$, or alternatively, $p(\theta|\mu, \sigma^2) = N(\mu, \sigma^2)$.

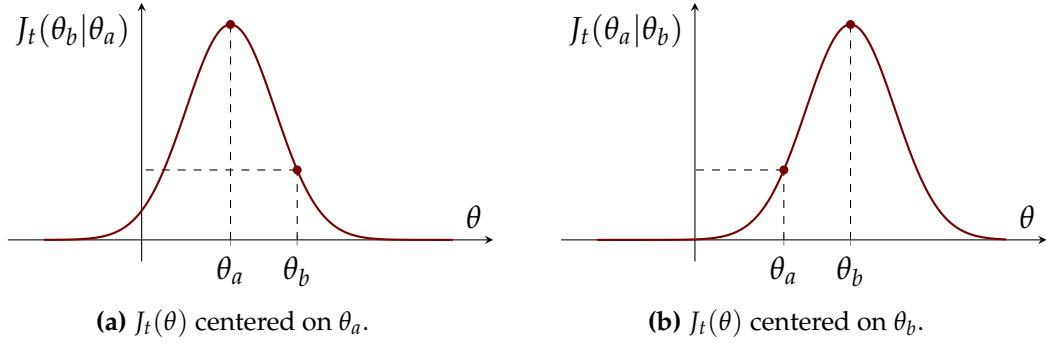


Figure C.1: A symmetric jumping distribution $J_t(\theta)$ has the property $J_t(\theta_b|\theta_a) = J_t(\theta_a|\theta_b)$.

2. For each following step t , sample a proposal state θ^* from a jumping (or proposal) distribution $J_t(\theta^*|\theta^{t-1})$ at time t .
3. In order to decide if the proposal state θ^* is accepted, calculate the Metropolis ratio

$$r = \frac{p(\theta^*|y)}{p(\theta^{t-1}|y)}. \quad (\text{C.5})$$

4. Set the new state θ^t according to

$$\theta^t = \begin{cases} \theta^* & \text{with probability } \alpha(\theta^{t-1}, \theta^*) = \min(r, 1) \\ \theta^{t-1} & \text{otherwise.} \end{cases} \quad (\text{C.6})$$

$\alpha(\theta^{t-1}, \theta^*)$ is called the acceptance probability. The proposal state θ^* is therefore accepted if $r > 1$. For $r < 1$, one samples a random variable U from $U(0, 1)$ and accepts θ^* as the new state if $U \leq r$.

The shape of the jumping distribution is not important, but finding an ideal proposal distribution J_t is not trivial [70]. A typical choice for $J_t(\theta^*|\theta^{t-1})$ is a (in general multi-dimensional) Gaussian distribution which is centered on θ^{t-1} . This choice also fulfills the specific property of the Metropolis algorithm, which requires that the jumping distribution is symmetric, i. e., $J_t(\theta_a|\theta_b) = J_t(\theta_b|\theta_a)$ for all θ_a, θ_b , and t , see Fig. C.1.

For the example of a Gaussian jumping distribution, one still needs to define its variance before starting the simulation. This is a trade-off: If the variance of the jumping distribution is too small, the random walk will only result in small steps so that the parameter space is explored slowly and the algorithm does not converge quickly. On the other hand, if the variance is large it is much more likely that new proposal states θ^* are rejected because of the decision step 4 in the algorithm above.

Proof that the Markov chain samples from the target distribution. A proof follows which shows that the target distribution is the stationary distribution of the Markov chain [70]: θ^{t-1} shall be a sample from the posterior $p(\theta^{t-1}|y)$, i. e., the target distribution. The Metropolis Markov chain defines the probability of drawing and accepting θ^t with

a probability of $p(\theta^t|\theta^{t-1}) = J_t(\theta^t|\theta^{t-1})\alpha(\theta^{t-1}, \theta^t)$. It follows for the joint probability $p(\theta^{t-1}, \theta^t)$ with Eq. (C.2) that

$$\begin{aligned}
 p(\theta^{t-1}, \theta^t) &= p(\theta^{t-1}|y)p(\theta^t|\theta^{t-1}) \\
 &= p(\theta^{t-1}|y)J_t(\theta^t|\theta^{t-1})\alpha(\theta^{t-1}, \theta^t) \\
 &= p(\theta^{t-1}|y)J_t(\theta^t|\theta^{t-1}) \min \left(1, \frac{p(\theta^t|y)}{p(\theta^{t-1}|y)} \right) \\
 &= \min(p(\theta^{t-1}|y)J_t(\theta^t|\theta^{t-1}), p(\theta^t|y)J_t(\theta^t|\theta^{t-1})) \\
 &= p(\theta^t|y)J_t(\theta^t|\theta^{t-1})\alpha(\theta^t, \theta^{t-1}) \\
 &= p(\theta^t|y)p(\theta^{t-1}|\theta^t).
 \end{aligned} \tag{C.7}$$

In summary,

$$p(\theta^{t-1}|y)p(\theta^t|\theta^{t-1}) = p(\theta^t|y)p(\theta^{t-1}|\theta^t), \tag{C.8}$$

which is also called the *detailed balance equation* [70]. The probability for a transition from θ^{t-1} to θ^t is the same as the probability for a transition from θ^t to θ^{t-1} , which means that the Markov chain generated by the Metropolis algorithm is stationary. So if an initial value is drawn from a distribution $p(\theta)$, all following samples generated by the Metropolis algorithm will be drawn from the same distribution.

Besides proving that the Metropolis algorithm generates samples from a stationary distribution, it must be shown that the samples from this stationary distribution are in fact drawn from the target distribution. This is achieved by considering the joint probability $p(\theta^{t-1}|y)p(\theta^t|\theta^{t-1})$ and integrating it with respect to θ^{t-1} to yield the marginal distribution of θ^t [70]:

$$\begin{aligned}
 \int_{-\infty}^{\infty} p(\theta^{t-1}|y)p(\theta^t|\theta^{t-1}) d\theta^{t-1} &= \int_{-\infty}^{\infty} p(\theta^t|y)p(\theta^{t-1}|\theta^t) d\theta^{t-1} \\
 &= p(\theta^t|y) \int_{-\infty}^{\infty} p(\theta^{t-1}|\theta^t) d\theta^{t-1} \\
 &= p(\theta^t|y).
 \end{aligned} \tag{C.9}$$

Glossary

C-band Radar frequency band from 4 GHz to 8 GHz [83].

calibration “[O]peration that, under specified conditions, in a first step, establishes a relation between the quantity values with measurement uncertainties provided by measurement standards and corresponding indications with associated measurement uncertainties and, in a second step, uses this information to establish a relation for obtaining a measurement result from an indication” [92].

correction “[C]ompensation for an estimated systematic effect” [92].

FEKO Computational electromagnetics software product developed by *EM Software & Systems-S. A. (Pty) Ltd.*

indication “[Q]uantity value provided by a measuring instrument or a measuring system” [92].

L-band Radar frequency band from 1 GHz to 2 GHz [83].

legal metrology “[P]art of metrology relating to activities which result from statutory requirements and concern measurement, units of measurement, measuring instruments and methods of measurement and which are performed by competent bodies” [130].

measurand “[Q]uantity intended to be measured” [92].

measurement procedure “[D]etailed description of a measurement according to one or more measurement principles and to a given measurement method, based on a measurement model and including any calculation to obtain a measurement result” [92].

measurement result “[S]et of quantity values being attributed to a measurand together with any other available relevant information” [92].

measurement standard “[R]ealization of the definition of a given quantity, with stated quantity value and associated measurement uncertainty, used as a reference” [92].

measurement unit “[R]eal scalar quantity, defined and adopted by convention, with which any other quantity of the same kind can be compared to express the ratio of the two quantities as a number” [92].

P-band Radar frequency band from 216 MHz to 450 MHz [83].

quantity “[P]roperty of a phenomenon, body, or substance, where the property has a magnitude that can be expressed as a number and a reference” [92].

quantity value “[N]umber and reference together expressing magnitude of a quantity” [92].

S-band Radar frequency band from 2 GHz to 4 GHz [83].

SI International system of units (French: *le système international d’unités*).

TerraSAR-X German X-band spaceborne SAR mission. The satellite was launched on June 15, 2007; the acquired data are used in Earth observation.

X-band Radar frequency band from 8 GHz to 12 GHz [83].

Acronyms

3TM	three-transponder method
ADC	analog-to-digital converter
ARC	active radar calibrator
BEM	boundary-element method
BIPM	Bureau International des Poids et Mesures
BW	bandwidth
CDF	cumulative distribution function
CEOS	Committee on Earth Observation Satellites
CW	continuous wave
DA	digital amplitude
DAC	digital-to-analog converter
DLR	German Aerospace Center
DN	digital number
DUT	device under test
ECAL	external calibration
EMC	electromagnetic compatibility
ERCS	equivalent radar cross section
ERS-1	European Remote Sensing Satellite 1
ERS-2	European Remote Sensing Satellite 2
ESA	European Space Agency
FDTD	finite-difference time-domain method
FEM	finite-element method
FFT	fast Fourier transform
FIFO	first-in, first-out
FM	frequency modulation
FPGA	field-programmable gate array
GO	geometrical optics
GUM	Evaluation of measurement data – Guide to the Expression of Uncertainty in Measurement [87]
H	horizontal

ICAL	internal calibration
IEC	International Electrotechnical Commission
IEEE	Institute of Electrical and Electronics Engineers
IFFT	inverse fast Fourier transform
ISO	International Organization for Standardization
JCGM	Joint Committee for Guides in Metrology
JS	James-Stein
LO	local oscillator
LTl	linear and time-invariant
MCMC	Markov chain Monte Carlo
MDA	MacDonald, Dettwiler and Associates Ltd.
MIMO	multiple-input multiple-output
ML	maximum likelihood
MLFMM	multilevel fast multipole method
MoM	method of moments
MSE	mean squared error
NVA	network vector analyzer
OFDM	orthogonal frequency division multiplexing
OIML	International Organization of Legal Metrology
PARC	polarimetric active radar calibrator
PDF	probability density function
PO	physical optics
PRF	pulse repetition frequency
PSF	point-spread function
PSLR	peak-to-sidelobe ratio
RAR	real aperture radar
RCMC	range cell migration correction
RCS	radar cross section
RDA	range-Doppler algorithm
RF	radio frequency
RMS	root mean square
RX	receiving
SAR	synthetic aperture radar
SIR	signal-to-interference ratio
SLC	single-look complex
SNR	signal-to-noise ratio
TCC	target correction coefficient
TEC	total electron content
TOPS	terrain observation by progressive scans

TSX	TerraSAR-X
TX	transmitting
UWB	ultra-wide bandwidth
V	vertical
WGCV	Working Group on Calibration and Validation
WSS	wide sense stationary

Notation

Symbols and Notational Conventions

$!$	Factorial
\angle	Angle
\leftarrow	Assignment operator in pseudo code
$*$	Convolution
\star	Cross correlation operation
∇	Nabla operator
$ \cdot $	Absolute value
$\ \cdot\ $	Euclidean norm
\sim	Example: $X \sim N(\mu, \sigma^2)$ means the random variable X is distributed normally with mean μ and variance σ^2
$[\cdot]^T$	Transposition of a matrix or vector
$g'(x)$	First derivative of $g(x)$ with respect to x
$g''(x)$	Second derivative of $g(x)$ with respect to x
$p(\cdot \cdot)$	Conditional probability
$\Re(z)$	Function returning the real part of a complex number z
$V[\cdot]$	Variance

Greek Letters

α	Angle; general cosine window tapering factor; confidence level; acceptance probability in MCMC
β	Radar backscatter; Kaiser window roll-off factor; angle
β^0	Radar brightness
β_r	Angular resolution (in radians)
$\delta(x)$	Dirac delta function
$\Delta\mathcal{E}_p$	Target correction coefficient
$\Delta\zeta_e$	ERCS variation
δ_a	Image pixel spacing in azimuth
δ_g	Image pixel spacing in ground range
δ_p	Image pixel spacing in plane perpendicular to line of sight from the sensor
δ_r	Image pixel spacing in slant range
ϵ_h	Energy spectral density of h

$\epsilon_{h,r}$	Range component of ϵ_h
ϵ_s	Energy spectral density of s_r
$\epsilon_{s,r}$	Range component of the energy spectral density of $s_r(t_r, t_a)$
γ^0	Backscatter coefficient with reference area perpendicular to line of sight
γ_T^0	Terrain corrected backscatter coefficient γ^0
λ	Wavelength
λ_0	Wavelength at carrier (center) frequency
μ	Mean of a random variable or probability distribution
μ_{15}	Expectation for target group "1.5 m corner reflector"
μ_{30}	Expectation for target group "3.0 m corner reflector"
μ_g	Expectation for target group g
μ_k^k	Scaled central moment k of $\epsilon_h(f)$
μ_s	Estimated daily transponder drift
$\mu_{s,d}$	Expectation of s_d
μ_t	Expectation for target group "transponder"
μ_X	Location of random variable X
μ_Y	Location of random variable Y
μ_Z	Location of random variable Z
Φ	Normal cumulative distribution function
ϕ	Phase; angle
φ	Angular rotational deviation of an antenna from a reference rotation
ψ	Angular coordinates formed by the polar and azimuth angles (θ, ϕ)
ψ_{ref}	Angular coordinates formed by the polar and azimuth angles (θ, ϕ) at which ζ_{ref} was determined
σ	Standard deviation
σ^0	Normalized radar cross section
σ_e^0	Equivalent normalized radar cross section
σ_{15}	Standard deviation for observations of target group "1.5 m corner reflector"
σ_{30}	Standard deviation for observations of target group "3.0 m corner reflector"
σ_g	Standard deviation for observations of target group g
σ_{ij}	Covariance of X_i and X_j
σ_q	Standard deviation of measurement quantity q
$\sigma_{\bar{q}}$	Best estimate of standard deviation of measurement quantity q , standard error, standard uncertainty
σ_s	Standard uncertainty in estimating μ_s
$\sigma_{s,d}$	Standard deviation of s_d
σ_t	Standard deviation for observations of target group "transponder"
σ_X^2	Variance of random variable X
σ_Y^2	Variance of random variable Y
σ_Z^2	Variance of random variable Z
ζ	Vector of three-transponder method (3TM) radar cross sections (RCSs)
ζ_0	Vector of fixed 3TM RCSs

$\hat{\zeta}$	Point estimator of ζ
$\hat{\zeta}^{\text{JS}}$	James-Stein estimator for ζ
$\hat{\zeta}^{\text{ML}}$	Maximum likelihood estimator for ζ
$\hat{\zeta}_{\zeta_0}^{\text{JS}}$	James-Stein estimator for ζ , shrinking toward ζ_0
ζ	Radar cross section
ζ_{CR}	Radar cross section of a trihedral corner reflector
ζ_{sphere}	Radar cross section of a perfectly conducting sphere
ζ_A	Radar cross section of transponder A
ζ_B	Radar cross section of transponder B
ζ_C	Radar cross section of transponder C
ζ_{DUT}	Radar cross section of a device under test (DUT)
ζ_e	Equivalent radar cross section (scalar factor describing the magnitude of the reflectivity)
ζ'_e	One-dimensional ERCS
$\zeta_{e,15}$	Equivalent radar cross section of a 1.5 m trihedral corner reflector
$\zeta'_{e,a}$	Azimuth component of ζ_e
$\zeta'_{e,r}$	Range component of ζ_e
$\zeta_{e,t}$	Equivalent radar cross section of a transponder
ζ_p	Radar cross section of a flat plate
ζ_{ref}	Reference (equivalent) radar cross section
ζ_t	Radar cross section of a transponder
ζ_X	Radar cross section of transponder X
ζ_Y	Radar cross section of transponder Y
θ	Angle; phase offset; population parameter
θ^*	Proposal state for MCMC iterations
θ^0	Initial state for MCMC iterations
θ^t	New state at MCMC iteration t
θ_a	Population parameter
θ_b	Population parameter
θ_i	Local incidence angle
ϑ	Reference stimulus to a measurement instrument
$\hat{\vartheta}$	Estimated quantity value

Roman Letters

A	Area; first antenna in three-antenna method; first transponder for the 3TM; probabilistic event
a	Radius; length; constant; amplitude; lower interval bound
$A(f, \psi)$	Frequency and angular dependent point target amplitude response function
A_0	Complex constant which describes the reflectivity of a point target
\hat{A}_{AB}	Constant component of A_{XY} for transponders A and B
\hat{A}_{AC}	Constant component of A_{XY} for transponders A and C
\hat{A}_{BC}	Constant component of A_{XY} for transponders B and C
A_β	Area of pixel in slant range geometry
A_e	Effective antenna area

A_γ	Area of pixel in plane perpendicular to line of sight from the sensor
a_i	Polynomial coefficient i of ϵ_s
A_p	Surface area of a flat plate
A_σ	Area of pixel in ground range geometry
A_{XY}	3TM root mean square (RMS) receive amplitude for transponders X (radar) and Y (radar target)
a_{ij}	Complex pixel value at index (i, j)
A_n	Integration area for a noise-only image
A_{nu}	Integration area for a distributed target, with receiver noise
A_u	Integration area for a distributed target
B	Second antenna for three-antenna method; second transponder for the 3TM; probabilistic event
b	Length; upper interval bound
C	Range-dependent system terms; constant scaling factor; third antenna for three-antenna method; third transponder for the 3TM
c	Speed of light; constant
c_i	Sensitivity coefficient i ; summand i
c_p	3TM sensitivity coefficient for P_{XY}
c_R	3TM sensitivity coefficient for the distance R
D	Largest dimension of a radiator
d	Diameter; day identifier
D_A	Additional attenuation of transponder A
D_X	Additional attenuation of transponder X
E	Expectation
\mathcal{E}	Energy in a SAR image patch after integration
e	Measurement error
E_ζ	Expectation of ζ
E_h^i	Horizontal component of \mathbf{E}^i
E_v^i	Vertical component of \mathbf{E}^i
E_h^s	Horizontal component of \mathbf{E}^s
E_v^s	Vertical component of \mathbf{E}^s
\mathcal{E}_c	Energy in a SAR image patch, which was processed with a correction point spread function, after integration of a point target
\mathcal{E}_e	Energy in a SAR image patch after integration of a point target with a normalized point-spread function
\mathbf{E}^i	Incident electrical field
\mathbf{E}^s	Scattered electrical field
\mathcal{E}_n	Energy in a noise-only patch
\mathcal{E}_{nu}	Energy in a SAR image patch of a homogeneous distributed target, with receiver noise
\mathcal{E}_p	Point target energy
\mathcal{E}_{pnu}	Point target energy in a clutter environment, with receiver noise
\mathcal{E}_{ref}	Integrated reference target pixel intensity
\mathcal{E}_t	Integrated transponder pixel intensity

\mathcal{E}_u	Energy in a SAR image patch of a homogeneous distributed target
F	Frequency domain representation of f
f	Frequency; function
\mathcal{F}	Fourier transformation operator
\mathcal{F}^{-1}	Inverse Fourier transformation operator
f	Measurement model
f_0	Frequency around which ϵ_s is developed
$f_{0,r}$	Frequency around which $\epsilon_{s,r}$ is developed
F_A	Cumulative density function of random variable A with $A \in [X, Y, Z, \tilde{Z}]$
f_A	Probability density function of random variable A with $A \in [X, Y, Z, \tilde{Z}]$
f_a	Azimuth-time dependent frequency
f_c	Carrier (center) frequency
f_r	Range frequency
f_{ref}	Reference frequency at which ζ_{ref} was determined
G	Antenna gain; frequency domain representation of g
g	Transmitted SAR pulse; function; target group identifier
\hat{g}	Estimated calibration function
G_{tr}	Transponder receive antenna gain
G_{tt}	Transponder transmit antenna gain
G_A	Antenna gain of antenna A
G_B	Antenna gain of antenna B
G_C	Antenna gain of antenna C
G_e	Transponder amplifier gain
G_l	Transponder loop gain
G_{rx}	Gain of a transponder's receive path
G_t	Antenna gain of the (radar's) transmit antenna
G_{tx}	Gain of a transponder's transmit path
G_P	SAR processing gain
G_R	One-way antenna gain of SAR instrument
H	Frequency domain representation of h
h	SAR matched filter in time domain; function
h'	SAR system impulse response
H_a	Azimuth component of H
H_r	Range component of H
H_t	Target transfer function
h_t	Point target's point-spread function
H_{tc}	Correction target transfer function
H_{tn}	Normalized target transfer function
h_{tc}	Point target's correction point-spread function
h_{tn}	Normalized point target's point-spread function
h_a	Azimuth point-spread function
I	Indication value
i	Integer; index variable
\mathbf{I}	Identity matrix

I_0	Zeroth-order Bessel function
I_{ref}	Reference backscatter intensity
j	Imaginary unit
J_t	Jumping distribution
K	Calibration factor
k	Wave number; order of moment μ_k^k ; frequency in Fourier domain
K_a	Azimuth FM rate
k_c	Coverage factor for combined uncertainty u_c
K_r	Pulse chirp FM rate
$k(t_a)$	Filter resulting from azimuth beam weighting and Doppler shift at azimuth time t_a
L	Losses; loss function
l	Inner-leg length of a trihedral corner reflector; length
L_a	Physical aperture size of SAR antenna in azimuth direction
$l(t_a)$	Azimuth processing filter
N	Integer count
n	Integer count
N	Normal distribution
N_g	Normal distribution of random variable g
N_p	p -dimensional multivariate normal distribution
$n(t_a)$	Receiver noise at azimuth time t_a
$O(f^a)$	Polynomial terms in f of order a and higher
P	Power
p	Integer count; probability or probability density function (depending on argument); p value
\tilde{P}_A	3TM receive-to-transmit power ratio for transponder A , in linear domain
P_{AB}	Measured ratio of receive-to-transmit power for transponders A and B
P_{AC}	Measured ratio of receive-to-transmit power for transponders A and C
\tilde{P}_B	3TM receive-to-transmit power ratio for transponder B , in linear domain
P_{BC}	Measured ratio of receive-to-transmit power for transponders B and C
\tilde{P}_C	3TM receive-to-transmit power ratio for transponder C , in linear domain
P_r^{DUT}	Received power (of the radar instrument) for a device under test (DUT)
P_r^{ref}	Received power (of the radar instrument) for a known reference target
P_r	Received power (of the radar instrument)
P_t	Transmitted power (of the radar instrument)
\tilde{P}_X	3TM receive-to-transmit power ratio for transponder X , in linear domain
P_{XY}	Measured ratio of receive-to-transmit power for transponders X and Y
P_{tr}	Received power by transponder
P_{tt}	Transmitted power by transponder
$\varphi(f, \psi)$	Frequency (and possibly angular) dependent (point target) phase response function

Q	Standard Gaussian random variable
q	Randomly distributed measurement quantity
R	(Slant range) Distance; risk function
r	Metropolis ratio
R_0	Slant range at closest approach
r_d	Daily RADARSAT-2 drift
$R_{\mathcal{E}u}$	Autocorrelation of square-law detected image of a homogeneous distributed target
R_{ha}	Autocorrelation function of h_a
R_S	Autocorrelation function of $S(t_a)$
\mathbf{S}	Complex scattering matrix with shape 2×2
S	Complex reflectivity
s_{out}	Complex SAR output signal after processing
$s_{\text{out},c}$	Complex SAR output signal after processing with corrected (target-dependent) filter
s_d	Daily transponder drift
S_{out}	Frequency domain representation of s_{out}
$ s_{\text{out}} ^2$	Square-law detected SAR image
$ s_{\text{out},e} ^2$	Square-law detected SAR image of a point target with a normalized point-spread function
S_r	Frequency domain representation of s_r
s_r	Received complex raw SAR data
s'_r	Received SAR pulse
$S_{r,a}$	Azimuth component of S_r
$s_{r,a}$	Received complex raw SAR data, azimuth component
$s'_{r,b}$	Received baseband SAR pulse
$S_{r,r}$	Range component of S_r
$s_{r,r}$	Received complex raw SAR data, range component
s_t	Transmit pulse
$S(t_a)$	Range-compressed complex reflectivity at azimuth time t_a
T	Pulse length; window size; test statistic
\mathcal{T}	Total electron content
t	Time; step index in MCMC iterations
T_a	Azimuth integration time
T_r	(Range) pulse length
t_r	Range (fast) time
t_a	Azimuth (slow) time
\tilde{x}	Noisy observation of \tilde{P}_X , in linear domain
U	Uniform distribution
U	Expanded uncertainty; random variable
u	Standard uncertainty
u_c	Combined standard uncertainty
v	Along-track velocity of a SAR sensor

w_a	Azimuth weighting function
w_{box}	Rectangular (boxcar) window
$w_c(t)$	General cosine window function
w_{DCR}	Backscatter amplitude envelope of a 1.0 m dihedral corner reflector
w_{CR15}	Backscatter amplitude envelope of a 1.5 m trihedral corner reflector
w_{CR28}	Backscatter amplitude envelope of a 2.8 m trihedral corner reflector
w_{field}	Backscatter amplitude envelope of a flashing field
W_g	Frequency domain representation of $w_g(t)$
$w_g(t)$	Weighting (window/envelope) function of g
W_h	Frequency domain representation of $w_h(t)$
$w_h(t)$	Weighting function of h
$w_k(t)$	Kaiser window function
w_r	(Range) pulse envelope/weighting function
w_{rect}	Backscatter amplitude envelope of an ideal target
W_s	Frequency domain representation of w_s
w_s	Envelope function of s_r
w_{snow}	Backscatter amplitude envelope of dry snow
X	Random variable; 3TM transponder operated as a radar instrument
x	First coordinate in a Cartesian coordinate system; observation; continuous variable
\tilde{X}	Standard normal random variable
\mathbf{X}	Vector of 3TM observations
x_A	3TM observation A
x_B	3TM observation B
x_C	3TM observation C
X_i	Input quantity i to measurement model; component of vector \mathbf{X}
x_i	Estimate of input quantity i to measurement model
Y	Output quantity from measurement model; 3TM transponder operated as a radar target; random variable
y	Estimate of output quantity Y ; second coordinate in a Cartesian coordinate system; continuous variable; data/observations
$y_{d,15}$	Observations for day d and target group "1.5 m corners"
$y_{d,30}$	Observations for day d and target group "3.0 m corners"
$y_{d,g}$	Observations for day d and target group g
$y_{d,t}^{\text{rep}}$	Observations for day d and target group "transponders"
$y_{d,t}$	Posterior predicted transponder data for day d
Z	Random variable
z	Continuous variable; third coordinate in a Cartesian coordinate system
\tilde{Z}	Random variable

Bibliography

- [1] Milton Abramowitz and Irene A. Stegun, eds. *Handbook of Mathematical Functions with Formulas, Graphs, and Mathematical Tables*. 10th ed. National Bureau of Standards, 1972.
- [2] Simpson B. Adler and Robert S. Johnson. “New Backscattering Computation and Tables for Dielectric and Metal Spheres”. In: *Applied Optics* 1.5 (Sept. 1962), pp. 655–660.
- [3] *ALOS Data Users Handbook*. Tech. rep. Revision C. Japan Aerospace Exploration Agency, 2008.
- [4] Jørgen Appel-Hansen. “Accurate Determination of Gain and Radiation Patterns by Radar Cross-Section Measurements”. In: *IEEE Transactions on Antennas and Propagation* AP-27.5 (Sept. 1979), pp. 640–646.
- [5] Kai Oliver Arras. *An Introduction to Error Propagation: Derivation, Meaning, and Examples of Equation $C_y = F_x C_x F_x^T$* . Tech. rep. September. École Polytechnique Fédérale de Lausanne, 1998.
- [6] Array Systems Computing Inc. *Synthetic Aperture Radar Simulation ToolBox*. On-line: http://www.array.ca/applications/radar/sar_toolbox.php (accessed on Jul. 3, 2011).
- [7] M. Aulard-Macler. *Sentinel-1 Product Definition*. Tech. rep. MacDonald, Dettwiler and Associates, 2011.
- [8] R. M. Axline, G. R. Sloan, and R. E. Spalding. “Radar Transponder Apparatus and Signal Processing Technique”. U.S. pat. 5486830. Jan. 23, 1996.
- [9] Christian G. Bachman. *Radar Targets*. Lexington Books, 1982.
- [10] Markus Bachmann, Marco Schwerdt, and Benjamin Bräutigam. “Accurate Antenna Pattern Modeling for Phased Array Antennas in SAR Applications – Demonstration on TerraSAR-X”. In: *International Journal of Antennas and Propagation* (Mar. 2009), pp. 1–9.
- [11] Markus Bachmann, Marco Schwerdt, and Benjamin Bräutigam. “TerraSAR-X Antenna Calibration and Monitoring Based on a Precise Antenna Model”. In: *IEEE Transactions on Geoscience and Remote Sensing* 48.2 (Feb. 2010), pp. 690–701.
- [12] Nicolas Baghdadi, Mohammad El Hajj, Pascale Dubois-Fernandez, Mehrez Zribi, Gilles Belaud, and Bruno Cheviron. “Signal Level Comparison Between TerraSAR-X and COSMO-SkyMed SAR Sensors”. In: *IEEE Geoscience and Remote Sensing Letters* 99 (July 2014).
- [13] Constantine A. Balanis. *Advanced Engineering Electromagnetics*. 2nd ed. John Wiley & Sons, 2012.

- [14] Constantine A. Balanis, ed. *Modern Antenna Handbook*. John Wiley & Sons, 2008.
- [15] M. J. Bayarri and J. O. Berger. "The Interplay of Bayesian and Frequentist Analysis". In: *Statistical Science* 19.1 (Feb. 2004), pp. 58–80.
- [16] Haym Benaroya, Seon Mi Han, and Mark Nagurka. *Probability Models in Engineering and Science*. CRC Press, 2005.
- [17] U. Benz, K. Strodl, and A. Moreira. "A Comparison of Several Algorithms for SAR Raw Data Compression". In: *IEEE Transactions on Geoscience and Remote Sensing* 33.5 (Sept. 1995), pp. 1266–1276.
- [18] Michael S. Bessell. "Standard Photometric Systems". In: *Annual Review of Astronomy and Astrophysics* 43.1 (Sept. 2005), pp. 293–336.
- [19] John Bird. *Higher Engineering Mathematics*. 5th ed. Newnes, 2006.
- [20] William M. Bolstad. *Introduction to Bayesian Statistics*. 2nd ed. John Wiley & Sons, 2007.
- [21] Benjamin Bräutigam. "Instrument Calibration of Spaceborne SAR Systems". Dissertation. Fakultät für Elektrotechnik und Informationstechnik, Karlsruher Institut für Technologie, 2014.
- [22] Benjamin Bräutigam, Jaime Hueso González, Marco Schwerdt, and Markus Bachmann. "TerraSAR-X Instrument Calibration Results and Extension for TanDEM-X". In: *IEEE Transactions on Geoscience and Remote Sensing* 48.2 (Feb. 2010), pp. 702–715.
- [23] H. Breit, B. Schättler, T. Fritz, U. Balss, H. Damerow, and E. Schwarz. "TerraSAR-X Payload Data Processing: Results from Commissioning and Early Operational Phase". In: *IEEE International Geoscience and Remote Sensing Symposium* (July 2008), pp. 209–212.
- [24] Helko Breit, Thomas Fritz, Ulrich Balss, Marie Lachaise, Andreas Niedermeier, and Martin Vonavka. "TerraSAR-X SAR Processing and Products". In: *IEEE Transactions on Geoscience and Remote Sensing* 48.2 (Feb. 2010), pp. 727–740.
- [25] Andreas R. Brenner. "Improved Radar Imaging by Centimeter Resolution Capabilities of the Airborne SAR Sensor PAMIR". In: *14th International Radar Symposium*. 2013, pp. 218–223.
- [26] P. A. Bromiley. *Products and Convolutions of Gaussian Probability Density Functions*. Tech. rep. 2003. Image Sciences Research Group, University of Manchester, Aug. 2014.
- [27] David R. Brunfeldt and Fawwaz T. Ulaby. "Active Reflector for Radar Calibration". In: *IEEE Transactions on Geoscience and Remote Sensing* GE-22.2 (Mar. 1984), pp. 165–169.
- [28] Emmanuel Candes. *Stats 300C: Theory of Statistics – Lecture 13*. Course notes. Stanford University, 2014.
- [29] Working group members of the CEOS WGCV-SAR. *CEOS 2015 Draft Recommendation: Equivalent Radar Cross Section (ERCS)*. Oct. 2015. URL: <http://sarcv.ceos.org/documents/doc/150/> (visited on 12/15/2015).
- [30] Richard Charnigo and Cidambi Srinivasan. "Stein's Phenomenon". In: *Philosophy of Statistics*. Ed. by Prasanta S. Bandyopadhyay and Malcolm R. Forster. Elsevier, 2011.

- [31] Peter Congdon. *Bayesian Models for Categorical Data*. John Wiley & Sons, 2007.
- [32] Ian G. Cumming and Frank H. Wong. *Digital Processing Of Synthetic Aperture Radar Data: Algorithms And Implementation*. Artech House, 2005.
- [33] John C. Curlander. *Synthetic Aperture Radar: Systems and Signal Processing*. John Wiley & Sons, 1991.
- [34] Andreas Danklmayer, Björn J. Döring, Marco Schwerdt, and Madhu Chandra. "Assessment of Atmospheric Propagation Effects in SAR Images". In: *IEEE Transactions on Geoscience and Remote Sensing* 47.10 (Oct. 2009), pp. 3507–3518.
- [35] Davide D'Aria, Alessandro Ferretti, Andrea Monti Guarnieri, and Stefano Tebaldini. "SAR Calibration Aided by Permanent Scatterers". In: *IEEE Transactions on Geoscience and Remote Sensing* 48.4 (Apr. 2010), pp. 2076–2086.
- [36] Wilbur B. Davenport and William L. Root. *An Introduction to the Theory of Random Signals and Noise*. IEEE-Wiley, 1987.
- [37] Francesco De Zan and Andrea Monti Guarnieri. "TOPSAR: Terrain Observation by Progressive Scans". In: *IEEE Transactions on Geoscience and Remote Sensing* 44.9 (Sept. 2006), pp. 2352–2360.
- [38] Stuart R. Degraaf. "Sidelobe Reduction via Adaptive FIR Filtering in SAR Imagery." In: *IEEE Transactions on Image Processing* 3.3 (Jan. 1994), pp. 292–301.
- [39] Björn J. Döring, Philipp Looser, Matthias Jirousek, and Marco Schwerdt. "Point Target Correction Coefficients for Absolute SAR Calibration". In: *IEEE Instrumentation and Measurement Technology Conference*. May 2011, pp. 1087–1092.
- [40] Björn J. Döring, Philipp Looser, Matthias Jirousek, and Marco Schwerdt. "Reference Target Correction Based on Point Target SAR Simulation". In: *IEEE Transactions on Geoscience and Remote Sensing* 50.3 (Mar. 2012), pp. 951–959.
- [41] Björn J. Döring, Philipp Looser, Matthias Jirousek, Marco Schwerdt, and Markus Peichl. "Highly Accurate Calibration Target for Multiple Mode SAR Systems". In: *Proceedings of the European Conference on Synthetic Aperture Radar*. June 2010.
- [42] Björn J. Döring, Jens Reimann, Sebastian Raab, Matthias Jirousek, Daniel Rudolf, and Marco Schwerdt. "Accurate Transponder Calibrations with the Novel Three-Transponder Method". In: *Advanced SAR Workshop*. Canadian Space Agency, Oct. 2015.
- [43] Björn J. Döring, Jens Reimann, Sebastian Raab, Matthias Jirousek, Daniel Rudolf, and Marco Schwerdt. "Accurate Transponder Calibrations with the Novel Three-Transponder Method". In: *CEOS SAR Workshop*. CEOS WGCV – SAR Subgroup, Oct. 2015.
- [44] Björn J. Döring, Jens Reimann, Sebastian Raab, Matthias Jirousek, Daniel Rudolf, and Marco Schwerdt. "The Three-Transponder Method: A Novel Method for Accurate Transponder RCS Calibration". In: *Progress In Electromagnetics Research B* 61 (Dec. 2014), pp. 297–315.
- [45] Björn J. Döring, Kersten Schmidt, Matthias Jirousek, Daniel Rudolf, Jens Reimann, Sebastian Raab, John Walter Antony, and Marco Schwerdt. "Hierarchical Bayesian Data Analysis in Radiometric SAR System Calibration: A Case Study on Transponder Calibration with RADARSAT-2 Data". In: *Remote Sensing* 5.12 (Dec. 2013), pp. 6667–6690.

- [46] Björn J. Döring, Dirk Schrank, Marco Schwerdt, and Robert Bauer. "Absolute Radiometric Calibration of TerraSAR-X – Approach and Ground Targets". In: *German Microwave Conference*. VDE, Mar. 2008, pp. 1–4.
- [47] Björn J. Döring and Marco Schwerdt. "Are Pixel Intensities Proportional to Radar Cross Section in SAR Images?" In: *IEEE International Geoscience and Remote Sensing Symposium*. IEEE, July 2012, pp. 3309–3311.
- [48] Björn J. Döring and Marco Schwerdt. "Equivalent Radar Cross Section: What Is It and Why Is It Important?" In: *CEOS SAR Workshop*. CEOS WGCV – SAR Subgroup, Oct. 2015.
- [49] Björn J. Döring and Marco Schwerdt. "Introducing Equivalent Radar Cross Section – A First Step Toward new Radiometric Requirement Definitions". In: *Proceedings of the European Conference on Synthetic Aperture Radar*. Committee on Earth Observation Satellites (CEOS) Working Group on Calibration and Validation (WGCV) – SAR Subgroup Workshop was held jointly. June 2014.
- [50] Björn J. Döring and Marco Schwerdt. "Learning from the Field of Photometry: The Way Towards Better Radiometric Measurements". In: *CEOS SAR Workshop*. CEOS WGCV – SAR Subgroup, Oct. 2013.
- [51] Björn J. Döring and Marco Schwerdt. "The Radiometric Measurement Quantity for SAR Images". In: *IEEE Transactions on Geoscience and Remote Sensing* 51.12 (Feb. 2013), pp. 5307–5314.
- [52] Björn J. Döring and Marco Schwerdt. "The SAR Passband Problem: Analytical Model and Possible Practical Solutions". In: *IEEE Transactions on Geoscience and Remote Sensing* (in press).
- [53] Björn Döring, Marco Schwerdt, Matthias Jirousek, Daniel Rudolf, Jens Reimann, and Sebastian Raab. "Verfahren zur absoluten radiometrischen Kalibrierung des Radarrückstreuquerschnitts von Radarzielen". German pat. DE 10 2014 110 079 B3 (Germany). July 9, 2015.
- [54] Robert B. Dybdal. "Radar Cross Section Measurements". In: *Proceedings of the IEEE* 75.4 (Apr. 1987), pp. 498–516.
- [55] Bradley Efron and Carl Morris. "Stein's Estimation Rule and Its Competitors – An Empirical Bayes Approach". In: *Journal of the American Statistical Association* 68.341 (1973).
- [56] Charles Elachi and Jakob van Zyl. *Introduction to the Physics and Techniques of Remote Sensing*. John Wiley & Sons, 2006.
- [57] S. Falzini, V. Speziale, and E. De Viti. "COSMO-SkyMed Active Calibrator: A Sophisticated Tool for SAR Image Calibration". In: *2007 IEEE International Geoscience and Remote Sensing Symposium* (July 2007), pp. 1577–1580.
- [58] L. J. Foged, M. Sierra-Castaner, and L. Scialacqua. "Facility Comparison Campaigns within EurAAP". In: *European Conference on Antennas and Propagation*. IEEE, July 2011.
- [59] G. Fornaro, G. Franceschetti, and S. Perna. "Motion Compensation Errors: Effects on the Accuracy of Airborne SAR images". In: *IEEE Transactions on Aerospace and Electronic Systems* 41.4 (Oct. 2005), pp. 1338–1352.

- [60] Giorgio Franceschetti, Maurizio Migliaccio, Daniele Riccio, and Gilda Schirinzi. "SARAS: A Synthetic Aperture Radar (SAR) Raw Signal Simulator". In: *IEEE Transactions on Geoscience and Remote Sensing* 30.1 (July 1992), pp. 110–123.
- [61] Anthony Freeman. "SAR Calibration: An Overview". In: *IEEE Transactions on Geoscience and Remote Sensing* 30.6 (Nov. 1992), pp. 1107–1121.
- [62] Anthony Freeman, Yuhshyen Shen, and Charles L. Werner. "Polarimetric SAR Calibration Experiment using Active Radar Calibrators". In: *IEEE Transactions on Geoscience and Remote Sensing* 28.7 (Mar. 1990), pp. 224–240.
- [63] Thomas Fritz and Michael Eineder. *TerraSAR-X: Basic Product Specification Document*. Tech. rep. Issue 1.6. DLR (German Aerospace Center), Mar. 2009.
- [64] Masaharu Fujita, Toshihiro Masuda, and Yoshiyuki Fujino. "Polarimetric Calibration of the SIR-C C-Band Channel using Active Radar Calibrators and Polarization Selective Dihedrals". In: *IEEE Transactions on Geoscience and Remote Sensing* 36.6 (Nov. 1998), pp. 1872–1878.
- [65] Andrew Gelman, John B. Carlin, Hal S. Stern, David B. Dunson, Aki Vehtari, and Donald B. Rubin. *Bayesian Data Analysis*. 3rd ed. Chapman & Hall/CRC, 2013.
- [66] Andrew Gelman, John B. Carlin, Hal S. Stern, and Donald B. Rubin. *Bayesian Data Analysis*. 2nd ed. Chapman & Hall/CRC, 2004.
- [67] Walton C. Gibson. *The Method of Moments in Electromagnetics*. Chapman and Hall/CRC, Nov. 2008.
- [68] J. Gorrone and F. Gascon. "ESA Sentinel-2 Radiometric Uncertainty: Level 2". In: *Proceedings of the 2013 ESA Living Planet Symposium*. European Space Agency, Sept. 2013.
- [69] A. Laurence Gray, Paris W. Vachon, Charles E. Livingstone, and Tom I. Lukowski. "Synthetic Aperture Radar Calibration using Reference Reflectors". In: *IEEE Transactions on Geoscience and Remote Sensing* 28.3 (May 1990), pp. 374–383.
- [70] Phil Gregory. *Bayesian Logical Data Analysis for the Physical Sciences*. Cambridge University Press, 2005.
- [71] T. Griesser and C. Balanis. "Backscatter Analysis of Dihedral Corner Reflectors using Physical Optics and the Physical Theory of Diffraction". In: *IEEE Transactions on Antennas and Propagation* AP-35.10 (Oct. 1987), pp. 1137–1147.
- [72] Charles Miller Grinstead and James Laurie Snell. *Introduction to Probability*. 2nd ed. American Mathematical Society, 2012.
- [73] Irena Hajnsek, Thomas Jagdhuber, Helmut Schön, and Konstantinos Panagiotis Papathanassiou. "Potential of Estimating Soil Moisture under Vegetation Cover by means of PolSAR". In: *IEEE Transactions on Geoscience and Remote Sensing* 47.2 (Feb. 2009), pp. 442–454.
- [74] Frederic J. Harris. "On the Use of Windows for Harmonic Analysis with the Discrete Fourier Transform". In: *Proceedings of the IEEE* 66.1 (Jan. 1978), pp. 51–83.
- [75] R. K. Hawkins, L. D. Teany, S. Srivastava, and S. Y. K. Tam. "RADARSAT Precision Transponder". In: *Advances in Space Research* 19.9 (Jan. 1997), pp. 1455–1465.

- [76] Anthony Hayter. *Probability and Statistics for Engineers And Scientists*. 4th ed. Brooks/Cole, 2012.
- [77] Eugene Hecht. *Optics*. 4th ed. Addison-Wesley, 2001.
- [78] T. J. Hestilow. "Simple Formulas for the Calculation of the Average Physical Optics RCS of a Cylinder and a Flat Plate over a Symmetric Window around Broadside". In: *IEEE Antennas and Propagation Magazine* 42.5 (Oct. 2000), pp. 48–52.
- [79] Peter D. Hoff. *Shrinkage Estimators*. Course notes. University of Washington, 2012.
- [80] K. Hongo. "Diffraction of Electromagnetic Wave by Disk and Circular Hole in a Perfectly Conducting Plane". In: *Progress In Electromagnetics Research* 68 (2007), pp. 113–150.
- [81] David Hounam and Karl-Hans Waegel. "Method and Device for Locating and Identifying Objects by Means of an Encoded Transponder". U.S. pat. 5821895. Oct. 13, 1998.
- [82] David Hounam and Karl-Hans Wägel. "A Technique for the Identification and Localization of SAR Targets Using Encoding Transponders". In: *IEEE Transactions on Geoscience and Remote Sensing* 39.1 (Jan. 2001), pp. 3–7.
- [83] IEEE. *IEEE Standard Letter Designations for Radar-Frequency Bands*. IEEE Std 512-2002. Institute of Electrical and Electronics Engineers, 2002.
- [84] IEEE. *IEEE Standard Test Procedures for Antennas*. ANSI/IEEE Std 149-1979 (R2008). Institute of Electrical and Electronics Engineers, 2008.
- [85] IEEE. *The Authoritative Dictionary of IEEE Standards Terms*. IEEE Std 100-2000. Institute of Electrical and Electronics Engineers, 2000.
- [86] Akira Ishimaru, Tsz-King Chan, and Yasuo Kuga. "An Imaging Technique using Confocal Circular Synthetic Aperture Radar". In: *IEEE Transactions on Geoscience and Remote Sensing* 36.5 (Sept. 1998), pp. 1524–1530.
- [87] JCGM. *Evaluation of measurement data – Guide to the Expression of Uncertainty in Measurement*. ISO/IEC Guide 98-3:2008. Joint Committee for Guides in Metrology, 2008.
- [88] Alan Julian Izenman. *Modern Multivariate Statistical Techniques: Regression, Classification, and Manifold Learning*. Springer, 2008.
- [89] Harry D. Jackson and Alan Woode. "Development of the ERS-1 Active Radar Calibration Unit". In: *IEEE Transactions on Microwave Theory and Techniques* 40.6 (June 1992).
- [90] Harry Jackson, Ian Sinclair, and Sebastian Tam. "ENVISAT/ASAR Precision Transponders". In: *Proceedings of the CEOS SAR Workshop*. 1999.
- [91] W. James and C. Stein. "Estimation with Quadratic Loss". In: *Proceedings of the Fourth Berkeley Symposium on Mathematical Statistics and Probability*. 1961.
- [92] JCGM. *International Vocabulary of Metrology – Basic and General Concepts and Associated Terms (VIM)*. JCGM 200. Joint Committee for Guides in Metrology, 2008.
- [93] Matthias Jirousek, Björn Döring, Daniel Rudolf, Sebastian Raab, and Marco Schwerdt. "Development of the Highly Accurate DLR Kalibri Transponder". In: *Proceedings of the European Conference on Synthetic Aperture Radar*. June 2014.

- [94] R. L. Jordan, B. L. Huneycutt, and M. Werner. "The SIR-C/X-SAR Synthetic Aperture Radar System". In: *IEEE Transactions on Geoscience and Remote Sensing* 33.4 (July 1995), pp. 829–839.
- [95] R. Kacker and A. Jones. "On use of Bayesian Statistics to Make the Guide to the Expression of Uncertainty in Measurement Consistent". In: *Metrologia* 40 (Sept. 2003).
- [96] Jung Hyo Kim, Marwan Younis, Alberto Moreira, and Werner Wiesbeck. "A Novel OFDM Chirp Waveform Scheme for Use of Multiple Transmitters in SAR". In: *IEEE Geoscience and Remote Sensing Letters* 10.3 (2013), pp. 568–572.
- [97] Jung-hyo Kim, Thomas Fügen, Christoph Heer, and Rolf Werninghaus. "Digital Calibration for HRWS SAR". In: *Proceedings of the European Conference on Synthetic Aperture Radar*. VDE Verlag GmbH, June 2014, pp. 118–120.
- [98] Helmut Klausing and Wolfgang Holpp. *Radar mit realer und synthetischer Apertur: Konzeption und Realisierung*. Oldenbourg Wissenschaftsverlag GmbH, 2000.
- [99] Kees van't Klooster, Björn Rommen, and Alexander Volvach. "Observation of Radiotelescope RT22 CrAO with the Synthetic Aperture Radar ENVISAT from Space". In: *Crimean Conference "Microwave & Telecommunication Technology"*. Jan. 2012, pp. 1057–1058.
- [100] Eugene F. Knott, John F. Shaeffer, and Michael T. Tuley. *Radar Cross Section*. 2nd ed. SciTech Publishing, 2004.
- [101] G. Krieger, I. Hajnsek, K. Papathanassiou, M. Eineder, M. Younis, F. De Zan, P. Prats, S. Huber, M. Werner, H. Fiedler, A. Freeman, P. Rosen, S. Hensley, W. Johnson, L. Villeux, B. Grafmueller, R. Werninghaus, R. Bamler, and A. Moreira. "The Tandem-L Mission Proposal: Monitoring Earth's Dynamics with High Resolution SAR Interferometry". In: *IEEE Radar Conference JUNE* (June 2009), pp. 1–6.
- [102] Gerhard Krieger. "MIMO-SAR : Opportunities and Pitfalls". In: *IEEE Transactions on Geoscience and Remote Sensing* 52.5 (2014), pp. 2628–2645.
- [103] Gerhard Krieger, Alberto Moreira, Hauke Fiedler, Irena Hajnsek, Marian Werner, Marwan Younis, and Manfred Zink. "TanDEM-X: A Satellite Formation for High-Resolution SAR Interferometry". In: *IEEE Transactions on Geoscience and Remote Sensing* 45.11 (Nov. 2007), pp. 3317–3341.
- [104] John K. Kruschke. *Doing Bayesian Data Analysis: A Tutorial with R and BUGS*. Elsevier, 2011.
- [105] Hiroshi Kumagai, Toshiaki Kozu, Makoto Satake, Hiroshi Hanado, and Ken'ichi Okamoto. "Development of an Active Radar Calibrator for the TRMM Precipitation Radar". In: *IEEE Transactions on Geoscience and Remote Sensing* 33.6 (Nov. 1995), pp. 1316–1318.
- [106] Wolfgang H. Kummer and Edmond S. Gillespie. "Antenna Measurements – 1978". In: *Proceedings of the IEEE* 66.4 (Apr. 1978).
- [107] Jan de Leeuw and Erik Meijer. *Handbook of Multilevel Analysis*. Springer, 2008.
- [108] Rainer Lenz. "Hochpräzise, kalibrierte Transponder und Bodenempfänger für satellitengestützte SAR-Missionen". PhD thesis. Institut für Höchstfrequenztechnik und Elektronik, Universität Karlsruhe (TH), 2007.

- [109] Rainer Lenz, Karin Schuler, Marwan Younis, and Werner Wiesbeck. "TerraSAR-X Active Radar Ground Calibrator System". In: *IEEE Aerospace and Electronic Systems Magazine* May (2006), pp. 30–33.
- [110] Charles S. Liang, Donald A. Streater, Jian-Ming Jin, Eric Dunn, and Timothy Rozendal. "A Quantitative Study of Luneberg-Lens Reflectors". In: *IEEE Antennas and Propagation Magazine* 47.2 (Apr. 2005), pp. 30–41.
- [111] Rudolf Karl Luneburg and Max Herzberger. *Mathematical Theory of Optics*. University of California Press, 1944.
- [112] Anthony Luscombe. "Image Quality and Calibration of RADARSAT-2". In: *IEEE International Geoscience and Remote Sensing Symposium* (July 2009), pp. 757–760.
- [113] Anthony P. Luscombe and Alan A. Thompson. "RADARSAT-2 Calibration: Proposed Targets and Techniques". In: *IEEE International Geoscience and Remote Sensing Symposium* (July 2001), pp. 496–498.
- [114] Soren Madsen. "Spectral Properties of Homogeneous and Nonhomogeneous Radar Images". In: *IEEE Transactions on Aerospace and Electronic Systems* AES-23.4 (July 1987), pp. 583–588.
- [115] D. Massonnet and J. C. Souyris. *Imaging with Synthetic Aperture Radar*. CRC Press, 2008.
- [116] G. L. Matthaei, Leo Young, and E. M. T. Jones. *Microwave Filters, Impedance Matching Networks and Coupling Structures*. Artech House, 1980.
- [117] John Peter Merryman Boncori and Giovanni Schiavon. "Signal Processing Issues for the Exploitation of Pulse-to-Pulse Encoding SAR Transponders". In: *IEEE Transactions on Geoscience and Remote Sensing* 46.4 (May 2008), pp. 1048–1057.
- [118] Adriano Meta, Josef Mittermayer, Pau Prats, Rolf Scheiber, and Ulrich Steinbrecher. "TOPS Imaging with TerraSAR-X: Mode Design and Performance Analysis". In: *IEEE Transactions on Geoscience and Remote Sensing* 48.2 (Feb. 2010), pp. 759–769.
- [119] Nicholas Metropolis, Arianna W. Rosenbluth, Marshall N. Rosenbluth, Augusta H. Teller, and Edward Teller. "Equation of State Calculations by Fast Computing Machines". In: *The Journal of Chemical Physics* 21.6 (June 1953), pp. 1087–1092.
- [120] Franz Meyer, Richard Bamler, Norbert Jakowski, and Thomas Fritz. "The Potential of Broadband L-Band SAR Systems for Small Scale Ionospheric TEC Mapping". In: *ESA Fringe 2005 Workshop* (Dec. 2005).
- [121] Douglas C. Montgomery and George C. Runger. *Applied Statistics and Probability for Engineers*. 6th ed. John Wiley & Sons, 2014.
- [122] Alberto Moreira. "Radar mit synthetischer Apertur: Grundlagen und Signalverarbeitung". Habilitation thesis. Fakultät für Elektrotechnik und Informationstechnik, Universität Fridericiana zu Karlsruhe, 2000.
- [123] Alberto Moreira and Yonghong Huang. "Airborne SAR Processing of Highly Squinted Data using a Chirp Scaling Approach with Integrated Motion Compensation". In: *IEEE Transactions on Geoscience and Remote Sensing* 32.5 (Sept. 1994), pp. 1029–1040.

- [124] Alberto Moreira, Pau Prats-Iraola, Marwan Younis, Gerhard Krieger, Irena Hajnsek, and Konstantinos P. Papathanassiou. "A Tutorial on Synthetic Aperture Radar". In: *Geoscience and Remote Sensing Magazine* (Apr. 2013).
- [125] L. C. Morena, K. V. James, and J. Beck. "An introduction to the RADARSAT-2 Mission". In: *Canadian Journal of Remote Sensing* 30.3 (June 2004), pp. 221–234.
- [126] Samuel P. Morgan. "General Solution of the Luneberg Lens Problem". In: *Journal of Applied Physics* 29.9 (Sept. 1958), pp. 1358–1368.
- [127] A. Newell, R. Baird, and P. Wacker. "Accurate Measurement of Antenna Gain and Polarization at Reduced Distances by an Extrapolation Technique". In: *IEEE Transactions on Antennas and Propagation* AP-21.4 (July 1973).
- [128] Michael E. Nord, Thomas L. Ainsworth, Jong-Sen Lee, and Nick J. S. Stacy. "Comparison of Compact Polarimetric Synthetic Aperture Radar Modes". In: *IEEE Transactions on Geoscience and Remote Sensing* 47.1 (Jan. 2009), pp. 174–188.
- [129] Armin W. Oerry and Billy C. Brock. *Radar Cross Section of Triangular Trihedral Reflector with Extended Bottom Plate*. Tech. rep. Albuquerque, New Mexico: Sandia National Laboratories, May 2009.
- [130] OIML. *International Vocabulary of Terms in Legal Metrology*. International Organization of Legal Metrology, 2000.
- [131] Chris Oliver and Shaun Quegan. *Understanding Synthetic Aperture Radar Images*. SciTech Publishing, 2004.
- [132] Alan V. Oppenheim and George C. Verghese. "Random Processes". In: *Signals, Systems and Inference*. Massachusetts Institute of Technology, 2010. Chap. 9.
- [133] Michael D. Perlman and Sanjay Chaudhuri. "Reversing the Stein Effect". In: *Statistical Science* 27.1 (Mar. 2012), pp. 135–143.
- [134] Simone Pettinato, Emanuele Santi, Simonetta Paloscia, Paolo Pampaloni, and Giacomo Fontanelli. "The Intercomparison of X-Band SAR Images from COSMO-SkyMed and TerraSAR-X Satellites: Case Studies". In: *Remote Sensing* 5.6 (June 2013), pp. 2928–2942.
- [135] Octavio Ponce, Pau Prats-Iraola, Muriel Pinheiro, Marc Rodríguez-Cassola, Rolf Scheiber, Andreas Reigber, and Alberto Moreira. "Fully Polarimetric High-Resolution 3-D Imaging with Circular SAR at L-Band". In: *IEEE Transactions on Geoscience and Remote Sensing* 52.6 (June 2014), pp. 3074–3090.
- [136] Pau Prats, Rolf Scheiber, Josef Mittermayer, Adriano Meta, and Alberto Moreira. "Processing of Sliding Spotlight and TOPS SAR Data using Baseband Azimuth Scaling". In: *IEEE Transactions on Geoscience and Remote Sensing* 48.2 (Feb. 2010), pp. 770–780.
- [137] Pau Prats-Iraola, Rolf Scheiber, Marc Rodríguez-Cassolà, Steffen Wollstadt, Josef Mittermayer, Benjamin Bräutigam, Marco Schwerdt, Andreas Reigber, and Alberto Moreira. "High Precision SAR Focusing of TerraSAR-X Experimental Starving Spotlight Data". In: *Proceedings of the IEEE International Geoscience and Remote Sensing Symposium* (July 2012).
- [138] S. Quegan, F. Rocca, and S. Saatchi. "The BIOMASS Mission – An ESA Earth Explorer Candidate to Measure the Biomass of the Earth's Forests". In: *IEEE International Geoscience and Remote Sensing Symposium* (July 2010), pp. 52–55.

- [139] Sebastian Raab. "Planung und Durchführung einer Freifeld-RCS-Messreihe zur genauen Kalibrierung von Referenzzielen". Master's thesis. Hochschule für angewandte Wissenschaften Würzburg-Schweinfurt, 2013.
- [140] Sebastian Raab. *Transponderausrichtung bei der Drei-Transponder-Methode: Anleitung und Protokoll zur Kampagne im Dezember 2013*. Tech. rep. Issue 1.0. DLR (German Aerospace Center), Jan. 2014.
- [141] *RADARSAT-2 Product Format Definition*. Tech. rep. 1/9. RN-RP-51-2713. MacDonald, Dettwiler and Associates, Jan. 2011.
- [142] Simon Ramo, John R. Whinnery, and Theodore Von Duzer. *Fields and Waves in Communication Electronics*. 3rd ed. John Wiley & Sons, 1994.
- [143] R. Raney. "SAR Response to Partially Coherent Phenomena". In: *IEEE Transactions on Antennas and Propagation* 28.6 (1980), pp. 777–787.
- [144] R. K. Raney, T. Freeman, R. W. Hawkins, and R. Bamler. "A Plea for Radar Brightness". In: *IEEE International Geoscience and Remote Sensing Symposium* (Aug. 1994), pp. 1090–1092.
- [145] Carl Edward Rasmussen and Christopher K. I. Williams. *Gaussian Processes for Machine Learning*. Vol. 14. 2. MIT Press, 2006.
- [146] A. Reigber, M. Jäger, J. Fischer, R. Horn, R. Scheiber, P. Prats, and A. Nottensteiner. "System Status and Calibration of the F-SAR Airborne SAR Instrument". In: *2011 IEEE International Geoscience and Remote Sensing Symposium*. IEEE, July 2011, pp. 1520–1523.
- [147] *Report for Mission Selection: BIOMASS. An Earth Explorer to Observe Forest Biomass*. Tech. rep. European Space Agency, 2012.
- [148] *RADARSAT-2 Product Description*. 1/9. MacDonnald, Dettwiler and Associates. 2011.
- [149] Paul A. Rosen, Scott Hensley, Ian R. Joughin, Fuk K. Li, Soren N. Madsen, Ernesto Rodriguez, and Richard M. Goldstein. "Synthetic Aperture Radar Interferometry". In: *Proceedings of the IEEE* 88.3 (Mar. 2000), pp. 333–382.
- [150] Ake Rosenqvist, Masanobu Shimada, Norimasa Ito, and Manabu Watanabe. "ALOS PALSAR: A Pathfinder Mission for Global-Scale Monitoring of the Environment". In: *IEEE Transactions on Geoscience and Remote Sensing* 45.11 (Nov. 2007), pp. 3307–3316.
- [151] B. Rosich and P. Meadows. *Absolute Calibration of ASAR Level 1 Products Generated with PF-ASAR*. Tech. rep. 1. European Space Agency, ESRIN, 2004.
- [152] R. A. Ross and G. N. Cohen. *Circular Polarization Scattering Coefficients for the Bistatic Scattering of Electromagnetic Waves from Perfectly Conducting Spheres*. Tech. rep. Lincoln Laboratory, Massachusetts Institute of Technology, July 1976.
- [153] Sheldon M. Ross. *Introductory Statistics*. 3rd ed. Academic Press, 2010.
- [154] Sheldon M. Ross. *Statistik für Ingenieure und Naturwissenschaftler*. 3rd ed. Spektrum Akademischer Verlag, 2006.
- [155] Daniel Rudolf, Björn J. Döring, Matthias Jirousek, Sebastian Raab, Jens Reimann, and Marco Schwerdt. "Absolute Radiometric Calibration of C-Band Transponders with Proven Plausibility". In: *Proceedings of the European Conference on Synthetic Aperture Radar*. Jan. 2014.

- [156] Daniel Rudolf, Sebastian Raab, Björn J. Döring, Matthias Jirousek, Jens Reimann, and Marco Schwerdt. "Absolute Radiometric Calibration of the Novel DLR "Kalibri" Transponder". In: *German Microwave Conference*. Jan. 2015, pp. 5–8.
- [157] Richard J. Samworth and Statslab Cambridge. "Stein's Paradox". In: *Eureka* 62 (Dec. 2012), pp. 38–41.
- [158] Kamal Sarabandi and Tsen-Chien Chiu. "Optimum Corner Reflectors for Calibration of Imaging Radars". In: *IEEE Transactions on Antennas and Propagation* 44.10 (Oct. 1996).
- [159] Kamal Sarabandi, Yisok Oh, and Fawwaz T. Ulaby. "Performance Characterization of Polarimetric Active Radar Calibrators and a New Single Antenna Design". In: *IEEE Transactions on Antennas and Propagation* 40.10 (Oct. 1992), pp. 1147–1154.
- [160] M. Schwerdt, K. Schmidt, N. Tous Ramon, G. Castellanos Alfonzo, B. Döring, M. Zink, and P. Prats. "Independent Verification of the Sentinel-1A System Calibration". In: *IEEE Journal of Selected Topics in Applied Earth Observations and Remote Sensing* (2015).
- [161] Marco Schwerdt, Benjamin Bräutigam, Markus Bachmann, Björn Döring, Dirk Schrank, and Jaime Hueso Gonzalez. "Final TerraSAR-X Calibration Results Based on Novel Efficient Methods". In: *IEEE Transactions on Geoscience and Remote Sensing* 48.2 (Feb. 2010), pp. 677–689.
- [162] Marco Schwerdt, Björn Döring, Manfred Zink, and Dirk Schrank. "In-Orbit Calibration Plan of Sentinel-1". In: *Proceedings of the European Conference on Synthetic Aperture Radar*. June 2010, pp. 350–353.
- [163] Marco Schwerdt, David Hounam, Josè-Luis Alvarez-Pères, and Thomas Molken-thin. "The Calibration Concept of TerraSAR-X: A Multiple-Mode, High-Resolution SAR". In: *Canadian Journal of Remote Sensing* 31.1 (Jan. 2005), pp. 30–36.
- [164] Marco Schwerdt, Jaime Hueso Gonzalez, Markus Bachmann, Dirk Schrank, Björn Döring, Nuria Tous Ramon, and John Mohan Walter Antony. "In-orbit Calibration of the TanDEM-X system". In: *IEEE International Geoscience and Remote Sensing Symposium*. 2011, pp. 2420–2423.
- [165] Marco Schwerdt, Kersten Schmidt, Nuria Tous Ramon, Gabriel Castellanos Alfonzo, Björn Döring, and Manfred Zink. "Independent Verification of the Sentinel-1A System Calibration: First Results". In: *Proceedings of the European Conference on Synthetic Aperture Radar*. VDE Verlag GmbH, June 2014, pp. 1259–1262.
- [166] Marco Schwerdt, Dirk Schrank, Markus Bachmann, Clemens Schulz, Björn Döring, and Jaime Hueso Gonzales. "TerraSAR-X Re-Calibration and Dual Receive Antenna Campaigns performed in 2009". In: *Proceedings of the European Conference on Synthetic Aperture Radar*. June 2010, pp. 218–221.
- [167] Krishnasamy T. Selvan. "A Modified Three-Antenna Gain Measurement Method To Simplify Uncertainty Estimation". In: *Progress In Electromagnetics Research* 57 (Jan. 2006), pp. 197–208.
- [168] Masanobu Shimada, Osamu Isoguchi, Takeo Tadono, and Kazuo Isono. "PAL-SAR Radiometric and Geometric Calibration". In: *IEEE Transactions on Geoscience and Remote Sensing* 47.12 (Aug. 2009), pp. 3915–3932.

- [169] J. D. Silverstein and R. Bender. "Measurements and Predictions of the RCS of Bruderhedrals at Millimeter Wavelengths". In: *IEEE Transactions on Antennas and Propagation* 45.7 (July 1997), pp. 1071–1079.
- [170] Merrill I. Skolnik, ed. *Radar Handbook*. 1st ed. McGraw-Hill, 1970.
- [171] Merrill I. Skolnik, ed. *Radar Handbook*. 3rd ed. McGraw-Hill, 2008.
- [172] Bob Slade. *RADARSAT-2 Product Description*. Tech. rep. 1/6. MacDonald, Detwiler and Associates, Nov. 2009.
- [173] David Small. "Flattening Gamma: Radiometric Terrain Correction for SAR Imagery". In: *IEEE Transactions on Geoscience and Remote Sensing* 49.8 (Aug. 2011), pp. 3081–3093.
- [174] David L. Smith, Tim J. Nightingale, Hugh Mortimer, Kevin Middleton, Ruben Edeson, Caroline V. Cox, Chris T. Mutlow, Brian J. Maddison, and Peter Coppo. "Calibration Approach and Plan for the Sea and Land Surface Temperature Radiometer". In: *Journal of Applied Remote Sensing* 8 (June 2014).
- [175] P. Snoeij, E. Attema, B. Rommen, N. Floury, M. Davidson, B. Duesmann, and D. Rowsell. "Transponder Development for Sentinel-1". In: *Proceedings of the European Conference on Synthetic Aperture Radar*. VDE VERLAG GmbH, June 2010, pp. 354–357.
- [176] T. T. Soong. *Fundamentals of Probabilities and Statistics for Engineers*. Vol. 29. John Wiley & Sons, 2004.
- [177] Mehrdad Soumekh. "Reconnaissance with Slant Plane Circular SAR Imaging". In: *IEEE Transactions on Image Processing* 5.8 (Aug. 1996), pp. 1252–1265.
- [178] Jean-Claude Souyris, Patrick Imbo, Roger Fjørtoft, Sandra Mongot, and Jong-Sen Lee. "Compact Polarimetry Based on Symmetry Properties of Geophysical Media: The $\pi/4$ Mode". In: *IEEE Transactions on Geoscience and Remote Sensing* 43.3 (Mar. 2005), pp. 634–646.
- [179] Rainer Speck. *SETES – SAR End-to-End Simulator*. Online: http://www.dlr.de/hr/en/desktopdefault.aspx/tabid-2434/3770_read-5675/ (accessed on Aug. 1, 2015).
- [180] S. K. Srivastava, S. Cote, P. Le Dantec, R. K. Hawkins, and K. Murnaghan. "RADARSAT-1 Calibration and Image Quality Evolution to the Extended Mission". In: *Advances in Space Research* 39 (Jan. 2007), pp. 7–12.
- [181] H. C. Stankwitz, R. J. Dallaire, and J. R. Fienup. "Nonlinear Apodization for Side-lobe Control in SAR Imagery". In: *IEEE Transactions on Aerospace and Electronic Systems* 31.1 (Jan. 1995), pp. 267–279.
- [182] Charles Stein. "Inadmissibility of the Usual Estimator for the Mean of a Multivariate Normal Distribution". In: *Proceedings of the Third Berkeley Symposium on Mathematical Statistics and Probability*. 4. Jan. 1956.
- [183] Charles M. Stein. "Estimation of the Mean of a Multivariate Normal Distribution". In: *The Annals of Statistics* 9.6 (Nov. 1981), pp. 1135–1151.
- [184] Julius Adams Stratton. *Electromagnetic Theory*. McGraw-Hill, 1941.
- [185] Christian Sturm and Werner Wiesbeck. "Waveform Design and Signal Processing Aspects for Fusion of Wireless Communications and Radar Sensing". In: *Proceedings of the IEEE* 99.7 (July 2011), pp. 1236–1259.

- [186] Warren L. Stutzmann and Gary A. Thiele. *Antenna Theory and Design*. 2nd ed. John Wiley & Sons, 1998.
- [187] Henry C. Thode. *Testing for Normality*. Marcel Dekker, 2002.
- [188] Manfred Thumm, Werner Wiesbeck, and Stefan Kern. *Hochfrequenzmesstechnik: Verfahren und Messsysteme*. 2nd ed. Stuttgart: Teubner, 1998.
- [189] Ramon Torres, Paul Snoeij, Dirk Geudtner, David Bibby, Malcolm Davidson, Evert Attema, Pierre Potin, Björn Rommen, Nicolas Floury, Mike Brown, Ignacio Navas Traver, Patrick Deghaye, Berthyl Duesmann, Betlem Rosich, Nuno Miranda, Claudio Bruno, Michelangelo L'Abbate, Renato Croci, Andrea Pietropaolo, Markus Huchler, and Friedhelm Rostan. "GMES Sentinel-1 Mission". In: *Remote Sensing of Environment* 120 (May 2012), pp. 9–24.
- [190] R. Touzi. "Extraction of Point Target Response Characteristics from Complex SAR Data". In: *IEEE Transactions on Geoscience and Remote Sensing* 30.6 (Nov. 1992), pp. 1158–1161.
- [191] Fawwaz T. Ulaby. *Handbook of Radar Scattering Statistics for Terrain*. Artech House, 1989.
- [192] Fawwaz T. Ulaby, Pascale C. Dubois, and Jakob van Zyl. "Radar Mapping of Surface Soil Moisture". In: *Journal of Hydrology* 4.1 (Oct. 1996).
- [193] Fawwaz T. Ulaby and David G. Long. *Microwave Radar and Radiometric Remote Sensing*. The University of Michigan Press, 2014.
- [194] L. M. H. Ulander, P. O. Frörlind, and T. Martin. "Processing and Calibration of Ultra-Wideband SAR Data from CARABAS-II". In: *CEOS SAR Workshop* (Oct. 1999), pp. 273–278.
- [195] Lars M. H. Ulander, Björn Flood, Per-Olov Frörlind, Tommy Jonsson, Anders Gustavsson, Johan Rasmusson, Gunnar Stenström, Arnold Barmettler, and Erich Meier. "Bistatic Experiment with Ultra-Wideband VHF-band Synthetic-Aperture Radar". In: *Proceedings of the European Conference on Synthetic Aperture Radar*. June 2008.
- [196] U. Wegmüller, M. Santoro, F. Mattia, A. Balenzano, G. Satalino, P. Marzahn, G. Fischer, R. Ludwig, and N. Floury. "Progress in the Understanding of Narrow Directional Microwave Scattering of Agricultural Fields". In: *Remote Sensing of Environment* 115.10 (Oct. 2011), pp. 2423–2433.
- [197] K. Weise and W. Wöger. "A Bayesian Theory of Measurement Uncertainty". In: *Measurement Science and Technology* 3 (Sept. 1992).
- [198] Rolf Werninghaus and Stefan Buckreuss. "The TerraSAR-X Mission and System Design". In: *IEEE Transactions on Geoscience and Remote Sensing* 48.2 (Nov. 2010), pp. 606–614.
- [199] Carl A. Wiley. "Synthetic Aperture Radars". In: *IEEE Transactions on Aerospace and Electronic Systems* AES-21.3 (May 1985).
- [200] Robin Willink. *Measurement Uncertainty and Probability*. Cambridge University Press, 2013.
- [201] Robin Willink and Rod White. *Disentangling Classical and Bayesian Approaches to Uncertainty Analysis*. Tech. rep. BIPM, 2012.

- [202] C. Wu. "A Digital System to Produce Imagery From SAR Data". In: *AIAA Systems Design Driven by Sensors*. Nov. 1976.
- [203] Wang Yiding and Tu Guofang. "Phase Shifting Error of Active Coded Transponder in SAR External Radiometric Calibration". In: *IEEE International Geoscience and Remote Sensing Symposium* (Aug. 2005), pp. 4150–4153.
- [204] Andrew T. Young. "Improvements to Photometry: High-Order Moments in Transformation Theory". In: *Astronomy and Astrophysics* 257 (Mar. 1992), pp. 366–388.
- [205] Marwan Younis, Johannes Boer, Carlos Ortega, Daniel Schulze, Sigurd Huber, and Josef Mittermayer. "Determining the Optimum Compromise between SAR Data Compression and Radiometric Performance: An Approach Based on the Analysis of TerraSAR-X Data". In: *International Geoscience and Remote Sensing Symposium*. IEEE, July 2008, pp. 107–110.
- [206] Marwan Younis, Christian Fischer, and Werner Wiesbeck. "Digital Beamforming in SAR Systems". In: *IEEE Transactions on Geoscience and Remote Sensing* 41.71 (July 2003), pp. 1735–1739.
- [207] Marwan Younis, Christopher Laux, Noora Al-Kahachi, Paco López-Dekker, Gerhard Krieger, and Alberto Moreira. "Calibration of Multi-Channel Spaceborne SAR: Challenges and Strategies". In: *Proceedings of the European Conference on Synthetic Aperture Radar*. June 2014, pp. 1–4.
- [208] Nazih N. Youssef. "Radar Cross Section of Complex Targets". In: *Proceedings of the IEEE* 77.5 (May 1989), pp. 722–734.
- [209] M. Zink and R. Bamler. "X-SAR Radiometric Calibration and Data Quality". In: *IEEE Transactions on Geoscience and Remote Sensing* 33.4 (July 1995), pp. 840–847.
- [210] Manfred Zink. "Kalibration von SAR-Systemen". PhD Thesis. Universität Stuttgart, 1993.
- [211] Jakob van Zyl. "On the Importance of Polarization in Radar Scattering Problems". PhD thesis. California Institute of Technology, 1986.
- [212] Jakob van Zyl and Yunjin Kim. *Synthetic Aperture Radar Polarimetry*. John Wiley & Sons, 2011.

Curriculum Vitae

Personal Information

Name	Björn J. Döring
Date of birth	July 23, 1980
Place of birth	Berlin, Germany
Citizenship	German

Education

04/2001–12/2005	Masters degree (Dipl.-Ing.) in electrical engineering from the Technical University Berlin. Main subjects: <ul style="list-style-type: none">• Theoretical electrical engineering• Communication systems• High frequency technologies
08/2013–04/2004	Exchange year at McGill University in Montreal, Canada

Work Experience

Since 01/2006	Research assistant at the German Aerospace Center (DLR): Planning and execution of calibration campaigns for <i>TerraSAR-X</i> , <i>TanDEM-X</i> , and <i>Sentinel-1</i>
since 2015	Project manager for the design and manufacturing of <i>RADARSAT Constellation Mission</i> (RCM) calibration transponders
2009–2014	Technical project manager for the development and manufacturing of accurate <i>Sentinel-1</i> calibration transponders